Universidade do Porto
Faculdade de Engenharia
FEUP

ANALYTICAL AND NUMERICAL MODELLING OF DAMAGE AND FRACTURE OF ADVANCED COMPOSITES

by

António Rui Melro

A Thesis submitted for the degree of Doctor of Philosophy of the University of Porto

February 2011

ABSTRACT

With the boom of the information age, the doors to novel techniques and more intensive computational processes have opened wide. What yesterday was impossible to achieve, today is becoming a reality. Concepts such as multiscale modelling, merging the worlds of macro- and micromechanics, are establishing themselves as viable alternatives to experimental procedures in the characterisation of the mechanical behaviour of complex materials.

Advanced composite materials are a perfect field for application of such modelling concepts. At the micro-scale level, composites exhibit two distinct phases – the fibrous reinforcements and the matrix resin. The fibres provide strength and stiffness while the matrix gives lateral support to the fibres. Micromechanics provides the means to analyse the constitutive behaviour of each of these constituents and study the influence of each one in the overall mechanical properties of the composite.

This thesis provides new tools for the micromechanical study of composite materials. An algorithm to generate a random distribution of fibres with a high fibre volume fraction is developed. The algorithm is statistically verified for the randomness of its results. The generated distributions are used to develop representative volume elements of real composite materials at the micro-scale.

The concept of periodic boundary conditions is applied throughout the thesis. This type of boundary conditions forces the continuity of the material in opposite faces of the representative volume element, as well as the continuity of the displacement field. Results from the micromechanical analyses are submitted to volumetric homogenisation to obtain the macromechanical behaviour of the homogenised composite.

A constitutive damage model has been developed for each constituent of the composite. A plasticity model is implemented to simulate the mechanical behaviour of the matrix, based on available experimental evidence. The plasticity model considers pressure dependency and different yield strengths in tension and compression. Both constituents follow damage evolution laws developed in the framework of thermodynamics of admissible processes. The implemented damage laws do not suffer from mesh dependency.

Both constitutive models were implemented in a commercial finite element software. The algorithms for generation of random distributions and application of periodic boundary conditions, as well as for post-processing results were all implemented in a package of scripts which provides the possibility to execute all required operations in a sequential and automatic way

without the need for user intervention.

Two applications of these methodologies are presented. The first involves the use of the implemented subroutines to plot failure envelopes of a uniaxial composite under different loading conditions. Results from the micromechanical modelling are compared with the results of an analytical failure criterion recently proposed for composite materials.

The constitutive damage models developed are also applied to textile composites. A 5-harness satin wet weave is modelled using CAD software and a representative unit-cell of the material is generated. The yarns are modelled using a transversely isotropic damage law while the matrix is considered to follow the elasto-plastic with damage constitutive law developed in this thesis. Different loading conditions are applied and the evolution of damage obtained from numerical analysis is compared with experimental information available in the literature.

RESUMO

Com o eclodir da era da informação, as portas de novas técnicas e processos computacionais mais intensivos foram abertas. O que ontem era impossível de atingir, hoje torna-se realidade. Conceitos como modelação em multi-escala, unificando os mundos da macro- e micromecânica, têm-se estabelecido como alternativas viáveis aos procedimentos experimentais de caracterização do comportamento mecânico de materiais complexos.

Materiais compósitos avançados são uma área perfeita para a aplicação de tais conceitos de modelação. Ao nível da micro-escala, os materiais compósitos exibem duas fases distintas – as fibras de reforço e a matriz. As fibras fornecem a resistência e rigidez enquanto a matriz providencia o apoio lateral às fibras. A micromecânica permite a análise do comportamento constitutivo de cada um dos constituintes e o estudo da influência de cada um nas propriedades mecânicas globais do compósito.

Esta tese fornece um conjunto de novas ferramentas para o estudo micromecânico de materiais compósitos. Foi desenvolvido um algoritmo capaz de gerar uma distribuição aleatória de fibras com uma fração volúmica elevada. A aleatoriedade dos resultados gerados é estatisticamente comprovada. As distribuições geradas são usadas para o desenvolvimento de elementos de volume representativos de materiais compósitos à micro-escala.

O conceito de condições fronteira periódicas é aplicado ao longo da tese. Este tipo de condições fronteira obriga à existência de continuidade do material em faces opostas do elemento de volume representativo, bem como a continuidade do campo de deslocamentos. Os resultados das análises micromecânicas são submetidas a homogeneização volumétrica de modo a obter o comportamento macromecânico do material compósito homogeneizado.

Um modelo constitutivo de dano foi desenvolvido para cada um dos constituintes do material compósito. O comportamento não-linear da matriz é modelado através de um modelo de plasticidade, escolhido com base em resultados experimentais recentes. O modelo de plasticidade entra em consideração com a dependência à pressão e diferentes tensões de cedência à tensão e à compressão. Os modelos constitutivos seguem leis de evolução de dano desenvolvidas no âmbito da termodinâmica dos processos reversíveis. É garantido que as leis de dano não sofrem de dependência do tamanho da malha.

Os dois modelos constitutivos foram implementados num software comercial de elementos finitos. Os algoritmos para geração de distribuições aleatórias e aplicação de condições fronteira periódicas, bem como para pós-

-processamento de resultados foram compilados num pacote de scripts que oferece a possibilidade de executar todas as operações de modo sequencial e automático sem necessidade de intervenção directa por parte do utilizador.

Duas aplicações destas metodologias são apresentadas. A primeira envolve o uso das subrotinas desenvolvidas na geração de envelopes de rutura de um material compósito uniaxial sob diferentes condições de carregamento. Os resultados da modelação micromecânica são comparados com as previsões de um modelo analítico de rutura recentemente proposto para materiais compósitos.

Os modelos constitutivos de dano desenvolvidos são também aplicados a materiais compósitos têxteis. Um tecido com a geometria de 5-harness satin é modelado recorrendo a software CAD e uma unidade-celular representativa do material é gerada com base nesse modelo. As fibras têxteis são modeladas usando uma lei de dano para materiais transversalmente isotrópicos, enquanto para a matriz se considera que esta segue a lei constitutiva elasto-plástica com dano desenvolvida nesta tese. Diferentes condições de carregamento mecânico são impostas e a evolução de dano obtida através de análise numérica é comparada com a informação experimental disponível na literatura.

RÉSUMÉ

Avec le boom de l'ère de l'information, les portes à nouvelles techniques et procédés de calcul plus intensive ont largement ouvert. Ce qui hier était impossible à réaliser, aujourd'hui, est devenue une réalité. Des concepts tels que la modélisation multi-échelle, la fusion des mondes de la macro- et micro-mécanique, s'établissent comme des alternatives viables à des procédures expérimentales dans la caractérisation du comportement mécanique des matériaux complexes.

Les matériaux composites avancés sont un domaine idéal pour l'application de ces concepts de modélisation. Au niveau micro-échelle, les matériaux composites présentent deux phases distinctes - les renforts fibreux et la matrice de résine. Les fibres offrent résistance et rigidité alors que la matrice donne un support latéral sur les fibres. La micromécanique fournit les moyens pour analyser le comportement constitutif de chacun de ces constituants et d'étudier l'influence de chacun d'eux dans les propriétés mécaniques du composite.

Cette thèse propose de nouveaux outils pour l'étude micromécanique des matériaux composites. On a développé un algorithme qui permet de générer une distribution aléatoire des fibres avec une fraction volumique élevé. L'algorithme est statistiquement vérifiée pour le caractère aléatoire de ses résultats. Les distributions générées sont utilisées pour le développement des éléments de volume représentantifs des matériaux composites réels à la micro-échelle.

La notion de conditions aux limites périodiques a été toujours présente pendent la formulation de cette thèse. Ce type de conditions aux limites force de la continuité de la matière dans les faces opposées de l'élément de volume représentatif, ainsi que la continuité du champ de déplacement. Les résultats des analyses micromécaniques sont soumis à une homogénéisation volumétrique pour obtenir le comportement macromécanique du matériel composite homogénéisé.

Un modèle d'endommagement constitutif a été élaboré pour chacun des constituants du composite. On a utilisé un modèle de plasticité pour simuler le comportement mécanique de la matrice, fondée sur les preuves expérimentales disponibles. Le modèle de plasticité considère la dépendance à la pression et différents limites d'élasticité en traction et compression. Les deux constituants suivent les lois d'évolution de l'endommagement développé dans le cadre de la thermodynamique des processus admissibles. Les lois d'endommagement qu'on a utilisées ne souffrent pas de dépendance à l'égard de la maille.

Les deux modèles constitutifs ont été implémentées dans un logiciel commercial d'éléments finis. Les algorithmes de génération de distributions aléatoires et d'application des conditions aux limites périodiques, ainsi que de post-traitement des résultats ont été tous mis en œuvre dans un ensemble de scripts qui prévoit la possibilité d'exécuter toutes les opérations nécessaires de façon séquentielle et automatique sans avoir besoin de l'intervention de l'utilisateur.

Deux applications de ces méthodes sont présentées. La première concerne l'utilisation des routines implémentées pour représenter graphiquement les enveloppes de rupture d'un composite uniaxial sous différentes conditions de chargement. Les résultats de la modélisation micromécanique sont comparés avec les résultats d'un critère de rupture analytique récemment proposé pour les matériaux composites.

Les modèles constitutifs développés sont aussi appliqués aux composites textiles. Un textile du type 5-harness satin est modélisé en utilisant un logiciel de CAO et une unité représentative de la matière est générée. Les fils sont modélisés avec une loi d'endommagement transversalement isotrope alors qu'on considère que la matrice a suivi le comportement élasto-plastique avec la loi constitutive développée dans cette thèse. Différentes conditions de chargement sont appliquées et l'évolution d'endommagement résultant de l'analyse numérique est comparée avec les informations expérimentales disponibles dans la littérature.

ACKNOWLEDGEMENTS

I wish to thank the patience and availability of both my supervisors, Prof. Pedro P. Camanho and Prof. Silvestre T. Pinho, who have tried to guide this blind monkey through the mysterious and intertwined paths of the PhD road. It has been a long road, riddled with the most diverse obstacles and Sisyphean tasks... But I hope the boat has reached safe harbour now.

During the initial stage of development of non-linear models, Prof. Francisco Pires provided a valuable start-up assistance with the understanding of the analytical and numerical pathways necessary to their successful implementation.

To Julieta Santos, one of the most tenacious people around me, but without who it would be fairly impossible for me to have reached this level in my life. Thank you for being always close and tender but, most importantly, thank you for giving me my wings.

I express my gratitude towards *Fundação para a Ciência e a Tecnologia* for awarding me a doctoral degree grant funded by POPH - QREN - Tipologia 4.1 - Formação Avançada, sponsored by Fundo Social Europeu. A reference also to the research grant awarded to me in the last year of doctoral studies from project PDCTE/EME/65099/2003 - Development of failure models and criteria for 5-harness satin weaved composite obtained by RTM.

To my workgroup and peer colleagues, Miguel Bessa, Giuseppe Catalanotti, Cassilda Tavares, Hannes Körber, Hilal Erçin, Matthias Vogler, Pedro Martins, Carla Roque, Marco Parente, and Jorge Belinha I thank their friendship, support and valuable discussions throughout this endeavour.

For their invaluable help with all the bureaucratic paperwork and contract signing, I thank Mrs. Júlia Meira, Mrs. Fernanda Fonseca, Mrs. Zélia Prior and Mrs. Luzia Monteiro.

Not to forget some of the most extraordinary students I was lucky to come across during my PhD years. I will not name any as I might forget some and that would be extremely unfair. It has been an enormous pleasure to have been granted the opportunity to share the little knowledge I have with all these young and bright minds of the future.

To all those whose simple existence has shed light on me in different levels of life, I thank you from the deep ends of my soul, independently of where and how you are in present day.

Table of Contents

List of Symbols

Chapter 2

a	Representative volume element size
E_i	Young's modulus in i-direction
$g(h)$	Pair distribution function
G_{ij}	Shear modulus in ij-plane
i_f	Counter of number of fibres in algorithm `RAND_uSTRU_GEN`
k	Random factor between 0 and 1 in Wongsto's perturbation process
$K(h)$	Ripley's K function
$\widehat{K}(h)$	Estimate of Ripley's K function
$K_H(h)$	Ripley's K function for a hard-core point pattern
$K_P(h)$	Ripley's K function for a Poisson point pattern
$\widehat{L}(h)$	Difference between $\widehat{K}(h)$ and $K_H(h)$
N_c	Number of iterations before changing criterion in step two of algorithm `RAND_uSTRU_GEN`
N_f	Number of fibre positions generated by `RAND_uSTRU_GEN`
N_g	Current number of attempts of fibre placement in step one of algorithm `RAND_uSTRU_GEN`
N_g^{max}	Maximum number of attempts of fibre placement in step one of algorithm `RAND_uSTRU_GEN`
N_i	Current number of iterations in algorithm `RAND_uSTRU_GEN`
N_i^{max}	Maximum number of iterations the algorithm `RAND_uSTRU_GEN` is allowed to execute
R	Fibre radius
S_o	Initial square size in step three of `RAND_uSTRU_GEN`
S^+	Increment to be given to square size in step three of `RAND_uSTRU_GEN`
v_f	Fibre volume fraction
v_f^{cur}	Current fibre volume fraction in `RAND_uSTRU_GEN`
v_f^{req}	Requested fibre volume fraction for `RAND_uSTRU_GEN`
δ	Ratio of representative volume element size to fibre radius

Δ_{min}	Minimum distance between fibres
$\boldsymbol{\varepsilon}$	Strain tensor
θ_w	Direction of displacement in Wongsto's perturbation process
ν_{ij}	Poisson's ratio
$\nu(x)$	Average of variable x
$\rho(x)$	Coefficient of variation of variable x
ρ_A	Coefficient of variation of areas of Voronoi cells
ρ_D	Coefficient of variation of neighbouring distances
ρ_w	Maximum distance in Wongsto's perturbation process
$\boldsymbol{\sigma}$	Stress tensor
$\sigma(x)$	Standard deviation of variable x
2D	2-Dimensional
3D	3-Dimensional
CDF	Cumulative Distribution Function
CFRP	Carbon Fibre Reinforced Polymer
CMC	Ceramic Matrix Composite
FEA	Finite Element Analysis
MMC	Metal Matrix Composite
PBC	Periodic Boundary Conditions
PDF	Probability Density Function
RVE	Representative Volume Element
SRVE	Statistical Representative Volume Element

Chapter 3

a	Width of representative volume element
b	Height of representative volume element
c	Thickness of representative volume element
$\boldsymbol{C}$	Stiffness tensor
C_{ijkl}	Stiffness tensor in Voigt notation
C^f_{ijkl}	Stiffness tensor of the fibre in Voigt notation
C^m_{ijkl}	Stiffness tensor of the matrix in Voigt notation
E_i	Young's modulus in i-direction
E_f	Young's modulus of isotropic fibre material
E_m	Young's modulus of isotropic matrix material
G_{ij}	Shear modulus in ij-plane
G_f	Shear modulus of isotropic fibre material
G_m	Shear modulus of isotropic matrix material
k_{23}	Plain strain bulk modulus
k_f	Plain strain bulk modulus of isotropic fibre material
k_m	Plain strain bulk modulus of isotropic matrix material
K	Bulk modulus
K_f	Bulk modulus of isotropic fibre material

K_m	Bulk modulus of isotropic matrix material
$\boldsymbol{S}$	Compliance tensor
S_{ijkl}	Compliance tensor in Voigt notation
S^f_{ijkl}	Compliance tensor of the fibre in Voigt notation
S^m_{ijkl}	Compliance tensor of the matrix in Voigt notation
u^n_i	Degree of freedom i of node n
V	Volume of representative volume element
V_f	Fibre volume fraction
V_m	Matrix volume fraction
W	Strain energy density function
$\boldsymbol{\varepsilon}$	Strain tensor
ε_{ij}	Strain tensor in Voigt notation
$\boldsymbol{\varepsilon^o}$	Far-field strain tensor
ν_{ij}	Poisson's ratio
ν_f	Poisson's ratio of isotropic fibre material
ν_m	Poisson's ratio of isotropic matrix material
$\boldsymbol{\sigma}$	Stress tensor
σ_{ij}	Stress tensor in Voigt notation
2D	2-Dimensional
3D	3-Dimensional
API	Application Programming Interface
CCA	Composite Cylinder Assemblage model
FEA	Finite Element Analysis
Hashin+	Upper Bound of Hashin's model
Hashin-	Lower Bound of Hashin's model
MMC	Metal Matrix Composite
PBC	Periodic Boundary Conditions
RVE	Representative Volume Element
StMat	Strength of Materials model

Chapter 4

$\boldsymbol{D}^e$	Elastic stiffness tensor
$\boldsymbol{D}^{ep}$	Elastoplastic tangent operator
E_i	Young's modulus in i-direction
E^{ep}	Elastoplastic tangent modulus
g	Non-associative flow potential
G	Elastic shear modulus
$\boldsymbol{H}$	Generalised hardening modulus
$\boldsymbol{I}$	Second order identity tensor
I_1	First invariant of stress tensor
I^{tr}_1	First invariant of trial stress tensor
J_2	Second invariant of deviatoric stress tensor

J_2^{tr}	Second invariant of deviatoric trial stress tensor
K	Elastic bulk modulus
$\boldsymbol{N}$	Flow vector
p	Hydrostatic pressure
p^{tr}	Hydrostatic component of trial stress tensor
$\boldsymbol{q}$	Set of variables affected by hardening
$\boldsymbol{S}$	Deviatoric stress tensor
$\boldsymbol{S}^{tr}$	Deviatoric trial stress tensor
$\boldsymbol{\alpha}$	Hardening variables
γ	Plastic multiplier
Δx	Increment of variable x
$\boldsymbol{\varepsilon}$	Strain tensor
$\boldsymbol{\varepsilon}^{tr}$	Trial strain tensor
$\boldsymbol{\varepsilon}^e$	Elastic strain tensor
$\boldsymbol{\varepsilon}_d^e$	Deviatoric component of elastic strain tensor
ε_v^e	Volumetric component of elastic strain tensor
$\boldsymbol{\varepsilon}^p$	Plastic strain tensor
$\boldsymbol{\varepsilon}_d^p$	Deviatoric component of plastic strain tensor
ε_e^p	Equivalent plastic strain
ε_v^p	Volumetric component of plastic strain tensor
ν_{ij}	Poisson's ratio
ν_p	Plastic Poisson's ratio
$\boldsymbol{\sigma}$	Stress tensor
σ_o	Uniaxial yield stress
σ_c	Compressive yield stress
σ_s	Shear yield stress
σ_t	Tensile yield stress
σ_{vm}	Von Mises stress
$\boldsymbol{\sigma}^{tr}$	Trial stress tensor
$\boldsymbol{\Phi}$	Yield surface
$\boldsymbol{\Psi}$	Flow potential

Chapter 5

$\boldsymbol{C}$	Damaged stiffness tensor
$\boldsymbol{C_f}$	Stiffness tensor of fibre material
$\boldsymbol{C_f^T}$	Constitutive tangent operator in damage model for fibre
$\boldsymbol{C_m}$	Stiffness tensor of matrix material
$\boldsymbol{C_m^T}$	Constitutive tangent operator in damage model for matrix
$\boldsymbol{C_o}$	Non-damaged stiffness tensor
d	Damage variable
d_f	Damage variable in fibre damage model
d_m	Damage variable in matrix damage model

E_i	Young's modulus in i-direction
E_m	Non-damaged Young's modulus of matrix material
E_o	Non-damaged Young's modulus
F_f^d	Damage activation function in damage model of fibre
F_m^d	Damage activation function in damage model of matrix
FI	Failure Index
G_{ij}	Shear modulus in ij-plane
G_o	Non-damaged shear modulus
G_{fe}	Fracture energy
G_{ff}	Fracture energy in mode I of fibre material
G_{fm}	Fracture energy in mode I of matrix material
$\mathscr{G}_m$	Complementary free energy density of matrix damage model
$\mathscr{G}_m^P$	Complementary free energy density of matrix damage model associated with plastic flow
$\mathscr{G}_f$	Complementary free energy density of fibre damage model
$\boldsymbol{H_f}$	Compliance tensor of fibre material
$\boldsymbol{H_m}$	Compliance tensor of matrix material
$\boldsymbol{H_f^o}$	Non-damaged compliance tensor of fibre material
$\boldsymbol{H_m^o}$	Non-damaged compliance tensor of matrix material
$\boldsymbol{I}$	Second order identity tensor
I_1	First invariant of stress tensor
$\tilde{I}_1$	First invariant of effective stress tensor
$\tilde{J}_2$	Second invariant of effective deviatoric stress tensor
K	Bulk modulus
K_o	Non-damaged bulk modulus
l^e	Characteristic element length
Q	Shear strength in xy-plane
r_f	Internal damage variable in damage model of fibre
r_m	Internal damage variable in damage model of matrix
R	Shear strength in xz-plane
S	Shear strength in yz-plane
S_L	Longitudinal shear strength
S_T	Transverse shear strength
u_i	Displacement in i-direction
U	Energy required for complete failure of one element
U_v	Dilatational energy density
X_C	Compressive strength in x-direction
X_T	Tensile strength in x-direction
X_f^T	Uniaxial tensile strength of fibre material
X_m^C	Uniaxial compressive strength of matrix material
X_m^T	Uniaxial tensile strength of matrix material
Y_C	Compressive strength in y-direction
Y_f	Associated thermodynamic force in damage model of fibre

Y_m	Associated thermodynamic force in damage model of matrix
Y_T	Tensile strength in y-direction
Z_C	Compressive strength in z-direction
Z_T	Tensile strength in z-direction
α	Fracture angle under transverse compressive loads
Γ_{ij}	Ultimate shear strain in ij-plane
$\boldsymbol{\varepsilon}$	Strain tensor
ε_{eq}	Equivalent strain
ε_{ij}^C	Ultimate compressive strain
ε_{ij}^T	Ultimate tensile strain
η_L	Longitudinal friction coefficient
η_T	Transverse friction coefficient
Ξ_f	Rate of energy dissipation per unit volume in fibre material
Ξ_m	Rate of energy dissipation per unit volume in matrix material
ν_{ij}	Poisson's ratio
ν_m	Non-damaged Poisson's ratio of matrix material
ν_o	Non-damaged Poisson's ratio
$\boldsymbol{\sigma}$	Stress tensor
$\tilde{\boldsymbol{\sigma}}$	Effective stress tensor
σ_n	Stress component normal to fracture plane
τ_L	Longitudinal shear component in fracture plane
τ_T	Transverse shear component in fracture plane
ϕ_f^d	Loading function for damage model of fibre
ϕ_m^d	Loading function for damage model of matrix
$\boldsymbol{\Psi}$	Energy dissipated per unit volume
$\boldsymbol{\Psi}_f$	Energy dissipated per unit volume in damage model of fibre
$\boldsymbol{\Psi}_m$	Energy dissipated per unit volume in damage model of matrix
BEM	Boundary Element Model
OHT	Open Hole Tensile geometry
RVE	Representative Volume Element
UMAT	User subroutine to define a material's mechanical behaviour in commercial finite element analysis software ABAQUS®
VCCT	Virtual Crack Closure Technique
WWFE	World Wide Failure Exercise

Chapter 6

E_i	Young's modulus in i-direction
G_{ij}	Shear modulus in ij-plane
S_L	Longitudinal shear strength
S_L^{is}	In-situ longitudinal shear strength
S_T^{is}	In-situ transverse shear strength
Y_C	Transverse compressive strength

Y_T	Transverse tensile strength
Y_T^{is}	In-situ transverse tensile strength
α	Fracture angle under transverse compressive loads
$\boldsymbol{\varepsilon}^o$	Far-field strain tensor
ε_1^T	Maximum tensile strain in longitudinal direction
η_L	Longitudinal friction coefficient
η_T	Transverse friction coefficient
ν_{ij}	Poisson's ratio
$\boldsymbol{\sigma}$	Stress tensor
$\boldsymbol{\sigma}^\phi$	Stress tensor in rotated reference frame
σ_I	Maximum principal stress on a transverse plane to the fibres
σ_N	Normal stress component in fracture plane
τ_L	Longitudinal shear component in fracture plane
τ_T	Transverse shear component in fracture plane
FFC	Failure criterion for fibre compression
FFT	Failure criterion for fibre tension
FK_{MC}	Failure criterion for matrix compression in rotated reference frame
FK_{MT}	Failure criterion for matrix tension in rotated reference frame
FMC	Failure criterion for matrix compression
FMT	Failure criterion for matrix tension

Chapter 7

a	Width of representative volume element
c	Thickness of representative volume element
E_i	Young's modulus in i-direction
E_i°	Young's modulus in i-direction of satin weave
F_N	Damage activation function in mode N
G_{ij}	Shear modulus in ij-plane
G_{12}°	Shear modulus in 12-plane of satin weave
G_{IC}^{FC}	Fracture toughness for longitudinal compression
G_{IC}^{FE}	Fracture toughness in mode I for longitudinal tension, exponential damage evolution law
G_{IC}^{FL}	Fracture toughness in mode I for longitudinal tension, linear damage evolution law
G_{IC}^{M}	Fracture toughness in mode I for transverse tension
G_{IIC}^{M}	Fracture toughness in mode II for transverse shear
r_N	Internal damage variable for failure mode N
S_L	Longitudinal shear strength
S_T	Transverse shear strength

u_i^n	Degree of freedom i of node n
X_C	Compressive strength
X_{PO}	Fibre pull-out strength
X_T	Tensile strength
Y_C	Transverse compressive strength
Y_T	Transverse tensile strength
α_{ii}	Coefficient of thermal expansion in i-direction
$\boldsymbol{\varepsilon}$	Strain tensor
$\boldsymbol{\varepsilon^o}$	Far-field strain tensor
ν_{ij}	Poisson's ratio
ν_{12}°	Poisson's ratio in 12-plane of satin weave
$\boldsymbol{\sigma^o}$	Homogenised stress tensor
$\tilde{\boldsymbol{\sigma}}$	Effective stress tensor
ϕ_N	Loading function in mode N
2D	2-Dimensional
CAD	Computer Aided Design
PBC	Periodic Boundary Conditions
RVE	Representative Volume Element

Chapter 8

I_1	First invariant of stress tensor
J_2	Second invariant of deviatoric stress tensor
J_3	Third invariant of deviatoric stress tensor
$\boldsymbol{\varepsilon}_P^\circ$	Strain tensor at integration point P at macro-scale
$\boldsymbol{\sigma}_P^\circ$	Stress tensor at integration point P at macro-scale
BOINC	Berkeley Open Infrastructure for Network Computing
CPU	Central Processing Unit
GNU	Gnu's Not Unix
GPU	Graphics Processing Unit
SETI@Home	Search for Extraterrestrial Intelligence at Home
WU	Work Unit

List of Figures

Chapter 2

Chapter 3

Chapter 4

Chapter 5

Chapter 6

Chapter 7

List of Tables

Chapter 6

Chapter 7

Chapter 1

Introduction

> There are two mistakes one can make along the road to truth: not going all the way, and not starting.
>
> Buddha

Composites are regarded as the materials of the future, which will revolutionise the industry, help improve environment conditions thanks to the savings they have to offer, provide more safety and easiness of use to different objects and machines, and allow for an even greater number of alternative applications in different fields of engineering.

However, what most people do not realise is that composite materials have in fact been a part of man's life since the early stages of human civilization. As a matter of fact, even of man himself. The muscular system of the human body is a perfect example of how the arrangement of multiple fibrous systems can provide strength, versatility and efficiency to a mechanical system. Indeed, there are in Nature several examples of composite materials. The most obvious and useful to man throughout centuries is undoubtedly wood. Wood is made out of an arrangement of cellulose fibres in a matrix of lignin. The fibres provide tensile strength to the wood while the matrix provides lateral support to the fibres and compressive resistance. And this is the easiest and most common definition of a composite material, taught in every engineering school: a composite is made of two or more constituent materials with different mechanical properties but when put together, each constituent plays a different role in the final mechanical behaviour of the composite.

First evidences of man-made composite materials appear in the cradle of human civilization, when straw and mud were burnt together to form bricks for construction purposes [1]. The technique was used by the Israelites in the Middle East for their Egyptian rulers and is described in the Book of Exodus. In the same epoch, for the manufacture of papyrus sheets for writing, ancient Egyptians stripped the stem of the papyrus plant into thin but long strips. These strips were then laid side by side. Another layer was laid on top of these, but with the fibres of the plant in a perpendicular direction to the first layer. Several layers were added afterwards to provide enough strength and durability to the papyrus papers for writing. Thus, the first orthotropic laminates were born, out of the simple human need to express itself...

Throughout the centuries, there was no strong reason for man to dedicate much of his time and ingenuity into improving the manufacture and applicability or explore all the potential that composite materials have to offer. Only after the industrial revolution and the growing need for stronger materials, engineers started looking again at combining different materials to obtain better overall mechanical properties. It was in the mid 1800's that the first attempts at creating a new building material capable of withstanding greater stresses began to take place. Joseph Louis Lambot found that the strength of the concrete could be increased by adding to it in its wet state thin bars of steel. Different companies attempted to develop a production process for this idea, but only in 1878 the first patent was issued, giving rise to the use of reinforced concrete in civil engineering. This new material quickly achieved high popularity since it brought to architecture and civil engineering the possibility to build higher while reducing material weight and increasing longevity of the constructions.

Advanced composite materials as they are known today began gaining shape in 1930 when almost by accident an engineer began wondering about a fibre which formed while applying lettering to a glass bottle [2]. Fibre glass began being manufactured and commercialised first as an insulation material, but soon after it began being applied in the quickly growing aeronautic industry, first in reinforced plastic dies for manufacture of prototype components, and later in jigs and fixtures for forming and holding aircraft sections and assemblies.

World War II provided the opportunity for the development of many components made of composite materials in the naval and aeronautic industry. A significant boost was given in the knowledge of polymers reinforced with fibre glass, their manufacture processes and applications. After the War, the composite industry began looking at different markets where the accumulated knowledge could be applied. The growing automobile industry provided the perfect field for commercial exploration of these materials.

The beginning of the space age in the 1950's brought the ultimate thrust for the development of advanced composite materials. In 1961 the first patent for production of carbon fibres was issued and soon after carbon fibres began being commercially available. This allowed for even greater stiffness to weight reductions. New, better, lighter, and stronger components for the aerospace industry began to appear along with new manufacturing processes such as the filament wounding technology. Boron and aramid fibres were respectively introduced in the late 1960's and early 1970's.

Not only the fibrous reinforcements suffered a significant evolution; new polymers were also introduced throughout the years allowing for the number of application fields of composites to increase tremendously, expanding from aerospace industry to sports equipment, medical apparatus, defence systems, thermally and chemically demanding environments, and electrical/electronic equipment. And to think it all began with simple mud and straw...

Throughout these years of growth in the composite industry, the only procedure to determine whether a given material or component was structurally fit to meet the needs was experimentation. The component needed to be manufactured and tested – most of the times to complete destruction – in order to determine its elastic and strength properties. Analytical methods were limited in their application and computers available at the time were not capable of performing advanced calculus in an acceptable time frame.

The computer age which began in the 1990's provided a magnificent tool for designers and engineers to model parts, components, assemblies, and structures to a level of detail where experimental data is only required for material characterisation purposes, leaving all the iterative process of part development and geometry optimisation to numerical analyses.

Macromechanical analysis is the easiest to perform and the one which requires less computational effort. It allows the designer to study stress patterns and stress concentration regions in the component assuming the composite to be an homogeneous material. Several failure criteria have been proposed throughout the years which can be applied at this level of analyses. The finite element method is seldom used in order to model the mechanical behaviour of the components.

A more detailed study can be performed with mesomechanical analysis. At this level, the mechanical behaviour of a lamina is modelled using constitutive material models which still consider the lamina as an homogeneous material. Computational effort is not very high and a more profound study of different damage mechanisms can be performed.

Thanks to the most recent advances in computer technology, network computing and distributed computing, a new level of analysis is rapidly gaining importance and making a stand for itself. Micromechanical analysis looks upon the behaviour of each constituent of the composite, i.e. the composite is seen as an heterogeneous material. Although computationally more expensive, it allows the analyst to have a good overview on the influence of each constituent in the mechanical behaviour of the composite. All kinds of damage mechanisms can be recreated at this level of analysis.

Thanks to numerical homogenisation techniques, the stress and strain fields acquired with micromechanical analyses can provide the constitutive behaviour of the lamina, or even of the laminate. If each of the constituents of the composite is modelled with a physically sound constitutive model, the composite's elastic, strength, and eventually non-linear properties can be fully determined.

Multi-scale analyses can be performed by using the best out of each level of analysis; meso- or macromechanical analyses provide far-field strain fields on each integration point while the stress field is computed through homogenisation techniques of micromechanical analyses results.

Thesis motivation

Most of the constitutive models presented to date which attempt to simulate the mechanical behaviour of the composite suffer from a predicament: they are not suited for prediction of the non-linear behaviour of the composite, namely under transverse shear, longitudinal shear, and transverse compression, or combinations of different loads.

Being able to predict the non-linear behaviour in composite materials under different loading conditions would allow analysts, designers and engineers to harness most of the features which still make advanced composites such a tantalising material to dimension and analyse in the most diverse applications. This non-linear behaviour of the composite is associated with one of the constituents – the matrix.

A possible approach to tackle this problem is by developing a continuum damage model for the matrix material which can be applied in a representative volume element of the microstructure of the composite. This representative volume element should be statistically equivalent to the real material and be able to represent the random distribution of reinforcements that is visible in micrographies of the transverse cross-section of the composite. The representative volume element needs to be loaded under the most general three dimensional strain state so that the influence of the different loading schemes and non-linear and damage mechanisms can be properly studied.

The results obtained from the micromechanical analyses on representative volume elements will need to be post-processed using homogenisation techniques in order to obtain the true non-linear behaviour at the lamina level. With the mechanical behaviour of the lamina properly characterised, it is possible to compare the results of the model with available experimental data and other analytical and/or numerical methods to estimate elastic and strength properties of the composite.

There are several limitations on what can be achieved with experimental work. Some loading conditions are extremely difficult to obtain or even impossible given the geometry of the test specimens. Thus, many analytical models for strength prediction can not be validated using experimental data. Three dimensional micromechanical analyses along with homogenisation techniques can provide very detailed and realistic information for any loading condition, allowing for a complete validation of any analytical model.

Micromechanical analyses, given the very detailed insight it is capable of providing on the influence of each constituent on the overall mechanical behaviour of the composite, will allow for a better understanding of the sequence of events from damage initiation to ultimate fracture of the composite. This knowledge can later be used to attempt to control how a specific damage mechanism is triggered, minimise its hazardous effects and extend the life of the structural component.

Reducing the need for extensive and prolonged experimental work can also be achieved thanks to micromechanical analyses. Considerable cost, material and time savings can be obtained if the micromechanical models are capable of reproducing the results commonly obtained only via experimental procedures.

Thesis objectives

Given the current state of the art in micromechanical analyses of unidirectional long-fibre reinforced composite materials, this thesis aims at addressing the issues of how to generate a representative volume element of the real material and, with the application of adequate boundary conditions, perform micromechanical numerical analyses on it.

The representative volume element will distinguish the two constituents of the composite material – matrix and fibre. Each constituent will have its mechanical behaviour modelled using a thermodynamically sound constitutive model, capable of harnessing both linear and non-linear behaviour.

Albeit complex and time-consuming, it is envisaged to implement both constitutive models in an implicit finite element scheme and apply them to the generated representative volume elements. Results will be put through a volumetric homogenisation process, thus achieving knowledge about the failure strength as well as about which damage mechanisms are associated with each loading scenario. This methodology should be easily reproducible and implemented in other types of composite materials, such as woven composites.

Thesis layout

The thesis has been structured so that each chapter approaches one different topic. Care was taken so that this work could be followed and understood by both experienced and untrained readers. Each chapter begins with a review of the state of the art on the subject the chapter is dedicated to, followed by a short but elucidative theoretical introduction to the concepts necessary for the development of the analytical or numerical models presented.

Chapter 2 presents a new algorithm capable of generating a statistically equivalent random distribution of reinforcements with a high fibre volume fraction in a very short period of time. The algorithm is validated using an array of statistical tools and numerical analyses. This algorithm allows for the generation of representative volume elements in three dimensions. How the finite element model can be created, including the application of three dimensional periodic boundary conditions, is presented in chapter 3. A sequence of numerical analyses on different generated distributions is performed in order to estimate the elastic constants of a composite material after homogenisation of the stress and strain fields obtained from the micromechanical analyses. A batch of parametric studies is also conducted in order to determine the influence of some geometrical parameters.

The constitutive model for an epoxy resin begins being developed in chapter 4. A plasticity model based on an experimental characterisation of an epoxy resin is implemented in a commercial finite element software. The model is capable of acquiring the most significant properties of an epoxy resin, such as different tensile and compressive yield strengths and pressure dependency. The implemented plasticity model was verified and validated using a sequence of loading conditions applied to different representative volume elements.

The constitutive model of an epoxy resin is completed in chapter 5 with the implementation of an isotropic damage model. This formulation has been developed with the aid of a crack band model capable of inducing mesh independency to the results obtained. Also the reinforcing material was the subject of development and implementation of a simple mesh-independent transversely isotropic damage model. Both damage models were validated for mesh independency. A similar sequence of analyses on different volume elements that had been performed in chapter 4 is executed here.

With the development of two constitutive models for each of the composite's constituents – matrix and fibre – it is now possible to perform full micromechanical analyses for complete numerical characterisation of a given composite system. Different failure envelopes are outlined in chapter 6, some of them almost impossible to obtain through experimental work, and the results compared with a three dimensional analytical damage model recently proposed.

Finally, in chapter 7 an application of the presented concepts to a textile composite is made. The constitutive damage model developed for the matrix is used on the embedding matrix of the textile, while the yarns are characterised using identical procedures to those in chapter 6 to determine the elastic and strength parameters. These properties are then fed to a transversely isotropic damage model previously developed.

The thesis wraps up in chapter 8 with a summary of achievements, suggestions for improvements on the presented methodologies and applications, and a discussion on possible follow-up work in the field of micromechanics using distributed computing.

Chapter 2

Development of a Statistically Representative Volume Element

What we call random is just
patterns we can't decipher.

Chuck Palahniuk

When diving into the micro-scale world of heterogeneous materials, there exist two possibilities to numerically model a part's mechanical behaviour: to mesh the complete part and all of its constituents or to consider the existence of a sufficiently small but representative volume element of the material at hand. While the first option is clearly out of question due to considerably high human and computational effort on meshing and analysis, the latter has been the subject of thorough studies as it provides a method to quantitatively characterize the material's mechanical behaviour without demanding for an exaggerated computational effort.

This chapter addresses some of the questions related with the application of the Representative Volume Element (RVE) concept to long fibre reinforced composites, its dimension, generation and statistical equivalence with the bulk material.

2.1 Introduction and state of the art

The mechanics of laminated composite materials can be tackled at three different scales, depending on the problem at hand [3]–[6]:

Micro-scale – This is the scale of the heterogeneity in the composite. The mechanical behaviour of the two constituents (fibre and matrix) is the main focus of the analyses performed at this scale. The interaction between constituents and the resulting behaviour of the composite (micro-strain and -stress fields) is the main concern of this scale level. Both constituents are seen as individual homogeneous materials. Micro-crack initiation and debonding between fibre and matrix can be easily modelled at this scale. One can also study the effects on the laminate's strength and stiffness of each individual constituent's properties.

Meso-scale – The scale of the ply thickness. The ply is taken as the building block of the composite, being considered as an homogeneous material with transverse isotropy in the case of unidirectional long fibre composites. The ply mechanical and elastic properties can be determined through experimentation, but modelling at this scale does not provide any information about the interaction between constituents. However, this scale can be much more easily applied to the analysis of large structures than the micro-scale as it does not demand too much computational effort. Delamination is normally predicted using this scale-level.

Macro-scale – The laminate and the structure are at this scale level. The material is assumed homogeneous and the effects of the constituent materials are represented only by averaged apparent properties of the composite material.

Although the meso- and macro-scale material properties can be determined experimentally, it is of interest to establish a relation between the macro-scale mechanical behaviour and the constituents' properties. This would allow considerable savings on experimental craft and work and provide a deeper knowledge about the real composite's behaviour leading to a more efficient tailoring of the laminates' properties according to the engineers' needs for a given application.

However, taking into account all the variables to be considered, performing a thorough analysis at the micro-scale level would be a nearly impossible task. To overcome this difficulty, the concept of statistically homogeneity is normally used [7]. It is considered that there exists a statistical homogeneous material with the same average properties (like stress and strain) as the heterogeneous material. Calculations can then be performed in this statistically equivalent material.

Assuming that there exists a scale-level for which the properties can be averaged and that this scale is small compared with the real laminate or structure dimensions, one can perform analysis on the material's response with reasonable computational effort and still consider the interactions between the constituents and their influence on micro-stress (and micro-strain) fields, micro-crack initiation, fibre-matrix interfacial damage, etc. This scale-level is known as a Representative Volume Element (RVE).

2.1.1 Representative Volume Element

The mechanical behaviour of heterogeneous materials can be described at an intermediate scale level by a Representative Volume Element (RVE). The first definition of a RVE dates back to 1963 when Hill [8] defined the concept as a microstructural sub-region that is representative of the entire microstructure in an average sense. The RVE must be [8]:

> *(a) structurally representative of the mixture of constituents on average, and (b) contain a sufficient number of inclusions for the apparent overall moduli to be effectively independent of the surface values of traction and displacement, as long as these are 'macroscopically uniform'.*

Drugan and Willis [9] use in their work a slightly different definition for RVE:

> *the smallest material volume element of the composite for which the usual spatially constant "overall modulus" macroscopic constitutive representation is a sufficiently accurate model to represent mean constitutive response.*

These definitions refer to an ideal infinite length RVE and so can not be used in computational mechanics. It is thus required to find a finite dimension for the RVE. Different approaches have been suggested in the literature. Some of the most relevant are presented in subsection 2.1.2.

2.1.2 Size of a RVE

The RVE can not have a too large dimension as that would endanger the possibility to numerically analyse it; however, it can not be too small either as this would jeopardise its representativeness of the material in analysis.

Using their definition of RVE, Drugan and Willis [9] demonstrated that the minimum RVE size needs to be at most twice the reinforcement diameter for any reinforcement volume fraction and for several sets of matrix and reinforcement moduli. Although this is computationally attractive, it should be kept in mind that only the global bulk properties were analysed. No attention was given to micro-stress and micro-strain distributions in the RVE nor the effects of a non-linear constitutive model were studied.

Shan et al. [10] studied the micro-structure of a Ceramic Matrix Composite (CMC) with random distribution and size of the reinforcement. The study made use of a digital-image analysis process [11] by which the reinforcement's spatial distribution would be statistically characterized using six parameters. A computer simulation of hard-core random fibre arrangement was then generated making use of those six parameters, creating fibre-rich and -poor regions which would have a statistically equivalent spatial distribution to the real material. They concluded that a window of approximately 40 times the average fibre radius for a volume fraction of 35% represented both geometrically (using a set of statistical functions to quantitatively evaluate the fibre distribution) and mechanically (through the analysis of the distribution of maximum principal stress on the matrix) the constitutive behaviour of the material. It should be noted though that the constituents' elastic moduli presented a ratio of 2.3 : 1. This is not the case for CFRP where ratios of 60 : 1 between the constituents' elastic moduli are common.

Swaminathan et al. presented a two-part study on a polymeric matrix reinforced with steel fibres [12]–[13] where in the first part the size of an SRVE[1] for unidirectional composite materials without damage was accessed, while in the second part, the same study was conducted but considering interfacial debonding. By using various statistical functions of geometry, stresses, and strains, the authors concluded that, just by including damage, the size of the SRVE had to be doubled in order to maintain a good estimate of the effective elastic stiffness tensor. This leads to the conclusion that the size of the SRVE must be determined considering the purpose of the analysis. If a linear elastic analysis is to be performed, the SRVE size can be considerably smaller than for a viscoelastic-plastic analysis with damage, for example.

Gitman et al. [14] demonstrated that the size of the RVE hardly depends on the loading scheme (tension and shear tests were performed) neither it does on a parameter of interest (stress based or stiffness based) judged using a chi-square criterion given by equation (2.1),

[1]The abbreviation SRVE will be used in this Thesis when there is a statistical equivalence to the bulk material while RVE refers only to the concept of representative volume element.

$$\chi^2 = \sum_{i=1}^{n} \frac{(a_i - \langle a \rangle)^2}{\langle a \rangle} \tag{2.1}$$

where a_i is the investigated parameter, $\langle a \rangle$ is the average of a_i and n is the number of realisations, i.e. there are n unit cells with the same size but different inclusion distributions. Five unit cells for each volume fraction studied were generated, each having a different spatial distribution of fibres.

However, Gitman et al. [14] also concluded that there is a strong dependence of the size of the RVE on the material properties of the constituents (like changing stiffness ratio) as well as of the volume fraction of reinforcement.

Trias et al. [15] performed a thorough study where the size of a RVE for long fibre reinforced composites was scrutinized. Various mechanical and statistical variables to analyse different sizes of RVEs were used. The functions and variables used as criteria were:

1. Fibre content.
2. Effective Properties.
3. Hill Condition, as defined by equation (2.2).

$$\langle \boldsymbol{\sigma} : \boldsymbol{\varepsilon} \rangle = \langle \boldsymbol{\sigma} \rangle : \langle \boldsymbol{\varepsilon} \rangle \tag{2.2}$$

4. Stress and Strain Fields.
5. Probability Density Functions (PDF) of stress and strain in the matrix.
6. Distance distributions.

Trias et al. [15] defined a parameter δ given by equation (2.3),

$$\delta = \frac{a}{R} \tag{2.3}$$

where a is the RVE edge length and R is the fibre radius. The results of this study are summarised in table 2.1.

Analysing table 2.1 and using equation (2.3) it can be seen that the minimum size for a SRVE is 50 times the fibre radius. This seems to be the most comprehensive study on the field of RVE size for analyses of long fibre reinforced composites made of a carbon fibre and epoxy matrix, the

Table 2.1: Summary of analysed criteria and results by Trias et al. [15].

Criteria	Description	Result
Fibre Content	Percentual difference lower than 10%	$\delta \geqslant 30$
Effective Properties	Percentual difference lower than 10%	$\delta \geqslant 30$
Hill Condition	Difference between energy bounds lower than 5%	$\delta \geqslant 15$
Strain field	Hypothesis test for the mean	$\delta \geqslant 15$
	Hypothesis test for the variance	$\delta \geqslant 25$
	Percentual difference of coefficient of correlation	$\delta \geqslant 50$
Stress field	Hypothesis test for the mean	$\delta \geqslant 10$
	Hypothesis test for the variance	$\delta \geqslant 25$
	Percentual difference of coefficient of correlation	$\delta \geqslant 50$
Strain in matrix PDF	Similarity of PDF	$\delta \geqslant 30$
Stress in matrix PDF	Similarity of PDF	$\delta \geqslant 25$
Distance distributions	Comparison with Poisson process	$\delta \geqslant 40$

very same materials that will be under consideration throughout this thesis. Thus, a parameter of $\delta \geqslant 50$ will be used hereafter unless otherwise specified.

With the dimension of the RVE sorted out, one other important issue must be addressed: *how to spatially model the constituents inside the RVE?*

2.1.3 Spatial distribution of fibres inside the RVE

The mechanical properties of unidirectional fibre reinforced composites depend mainly on geometric attributes: fibre size distribution, volume fraction, and spatial arrangement of fibres in the matrix. This spatial arrangement is usually *not* periodic and it is highly dependent upon the manufacturing process.

Brockenbrough et al. [16] have shown that in the plastic regime, the transverse deformation can not be predicted correctly if the analyst uses a periodic fibre distribution. Sorensen and Talreja [17] demonstrated that the local residual stresses due to cool-down during processing depend significantly on deviations from uniformity of the spatial fibre distribution. Pyrz [18]–[19] observed for polymer matrix composites that the transverse constitutive behaviour and fracture angle of the specimens are a function of the spatial arrangement of the reinforcements.

Figure 2.1 shows two typical periodic fibre distribution patterns. As the discussion above shows, these patterns are not suitable for micromechanical stress analysis as they neither correctly represent the internal fibre distribution nor the micro-stress and -strain fields. Therefore, they should not be used for neither plastic deformation nor damage onset and evolution on the transverse section of the composite.

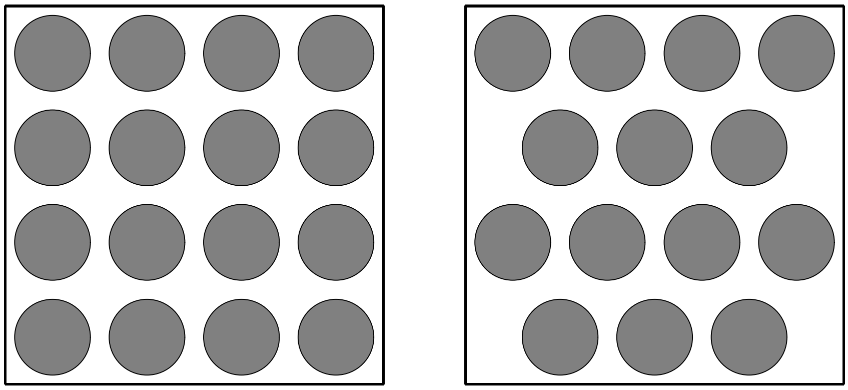

(a) Quadrangular Periodic (b) Hexagonal Periodic

Figure 2.1: Two patterned spatial distributions of reinforcements.

Matsuda et al. [20] compared the elastic-viscoelastic behaviour of long fibre reinforced laminates subjected to in-plane tensile loading using homogenization theory. Three different fibre distributions were used in this study: one hexagonal pattern (as represented in figure 2.1(b)), and the two patterns represented in figure 2.2.

Each distribution is obtained from a unit cell represented in one quarter of figure 2.2(a). Inside the unit cell, the fibres are randomly distributed. The Y-distribution results from repeating this unit cell several times in both horizontal and vertical directions. The point distribution is generated by rotating the unit cell 180° around the middle point of each of its sides (small circles in figure 2.2(b)). This last distribution was considered by Matsuda

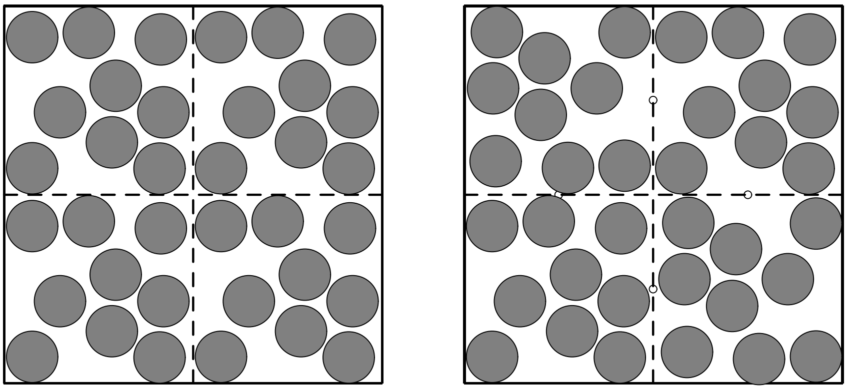

(a) Y-distribution (b) Point distribution

Figure 2.2: Matsuda et al. [20]'s spatial distributions of reinforcements.

et al. as being "*considerably random*".

Matsuda et al. concluded that the spatial distribution of the reinforcements in the RVE does not affect the macroscopic response of laminates, but it significantly affects the microscopic distribution of stress. It is thus important to consider transverse randomness of fibre distribution for studying the onset and evolution of damage in the matrix.

Characterisation studies of a unidirectional glass/epoxy composite which was found to be transversely randomly packed using digital image analysis were conducted by Gusev et al. [21]. Different fibre diameters were used in the same image and different fibre volume fractions were also used in this study. It was concluded that the effect of fibre diameter distribution on the composite elastic constants is very small. Apparently, it is the fibre volume fraction which predominantly determines the composite's elastic constants. The experimentally measured constants were then compared with calculated ones using random and periodic distributions of fibres. In table 2.2, *Random identical* is the random distribution of fibres obtained using a digital image analysis procedure, *Random different* means a randomly generated fibre distribution with the same statistical properties as the original, and *Hexagonal identical* and *Square identical* respectively correspond to hexagonal and square periodic patterns of fibres with the same volume fraction as the one measured by the digital image process. It is thus shown that random distributions predict with higher accuracy the elastic constants of the material.

In the light of these findings, one can only conclude that, in order to properly model micro-stress and -strain fields as well as try to predict the

Table 2.2: Comparison of measured and calculated engineering constants by Gusev [21].

	Measured	Random different	Random identical	Hexagonal identical	Square identical
E_{22} [GPa]	17.1	16.0	16.0	15.1	18.2
ν_{23}	0.391	0.413	0.410	0.430	0.551
G_{23} [GPa]	6.07	5.63	5.61	5.25	4.23
E_{11} [GPa]	41.5	41.6	41.6	41.6	41.6
ν_{21}	0.316	0.265	0.265	0.265	0.265
G_{21} [GPa]	5.63	5.75	5.75	5.75	5.75

micro-scale effective properties, a random distribution of reinforcements in the transverse surface of the material must be used.

2.1.4 Methodologies to generate transverse randomness of reinforcement

In order to model the random distribution of the fibres inside the RVE, different methodologies have been suggested. This subsection provides a description of some of the most used techniques to achieve that goal.

Poisson distribution

The Poisson distribution generates a uniform arrangement of points inside a certain area. The probability of finding a point in any coordinate of the area of interest is exactly the same. However, this method can not be directly applied to this study since we are dealing with fibres which have a finite radius and not with points of zero radial dimension.

However, the Poisson distribution is completely described in the literature, as well as its various statistical parameters, and can be used for comparison purposes. The Poisson point pattern can be quite useful in a comparative basis when it comes to recognizing aggregated or regular patterns.

Hard-core model

In an attempt to overcome the problems raised by the Poisson point distribution, a hard-core model was developed. Here, each point is seen as the centre of each fibre[2]. The model defines that the probability of finding a point at a distance to another point less or equal the fibre diameter plus a specified small distance is null. This small distance represents the minimum gap between any two fibres.

This way, the null-radius problem of the Poisson distribution is solved; however, the statistical parameters found on the literature for the Poisson point distribution can no longer be applied here.

The hard-core model has one fundamental problem which does not allow it to be straightforwardly applied in long carbon fibre reinforced polymers: it is virtually impossible to achieve fibre volume fractions greater than 55% [22]. For CFRPs, fibre volume fraction is commonly between 55% and 65%.

In the present chapter, it will be considered that the size of the SRVE is $a \geqslant 50 \times R$, which equals to say that the radius of the fibre, R, is much smaller than the sample window. Under these circumstances, it is valid to state that the hard-core model is statistically equivalent to the Poisson model and the parameters found in the literature for the Poisson model can be used to assess the statistical validity of the hard-core models developed.

Trias [23] uses a modification of the hard-core model using *Random Close Packing* algorithms. This allowed him to achieve fibre volume fractions of 59%. Unfortunately, this method demands high computational effort. Table 2.3 provides the average time it is necessary to reach an initially requested fibre volume. The model was run on an Intel Pentium IV 1.4 GHz.

Digital image analysis

Digital image analysis was also used by Trias [23]. The technique starts by acquiring several microscopies of the material in study and by joining all these images in a mosaic. This allows the generation of a high-resolution image of a vast area of the transverse section.

Considerable image processing is required to compensate for shadowed and bright areas and to binarise the image, i.e. to establish a clear contrast between fibre and matrix by making the fibre perfectly white and the matrix perfectly black.

[2]Throughout this thesis it will always be considered that the fibres are perfectly circular and have always the same diameter.

Table 2.3: Simulation times to obtain different volume fractions, according with Trias' model [23].

v_f	Time [min]	v_f	Time [min]
0.40	0.52	0.53	22.54
0.45	1.67	0.54	32.67
0.48	2.48	0.55	44.86
0.49	5.82	0.56	60.33
0.50	7.43	0.57	80.17
0.51	13.56	0.58	95.72
0.52	18.32	0.59	127.67

Although this technique allows the analyst to have a perfect replica of a sample of the transverse section of the composite, it can be extremely time and resource consuming as it requires specific software and hardware for image acquisition and processing, and material to be analysed.

Yang et al. [11] used this method along with a digital image processing technique. They statistically evaluated the fibre distribution of Nicalon fibres in a CMC and developed a model to generate a fibre distribution which would match the two measured statistical parameters: nearest neighbour distance and radial distribution function[3].

Randomness through perturbation of periodic pattern

Wongsto and Li [24] proposed an algorithm that can generate a fibre distribution with a high fibre volume fraction based on a perturbation process of an hexagonally periodic pattern. This process allows the generation of a reinforcement arrangement with high fibre volume fraction in only a few minutes.

Starting from the hexagonally arranged fibres, a perturbation process is applied to each fibre as demonstrated in figure 2.3.

A random angle θ_w is generated between 0 and 2π. This angle defines the direction the centre of the fibre will move. Along this direction, a maximum distance ρ_w can be found, which is the smallest of the distances to the borders of the RVE and to the point where the fibre collides with one other fibre (as per figure 2.3). This distance ρ_w is then multiplied by a

[3]An extensive description of these and other statistical parameters is given in subsection 2.1.5

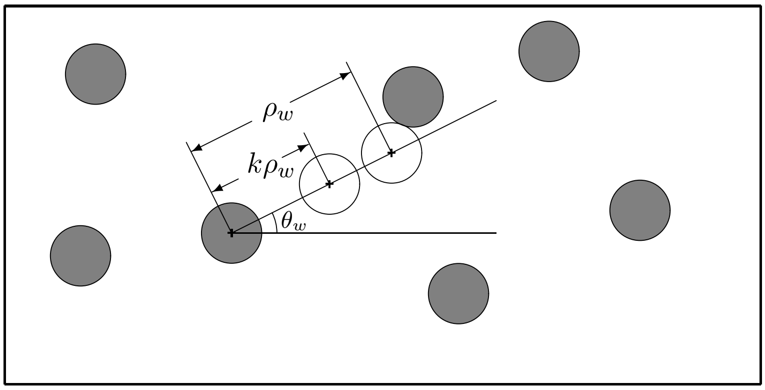

Figure 2.3: Perturbation process proposed by Wongsto and Li [24].

random factor k generated between 0 and 1. The product $k\rho_w$ is the final distance the fibre will be displaced along the line defined by the angle θ_w. This perturbation process is then repeated for all fibres present in the RVE, completing one iteration.

In their contribution, Wongsto and Li [24] use a minimum of 250 iterations. After that, the achieved fibre volume fraction on the RVE is the stoppage criterion. When the error between the achieved and the required volume fraction is below 2%, the perturbation process ends.

This method provides an interesting way to model RVEs with high fibre volume fractions. For a RVE with $a = 50 \times R$ and a fibre volume fraction of 65% the algorithm takes approximately $6 \sim 8$ minutes in a standard computer[4]. However, there is the risk that the algorithm falls into a never-ending number of iterations trying to reach a fibre volume fraction with an error less than 2%. This is due to the very random nature of the generation of the angle θ_w.

2.1.5 Statistical spatial descriptors

This section presents the definition of the statistical functions and operators commonly used in the literature to quantitatively characterise spatial distributions of points. Here, a point should be interpreted as the centre of each fibre.

[4]These values are based on simulations run by the author of this thesis and *not* from Wongsto's contribution [24].

Voronoi polygon areas

A Dirichlet tessellation is defined as a subdivision of a region, determined by a set of points, where each point has associated with it a region that is closer to it than to any other. These regions are named Voronoi cells. If $\boldsymbol{P}_1(x_1), \boldsymbol{P}_2(x_2), \ldots, \boldsymbol{P}_n(x_n)$ denote a set of n random points in a bounded region $\boldsymbol{W}$, the interior of a Voronoi cell associated with the i^{th} point $\boldsymbol{P}_i$ is the region $\boldsymbol{D}_i$ defined as

$$\boldsymbol{D}_i = \{x \in \boldsymbol{W} : |\mathbf{x} - \mathbf{x}_i| < |\mathbf{x} - \mathbf{x}_j|, \forall j \neq i, \boldsymbol{P}_j \in \boldsymbol{W}\} \tag{2.4}$$

The aggregate of all such regions $\boldsymbol{D}_i$, constitutes the Dirichlet tessellation in a plane. Figure 2.4(a) shows an example of such tessellation for a random distribution of points while figure 2.4(b) provides the tessellation for a periodic square distribution. Each polygon represents a Voronoi cell.

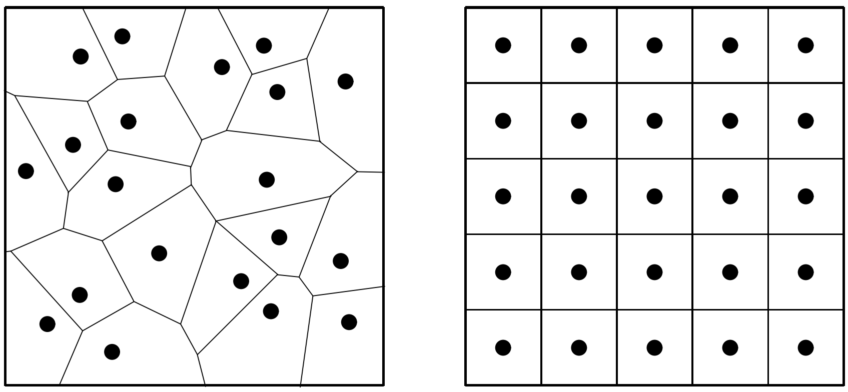

(a) Random distribution (b) Square distribution

Figure 2.4: Voronoi cells. Each fibre defines a region around itself as per equation (2.4).

A Voronoi cell immediately identifies the region of immediate influence for each fibre. The number of neighbouring cells also provides insight to the clustering that the fibre belongs to or if it is an isolated fibre.

One can calculate the standard deviation of the areas of the Voronoi polygons and thus infer about the quality of the spatial distribution of the fibres; for a periodic distribution, for example, the standard deviation is nil as all Voronoi cells have equal area (figure 2.4(b)).

Neighbouring fibre distances

With the definition of a Voronoi cell for each fibre, one can also calculate the standard deviation of the average of the distances between fibre centres to the neighbouring fibres. A neighbouring fibre is one which shares a side of the Voronoi polygon with the fibre of interest.

This measure functions the same way as the previous providing an insight into the degree of clustering or spacing between the fibres. A value close to zero indicates that the fibres are all at an approximately equal distance from each other (or, if the value is 0, exactly at the same distance as is the case of periodic distributions).

The two procedures mentioned above using Voronoi cells were applied by Matsuda et al. [20] to compare the spatial distribution of fibres shown if figure 2.2 with an hexagonal distribution used in their calculations in a previous contribution [25].

Nearest neighbour distances

This measure can be obtained easily as the Probability Density Function (PDF) of the distance from one given fibre to its nearest one. Identically, 2^{nd} nearest and 3^{rd} nearest neighbour distances can be computed.

The resulting probability density functions provide information on the short-distance fibre interaction. For a square point pattern as represented in figure 2.4(b), the nearest neighbour is always at the same distance, so the PDF plot would be a straight vertical line.

This function also provides some information on point clustering. If the PDF plot of the nearest neighbour distances shows a peak for a specific distance followed by a steep decrease, this is an indication that the fibres could be clustered. On the contrary, if the 2^{nd} and 3^{rd} neighbour distances show a more smooth decrease than the nearest neighbour distance, than this indicates that there is no clustering but, because of the high fibre volume fraction on the sample, the nearest neighbour distance naturally becomes very close to a peak at a specific distance. This is to be expected as the more fibres there are in the representative volume element, the more packed they have to be for them all to fit.

Nearest neighbour orientation

Using the information about the nearest fibre position determined in the previous statistical spatial descriptor, the orientation at which the nearest fibre is positioned can be determined and studied. This descriptor is usually given by a Cumulative Distribution Function (CDF) which represents the total number of fibres that have the nearest neighbour oriented along a certain direction, measured clockwise with respect to the horizontal axis. This CDF is normalised with respect to the total number of fibres.

The CDF representation for a perfectly random distribution of inclusions is a straight diagonal line meaning that a given orientation has the same probability of occurring has any other orientation. Deviations from this line will be visible if there is a preferred orientation on the fibre spatial arrangement as is the case of periodic distributions.

Ripley's K function

Ripley's K function, also known as the second order intensity function, has been demonstrated to be one of the most informative descriptors of spatial patterns by Pyrz [19].

Unlike the nearest neighbour functions which analyse short range interaction between the fibres, Ripley's K function (hereafter referred to as $K(h)$) provides some insight about the pattern at several distances. $K(h)$ is also independent on the direction of analysis – it is an isotropic function – depending only on the distance.

In words, $K(h)$ can be defined as the number of extra points expected to lie within a radial distance r of an arbitrary point and divided by the number of points per unit area. The $K(h)$ function is defined by equation (2.5) [26],

$$K(h) = \lambda^{-1} E \tag{2.5}$$

where λ is the density (number per unit area in the case of 2D analyses) of fibres, h is the distance, and E is the number of extra fibres within distance h of a randomly chosen fibre.

$K(h)$ can be estimated by equation (2.6) [26],

$$\widehat{K}(h) = \frac{A}{N^2} \sum_i \sum_{j \neq i} I\left(d_{ij} \leqslant h\right) \tag{2.6}$$

where A is the area of the study region, N is the total number of fibres, d_{ij} is the distance between points i and j, and $I()$ is an indicator function having the value 1 if the condition between brackets holds true and the value 0 if the condition is false. In order to account for edge effects, equation (2.6) must be corrected to [27]:

$$\widehat{K}(h) = \frac{A}{N^2} \sum_i \sum_{j \neq i} \frac{I\left(d_{ij} \leqslant h\right)}{w\left(l_i, l_j\right)} \tag{2.7}$$

with $w\left(l_i, l_j\right)$ serving as a weight function having the value 1 if the circle with centre at point l_i and radius d_{ij}, i.e. passing by point l_j, is completely inside the area of study. If not, $w\left(l_i, l_j\right)$ is the proportion of the circumference of that circle lying in the study area.

Edge effects are most important for large values of h. This is why this correction should be used for values of the distance lesser than half the dimension of the SRVE. Pyrz [19] recommends that h should be between $0 - 0.3$, considering the measure frame as a unit square.

$K(h)$ can also be compared with theoretical models like the Poisson point pattern or the hard-core model. Ripley's K function for the Poisson point pattern, $K_P(h)$, is given by

$$K_P(h) = \pi h^2 \qquad h > 0 \tag{2.8}$$

while for the hard-core model, $K_H(h)$, is given by

$$K_H(h) = \pi \left(h - h_{min}\right)^2 \qquad h - h_{min} > 0 \tag{2.9}$$

where h_{min} is the minimum distance between fibres.

If the spatial distribution in analysis provides a plot of $\widehat{K}(h)$ below the Poisson curve, then there likely is some degree of regularity on the distribution. If, on the other hand, $\widehat{K}(h)$ is above the Poisson curve, the distribution is exhibiting clustering. A stair-shaped plot of $\widehat{K}(h)$ is an indication of a perfect pattern like a square or a hexagonal distribution of fibres as represented in figure 2.1.

One can study the difference between a Poisson distribution and the spatial distribution in analysis by making use of the $\widehat{L}(h)$ function defined as [28]

$$\widehat{L}(h) = \sqrt{\frac{\widehat{K}(h)}{\pi}} - h \tag{2.10}$$

Peaks of positive values in a plot of $\widehat{L}(h)$ would indicate clustering while negative troughs indicate regularity, for the corresponding distance h.

Pair distribution function

The pair distribution function, $g(h)$, is defined as the probability of finding the centre of a fibre inside an annulus of internal radius h and thickness dh with centre at a randomly selected fibre. The concept can be defined by equation (2.11).

$$g(h) = \frac{1}{2\pi h} \frac{\mathrm{d}K(h)}{\mathrm{d}h} \tag{2.11}$$

Matsuda et al. [20] use a discretised definition for the pair distribution function, given by equation (2.12).

$$g(h) = \frac{1}{2\pi h \rho \mathrm{d}h} \frac{1}{N} \sum_{i=1}^{N} n_i(h) \tag{2.12}$$

Although there is a clear relation between the pair distribution function and Ripley's K function, as expressed by equation (2.11), the two functions have different meanings. While Ripley's K function can distinguish between different patterns, $g(h)$ describes the intensity of fibre distances. For a periodic pattern, for example, the plot of $g(h)$ will show sharp peaks corresponding to the distances between the periodically arranged fibres.

In a Poisson point distribution, the complete randomness of the fibre distribution will assure that $g(h) = 1$ for all distances considered. A good fibre distribution can be judged by the proximity of $g(h)$ towards 1 when the distance h increases.

Figure 2.5 show examples of $K(h)$ and $g(h)$ plots for regular (periodic), hard-core and Poisson distributions of fibres.

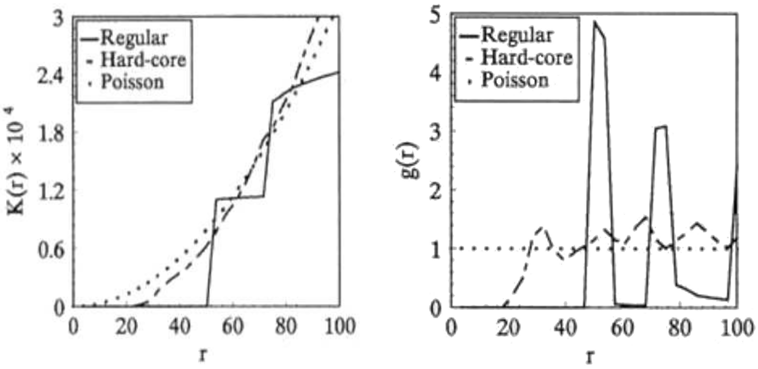

(a) Ripley's K Function (b) Pair distribution function

Figure 2.5: Examples of $K(h)$ and $g(h)$ functions by Pyrz [19].

2.1.6 Conclusion

From the above, one can conclude that the dimension of the SRVE is very well defined and characterised by Trias [23]. Hence, the minimum dimension for the SRVEs generated in this chapter will be given by the parameter δ as defined in equation (2.3) and table 2.1, i.e. the size of the SRVE will be such that $\delta \geqslant 50 \times R$.

However, there is still the need for a stable algorithm capable of generating a statistically equivalent fibre distribution to the one seen in real long fibre reinforced composites. This algorithm should also be fast and efficient and be applicable for fibre volume fractions between 55% and 65% – values considered normal for CFRPs. The generated distribution of fibres should also possess material simmetry in opposite edges.

The statistical equivalence of the generated SRVE should be verified using the functions defined in subsection 2.1.5. Material equivalence should also be proved to exist. Finite element analyses should be carried out on the generated SRVE to assess for transverse isotropy of the material.

2.2 MATLAB® script to generate a statistically representative volume element

In order to overcome the difficulty in obtaining a SRVE with a high fibre volume fraction in a short amount of time, a new algorithm was developed. It is founded in very simple mathematics and it is based only in moving those fibres which can be moved around and not touching those which can not be moved. The following subsections detail the flowchart of this algorithm and provide insight on the two heuristics developed for it.

2.2.1 Definition of the SRVE

Following Trias' conclusions [23] about the dimension of a SRVE, a value of $\delta = 50$ is chosen. This means that the dimension a of the SRVE will be $50\times$ the dimension of the fibre radius, considered constant throughout this thesis.

The SRVE is split into 9 regions as represented in figure 2.6. This figure is not to scale and the size of one fibre is given by the shadowed circle. The thick lines define the SRVE boundaries. The dashed lines are positioned at the distance of one fibre radius to each side of the SRVE limits. The outer

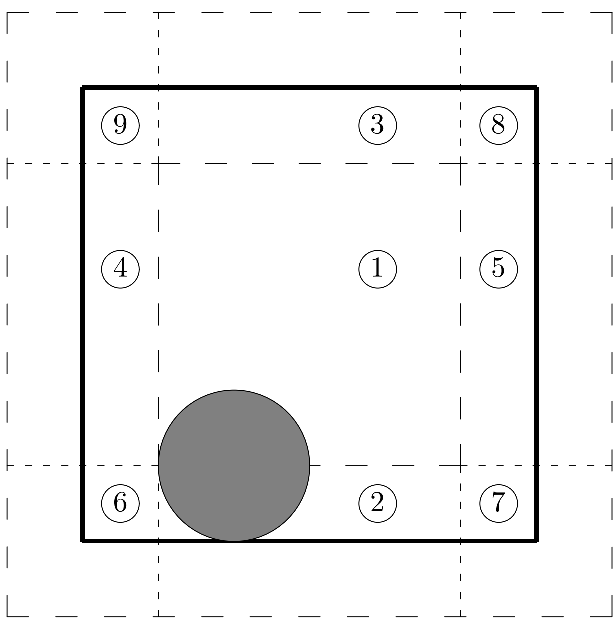

Figure 2.6: Definition of SRVE regions.

square delimits the region where a fibre centre can be positioned. The inner square (region 1 in figure 2.6) delimits the area where a fibre positioned there is completely inside the SRVE.

Considering the need to perform finite element analyses using the distributions generated by this algorithm, it was decided that the boundaries of the SRVE should respect the conditions of material symmetry. This will force a fibre positioned in, for example, region 2 of figure 2.6 to be split into two parts, where one part will stay in region 2 inside the SRVE (thick line), while the remaining part of that fibre will be positioned in region 3 guaranteeing material symmetry. The same applies to regions 4 and 5 thus enforcing material symmetry along opposite sides of the SRVE. For fibres positioned in regions 6, 7, 8, and 9, these are split in four parts, positioned one part in each of these regions in such a way that the material symmetry of the SRVE is respected in its corners as well.

Also due to the future need to perform FEAs, a minimum distance between any two neighbouring fibres is imposed. This will help inhibiting regions of poor mesh quality between fibres.

2.2.2 Main flowchart

An algorithm called `RAND_uSTRU_GEN` was created using MATLAB® [29]. The name comes from *Random Microstructure Generator*. It provides a fast and computationally efficient way of generating a microstructure for long fibre reinforced composites as it is seen in the transverse section of real materials.

The flowchart of this algorithm is presented in figure 2.7. Each iteration of the algorithm is composed of three steps. The first step corresponds to the hard-core model as it was defined in subsection 2.1.4. Steps two and three are heuristics developed for this algorithm.

One iteration of the algorithm corresponds to one run through all three steps. By the end of an iteration, the current fibre volume fraction, v_f^{cur}, is compared to the fibre volume fraction requested at the beginning of the algorithm by the user, v_f^{req}. If v_f^{cur} is greater or equal than v_f^{req}, the algorithm stops and outputs the results. If the condition is not yet verified, then the algorithm moves on to the next iteration until the condition is satisfied.

There are 13 input variables, some of them related with how the results are outputted:

R − Fibre radius.

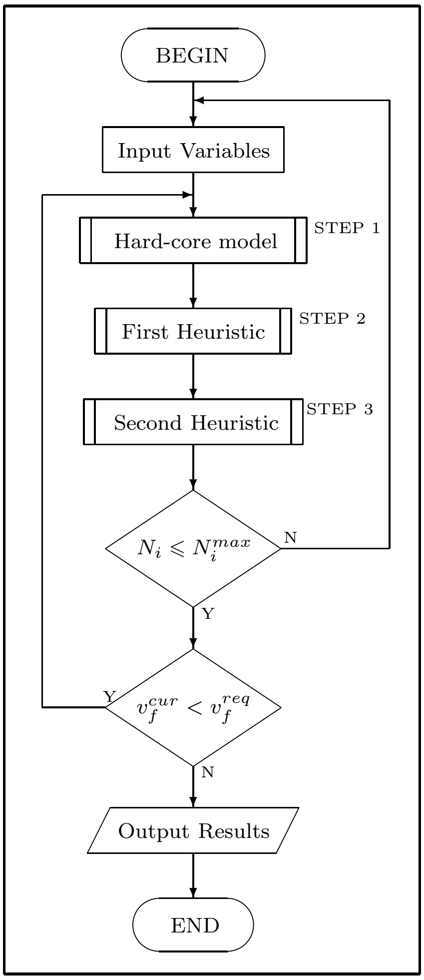

Figure 2.7: Flowchart of algorithm `RAND_uSTRU_GEN`.

delta – Value of δ, defined by equation (2.3).

Vol_fibre_req – Fibre volume fraction requested by user, v_f^{req}.

DISTMIN – Minimum distance between any two fibre centres, Δ_{min}.

N_guesses_max – Number of attempts of fibre placement in step one, N_g^{max}.

N_cycles_max – Maximum number of iterations the algorithm is allowed to perform, N_i^{max}.

N_change – Number of iterations before changing criteria in step two, N_c.

Square_size – Distance of square size in step three, S_o.

Square_inc – Increment to be given to S_o in step three, S^+.

quant_option – Binary variable that allows for a statistical characterisation of the fibre spatial distribution.

image_option – Binary variable that allows for printing of fibre distribution at the end of each step.

finim_option – Binary variable to generate an image with the final fibre distribution.

vorim_option – Binary variable to generate the Voronoi cells along with the final fibre distribution.

Binary variables use the value 0 for *NO* and 1 for *YES*. All the above mentioned variables will be properly defined in the next subsections. Focus will be shifted now on what takes place inside each of the three main steps of the algorithm.

A counter of the number of iterations the algorithm performs, N_i, is checked in every iteration. This check acts as a safeguard against any possible jamming scenarios which might occur. The maximum number of iterations is given by the input variable N_i^{max} and, by default, is set to 20. If this maximum is reached, then the algorithm will simply restart fresh.

2.2.3 STEP ONE – Hard-core model

The first step of the algorithm is equal to the hard-core model as it was defined in subsection 2.1.4. The corresponding flowchart can be seen in figure 2.8.

This step starts by randomly generating the position of one fibre inside region 1 in figure 2.6. This position is used as a reference for subsequent calculations. It then tries to generate another fibre position. A compatibility check with all the previous fibres generated and accepted is performed. If the new position does not collide with the previous generated fibres, then the new position is accepted, a new fibre is added on that position, and the current fibre volume fraction, v_f^{cur} is updated. A new check to see if v_f^{req} has been achieved is performed and if so, the results are outputted. If the new position generated did not pass on the compatibility check, the algorithm just ignores this position and generates a new one.

In order to guarantee that the periodicity of the generated geometry is kept, it is required to check whether the new position randomly picked is either in region 1 of figure 2.6 or in any of the other regions. If the

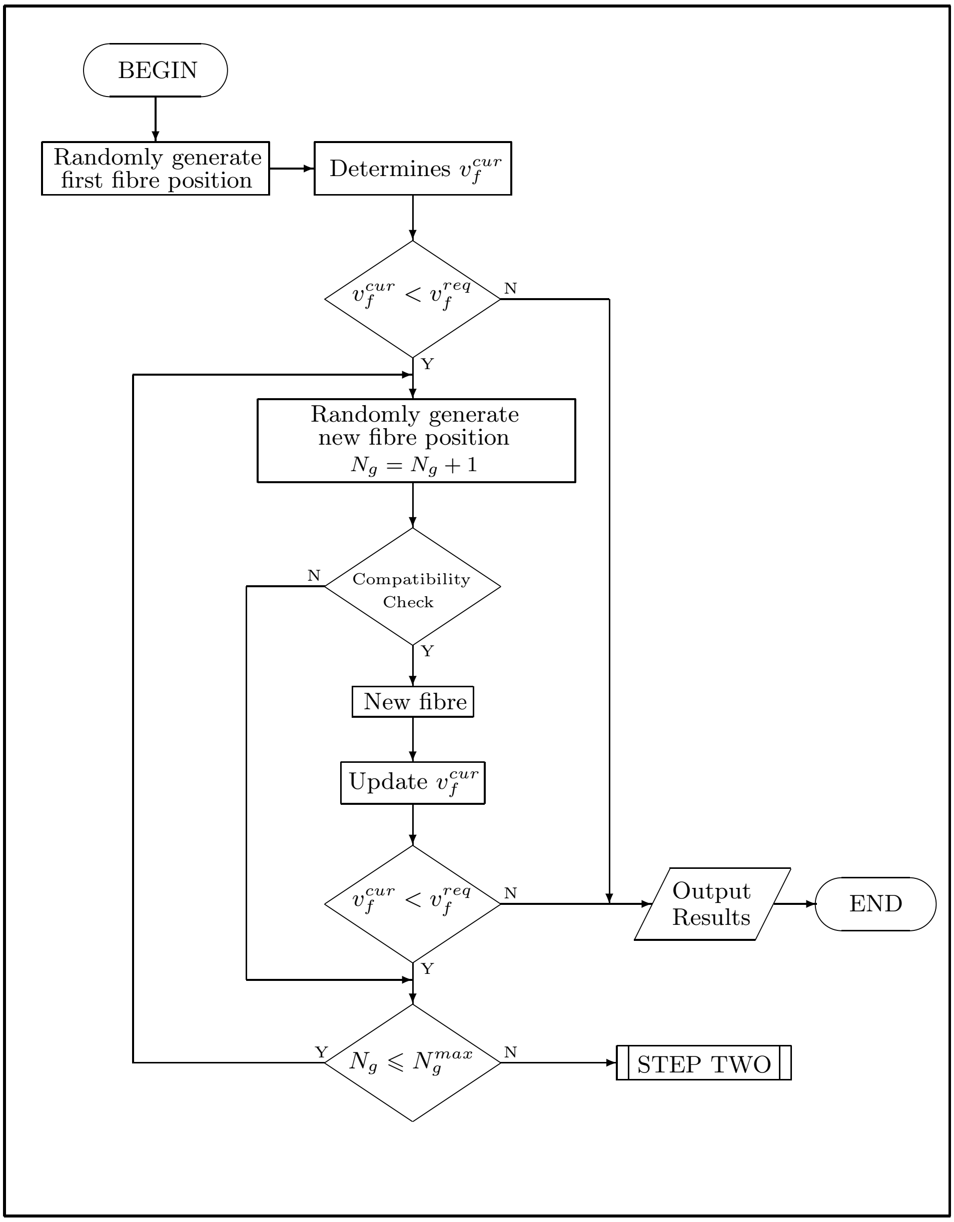

Figure 2.8: Flowchart of STEP ONE in algorithm `RAND_uSTRU_GEN`.

new position is along the sides of the SRVE, a second compatibility check (not represented in figure 2.8) is performed, but on the opposite side of the SRVE to confirm that a second fibre can be added. If the two positions are acceptable, then two fibres in opposite sides of the SRVE are added to the list of fibres. However, one must remember that only a fraction of each of these two fibres is inside the SRVE, but the sum of the fractions equals the area of a complete fibre.

The same reasoning can be made for positions randomly picked in one of regions 6, 7, 8, and 9, i.e. the corners of the SRVE. There is the need to perform not two, but four compatibility checks, one for each corner since, in order to guarantee symmetry, four more fibres need to be added to the list of fibres. Again, the sum of the fractions of these four fibres inside the SRVE equals to the area of a complete fibre.

While these actions take place, a counter controls how many attempts of fibre placement are executed in the step. When this counter reaches the limit given by N_g^{max}, it stops the process and moves on to step two. The value of N_g^{max} has been set to 50000 as it was shown by experience that it was able to provide a good amount of valid fibre placements. Greater values just increased the computation time and did not improve the number of valid fibre placements.

2.2.4 STEP TWO – Stirring the fibres

Step two can be seen as an heuristic as it helps the algorithm to create matrix-rich areas on the SRVE that increase the probability of success of the hard-core model in allocating new fibres. Its flowchart is presented in figure 2.9. Variable i_f represents a counter and N_f the total number of fibres already assigned to the SRVE in previous iterations.

The matrix-rich areas are created by stirring the fibres. The small displacements imposed on the fibres are a consequence of searching for one of the closest (*not* necessarily *the* closest) fibres and moving the fibre in that direction. Figure 2.10 helps to understand the concept.

Let us consider four fibres – A, B, C, and D – positioned as displayed in figure 2.10. For the sake of simplicity, let us also consider that fibres B, C, and D are fixed and so are not affected by this stirring process. A_0 represents the starting position of fibre A. If the algorithm is in its first iteration, fibre A will be displaced in the direction of the closest fibre – fibre B, in the present case. The direction of the motion is defined by the vector M1 while the length of the displacement is a random number between 0 and $l_{A_0B} - \Delta_{min}$, being Δ_{min} the input variable that defines the minimum distance between any two fibre centres, and l_{A_0B} the distance between fibres A and B. The final position is denoted by A_1.

In the next iteration, the fibre in A_1 will be shifted in the direction of the closest fibre, but not considering the last fibre used as a reference. Looking at figure 2.10, the closest fibre to A_1 is B, but it was also the fibre used as

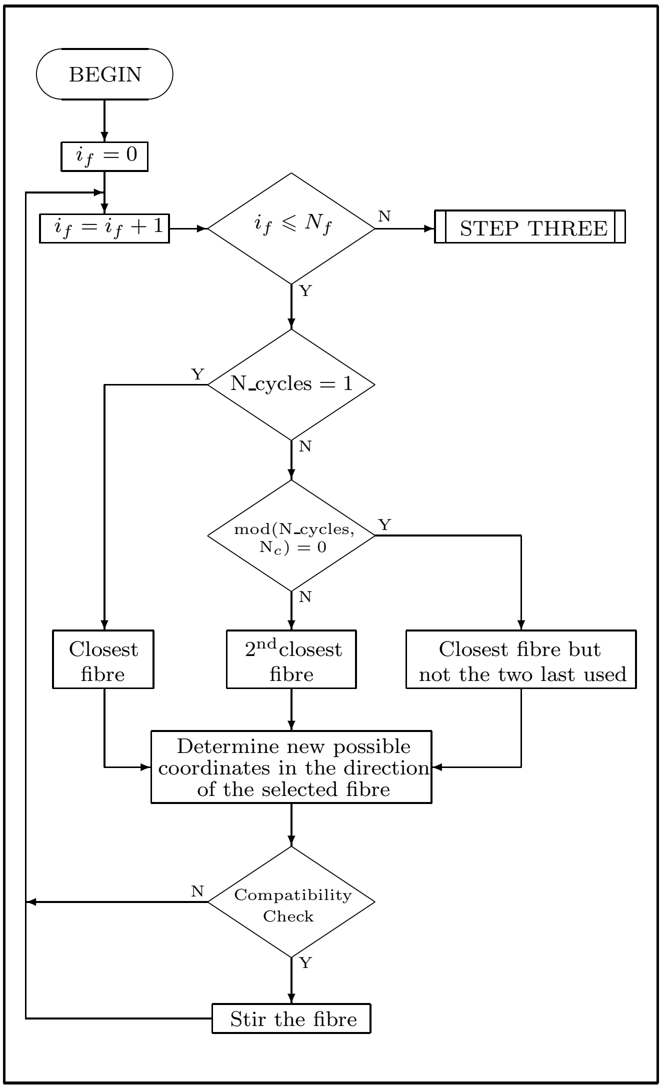

Figure 2.9: Flowchart of STEP TWO in algorithm `RAND_uSTRU_GEN`.

reference in the previous iteration. The reference fibre for the present cycle is thus fibre C. Again, M2 defines the direction of the motion while the length of the displacement is defined by a random number between 0 and $l_{A_1C} - \Delta_{min}$. Excluding the first iteration, where there simply is no previous iteration, this is the standard concept for fibre displacements in step two of the algorithm.

The next iteration is not so linear as the previous two. The input variable N_c controls in how many iterations the stirring criteria is changed. By default, N_c has the value 3 since it was found by experience that it is the

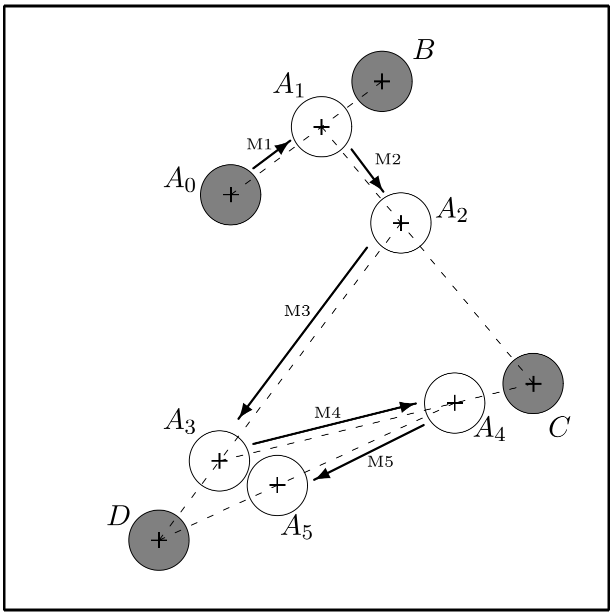

Figure 2.10: Concept behind STEP TWO.

optimum value in terms of computational efficiency. This means that every 3 iterations the algorithm changes the stirring criteria. The third iteration will now apply a displacement to the fibre in A_2 and the direction of the movement will be towards the closest fibre, but not considering the previous *two* used as reference. In the current example, fibres B and C were used as reference in the previous two iterations respectively, so only fibre D can be used as reference for the current iteration. Fibre A is thus displaced from A_2 to A_3. M3 is the direction vector and the length of the displacement is still randomly selected between 0 and $l_{A_2D} - \Delta_{min}$.

This new criterion only affects cycles which are multiple of the value in the input variable N_c – as per flowchart in figure 2.9. If N_c has the value 3, then only cycles 3, 6, 9, ..., $3n$ are affected.

Next cycle will obey to the standard criterion for fibre displacement, that is, it will look for the closest fibre but not considering the last fibre used as reference for displacement. Therefore, iterations 4 and 5 will cause displacement of fibre A from A_3 to A_4 along M4 towards fibre C, and from A_4 to A_5 along M5 towards fibre D, respectively.

Iteration 6 is not represented in figure 2.10 but it will use the same criterion as iteration 3 and will move fibre A from A_5 towards neither fibres C nor D, but towards fibre B.

The example in figure 2.10 does not correspond completely to what really happens during this step since *all* fibres can be stirred and there are many more fibres besides the ones represented – there can easily be up to 500 fibres in the SRVE. This assures a very dynamic process where very few fibres are left in the same place as they were when the step started.

It should be noted that before assigning a new position to the fibre to be displaced, a compatibility check with the other fibres must be performed to guarantee the safeguard of the minimum distance between fibre centres defined by input variable Δ_{min}. If the check is negative, then the fibre is not stirred.

The step ends when all fibres were attempted to be stirred, causing the algorithm to move on to step three.

2.2.5 STEP THREE – Fibres in the outskirts

Step three makes use of a second heuristic which has a dramatic effect on the time the algorithm takes to reach the requested fibre volume fraction. However, this step must be used cautiously since it could lead to fibre clustering. A good control over some of the input variables is required in order to achieve statistically satisfactory results. The flowchart of this step is presented in figure 2.11.

This step affects only the fibres placed in the outskirts of the SRVE. The stirring of these fibres will create matrix-rich areas which increase the success rate of fibre positioning during step one.

The variables i_f and N_f are defined in the same way as in the previous step. First, it is required to check if the current fibre is on the outskirts of the SRVE or not. For this, a definition for the outskirts must be provided. Figure 2.12 illustrates the concept.

The variable S_o defines the initial dimension of the square – identified by B1 in figure 2.12 – that will be delimiting the outskirts. By default, this variable is set to $3 \times R$. All the fibres with their centres positioned outside square B1 will be affected during this step. The outer region of square B1 is split in 8 different regions. In each region, a different movement will be applied to the fibres in those regions, but always towards the interior of square B1, and away from the edges of the SRVE. For example, fibres in region 1 will be moved rightwards in an angle between $-\pi/2$ and $\pi/2$ with the horizontal. Regions in the corners of the SRVE – regions 5, 6, 7, and 8 – will be stirred away from both edges of the SRVE meeting in that corner. For example, fibres in region 5 will be stirred rightwards as well as upwards

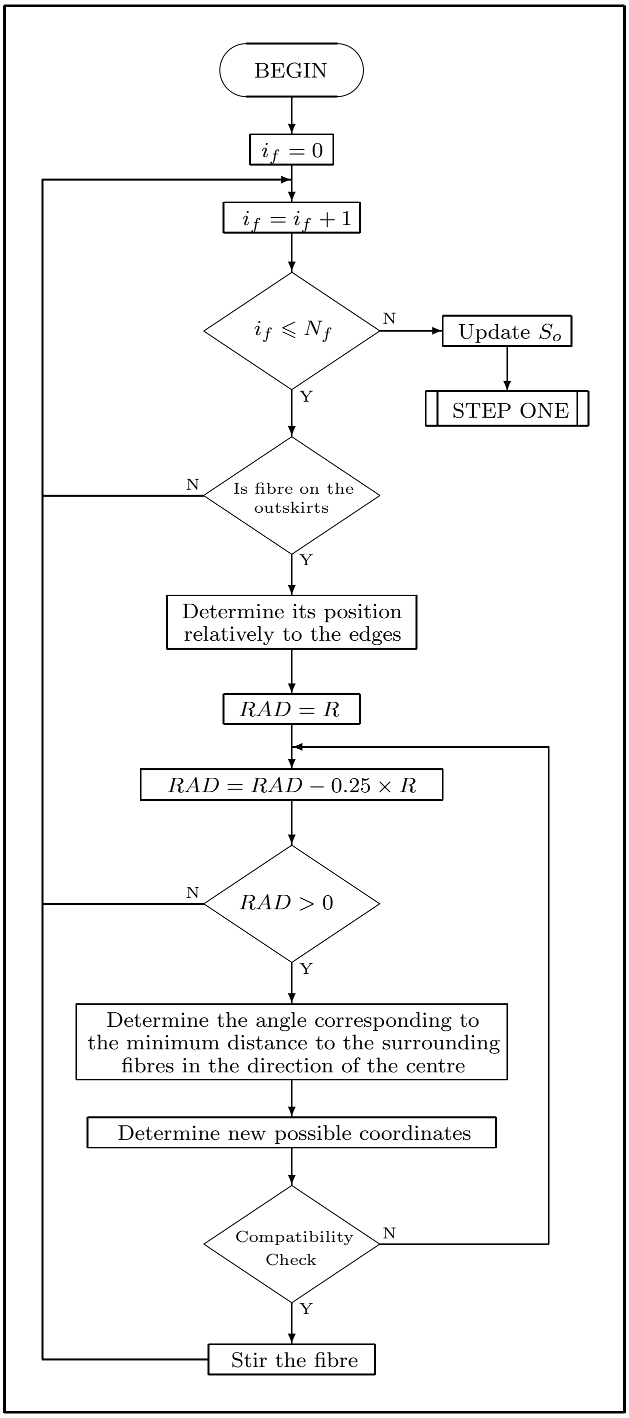

Figure 2.11: Flowchart of STEP THREE in algorithm `RAND_uSTRU_GEN`.

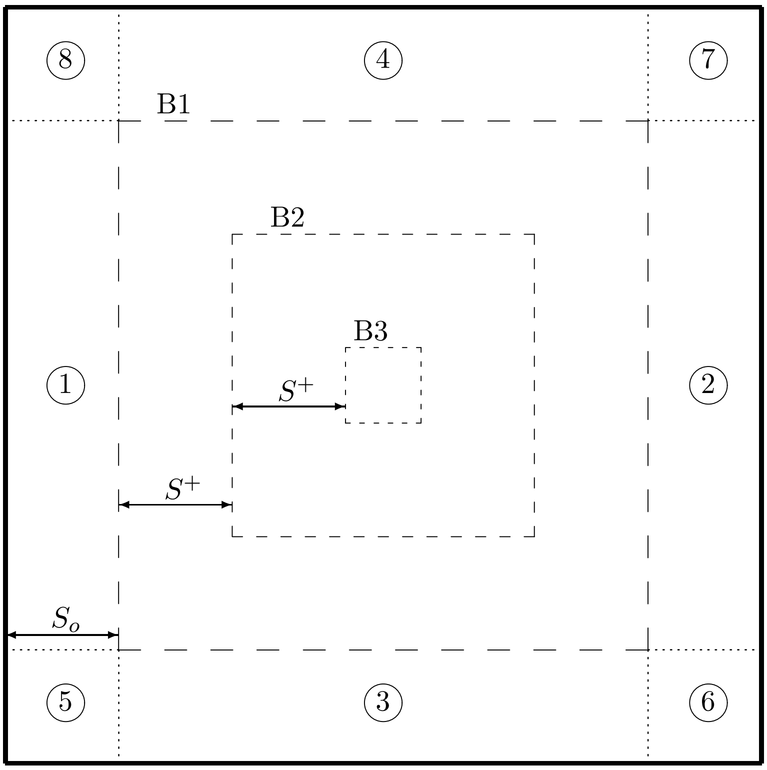

Figure 2.12: Definition of the outskirts in STEP THREE.

in an angle between 0 and $\pi/2$.

The stirring lengths can only be $0.75 \times R$, $0.5 \times R$, and $0.25 \times R$. Each possible length is tested for all angles and if it does not comply with the compatibility check for any angle, then the next smaller length is checked. If none of the lengths allows the fibre to be displaced, then the fibre is ignored and it is left where it was. The stirring angles are defined between the limits defined for each region. The exact value is chosen as the one that most reduces the gap to the other fibres.

As the number of iterations increases, the fibres outside square B1 will get compacted against each other along the edge of the square, creating a region rich in fibres. In order to avoid this, one other input variable is defined. Variable S^+ affects the size of the square defining the outskirts region throughout the consecutive iterations. Its effect can be seen in figure 2.12. At the end of each iteration, the size of the square decreases by the value of S^+ in each side. Observing figure 2.12, in the first iteration the size of the square is given by B1; but in the second iteration will be B2, in the third, B3, and so on. This alone avoids the clustering of fibres in the outskirts. By default, S^+ is set to $\left(8.5 - 10 \times v_f^{req}\right) \times R$, which has been determined by experience.

Since the generated distribution from this algorithm will have to go through a meshing technique for FEAs, it was decided to perform a position check on all fibres and remove/reallocate those which were positioned in a highly tangent locus to the SRVE's boundaries. This alone will allow for an overall better mesh quality.

The step will terminate when all fibres along the outskirts have been attempted to be stirred. This step can be skipped over by controlling the values of the input variables S_o and S^+. If the first assumes the value $-R$ and the second 0, none of the fibre centres will be located outside the square initially defined, hence no fibre will be stirred.

2.2.6 Auxiliary functions

A few MATLAB® [29] functions were written to complement the main algorithm. The most important one and widely used throughout the algorithm is `f_overlap`, which determines if the possible new position of a fibre when affected by one of the stirring processes or generated by the hard-core model is compatible with the already existing fibres, i.e. if the new position overlaps with any of the other fibres and respects the minimum distance specified by the input variable Δ_{min}.

One other function is `f_image`. It allows the user to generate a plot of the fibre distribution at the end of each step (controlled by the input variable `image_option`) or to generate the same plot but at the end of the algorithm (input variable `finim_option`). If the user wishes so, the Voronoi cells corresponding to the fibre distribution can also be plotted in the same figure using the input variable `vorim_option`. All these images are saved in .BMP format in the working directory.

Statistical characterization of the developed fibre spatial distribution also needs to be performed if we want to judge the quality of the generated SRVE. Input variable `quant_option` allows the algorithm to call function `f_characterize` and run all the statistical analysis tools and functions defined in subsection 2.1.5. The results are either plotted or printed in the commands window of MATLAB® [29], depending on the statistical function.

2.2.7 Examples of generated fibre spatial distributions

Figures 2.13 to 2.19 show the evolution of the fibre spatial distribution for $v_f^{req} = 65\%$. A plot of the fibre distribution after each step has been performed.

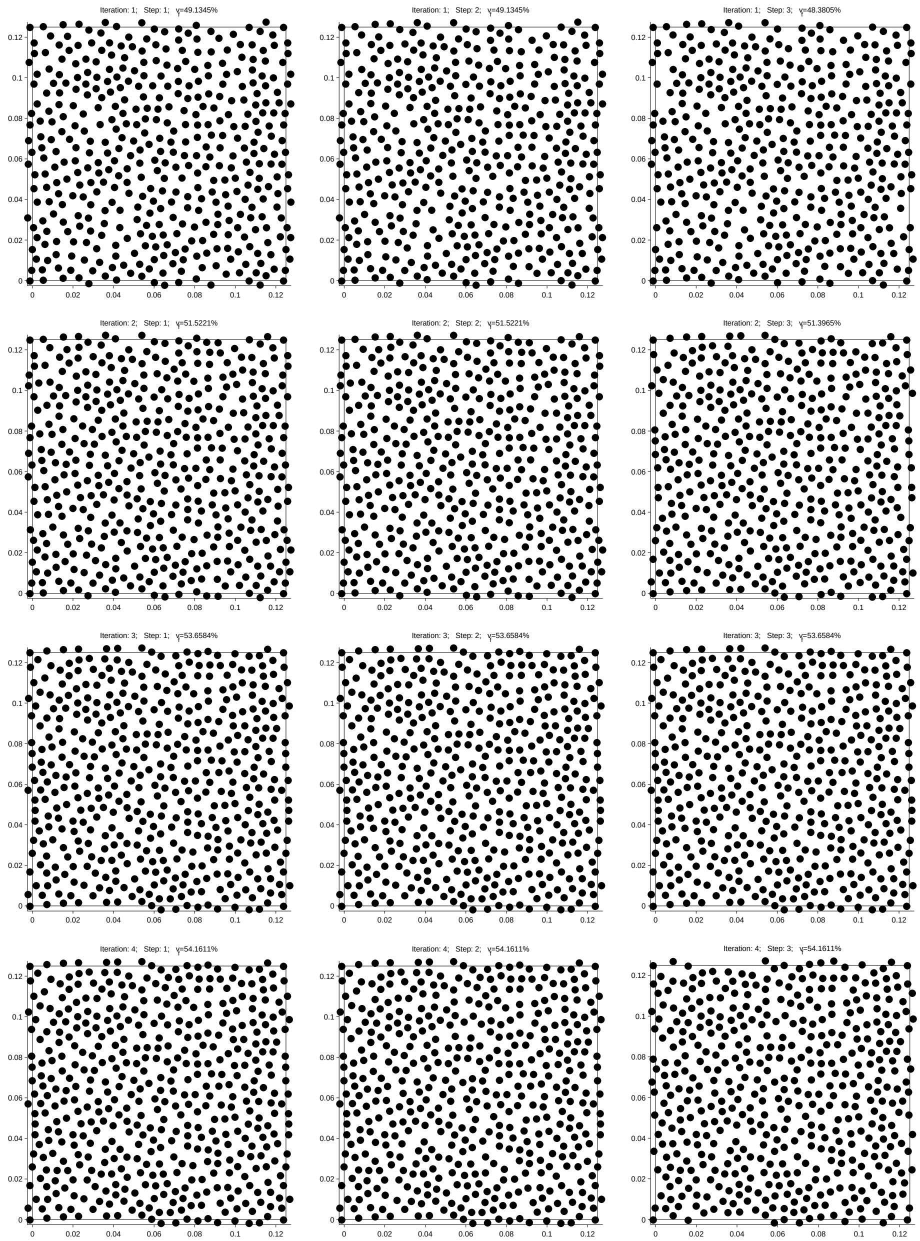

Figure 2.13: Evolution of fibre spatial distribution – sequence 1.

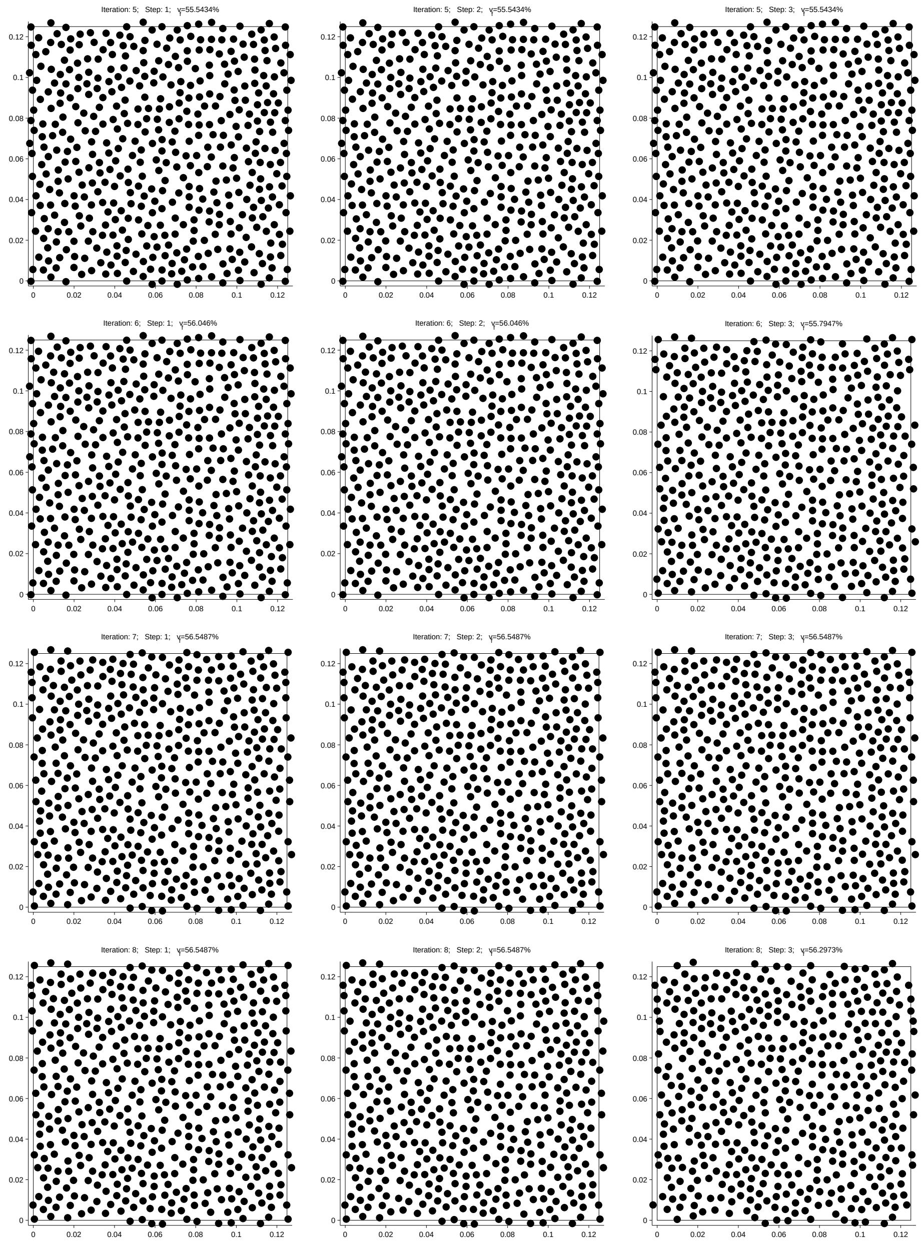

Figure 2.14: Evolution of fibre spatial distribution – sequence 2.

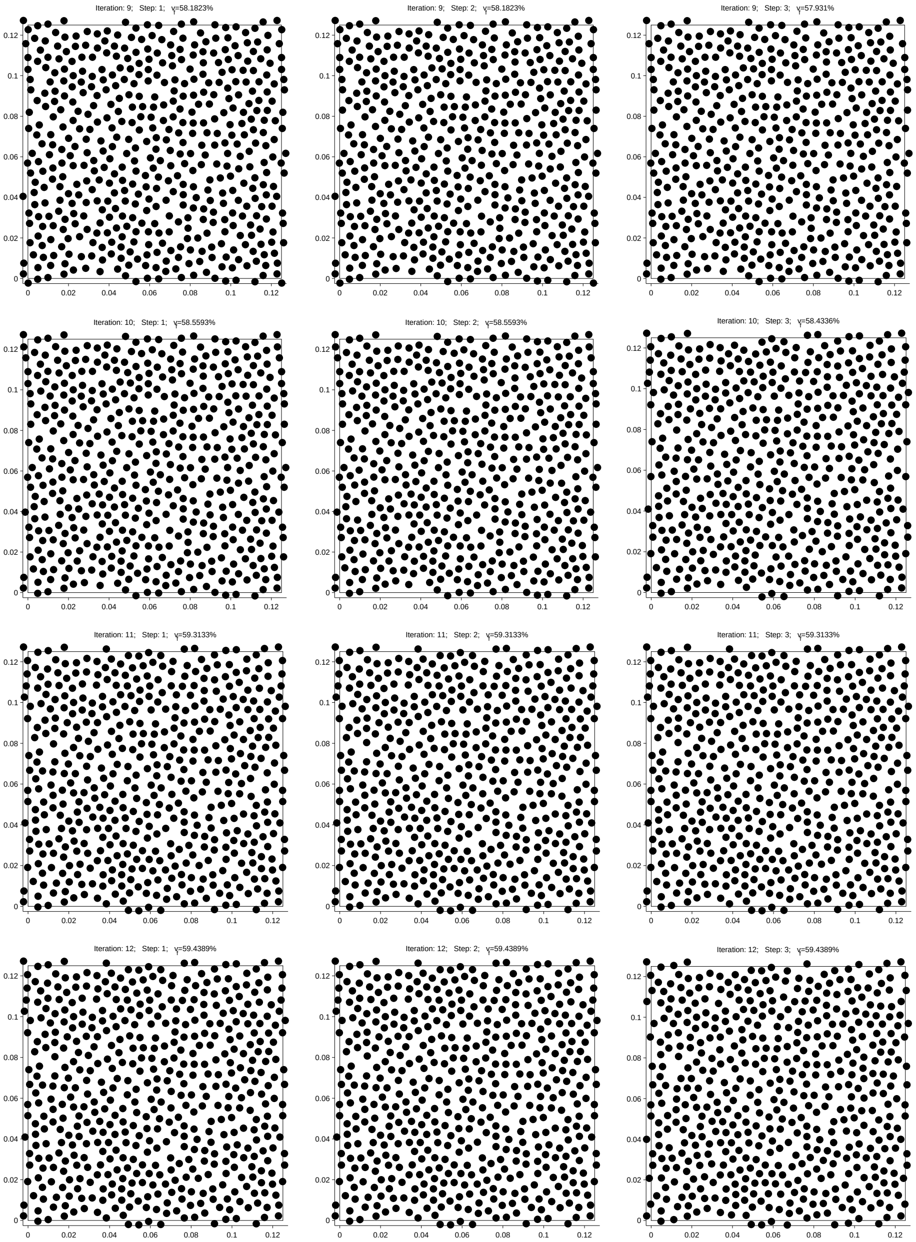

Figure 2.15: Evolution of fibre spatial distribution – sequence 3.

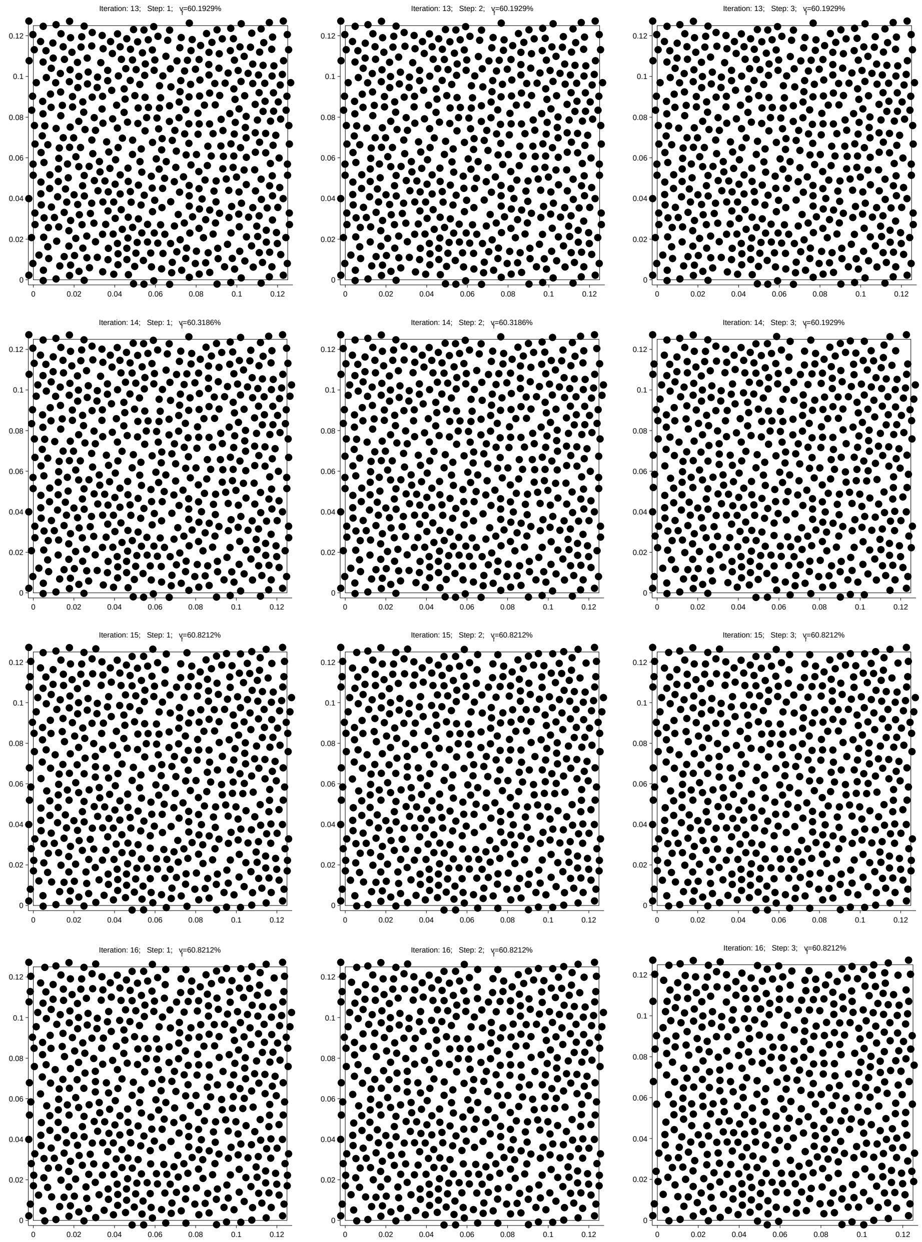

Figure 2.16: Evolution of fibre spatial distribution – sequence 4.

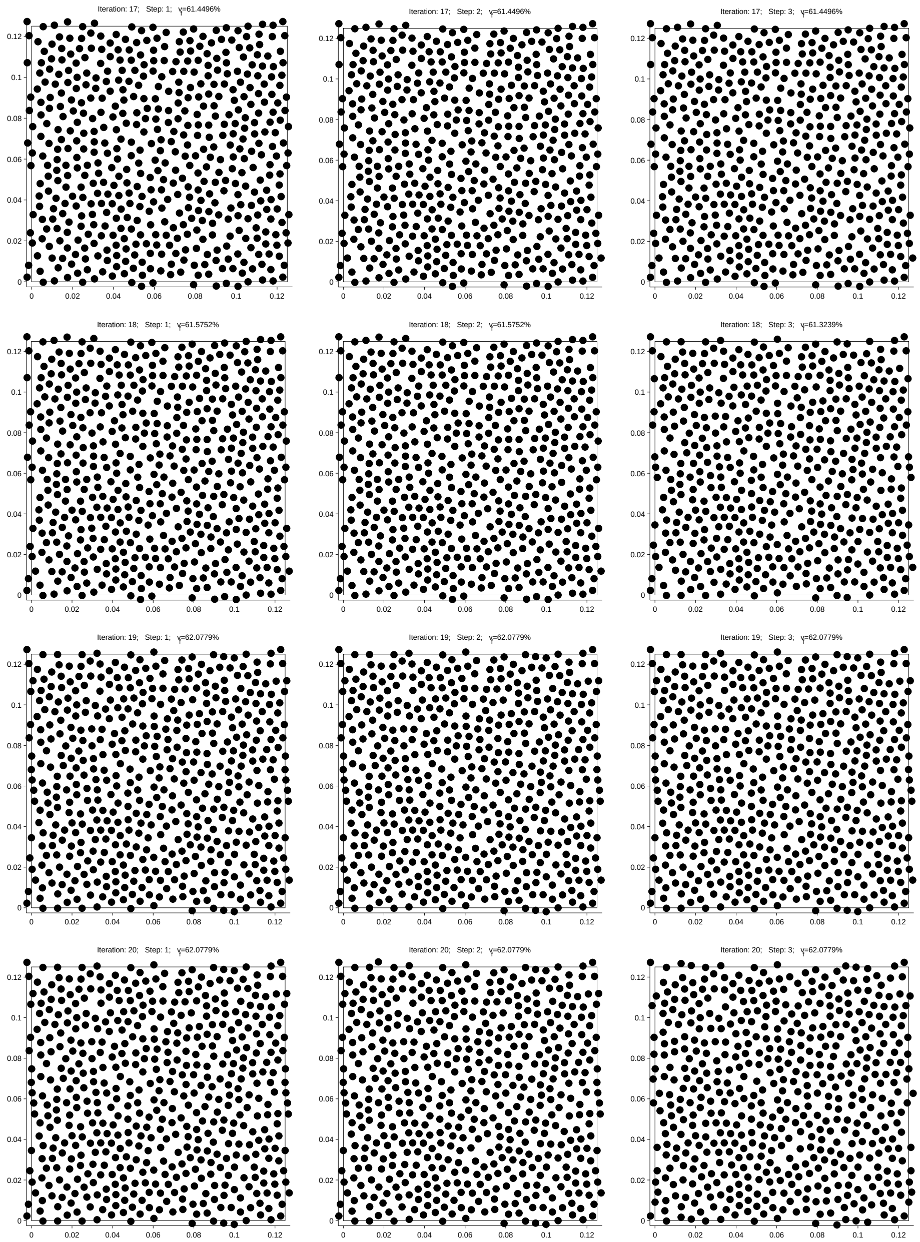

Figure 2.17: Evolution of fibre spatial distribution – sequence 5.

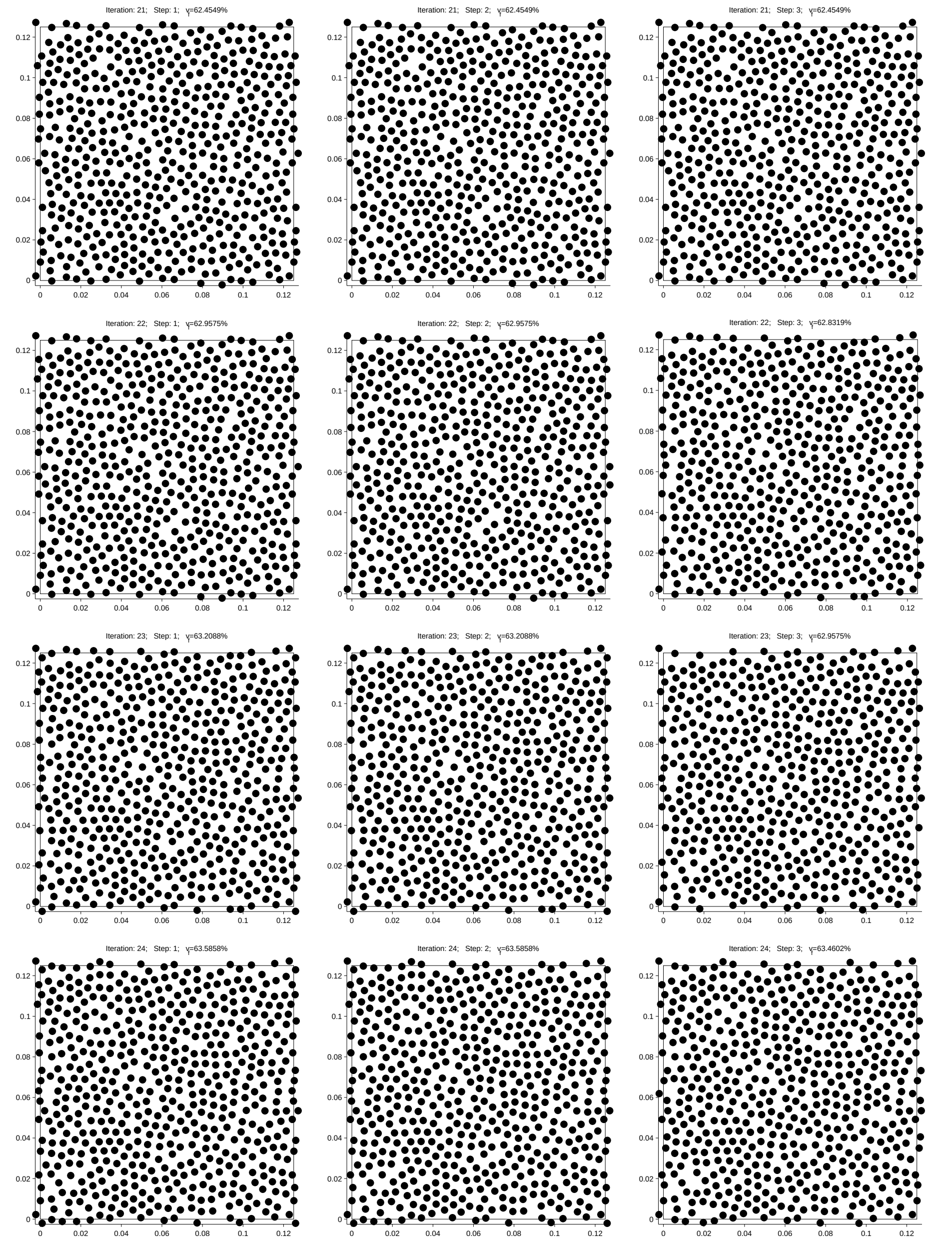

Figure 2.18: Evolution of fibre spatial distribution – sequence 6.

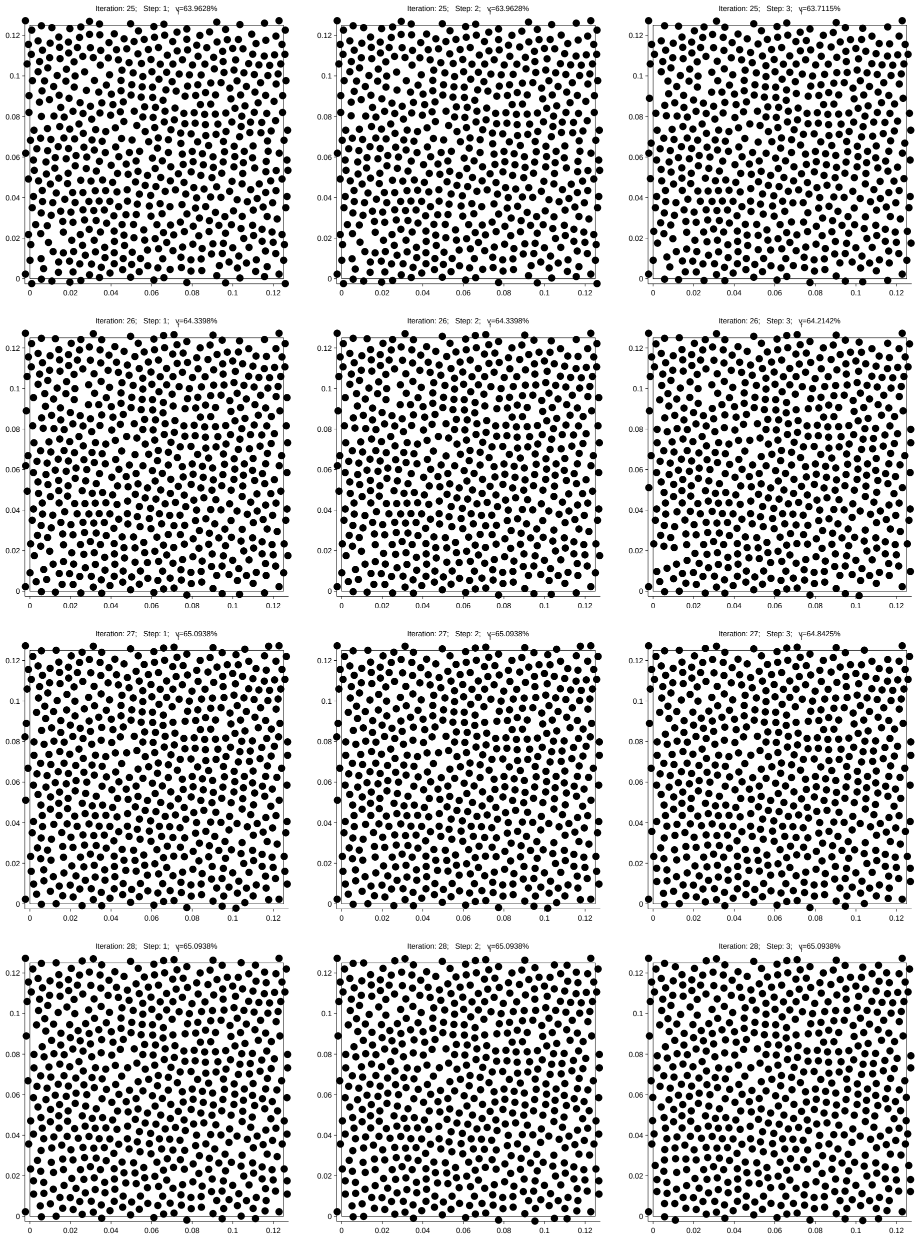

Figure 2.19: Evolution of fibre spatial distribution – sequence 7.

2.3 Statistical characterisation of script `RAND_uSTRU_GEN`

In this section, the statistical analysis tools presented in subsection 2.1.5 will be used to quantitatively characterise the fibre spatial distribution obtained from the `RAND_uSTRU_GEN`. The results will be compared with those obtained using Wongsto and Li's algorithm [24] and with the two periodic distributions represented in figure 2.1.

Unless otherwise specified, the values of the input variables used throughout these analyses are:

$$\begin{aligned} &R = 0.0026 \ \mathtt{mm} \\ &\delta = 50 \\ &\Delta_{min} = 2.07 \times R \end{aligned} \tag{2.13}$$

All runs were performed in a desktop computer with a Pentium IV 3.0 GHz processor, 1GB of RAM memory and *hyperthreading* turned ON. It should also be mentioned that Wongsto's method was programmed based on the description of the algorithm in reference [24].

2.3.1 Time

The first analysis performed was on the time required by each algorithm to run. Table 2.4 resumes the results for different fibre volume fractions. Periodic distributions are not presented here for comparison since those are generated almost instantaneously. The method used by Trias [23] is also presented for comparison.

The values presented are the average of five runs for each fibre volume fraction. It is clear that `RAND_uSTRU_GEN` is the fastest of the three. Wongsto's method always needs at least 250 iterations, so the time it takes to finish is approximately the same for all values of v_f^{req}. However, if the condition $\delta \geqslant 50$ was relaxed or if the number of fibres reduced[5], the time these algorithms would require to run would decrease considerably. Just for comparison, digital image treatment of real micrographies can take up to 7 minutes [23].

[5] In [24], Wongsto et al. used only 105 fibres.

Table 2.4: Average and standard deviations of time in minutes required to run each algorithm. Values marked with [a] were extrapolated.

	RAND_uSTRU_GEN		Wongsto [24]		Trias [23]
v_f^{req}	$\mu(time)$	$\sigma(time)$	$\mu(time)$	$\sigma(time)$	$\mu(time)$
0.45	0.03	0.01	7.23	1.27	1.67
0.48	0.12	0.04	6.90	0.72	2.48
0.49	0.15	0.01	6.46	0.80	5.82
0.51	0.28	0.05	6.92	0.77	13.56
0.53	0.44	0.07	6.92	0.61	22.54
0.55	0.68	0.01	7.91	0.57	44.86
0.57	1.04	0.08	7.26	0.77	80.17
0.59	1.34	0.12	7.66	0.80	127.67
0.61	1.75	0.16	8.03	1.07	331.05[a]
0.63	2.37	0.10	7.12	0.49	615.70[a]
0.65	3.31	0.16	7.20	0.45	1145.09[a]

2.3.2 Voronoi polygon areas and neighbouring distances

For this test, the coefficient of variation will be used instead of the simple standard deviation. It is defined according to equation (2.14).

$$\rho(x) = \frac{\sigma(x)}{\mu(x)} \tag{2.14}$$

The variable x represents the areas of the Voronoi cells or the distances to neighbouring fibres corresponding to the spatial fibre distribution in analysis. Table 2.5 shows the coefficient of variation of both areas of Voronoi cells and neighbouring distances for each method. Periodic distributions obviously have $\rho_A = \rho_D = 0$. Two similar tests were performed – one with 56% in v_f^{req} and a second with 65%. The results for 56% are also compared with values from Matsuda et al. [20] using the fibre distributions represented in figure 2.2. The values presented for RAND_uSTRU_GEN and Wongsto's method are the average of five runs.

For v_f^{req} of 56% the coefficients of variation of the Voronoi polygon areas are all very close to each other except for Matsuda's Y-distribution that presents poorer performance. As for the distance to neighbouring fibres, Matsuda's Point distribution provides better results while all others are at the same level.

Table 2.5: Coefficient of variation for Voronoi polygon areas and distances to neighbouring fibres.

56%	ρ_A	ρ_D
`RAND_uSTRU_GEN`	0.137	0.196
Wongsto's method	0.129	0.190
Matsuda's Y-distribution [20]	0.106	0.190
Matsuda's Point distribution [20]	0.135	0.256
65%	ρ_A	ρ_D
`RAND_uSTRU_GEN`	0.099	0.170
Wongsto's method	0.077	0.125

When we increase the fibre volume fraction, we are also compacting the fibres and decreasing the distance that the fibres can be stirred by both methods. This means that the fibres will have less chance to move around and for Wongsto's method this has a significant impact since the fibres start from a periodic array and have difficulty leaving that periodicity. This can be seen for $v_f^{req} = 65\%$. The coefficient of variation for both functions diverge from each other, leaving `RAND_uSTRU_GEN` with a better performance since it does not depend on a previously established periodic distribution, but is an almost purely random algorithm for generating fibre spatial distributions.

2.3.3 Ripley's K function

For the next three subsections, two fibre volume fractions were used – 56% and 65%. For each volume fraction, twenty different distributions were generated and analysed. Figures 2.20 and 2.21 show examples of the generated distributions, for different fibre volume fractions and methods of generation. The square in thick line represents the border of the SRVE.

Function $L(h)$, which measures the difference between the K function of a Poisson distribution and the estimate of $K(h)$ of any other distribution, is represented in figures 2.22 and 2.23, each figure for each fibre volume fraction. Each curve represents the average value of the twenty generated distributions and the maximum and minimum values were added as error bars. Values for the two periodic distributions are also shown for comparison.

The two periodic distributions exhibit a saw-shaped function since the distances between fibres are regularly pre-defined. One interesting aspect is the evolution of $\widehat{K}(h)$ for the Wongsto model: at short distances, the curve

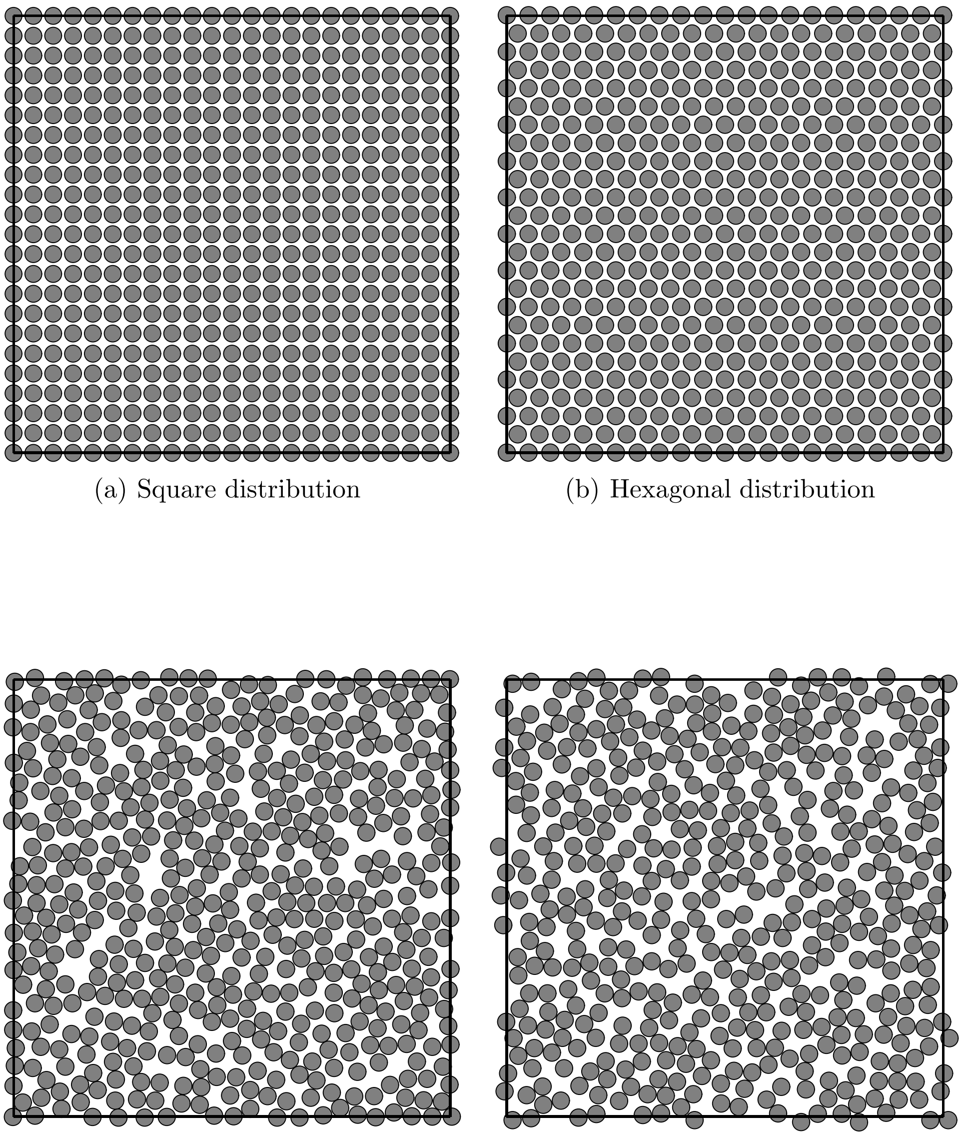

(a) Square distribution

(b) Hexagonal distribution

(c) Wongsto's method

(d) `RAND_uSTRU_GEN`

Figure 2.20: Fibre distributions in analysis with $v_f^{req} = 56\%$.

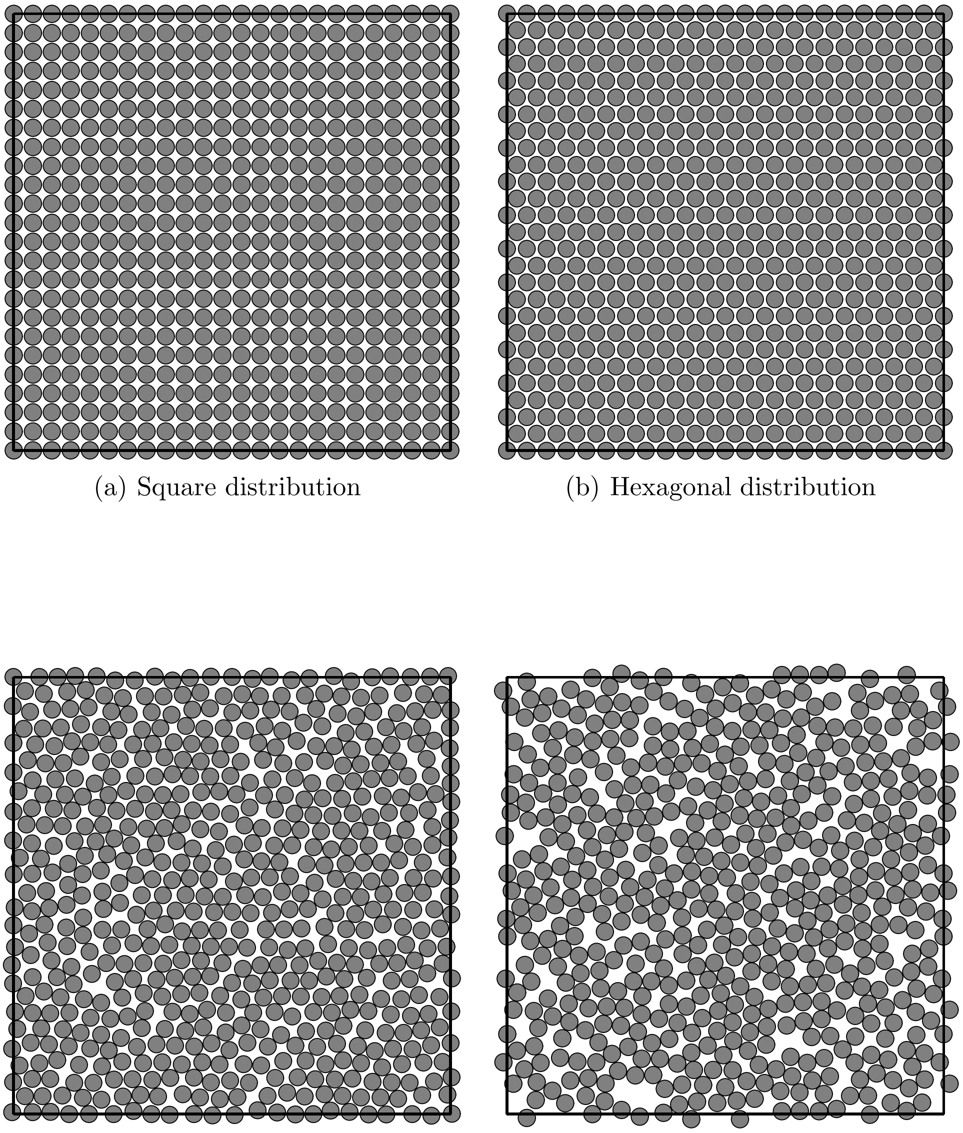

(a) Square distribution

(b) Hexagonal distribution

(c) Wongsto's method

(d) `RAND_uSTRU_GEN`

Figure 2.21: Fibre distributions in analysis with $v_f^{req} = 65\%$.

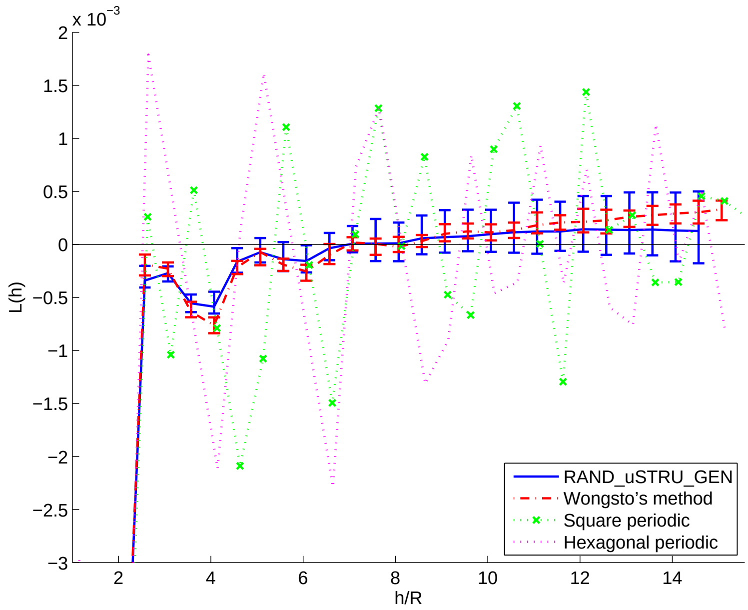

Figure 2.22: $L(h)$ function for $v_f^{req} = 56\%$.

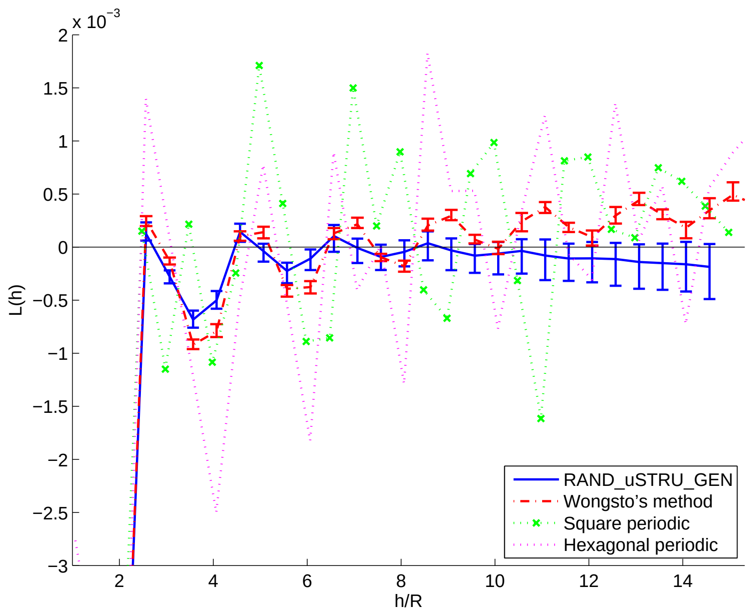

Figure 2.23: $L(h)$ function for $v_f^{req} = 65\%$.

is below $K_P(h)$, while for long distances the curve is above $K_P(h)$ with tendency to diverge from it. This means that for short distances the method exhibits regularity – probably because it starts with a regular pattern – while for long distances the algorithm creates some degree of clustering – probably because the fibres get too much accommodated on the edges of the SRVE.

Also visible in the plots is the increasing difficulty of Wongsto's method to break free of its initial periodic arrangement. In figure 2.23, it shows the same saw-shaped evolution of an hexagonal periodic distribution (same peaks and same throughs). On the other hand, `RAND_uSTRU_GEN` is capable of maintaining itself parallel and close to a Poisson distribution.

2.3.4 Pair distribution function

The pair distribution function is plotted in figures 2.24 and 2.25 for all four fibre distribution methods under analysis, each figure for each fibre volume fraction considered.

It clearly shows the peaks normally detected for periodic distributions, but it also shows that both Wongsto's method and `RAND_uSTRU_GEN` tend to oscillate close to 1, which is the pair distribution function of a perfect Poisson distribution.

Increasing the fibre volume fraction does not create any substantial differences.

2.3.5 Nearest neighbours

As was described in subsection 2.1.5, nearest neighbour distances provide information regarding the short range interaction of fibres. It is important that this statistical tool is well reproduced since experience shows that damage initiation is likely to occur in regions where the fibres are closer together. Figures 2.26 to 2.31 show the probability density functions for the first, second and third nearest neighbours.

It can be seen in the figures that the PDF plots for periodic distributions are nothing more than straight vertical lines or very steep curves, not reproducing the short range interaction of fibres of the bulk material. Increasing the fibre volume fraction leads to a shift in the curves to the left, signalling that the fibres are closer now than before.

Visible in figures 2.26 and 2.27 is the very steep curve of both random distributions. This happens not because of regularity in the distribution,

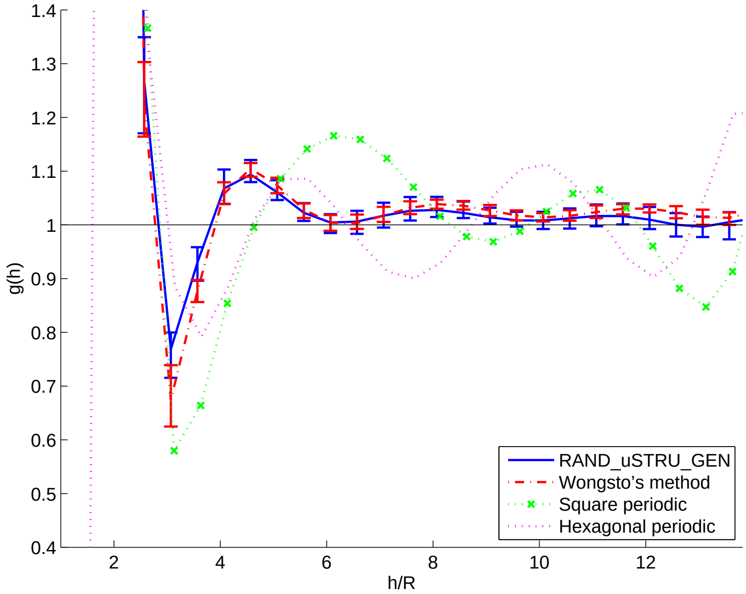

Figure 2.24: Pair distribution function for $v_f^{req} = 56\%$.

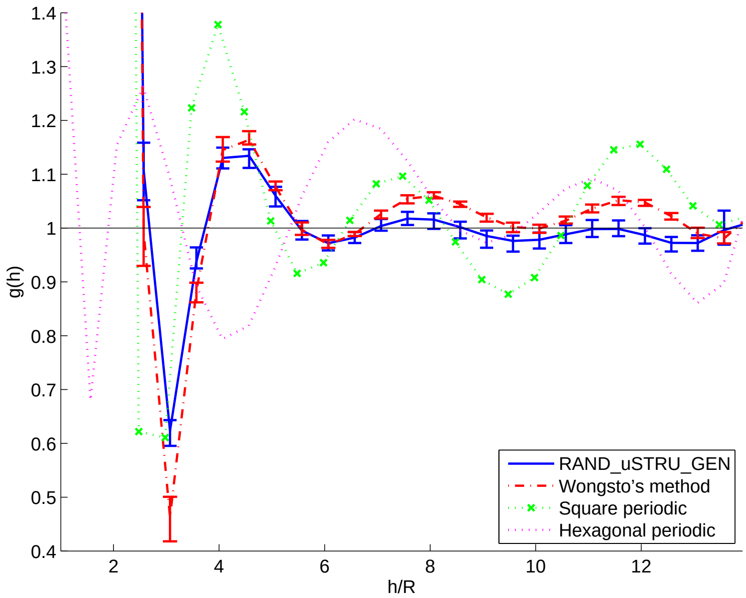

Figure 2.25: Pair distribution function for $v_f^{req} = 65\%$.

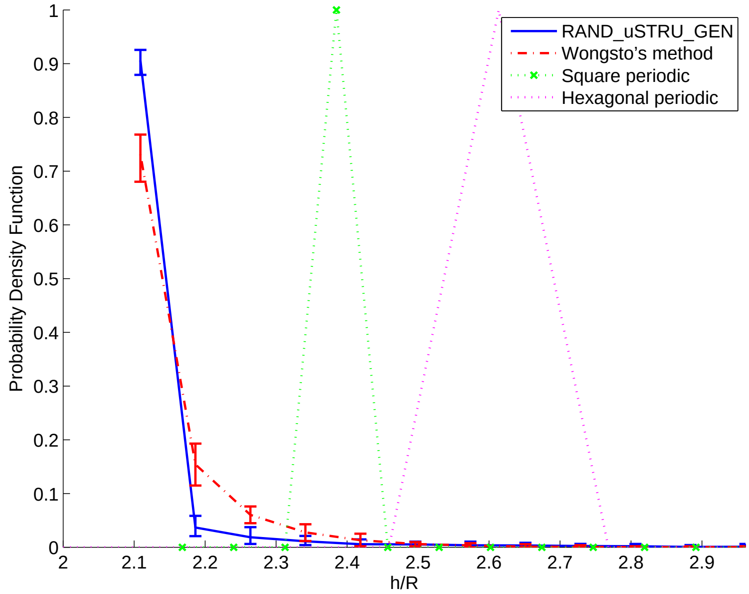

Figure 2.26: First nearest neighbour function for $v_f^{req} = 56\%$.

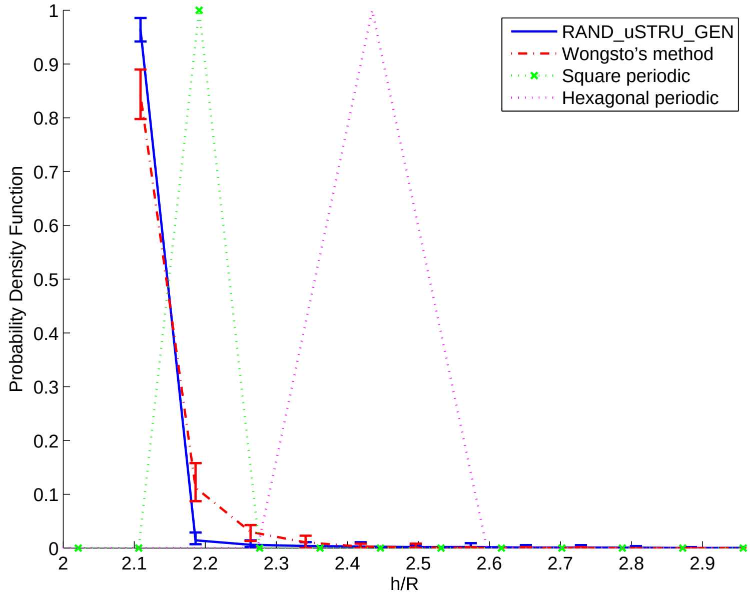

Figure 2.27: First nearest neighbour function for $v_f^{req} = 65\%$.

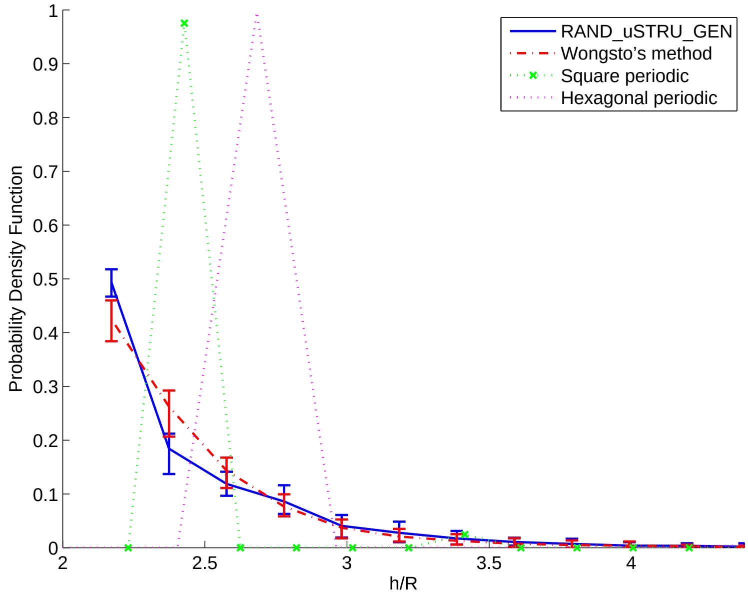

Figure 2.28: Second nearest neighbour function for $v_f^{req} = 56\%$.

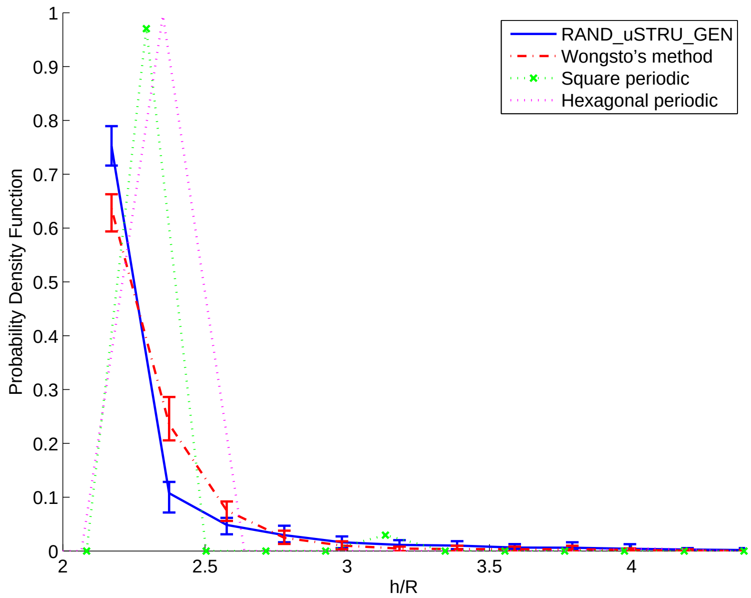

Figure 2.29: Second nearest neighbour function for $v_f^{req} = 65\%$.

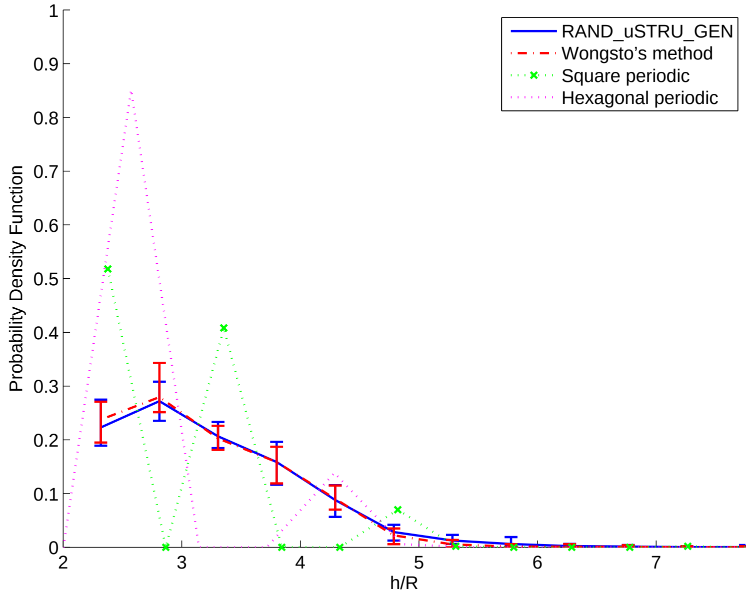

Figure 2.30: Third nearest neighbour function for $v_f^{req} = 56\%$.

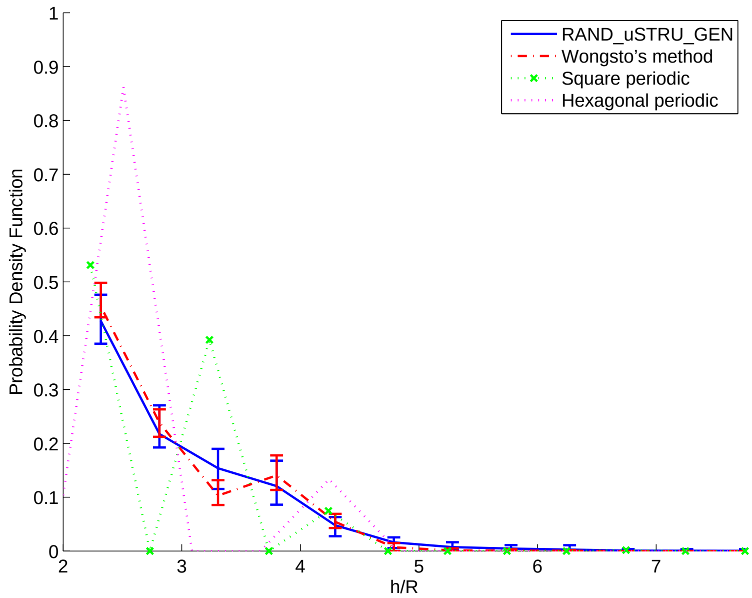

Figure 2.31: Third nearest neighbour function for $v_f^{req} = 65\%$.

but because the fibres are so densely compacted against each other due to the high fibre volume fraction, that the distance between any fibre and its first nearest neighbour will be almost the same all the times and very close to the specified minimum distance between any two fibres controlled by variable Δ_{min}. Hence the peak for very short distances in the curves of both random distributions and the even steeper curve for greater fibre volume fractions. The same does not happen in figures 2.28 to 2.31 which show a smooth decrease in the second and third nearest neighbour probability density functions meaning a lesser denseness on the second and third nearest neighbours throughout the generated distributions.

2.3.6 Nearest neighbour orientations

This statistical descriptor can be used to better understand the distribution of fibres and how random their arrangement truly is. Figures 2.32 and 2.33 show the Cumulative Distribution Function (CDF) for the two fibre volume fractions in analysis.

It can be seen that for a fibre volume fraction of 56% the two periodic distributions exhibit preferable orientations of the nearest fibre as indicated by the stair-shaped plots. Both Wongsto's algorithm and `RAND_uSTRU_GEN` perform very well following the Poisson's straight line of cumulated probability.

However, for a fibre volume fraction of 65% it is visible some degree of preference on the orientation of the nearest fibre in Wongsto's algorithm denounced by its stair-shaped plot. This is due to the fibres being too close to each other on an originally periodic arrangement and have some difficulty abandoning that original arrangement throughout the iterations of the algorithm. `RAND_uSTRU_GEN` maintains its almost perfect random orientation of nearest fibre even for high fibre volume fractions.

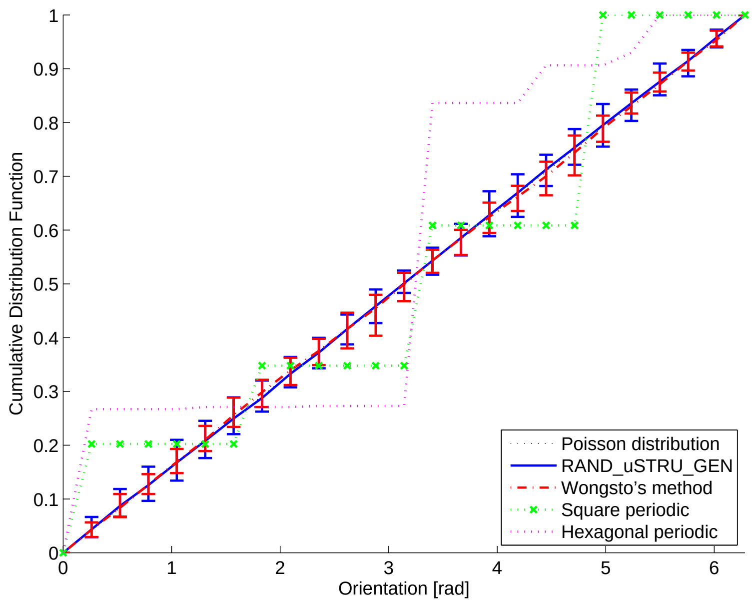

Figure 2.32: Nearest neighbour orientation for $v_f^{req} = 56\%$.

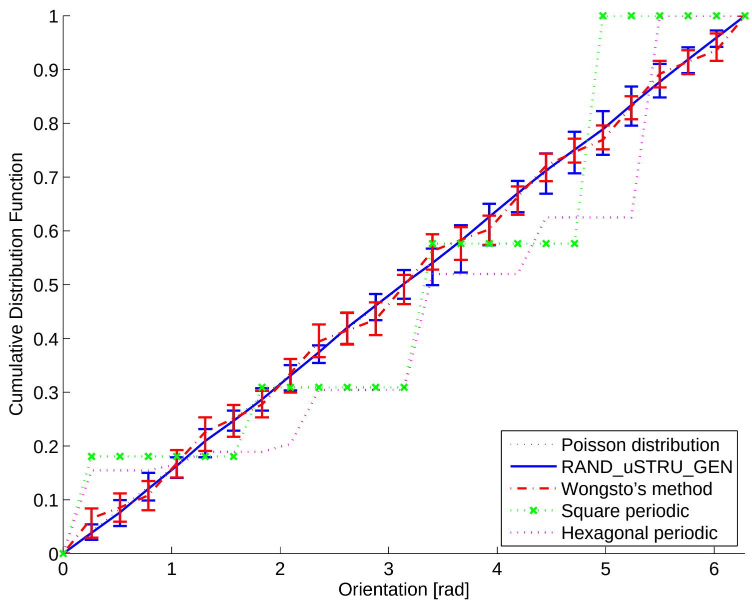

Figure 2.33: Nearest neighbour orientation for $v_f^{req} = 65\%$.

2.4 Material characterisation of generated SRVE

A very important characteristic of real long fibre reinforced composites is the transversal isotropy in the plane perpendicular to the fibre direction for any individual ply in a laminate. It is thus required to verify if the generated random spatial distribution of fibres is able to adequately model this property. Obviously, periodic fibre distributions do represent this property very well.

To demonstrate this, two hundred and fifty fibre spatial distributions were generated using `RAND_uSTRU_GEN`. ABAQUS® [30] software was used to run the finite element analyses. The procedure followed and assumptions made will be described in this section.

2.4.1 Generated SRVEs

Two hundred and fifty fibre spatial distributions with $v_f^{req} = 60\%$ were generated in order to demonstrate the existence of transverse isotropy in random fibre distributions obtained using the algorithm `RAND_uSTRU_GEN`. Figure 2.34 shows two examples of these distributions.

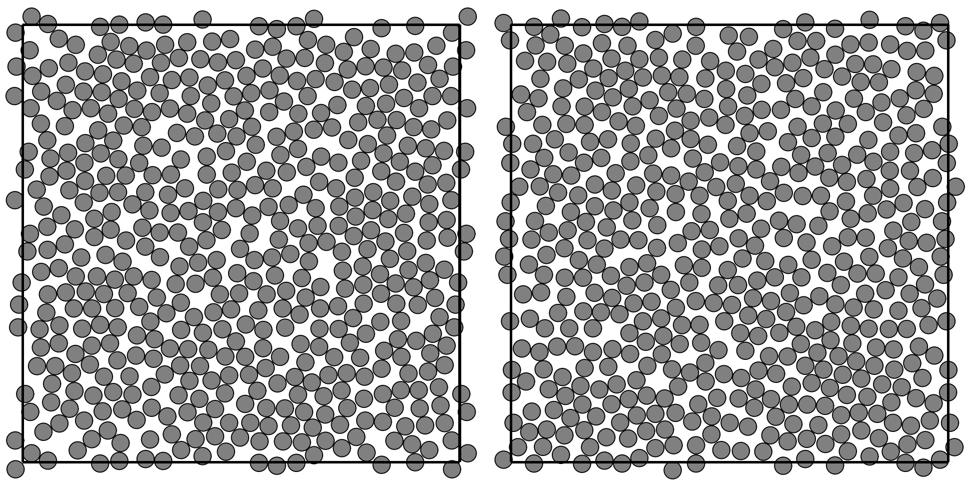

Figure 2.34: Generated SRVEs for transversal isotropy demonstration.

2.4.2 Finite element modelling

A MATLAB® [29] script was developed to generate a triangular mesh of the generated spatial distribution. This script makes use of a pre-defined node position for the fibres (they are all circular and of the same diameter). The nodes for the matrix follow a simple rectangular grid interrupted only by the presence of the fibres.

The elements are generated making use of MATLAB®'s Delaunay triangulation algorithm [29]. The resulting mesh is then exported to an ABAQUS® standard input file. This script can be found in appendix A. Figure 2.35 shows a detailed view of the generated mesh.

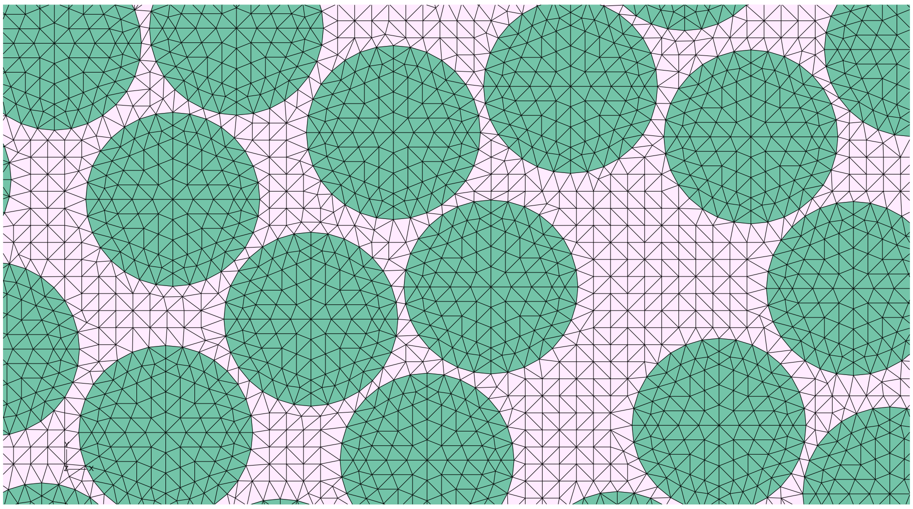

Figure 2.35: Generated triangular mesh.

One of the material sets considered at the World Wide Failure Exercise (WWFE) [31] was chosen for the analyses - E-glass/MY750/HY917/DY063. Both fibre and matrix are considered isotropic materials. Their elastic properties are summarised in table 2.6.

Table 2.6: Elastic properties of constituents [31].

	Fibre	Matrix
Young Modulus [GPa]	74	3.35
Coefficient of Poisson	0.2	0.35

For the analyses, generalised plane strain 3-node linear elements were used from ABAQUS® [30] element library – elements CPEG3. Rigid boundary conditions were discarded since these would force the same displacements to different materials along the SRVE's edges [32].

Following Van der Sluis et al. [32] and Smit et al. [33], Periodic Boundary

Conditions (PBCs) were applied to the SRVE. The right and top sides as well as the right-bottom and left-top corners of the SRVE have independent degrees of freedom. The left-bottom corner is constrained to prevent rigid body motions. PBCs force the remaining corners and sides to have their displacements related with the former by the following equations:

$$\begin{aligned}
&\mathbf{u}_B - \mathbf{u}_T + \mathbf{u}_{LT} = 0 \\
&\mathbf{u}_L - \mathbf{u}_R + \mathbf{u}_{RB} = 0 \\
&\mathbf{u}_{RT} - \mathbf{u}_{RB} - \mathbf{u}_{LT} = 0
\end{aligned} \tag{2.15}$$

where B,T,L, and R correspond to Bottom, Top, Left, and Right edges. When referring to the displacement of a corner, two letters are used corresponding to the edges intersecting on that corner. Figure 2.36 shows an example of a deformed SRVE under periodic boundary conditions.

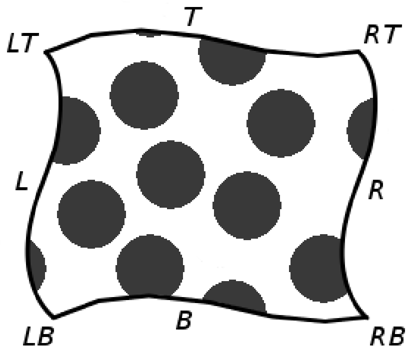

Figure 2.36: Periodic boundary conditions.

By applying different displacement sets to the independent degrees of freedom, one can determine different material properties. E_2 and ν_{23} are determined by applying an horizontal movement to the right side while to determine E_3 and ν_{32} a vertical displacement is applied to the top side. G_{23} is determined by applying horizontal displacement on the top side and a vertical displacement to the right side. The elastic properties were obtained through averaging techniques [34] using equations (2.16),

$$E_k = \frac{\sum_{i=1}^{N} \sigma_{kk}^i A^i}{\sum_{i=1}^{N} \varepsilon_{kk}^i A^i} \qquad \nu_{jk} = -\frac{\sum_{i=1}^{N} \varepsilon_{kk}^i A^i}{\sum_{i=1}^{N} \varepsilon_{jj}^i A^i} \qquad G_{23} = \frac{\sum_{i=1}^{N} \sigma_{23}^i A^i}{\sum_{i=1}^{N} \varepsilon_{23}^i A^i} \tag{2.16}$$

where N is the total number of integration points considered, σ^i_{kk} and ε^i_{kk} respectively represent the k-component of stress and strain calculated in the integration point of each element and A^i is the area of that element.

2.4.3 Analyses and Results

The transverse material properties were computed for each of the two hundred and fifty distributions generated. Figures 2.37 and 2.38 present the results in histogram format. Table 2.7 provides a summary of the results.

The well known relation shown in equation (2.17) between the two Young's moduli and Poisson's ratios allows to better compare these results.

$$\frac{\nu_{23}}{E_2} = \frac{\nu_{32}}{E_3} \Leftrightarrow \frac{E_2\nu_{32}}{E_3\nu_{23}} = 1 \tag{2.17}$$

The transversal isotropy can also be described by $E_2 = E_3$, $\nu_{23} = \nu_{32}$ and $G_{23} = \frac{E_2}{2(1+\nu_{23})}$. Table 2.8 provides the results of applying these equations and equation (2.17) to the calculated values in table 2.7. It can be seen that all values are very close to 1 in all ratios. It can thus be concluded that the generated random spatial distributions of fibres respect the transverse isotropy of the material in the perpendicular plane to the fibre direction.

Table 2.7: Calculated effective properties.

	Mean	St. Deviation	Experimental	Error (%)
E_2 [MPa]	13367	101	16200	17,5
E_3 [MPa]	13387	113	16200	17,4
ν_{23}	0,370	0,004	0,400	7,5
ν_{32}	0,371	0,004	0,400	7,3
G_{23} [MPa]	4851	43	$5786^{(a)}$	16,2
G_{23}^{calc} [MPa] $^{(a)}$	4878	-	5786	-

$^{(a)}$Values calculated assuming transverse isotropy.

Table 2.8: Proof of transverse isotropy.

	$\frac{E_2\nu_{32}}{E_3\nu_{23}}$	$\frac{E_2}{E_3}$	$\frac{\nu_{23}}{\nu_{32}}$	$\frac{G_{23}^{calc}}{G_{23}}$
Mean Values	1.000	0.999	0.999	1.006

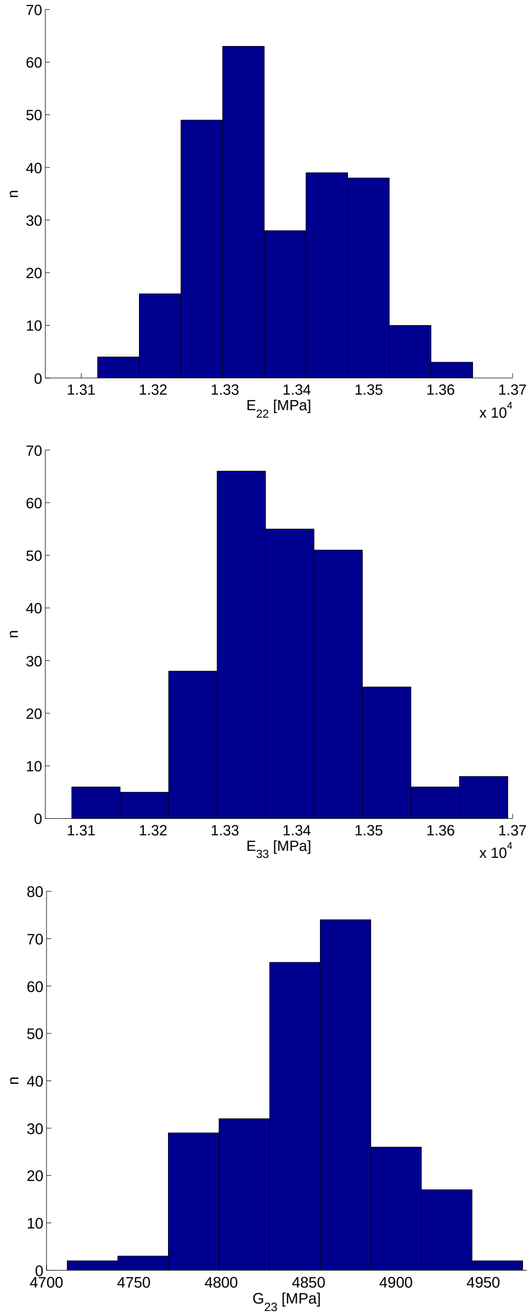

Figure 2.37: Young's moduli and transverse shear modulus.

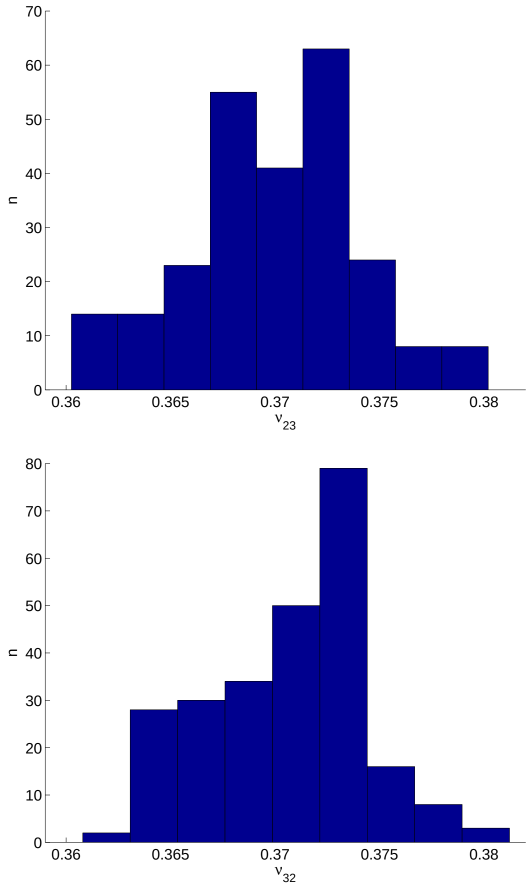

Figure 2.38: Poisson's ratios.

2.5 Conclusions

In this chapter, a new algorithm named `RAND_uSTRU_GEN` to generate random spatial distributions of fibres has been presented. The new algorithm was developed making use of the latest studies on statistical representative volume elements and how SRVEs can be applied in the study of long fibre reinforced composites.

The new algorithm is able to generate random distributions for high values of fibre volume fractions in a very short amount of time. For that, it makes use of two heuristics especially developed. The algorithm gives the user a high level of control through the several input variables it requires. Geometrical continuity between opposite sides of the generated distribution is imposed. This is required for the later application of periodic boundary conditions on the representative volume elements generated.

The generated distributions were analysed using statistical functions and descriptors and the algorithm's performance was compared with the completely spatial randomness of a Poisson distribution. A good agreement was found in all statistics analysed.

A numerical study to demonstrate that the generated fibre distributions were able to represent the transverse isotropy of the material was conducted. A good agreement between independently calculated material properties in different loading schemes was found to exist.

It can therefore be concluded that the new algorithm is able to adequately generate a random fibre distribution that is materially and statistically equivalent to that of real long fibre reinforced materials.

In the next chapter, this algorithm will be used to generate random distributions of fibres and through FEA, the material's mechanical properties will be estimated using the concept of representative volume element as it was described on this chapter and results compared with experimental data available in the literature.

Chapter 3

Elastic properties

I am constant as the Northern Star...

Caesar *by* William Shakespeare

With the algorithm described in chapter 2 it is now possible to rapidly obtain a random distribution of fibres with a volume fraction similar to those of real life fibre reinforced composite materials. With this difficulty overcome, it is possible to easily perform simple homogenisation analyses to determine the effective elastic properties of the composite.

The present chapter starts by reviewing some of the analytical and numerical methods used to determine the elastic properties of composite materials found in the literature. An explanation on the automatic process developed here to perform all the pre-processement required for finite element analysis is presented next. Finally, a comparison of predicted elastic properties is performed.

3.1 Introduction and state of the art

When dealing with an isotropic homogeneous material, it is well known how to determine its two independent elastic properties. In the case of composites, being heterogeneous materials constituted by two or more phases, and possessing transverse isotropy, the number of independent properties increases and not all of them are easy to obtain experimentally.

In order to overcome this difficulty, a number of analytical and numerical processes were developed. Each constituent is treated separately with its own elastic properties. Also, the geometric information of the material at the micromechanical level is most of the times a variable in the process with the reinforcement volume fraction and shape being taken into consideration.

3.1.1 Effective properties of transverse isotropic materials

This chapter will deal only with linear elastic material response. The constitutive equations establishing the relation between stresses and strains are known as the generalized Hooke's law and their most general form in tensorial notation is:

$$\sigma_{ij} = C_{ijkl}\varepsilon_{kl} \tag{3.1}$$

with C_{ijkl} being the stiffness tensor, σ_{ij} the stress tensor and ε_{ij} the strain tensor. In 3D analysis, equation (3.1) contains a set of 81 elastic constants. Invoking symmetry of the stress tensor gives $C_{ijkl} = C_{jikl}$. Similarly, symmetry of the strain tensor provides $C_{ijkl} = C_{ijlk}$. This allows to reduce the number of elastic constants from 81 to 36.

Defining a strain energy density function W such that:

$$W = \frac{1}{2}C_{ijkl}\varepsilon_{ij}\varepsilon_{kl} \tag{3.2}$$

with the property

$$\sigma_{ij} = \frac{\partial W}{\partial \varepsilon_{ij}} \tag{3.3}$$

it is possible to prove that the tensor C_{ijkl} is symmetric and the number of independent elastic constants reduces from 36 to 21. Function W's existence is proved by the first and second laws of thermodynamics, as it depends only on the final strain state, and not on the path followed to obtain such state.

Further simplification on the number of independent elastic constants is possible if material symmetry is considered. Monoclinic materials contain one plane of symmetry and allow to reduce to 13 the number of independent constants. Orthotropic materials contain two planes of symmetry allowing to reduce even further to 9 independent constants.

Unidirectional fibre-reinforced composite plies however, are typically assumed to exhibit transverse isotropy, which implies that material behaviour is independent of the direction in one plane. This allows for a further reduction to only 5 independent elastic properties. The stiffness tensor is thus defined by:

$$C_{ijkl} = \begin{bmatrix} C_{1111} & C_{1122} & C_{1122} & 0 & 0 & 0 \\ C_{1122} & C_{2222} & C_{2233} & 0 & 0 & 0 \\ C_{1122} & C_{2233} & C_{2222} & 0 & 0 & 0 \\ 0 & 0 & 0 & C_{4444} & 0 & 0 \\ 0 & 0 & 0 & 0 & C_{4444} & 0 \\ 0 & 0 & 0 & 0 & 0 & \frac{C_{2222}-C_{2233}}{2} \end{bmatrix} \tag{3.4}$$

It is easier to define the constants in the stiffness tensor as engineering elastic constants. Normally, the five independent engineering constants defined for transverse isotropic materials are the longitudinal and transverse Young's moduli, E_1 and E_2, the longitudinal and transverse shear moduli, G_{12} and G_{23}, and the longitudinal Poisson's ratio, ν_{12}. Sometimes, the transverse Poisson's ratio is also defined instead of the transverse shear modulus. They relate with the stiffness tensor constants according to equations (3.5).

$$\begin{aligned} E_1 &= C_{1111} - \frac{2C_{1122}^2}{C_{2222}+C_{2233}} \\ \nu_{12} &= \frac{C_{1122}}{C_{2222}+C_{2233}} \\ E_2 &= C_{2222} + \frac{C_{1122}^2\left(C_{2233}-C_{2222}\right)+C_{2233}\left(C_{1122}^2-C_{1111}C_{2233}\right)}{C_{1111}C_{2222}-C_{1122}^2} \\ G_{12} &= C_{4444} \\ G_{23} &= C_{6666} = \frac{1}{2}\left(C_{2222}-C_{2233}\right) \\ \nu_{23} &= \frac{C_{1111}C_{2233}-C_{1122}^2}{C_{1111}C_{2222}-C_{1122}^2} \end{aligned} \tag{3.5}$$

Also, a characteristic of transversely isotropic materials is the relation between the transverse properties: shear modulus, Young's modulus and Poisson's ratio, defined by equation (3.6).

$$G_{23} = \frac{E_2}{2\left(1+\nu_{23}\right)} \tag{3.6}$$

Also of interest is the definition of the plane strain bulk modulus, k_{23}, of the composite, according to equation (3.7).

$$k_{23} = \frac{1}{2}\left(C_{2222}+C_{2233}\right) \tag{3.7}$$

Equations (3.5) can be reversed and written in function of the engineering properties according with equations (3.8).

$$
\begin{aligned}
C_{1111} &= E_1 + 4\nu_{12}^2 k_{23} \\
C_{1122} &= 2k_{23}\nu_{12} \\
C_{2222} &= G_{23} + k_{23} \\
C_{2233} &= k_{23} - G_{23} \\
C_{4444} &= G_{12}
\end{aligned}
\tag{3.8}
$$

Also the bulk modulus for isotropic and transverse isotropic materials – K_{iso} and K_{trans_iso} – should be defined:

$$K_{iso} = \frac{E}{3(1-2\nu)} \tag{3.9}$$

$$\frac{1}{K_{trans\_iso}} = \frac{1-4\nu_{12}}{E_1} + \frac{2(1-\nu_{23})}{E_2} \tag{3.10}$$

Determining each of the five engineering constants is the purpose of this chapter. Through the next pages, a number of analytical and numerical methods to determine these constants will be presented. An automated process to perform this task based on the algorithm described in chapter 2 will be presented next. The chapter will wrap up with a comparison of the predicted elastic constants by the different methods presented and some parametric studies for the composite.

3.1.2 Analytical methods

The average properties of heterogeneous materials can be obtained by analytical methods. This subsection will present some of the most used methods introduced over the years.

Voigt model

The Voigt model [35] (also known as *the rule of mixtures*) assumes that the strains are constant throughout the composite (both fibre and matrix). The composite effective stiffness tensor can thus be calculated by

$$C_{ijkl} = V_m C_{ijkl}^m + V_f C_{ijkl}^f \tag{3.11}$$

where V_m and V_f represent the volume fraction for matrix and fibre, respectively.

Reuss model

This model was first introduced by Reuss [36] and is known as the *inverse rule of mixtures*. In his work, Reuss assumed that the stress tensors in the fibre, matrix and composite are always the same. This way, the compliance effective tensor for the composite is defined by equation (3.12).

$$S_{ijkl} = V_m S_{ijkl}^m + V_f S_{ijkl}^f \tag{3.12}$$

Paul [37] demonstrated that the Voigt model represents an upper bound and the Reuss model a lower bound on the stiffness coefficients (and not the engineering constants).

Strength of materials approximation

Herakovich [1] provides a simple approximation based on a series of assumptions which do not necessarily satisfy the requirements of an exact elasticity solution, but the results achieved provide reasonable first hand approximations. Also, it only allows to determine four out of the five independent engineering constants typical of transverse materials such as composites: the longitudinal and transverse Young's moduli, longitudinal Poisson's ratio and longitudinal shear modulus. The demonstration can be found in [1]. The final equations to determine these four engineering constants are:

$$\begin{aligned}
E_1 &= V_m E_m + V_f E_f \\
E_2 &= \frac{E_m}{V_f\left(\dfrac{E_m}{E_f} - 1\right) + 1} \\
\nu_{12} &= V_f\left(\nu_f - \nu_m\right) + \nu_m \\
G_{12} &= \frac{G_m}{V_f\left(\dfrac{G_m}{G_f} - 1\right) + 1}
\end{aligned} \tag{3.13}$$

As can be seen from equations (3.13), the longitudinal properties are determined by simple rule of mixtures while the transverse properties derive from the inverse rule of mixtures.

Hashin-Hill bounds

Using the minimum theorems of elasticity, Hashin and Shtrickman [38] developed a set of tighter and more meaningful bounds than those of Voigt and Reuss for isotropic materials with arbitrary internal geometry. Later, Hashin [39] and Hill [40] deduced equations for the bounds of transversely isotropic composites with isotropic constituents. If the constituents happen to be transversely isotropic, the equations are still valid, if the appropriate modifications are performed for transverse isotropic properties. The bounds were deduced for axial Young's modulus, axial and transverse shear moduli, axial Poisson's ratio, and plane strain bulk modulus.

$$
\begin{gathered}
k_m + \frac{V_f}{\dfrac{1}{k_f - k_m} + \dfrac{V_m}{k_m + G_m}} \leqslant k_{23} \leqslant k_f + \frac{V_m}{\dfrac{1}{k_m - k_f} + \dfrac{V_f}{k_f + G_f}} \\
G_m + \frac{V_f}{\dfrac{1}{G_f - G_m} + \dfrac{V_m\left(k_m + 2G_m\right)}{2G_m\left(k_m + G_m\right)}} \leqslant \\
G_{23} \leqslant G_f + \frac{V_m}{\dfrac{1}{G_m - G_f} + \dfrac{V_f\left(k_f + 2G_f\right)}{2G_f\left(k_f + G_f\right)}} \\
G_m + \frac{V_f}{\dfrac{1}{G_f - G_m} + \dfrac{V_m}{2G_m}} \leqslant G_{12} \leqslant G_f + \frac{V_m}{\dfrac{1}{G_m - G_f} + \dfrac{V_f}{2G_f}} \\
\frac{V_m V_f}{\dfrac{V_f}{k_m} + \dfrac{V_m}{k_f} + \dfrac{1}{G_m}} \leqslant \frac{E_{11} - V_f E_f - V_m E_m}{4\left(\nu_f - \nu_m\right)^2} \leqslant \frac{V_f V_m}{\dfrac{V_f}{k_m} + \dfrac{V_m}{k_f} + \dfrac{1}{G_f}} \\
\frac{V_m V_f}{\dfrac{V_f}{k_m} + \dfrac{V_m}{k_f} + \dfrac{1}{G_m}} \leqslant \frac{\nu_{12} - V_f \nu_f - V_m \nu_m}{\left(\nu_f - \nu_m\right)\left(\dfrac{1}{k_m} - \dfrac{1}{k_f}\right)} \leqslant \frac{V_f V_m}{\dfrac{V_f}{k_m} + \dfrac{V_m}{k_f} + \dfrac{1}{G_f}}
\end{gathered}
\tag{3.14}
$$

Composite cylinder assemblage model

Since the bounds in equations (3.14) do not provide a good approximation on the elastic properties, it was necessary to develop alternative methods which would account for the internal geometry of the composite. Hashin and Rosen [41] proposed a model in which the engineering constants of a transversely isotropic heterogeneous material could be determined from the properties of its constituents. The model admits the existence of an assemblage of concentric cylinders, made of two phases: one central part representing the fibre, and one annulus surrounding it representing the matrix. These cylinders can have different diameters so that they accommodate on each other very easily, thus completely filling the volume of the composite. For each cylinder, the radius of the central part would be such that the volume fraction of the central part in the cylinder would be equal to the global fibre volume fraction of the composite. Although this geometry does not represent the actual geometry, it does take into consideration a certain degree of randomness typical of composites. Figure 3.1 represents the idea.

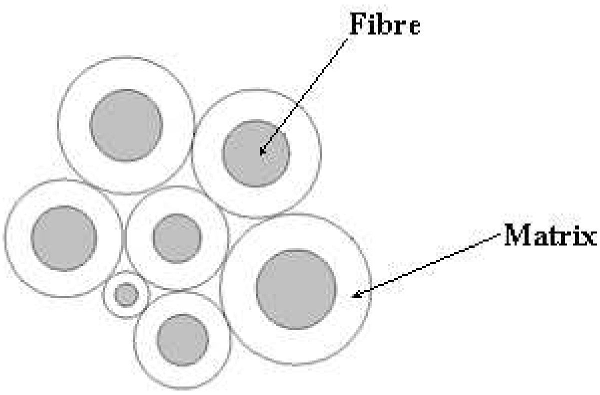

Figure 3.1: Composite cylinder assemblage model (image from [42]).

However, this model only allows to determine four of the five engineering properties. Equations were deduced for longitudinal Young's modulus, longitudinal Poisson's ratio, longitudinal shear modulus, and plane strain bulk modulus. The fifth property, the transverse shear modulus, can be determined by a three-phase cylinder model, where all the cylinders except one are replaced by equivalent homogeneous material with properties equal to those of the composite. The geometry of this alternative model is considered to be intimately related with the original cylinder assemblage. Detailed deduction of the equations can be found in Hashin and Rosen [41], Herakovich [1], Christensen and Lo [43], or Christensen [42]. For the sake of simplicity, only the final equations are shown here:

$$E_1 = V_f E_f + V_m E_m + \frac{4V_f V_m (\nu_f - \nu_m)^2 G_m}{\dfrac{V_m G_m}{K_f + \dfrac{G_m}{3}} + \dfrac{V_f G_m}{K_m + \dfrac{G_m}{3}} + 1}$$

$$\nu_{12} = V_m \nu_m + V_f \nu_f + \frac{V_f V_m (\nu_f - \nu_m)\left(\dfrac{G_m}{K_m + \dfrac{G_m}{3}} - \dfrac{G_m}{K_f + \dfrac{G_f}{3}}\right)}{\dfrac{V_m G_m}{K_f + \dfrac{G_f}{3}} + \dfrac{V_f G_m}{K_m + \dfrac{G_m}{3}} + 1}$$

$$k_{23} = K_m + \frac{G_m}{3} + \frac{V_f}{\dfrac{1}{\left(K_f - K_m + \frac{1}{3}(G_f - G_m)\right)} + \dfrac{V_m}{K_m + \frac{4}{3}G_m}} \tag{3.15}$$

$$G_{12} = G_m \frac{G_f (1 + V_f) + G_m V_m}{G_f V_m + G_m (1 + V_f)}$$

$$G_{23} = G_m \frac{\sqrt{B^2 - AC} - B}{A}$$

where K_m and K_f are the bulk moduli of matrix and fibre respectively. The unknown parameters for determining the transverse shear modulus are defined by equations (3.16).

$$\begin{aligned}
A &= 3V_f V_m^2 \delta\alpha + \left(\gamma - 1 + \eta_f \eta_m - \beta V_f^3\right)(V_f \eta_m \delta - \gamma) \\
B &= -3V_f V_m^2 \delta\alpha + \frac{1}{2}(\gamma + \delta V_f)\left(\alpha(\eta_m - 1) - 2\beta V_f^3\right) + \cdots \\
&\quad \cdots + \frac{V_f}{2}(\eta_m + 1)\delta\left(\frac{G_{23}^f}{G_m} + \eta_f + \beta V_f^3\right) \\
C &= 3V_f V_m^2 \delta\alpha + (\gamma + \delta V_f)\left(\frac{G_{23}^f}{G_m} + \eta_f + \beta V_f^3\right) \\
&\eta_m = 3 - 4\nu_m, \quad \eta_f = 3 - 4\nu_{23}^f, \quad \alpha = \frac{G_{23}^f}{G_m} + \eta_f \\
&\beta = \frac{G_{23}^f}{G_m}\eta_m - \eta_f, \quad \gamma = \frac{G_{23}^f}{G_m}\eta_m + 1, \quad \delta = \frac{G_{23}^f}{G_m} - 1
\end{aligned} \tag{3.16}$$

Mori-Tanaka method

This method was originally proposed by Mori and Tanaka [44]. It assumes that the average strain in a single reinforcement is related to the average strain in the matrix by a fourth order tensor. This tensor states the relation between the uniform strain in a single reinforcement embedded in an infinite matrix with an imposed uniform strain at infinity. The equations relating the engineering properties with a transversely isotropic constituent are:

$$\begin{aligned}
m^* &= \frac{m_m m_f \left(k_m + 2m_m\right) + k_m m_m \left(V_f m_f + V_m m_m\right)}{k_m m_m + \left(k_m + 2m_m\right)\left(V_f m_m + V_m m_f\right)} = G_{23} \\
p^* &= \frac{2V_f p_f p_m + V_m \left(p_f p_m + p_m^2\right)}{2V_f p_m + V_m \left(p_f + p_m\right)} = G_{12} \\
l^* &= \frac{V_f l_f \left(k_m + m_m\right) + V_m l_m \left(k_f + m_m\right)}{V_f \left(k_m + m_m\right) + V_m \left(k_f + m_m\right)} = 2k^* \nu_{12} \\
n^* &= V_f n_f + V_m n_m + \left(l^* - V_f l_f - V_m l_m\right) \frac{l_f - l_m}{k_f - k_m} = E_1 + 4k^* \nu_{12}^2 \\
k^* &= \frac{k_f k_m + m_m \left(V_f k_f + V_m k_m\right)}{V_f k_m + V_m k_f + m_m} = -\left(\frac{1}{G_{23}} - \frac{4}{E_2} + \frac{4\nu_{12}^2}{E_1}\right)^{-1}
\end{aligned} \tag{3.17}$$

3.1.3 Numerical methods

Along with the development of faster and more reliable computers, a large number of researchers started focusing on how to determine the effective elastic properties of an heterogeneous material by means of micromechanics using finite element analysis. This subsection presents three methodologies to simulate the composite material at the micromechanical level.

Unit cell

The simplest way to tackle the problem of representing the heterogeneity of the material without compromising the amount of resources and time needed to perform a numerical analysis, is by admitting that the reinforcements are periodically distributed along the composite material.

Different types of periodicity have been studied, being the square and hexagonal the two most frequent ones (see figure 3.2). Such geometrical arrangements allow that only a small portion of the composite needs to be represented for finite element analysis, as depicted in figure 3.2 for square and hexagonal cases respectively, by the dashed boxes.

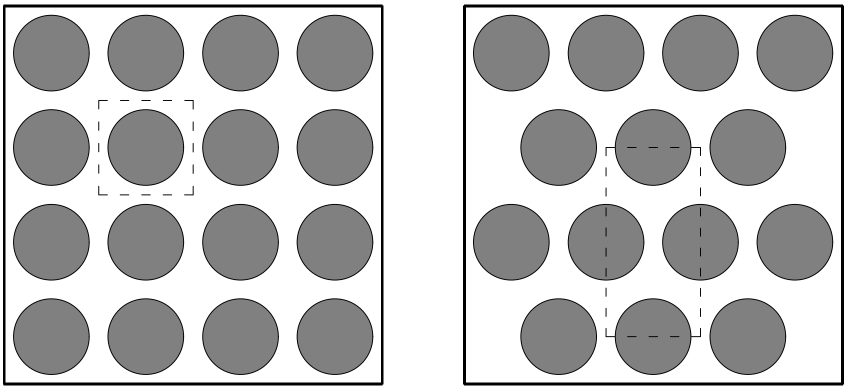

(a) Square Periodic (b) Hexagonal Periodic

Figure 3.2: Unit cell RVEs (dashed boxes) based on periodic distributions.

Li [45] presented in 2001 a review on the two periodic arrangements shown in figure 3.2. In his communication, Li establishes equations for the displacement and traction boundary conditions and defines the application of loads based on macroscopic stresses and effective properties. Li also considers thermal loading. The macroscopic strains are taken as individual degrees of freedom to be applied to the nodes along the edges and vertices of the unit cells.

Aghdam et al. [46] performed 2D and 3D FEA assuming square periodicity on SiC/Ti MMCs. Periodic boundary conditions[1] were used and both longitudinal and transverse loads were applied, as well as off-axis loads and thermal residual stresses. The effects of debonding with friction of the interface between the reinforcement and the matrix were also considered. A good agreement was achieved for stress-strain behaviour, Young's modulus, elastic limit and tensile strength. However, there is no information on what should be the friction coefficient on the interface in order to achieve good results. Also, the interface conditions play a role on the quality of the predictions, varying with the magnitude of the applied load.

Asp and co-workers [47] performed failure analysis on unidirectional fibre reinforced composites under transverse tension, assuming three different

[1]The concept of periodic boundary conditions will be properly introduced in section 3.1.4.

periodic arrangements: square, hexagonal and diamond. It was found that each arrangement led to different micro-stress and micro-strain distributions on the matrix, consequently leading to different failure predictions.

Sluis et al. [32] performed a comparative study of unit cells. It was considered that the periodicity rules are not broken if one considers a unit cell with an off-centre reinforcement. It was concluded that this can be done only if periodic boundary conditions are also applied to the off-centre unit cell. If mixed (displacement and traction) boundary conditions are applied, the apparent properties diverge from the effective ones.

In real life, however, it is impossible to manufacture composites with the precision required to position all the fibres in such periodic arrangements. The distribution of the reinforcements will always be a random one. In other words, considering that such periodicity exists might lead to erroneous predictions of mechanical behaviour, especially in non-linear analyses, where the spatial randomness will lead to different regions of the matrix to be under different mechanical conditions.

Several contributions, like the ones from Gusev et al. [21] or Trias et al. [34], compared the predictions for effective properties given by periodic arrangements and random distributions. Random distributions always proved more effective when comparing the results with experimental data.

Random distribution of reinforcements without periodicity

A more complex way of performing micromechanics analyses, is by accepting that the random distribution of reinforcements is unavoidable, and model it in a finite element analysis. Most contributions found in the literature until today make use of algorithms not capable of generating a random spatial distribution with a high volume fraction of reinforcement, or prefer to retrieve the spatial distribution from micrographs using digital image analysis. In this last alternative, the representative volume element is an exact copy of a portion of the real material.

In either case, there is no care taken regarding the boundaries of the volume element, i.e. there is no geometrical relation between opposite edges and/or faces of the volume element. Under these circumstances, it is not possible to adequately apply periodic boundary conditions to the volume element. Several attempts to deal with this problem can be found in the literature.

Bulsara et al. [48] and Oh et al. [49] both have performed finite element analyses on random distributed media using a set of rigid boundary conditions (figure 3.3). Bulsara confirmed that there is a strong dependence of damage initiation on the fibre distribution, especially if a large mismatch on the elastic properties of the constituents exists. Oh and colleagues [49] also determined that randomness has a significant influence on the strain at the fibre-matrix interface, especially for high fibre volume fractions.

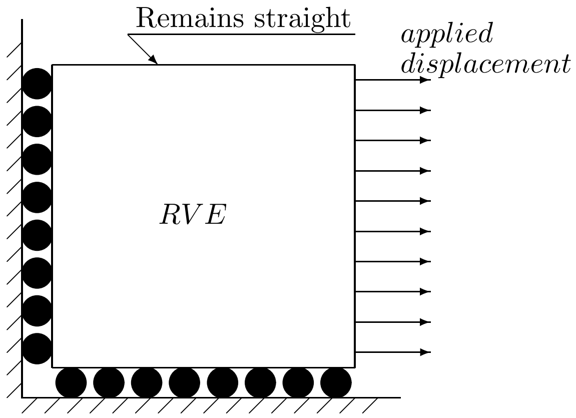

Figure 3.3: Rigid boundary conditions.

Wongsto and Li [24] analysed the stress variation pattern of square and hexagonal unit cells and determined that by applying incorrect boundary conditions, a region of approximately 4× the fibre radius would be compromised all around the volume element. With this in mind, Wongsto and Li performed an analysis where the volume element with a random distribution of reinforcements would have all its boundaries rigidly constrained, but only a region in the interior of this volume element, at a distance of 4× the fibre radius, should be considered for micromechanical analysis and consequent homogenisation.

An embedded cell approach was used by Trias et al. [50] and Shan and Gokhale [10]. This method tries to minimise the erroneous effects caused by the lack of geometrical periodicity by embedding the volume element in an homogeneous material with the same properties of the real composite material (figure 3.4). This requires either an iterative process to determine those properties, or an a priori assumption or determination through analytical methods of those properties, or even a combination of these methods.

Terada et al. [51] performed a series of numerical analyses to representative volume elements of different dimensions and without geometrical periodicity along their edges. It was demonstrated that periodic boundary conditions are the most appropriate to be used in micromechanical analyses.

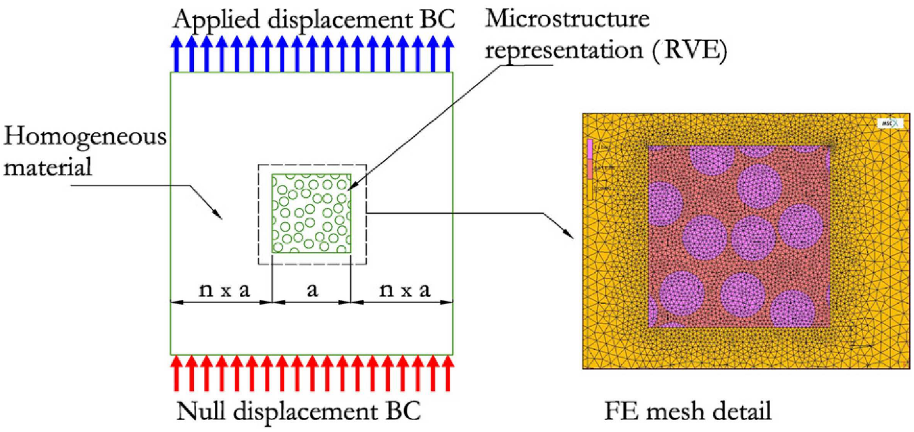

Figure 3.4: Embedded cell approach (Trias et al. [50]).

It was also shown that even though there was no geometrical periodicity, if the volume element is big enough, the effective elastic properties can be determined with a good approximation as long as periodic boundary conditions are used. Terada et al. also performed non-linear analyses and concluded that non-linear mechanical behaviour has a strong negative effect on the reliability of the predictions performed this way, requiring a much bigger volume element to achieve good results.

Random distribution of reinforcements with periodicity

As seen in the previous section, the lack of geometrical periodicity can lead to erroneous predictions of the material behaviour, especially if non-linear mechanical behaviour is considered. The use of periodic boundary conditions becomes a lot easier if there is also geometrical periodicity on opposite edges and/or faces of the volume element. This approach is based on the assumption that the volume element is part of a much larger specimen. Edge effects (or face effects, in 3D analyses) are also completely eliminated as noted by Gitman [14].

Llorca and co-workers [52]–[56] have been conducting finite element analyses in representative volume elements using this methodology in both long--fibre and sphere reinforced composites with good results.

The use of periodic boundary conditions is also encouraged by the works of Ostoja-Starzewski [57] and Terada et al. [51] which demonstrate that the effective properties obtained under these conditions are always bounded by those obtained under displacement and traction boundary conditions.

This will be the methodology used in this thesis. The fibre spatial distributions generated by the algorithm presented in chapter 2 will be operated on in order to create a 3D representative volume element, with periodic boundary conditions and geometrical periodicity. The next subsection describes how the periodic boundary conditions are applied in a 3D representative volume element.

3.1.4 Periodic boundary conditions in 3D

The importance of periodic boundary conditions in the world of micromechanical analysis has been demonstrated by several authors. The present subsection is devoted to the derivation of the equations to be applied to the RVE's mesh in order to implement this type of boundary conditions.

Periodic boundary conditions force such a deformation on the volume element that the displacement of one of the nodes belonging to one edge must be related to the displacement of the corresponding node in the opposite edge. Figure 3.5 exemplifies the final result.

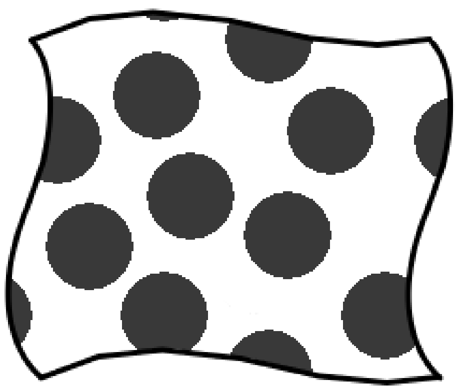

Figure 3.5: Periodic boundary conditions.

Barbero [58] provides a set of equations that allow the application of periodic boundary conditions in a 3D representative volume element. All equations must be applied to opposite nodes on the faces, edges and vertices of the RVE. Not only the degrees of freedom of these nodes are variables in these equations but also the far-field applied strains. Depending on which position the nodes are – faces, edges or vertices – a different set of equations must be applied to its degrees of freedom. These equations can be incorporated in a finite element analysis by using linear multi-point constraints.

These are nothing more than kinematic constraints imposed on the degrees of freedom of each pair of nodes.

Faces

Figure 3.6 shows the location and numbering used for the faces of the RVE to apply periodic boundary conditions.

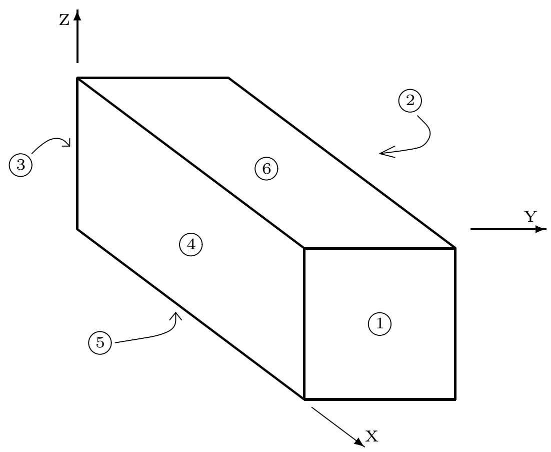

Figure 3.6: Face numbering of RVE for application of PBC.

Each node positioned on one face will have its degrees of freedom combined with a node placed in the opposite face. The numbering used for the faces in equations (3.18) is established according with figure 3.6:

$$\begin{aligned} u_i^1 - u_i^3 - c\varepsilon_{i1}^0 &= 0 \\ u_i^2 - u_i^4 - a\varepsilon_{i2}^0 &= 0 \\ u_i^6 - u_i^5 - b\varepsilon_{i3}^0 &= 0 \end{aligned} \tag{3.18}$$

In equations (3.18), u_i^n represents the degree of freedom i of node n. The numbering of the nodes is shown in figure 3.6. The variables a, b, and c represent the dimension of the RVE in the y, z, and x directions, respectively. The applied far-field strain components are represented by ε_{ij}^0. Please note that the far-field strain is a symmetric tensor and is defined in terms of tensorial shear strains.

Edges

Figure 3.7 shows the location and numbering used for the edges of the RVE to apply periodic boundary conditions.

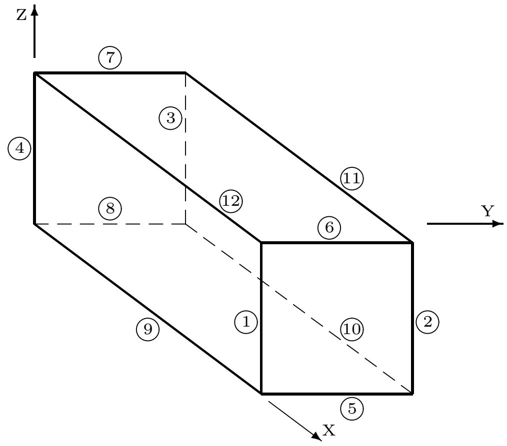

Figure 3.7: Edge numbering of RVE for application of PBC.

Each node along one edge of the RVE combines with the node on the parallel but opposite edge, making a total of six possible edge combinations. Although two faces converge on an edge, it is impossible to apply more than one kinematic constraint in the same degree of freedom. This justifies the need to develop different sets of equations for faces, edges and vertices. The numbering used in the following equations identifies the edge according with figure 3.7:

$$\begin{aligned}
&u_i^2 - u_i^4 - c\varepsilon_{i1}^0 - a\varepsilon_{i2}^0 = 0 \\
&u_i^1 - u_i^3 - c\varepsilon_{i1}^0 + a\varepsilon_{i2}^0 = 0 \\
&u_i^6 - u_i^8 - c\varepsilon_{i1}^0 - b\varepsilon_{i3}^0 = 0 \\
&u_i^5 - u_i^7 - c\varepsilon_{i1}^0 + b\varepsilon_{i3}^0 = 0 \\
&u_i^{11} - u_i^9 - a\varepsilon_{i2}^0 - b\varepsilon_{i3}^0 = 0 \\
&u_i^{10} - u_i^{12} - a\varepsilon_{i2}^0 + b\varepsilon_{i3}^0 = 0
\end{aligned} \tag{3.19}$$

Vertices

Figure 3.8 shows the location and numbering used for the vertices of the RVE to apply periodic boundary conditions.

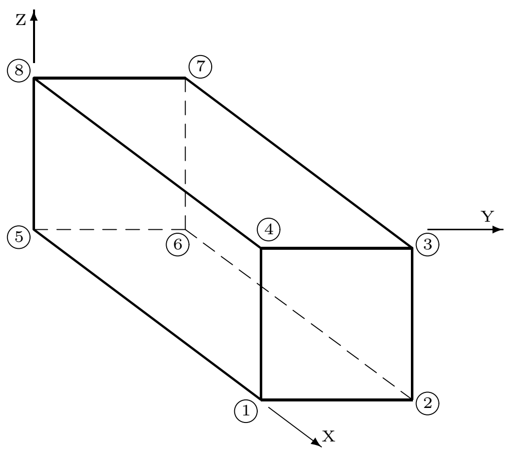

Figure 3.8: Vertex numbering of RVE for application of PBC.

As mentioned above for edges, also for the vertices we can not apply more than one kinematic constraint to each degree of freedom of a node despite the convergence of three edges in a vertex. Each vertex of the RVE will combine with its diagonally opposed vertex in the following manner [58].

$$\begin{aligned}
u_i^3 - u_i^5 - c\varepsilon_{i1}^0 - a\varepsilon_{i2}^0 - b\varepsilon_{i3}^0 &= 0 \\
u_i^2 - u_i^8 - c\varepsilon_{i1}^0 - a\varepsilon_{i2}^0 + b\varepsilon_{i3}^0 &= 0 \\
u_i^7 - u_i^1 + c\varepsilon_{i1}^0 - a\varepsilon_{i2}^0 - b\varepsilon_{i3}^0 &= 0 \\
u_i^4 - u_i^6 - c\varepsilon_{i1}^0 + a\varepsilon_{i2}^0 - b\varepsilon_{i3}^0 &= 0
\end{aligned} \tag{3.20}$$

Most analysts apply equations (3.18) to (3.20) by hand, i.e. the nodes are selected individually and their counterparts as well. Since the dimension of the volume elements to be used in this thesis is significantly large, an automatic procedure was developed to perform the generation of the mesh, definition of periodic boundary conditions, specification of constituent properties, definition of applied loads and finite element analysis execution. The following section presents how this is achieved.

3.2 Generation of the RVE

The commercial software package ABAQUS® [30] for finite element analysis developed by HKS Inc. was chosen to run all the analyses required throughout this thesis. Since the script to generate the distribution of fibres has been written in MATLAB® [29], it was required to establish a bridge between the two programmes/programming languages.

ABAQUS® provides an Application Programming Interface (API) called Abaqus Scripting Interface® [30]. In reality, this is an extension of the Python object-oriented programming language. The scripting capability of ABAQUS® allows the user to access all of its components such as parts, models, meshes, execute analyses, post-process results, etc, via a simple script written in Python.

In order to have proper communication between the MATLAB® [29] algorithm and ABAQUS® [30] it was required to convert, not the script itself but the output data, into a Python language script capable of being interpreted by ABAQUS® [30].

In appendix B, the MATLAB® [29] script capable of converting the output data from MATLAB® [29] to Python language for ABAQUS® [30] analysis is presented. This script is also capable of reading output data from ABAQUS® [30] such as mesh information in `.inp` files and process that information. It can be seen that the script is fully automatic. The user only needs to specify initial parameters such as material properties of constituents and what analysis should be performed. The present section provides a more detailed explanation of this script.

3.2.1 3D geometry and mesh

For ease of processes, it was decided to export the generated distribution of fibres directly to ABAQUS® [30]. This distribution contains only 2D data, i.e. it contains only the coordinates of the centre and the radius of each fibre as well as the size of the RVE. This geometrical information is used to build a sketch using ABAQUS® CAE [30] for both matrix and fibre. The fibre sketch will contain all fibres as if they were all complete circles – including the fibres along the edges – while the matrix will only have the shape of a rectangle the size of the RVE.

The Python script proceeds with instructions to extrude these geometries and create two 3D solids: one for the matrix and one for the fibre. After a serious of boolean operations with these solids, we achieve the final shape of both the matrix and the set of fibres, as represented in figure 3.9. Merging these two solids without deleting the contact areas between them generates a parallelepiped box with the boundaries between fibre and matrix perfectly defined, as represented in figure 3.10.

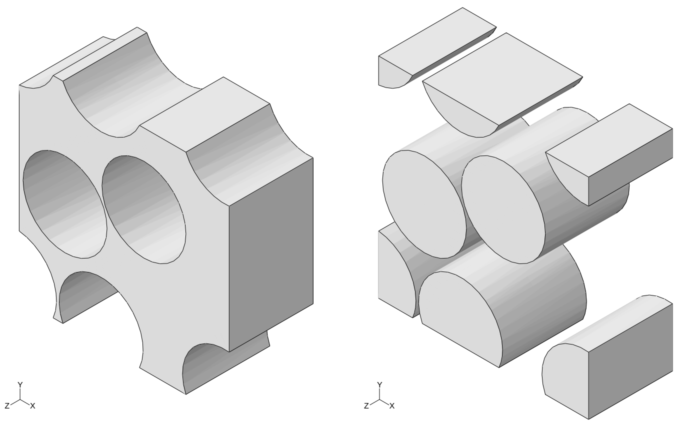

Figure 3.9: Solids for both matrix and fibre set.

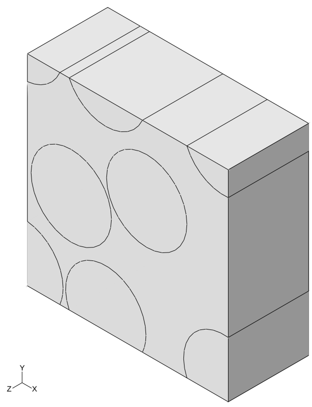

Figure 3.10: Final solid with generated random distribution of fibres.

By default, the sketch is created on the XY plane, leaving the fibres aligned with the Z axis. To simplify posterior post-processing of results, a rotation of the solids is performed in order to align the fibre axis with the X axis and the thickness direction of the laminate with the Z axis.

Finally, the mesh is generated. Unfortunately, ABAQUS® [30] does not have any built-in function to force the existence of periodic boundary conditions, i.e. it does not posses an algorithm which forces the presence of two nodes positioned in opposite sides of the RVE. In order to overcome this problem, it is required to use a combination of element types: reduced integration 8-node hexahedron elements, C3D8R, and 6-node wedge element, C3D6. Hexahedron elements are preferred while wedge elements are only positioned in difficult regions to mesh such as between any two very close fibres. Figure 3.11 shows the final mesh obtained for the geometry in figure 3.10.

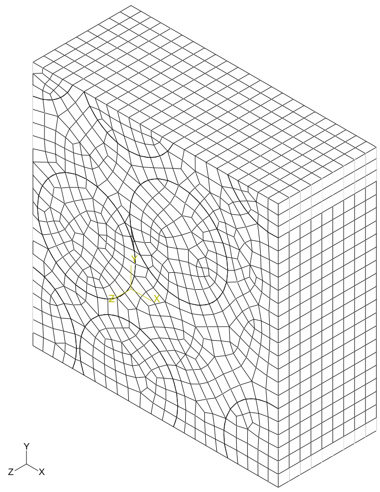

Figure 3.11: Final mesh of generated random distribution of fibres.

Since the kinematic constraints associated with the periodic boundary conditions can not be applied directly by ABAQUS® [30], the subsequent step must be performed again with the help of an auxiliary method. After finishing the mesh generation, ABAQUS® [30] exports the mesh data to a `.inp` file. This file is then read and interpreted with MATLAB® [29].

3.2.2 Definition of PBC's and pre-processing for FE analysis

After reading and understanding the generated mesh, MATLAB® [29] identifies which elements belong to each material – fibre or matrix – and identifies the nodes of each face, edge and vertex and pairs them with their counterparts on opposite faces, edges and vertices. For each of these pairs of nodes, a set of equations limiting their degrees of freedom must be satisfied (as per subsection 3.1.4). These equations are provided to ABAQUS® [30] as a set of linear multi-point constraints and will be responsible for the appropriate definition of periodic boundary conditions (PBC).

In order to apply the periodic boundary conditions, one must define how the far-field strains will be given into ABAQUS® [30]. Creating two dummy nodes, not attached to any element, is the best way to do so. Two nodes are needed because each node in 3D FEA contains three degrees of freedom and six components of the far-field strain tensor need to be defined. The correspondence used between each degree of freedom of the dummy nodes and the far-field strain tensor components is:

$$\begin{aligned} u_1^{d1} &= \varepsilon_{11}^0 & \qquad u_1^{d2} &= \varepsilon_{12}^0 \\ u_2^{d1} &= \varepsilon_{22}^0 & \qquad u_2^{d2} &= \varepsilon_{13}^0 \\ u_3^{d1} &= \varepsilon_{33}^0 & \qquad u_3^{d2} &= \varepsilon_{23}^0 \end{aligned} \tag{3.21}$$

where u_i^{dj} represents the degree of freedom i of dummy node dj. As can be seen, the first dummy node corresponds to normal strains, while the second to shear strains.

The equations are transformed in a set of keywords, according with ABAQUS® documentation [30] for the implementation of multi-point constraints. These keywords are written in a separate text file. The mesh information – node coordinates and connectivity matrix – is also written in a separate file.

The material properties of each constituent of the composite are given through an external text file. The data there included is converted into ABAQUS® [30] keywords and written in an individual file. This script creates yet another file, this time with information regarding important node sets that can be used for later post-processing, for example, a group of nodes belonging to a face of the RVE.

One last file is created, and this will be the *master* file of them all. It will be a typical `.inp` file used by ABAQUS® [30] with `INCLUDE` keywords for the previously mentioned files, and all the `STEP`-related data required to perform a finite element analysis – boundary conditions, applied loads, step options, output requests, convergence criteria, etc.

3.2.3 Obtaining the elastic properties

The objective of this chapter is to present an easy and automatic process to determine the elastic properties of a composite material from its constituents' material properties.

Hook's law for transverse isotropic materials was defined in equation (3.4), and it is repeated here for convenience:

$$\begin{Bmatrix} \bar{\sigma}_{11} \\ \bar{\sigma}_{22} \\ \bar{\sigma}_{33} \\ \bar{\sigma}_{12} \\ \bar{\sigma}_{13} \\ \bar{\sigma}_{23} \end{Bmatrix} = \begin{bmatrix} C_{1111} & C_{1122} & C_{1122} & 0 & 0 & 0 \\ C_{1122} & C_{2222} & C_{2233} & 0 & 0 & 0 \\ C_{1122} & C_{2233} & C_{2222} & 0 & 0 & 0 \\ 0 & 0 & 0 & C_{4444} & 0 & 0 \\ 0 & 0 & 0 & 0 & C_{4444} & 0 \\ 0 & 0 & 0 & 0 & 0 & \frac{C_{2222}-C_{2233}}{2} \end{bmatrix} \begin{Bmatrix} \bar{\epsilon}_{11} \\ \bar{\epsilon}_{22} \\ \bar{\epsilon}_{33} \\ \bar{\epsilon}_{12} \\ \bar{\epsilon}_{13} \\ \bar{\epsilon}_{23} \end{Bmatrix} \tag{3.22}$$

where an overline indicates volume average. Once the components of the stiffness tensor are known, the five independent elastic properties of the composite can be determined by equations (3.5). The far-field strain applied to the RVE by equations (3.18) to (3.20), ε_{ij}^0, will cause a complex state of stress and strain on the RVE. However, the volume average of strain in the RVE equals the applied far-field strain:

$$\bar{\epsilon}_{ij} = \frac{1}{V}\int_V \varepsilon_{ij} dV = \varepsilon_{ij}^0 \tag{3.23}$$

In order to determine the entire stiffness tensor, all that is required is to perform a sequence of six analyses, one analysis for each column of the stiffness tensor. The applied strain is a unit value for one of the far-field strain components (corresponding to the column we want to determine) and zero to all other strain components. This way, each component of the stiffness tensor will be equal to the volume average of the stress field:

$$C_{ijkl} = \bar{\sigma}_{ij} = \frac{1}{V}\int_V \sigma_{ij} dV \qquad \text{with} \quad \varepsilon_{kl}^0 = 1 \tag{3.24}$$

For example, in order to determine the components of the second column, the applied far-field strains in equations (3.18) to (3.20) would be:

$$\varepsilon_{22}^0 = 1 \qquad \varepsilon_{11}^0 = \varepsilon_{33}^0 = \varepsilon_{12}^0 = \varepsilon_{13}^0 = \varepsilon_{23}^0 = 0 \tag{3.25}$$

Since ABAQUS® [30] software is being used, one has to be careful when applying these loading conditions because the software interprets only engineering shear strains and not tensor shear strains. This means that when determining components for columns four to six, the applied strain needs to be half of a unit value.

After running all six analyses, the results are post-processed by a Python script and the five independent material properties of the transverse isotropic composite determined.

3.3 Comparison of methods

After presenting the different methodologies – analytical and numerical – to estimate the effective elastic properties of composite materials from the elastic properties of their constituents, a comparison of estimates will be performed.

Two composites were chosen from the World Wide Failure Exercise [31] for this comparative study: AS4 carbon fibre with 3501-6 epoxy matrix and Silenka E-glass fibre with MY750/HY917/DY063 epoxy matrix. The constituents properties are shown in table 3.1.

Table 3.1: Material properties.

Material	E_1 [GPa]	E_2 [GPa]	G_{12} [GPa]	ν_{12}	G_{23} [GPa]
Fibres					
AS4	225	15	15	0.2	7
Silenka E-glass	74	74	30.8	0.2	30.8
Matrices					
3501-6	4.2	4.2	1.567	0.34	1.567
MY750/HY917/DY063	3.35	3.35	1.24	0.35	1.24

The study was performed by estimating the elastic properties for a range of fibre volume fractions typical of long-fibre reinforced composites. The considered range is from 45% to 65%. Figures 3.12 to 3.17 show the computed estimates for six engineering properties – longitudinal and transverse Young's moduli, longitudinal Poisson's ratio, longitudinal and transverse shear moduli and transverse Poisson's ratio – for AS4/3501-6 composite. Engineering constants for Silenka E-glass/MY750/HY917/DY063 are shown in figures 3.18 to 3.23. Available experimental data from the World Wide Failure Exercise [31] is also shown for reference.

The analytical methods used for these predictions are marked with: *Voigt* and *Reuss* for both Voigt and Reuss models, respectively; *StMat* for Strenght of Materials model; *CCA* for Composite Cylinder Assemblage model; *Hashin+* and *Hashin-* for the upper and lower Hashin-Hill bounds, respectively; *Mori-Tanaka* for the Mori-Tanaka model; *Square* and *Hex* for the two unit-cell numerical analysis using a square or an hexagonal periodic distribution, respectively; *Rigid* for a random distribution of fibres but with rigid boundary conditions applied to the edges; and *RAND_uSTRU_GEN* for the model presented here with geometrical periodicity on the edges.

According with table 2.1 for the determination of effective properties of a

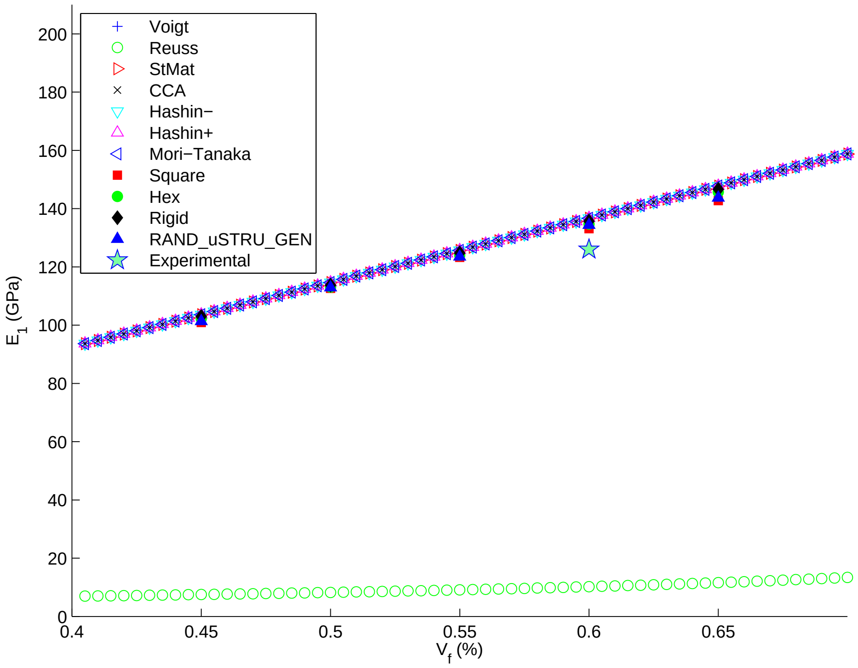

Figure 3.12: Longitudinal Young's modulus for AS4/3501-6.

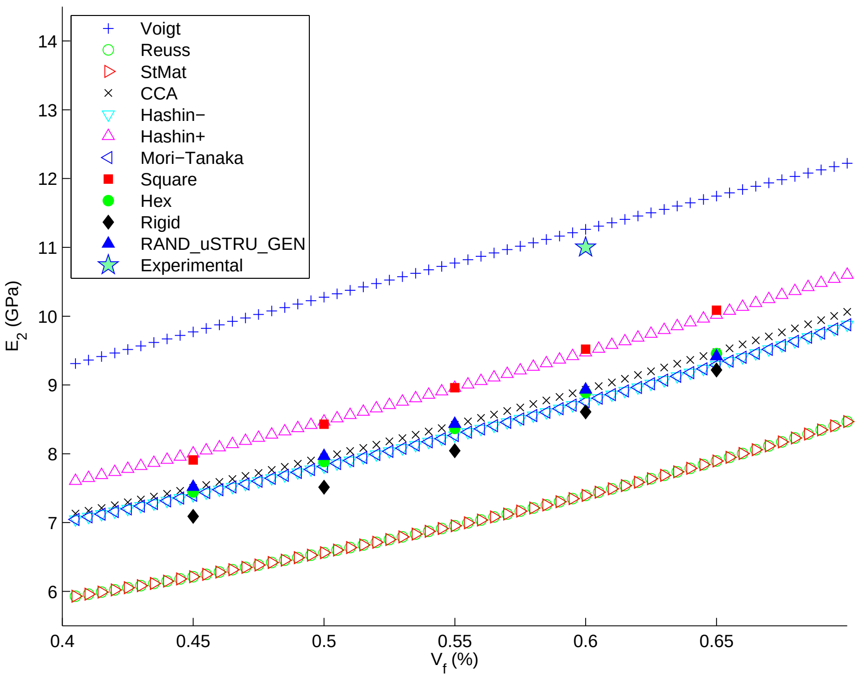

Figure 3.13: Transverse Young's modulus for AS4/3501-6.

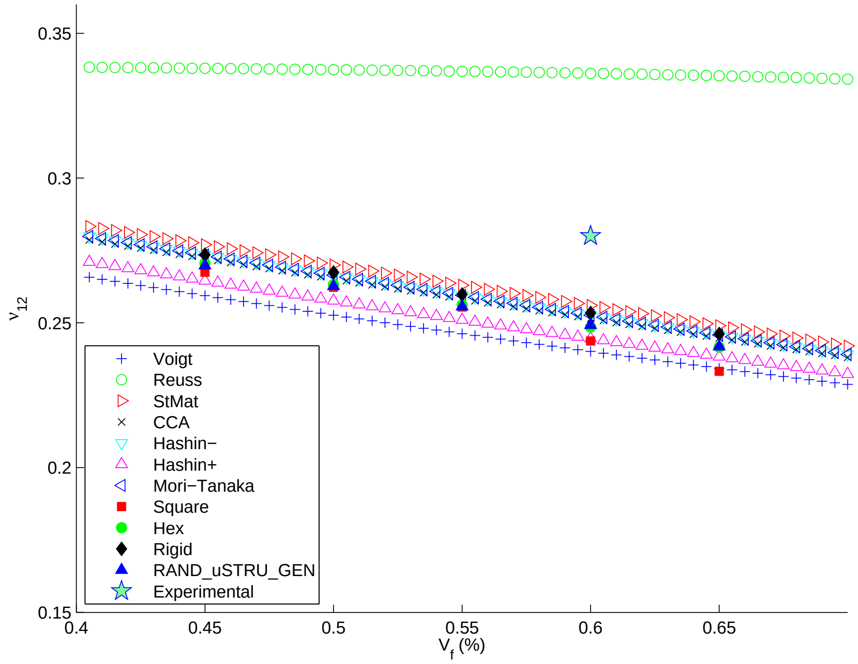

Figure 3.14: Longitudinal Poisson's ratio for AS4/3501-6.

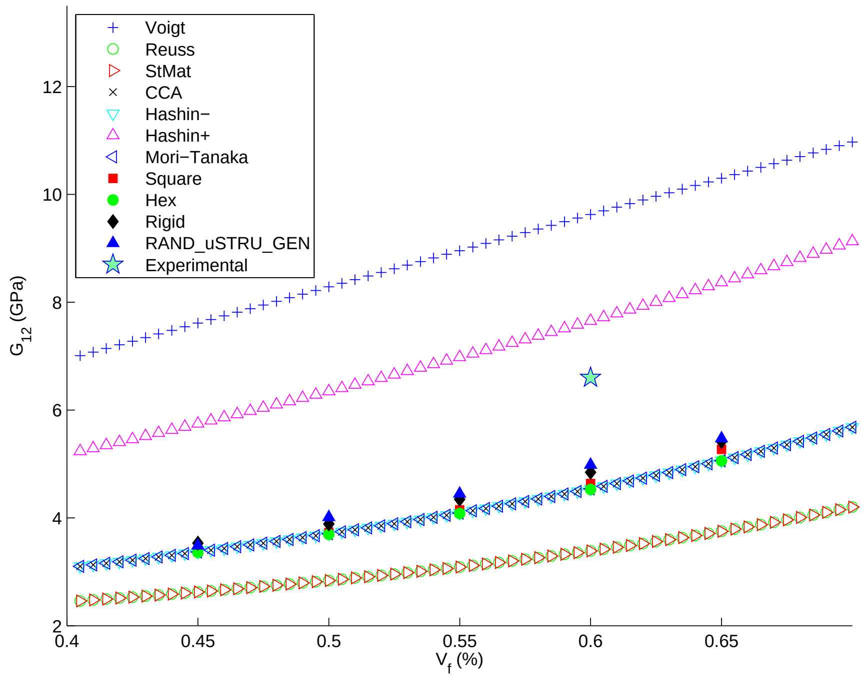

Figure 3.15: Longitudinal shear modulus for AS4/3501-6.

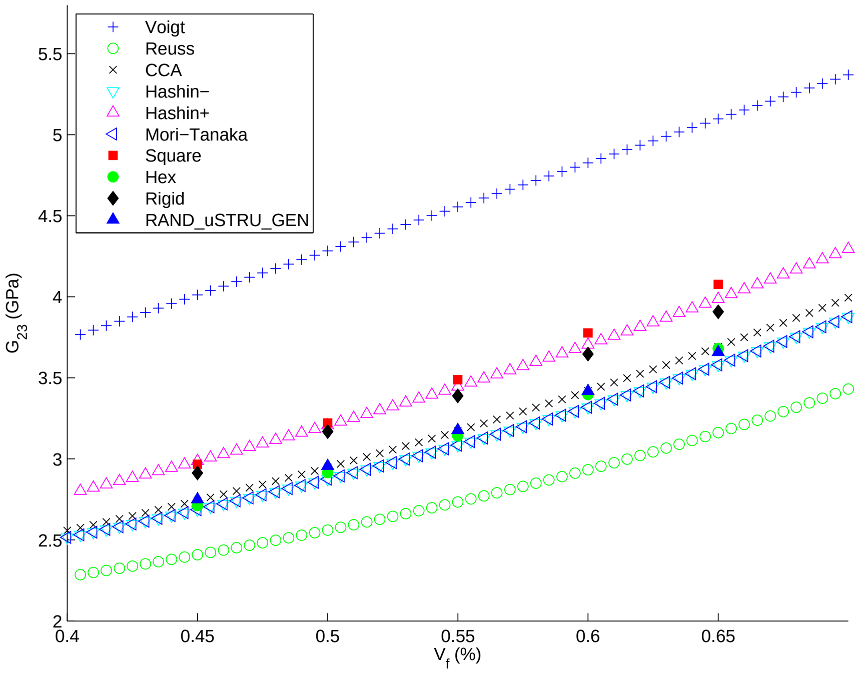

Figure 3.16: Transverse shear modulus for AS4/3501-6.

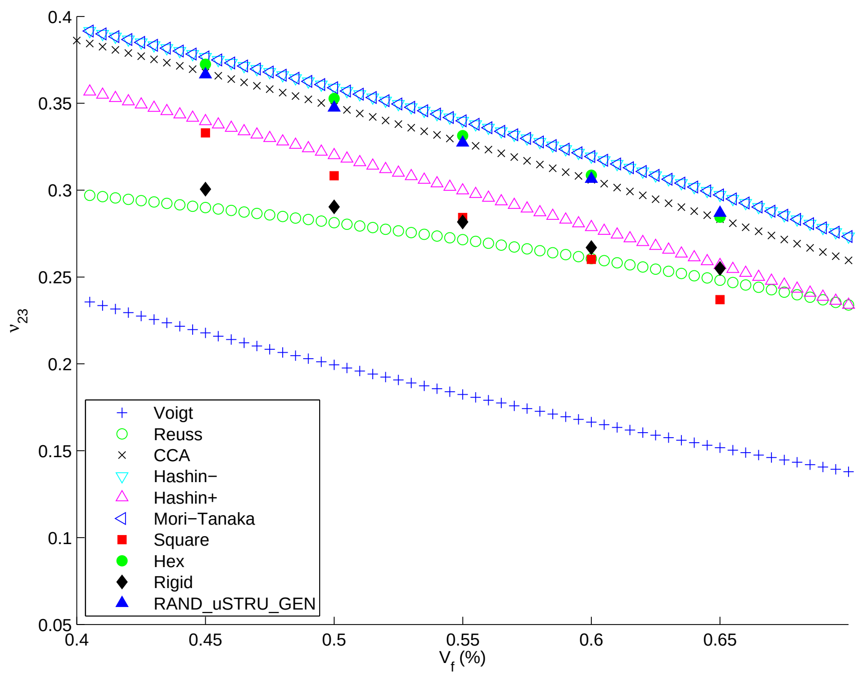

Figure 3.17: Transverse Poisson's ratio for AS4/3501-6.

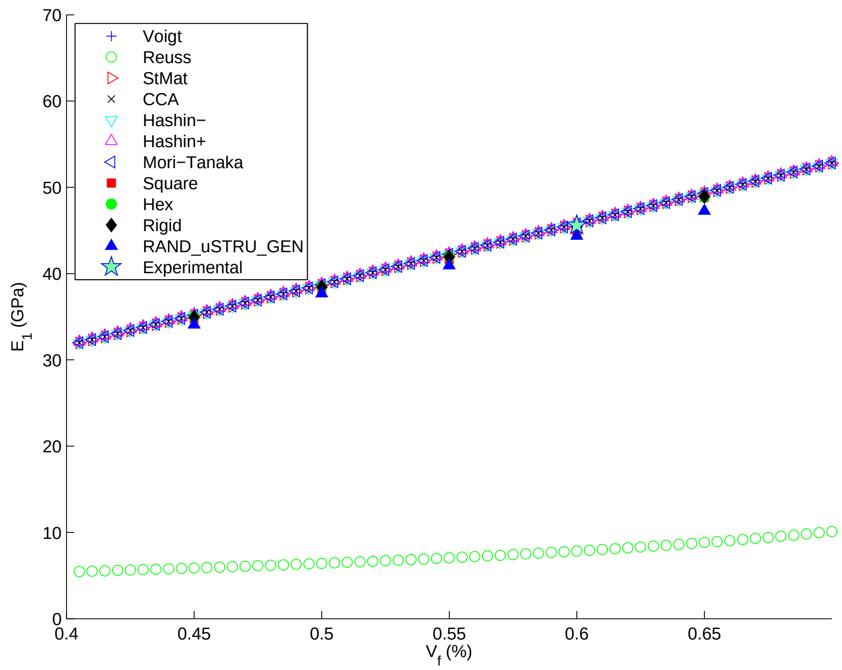

Figure 3.18: Longitudinal Young's modulus for Silenka/MY750/HY917/DY063.

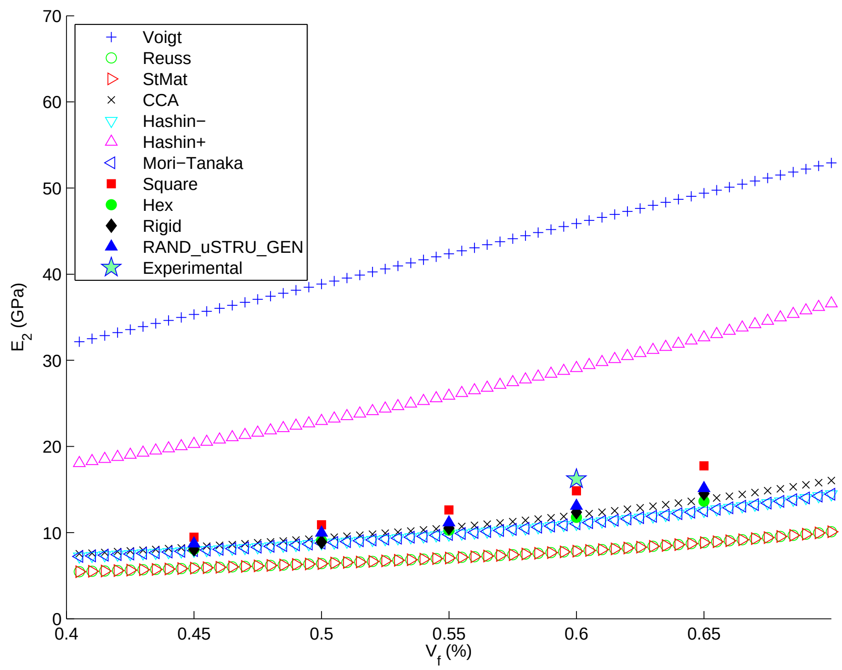

Figure 3.19: Transverse Young's modulus for Silenka/MY750/HY917/DY063.

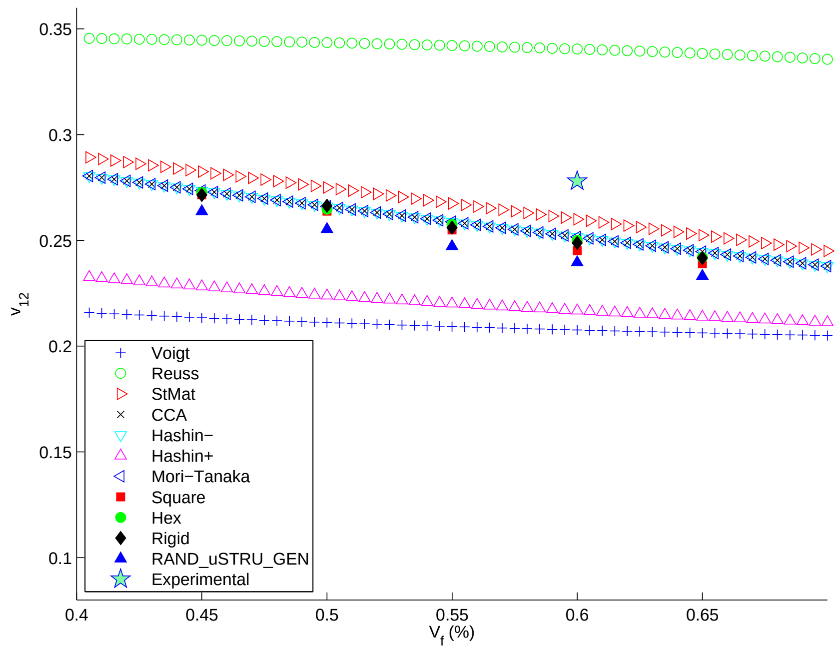

Figure 3.20: Longitudinal Poisson's ratio for Silenka/MY750/HY917/DY063.

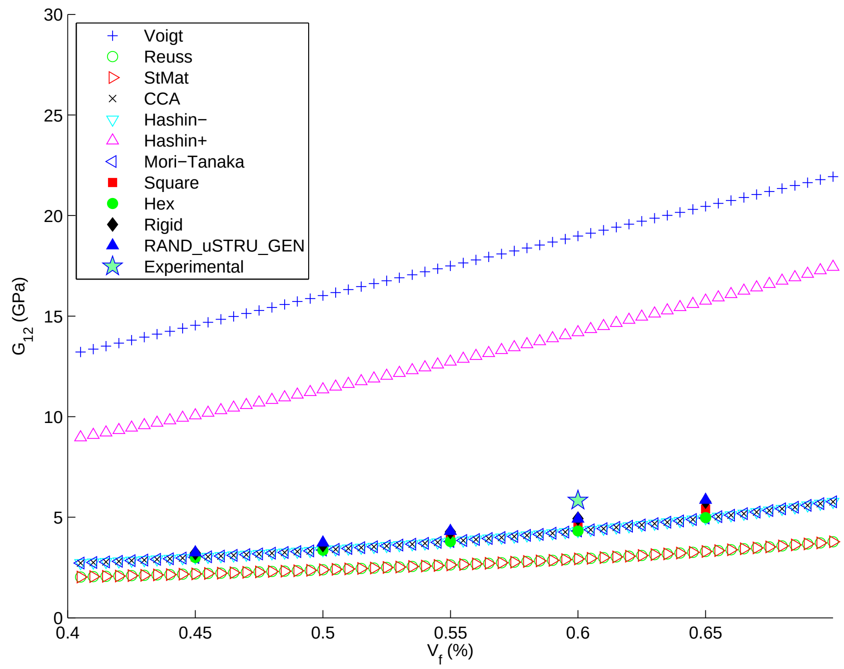

Figure 3.21: Longitudinal shear modulus for Silenka/MY750/HY917/DY063.

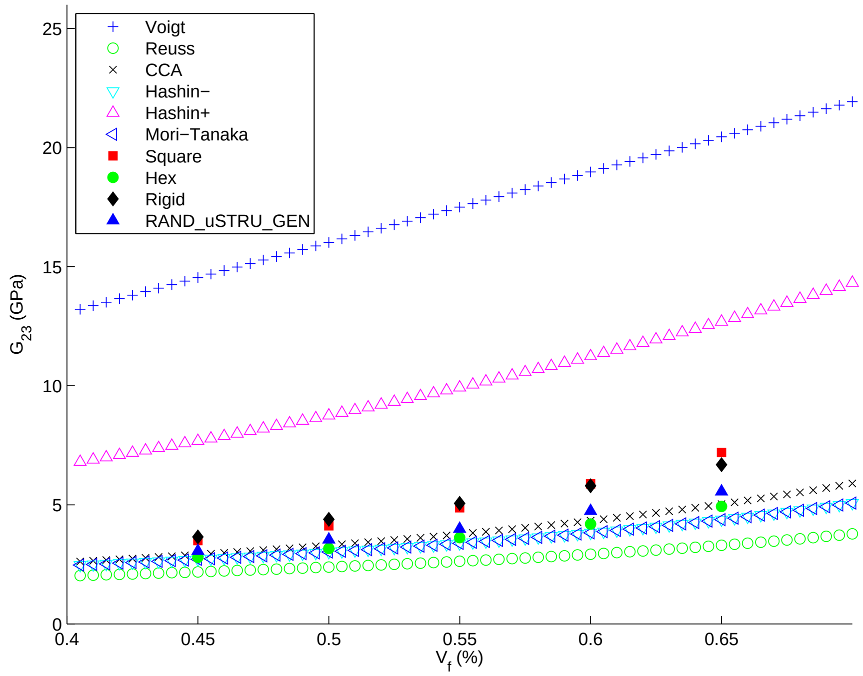

Figure 3.22: Transverse shear modulus for Silenka/MY750/HY917/DY063.

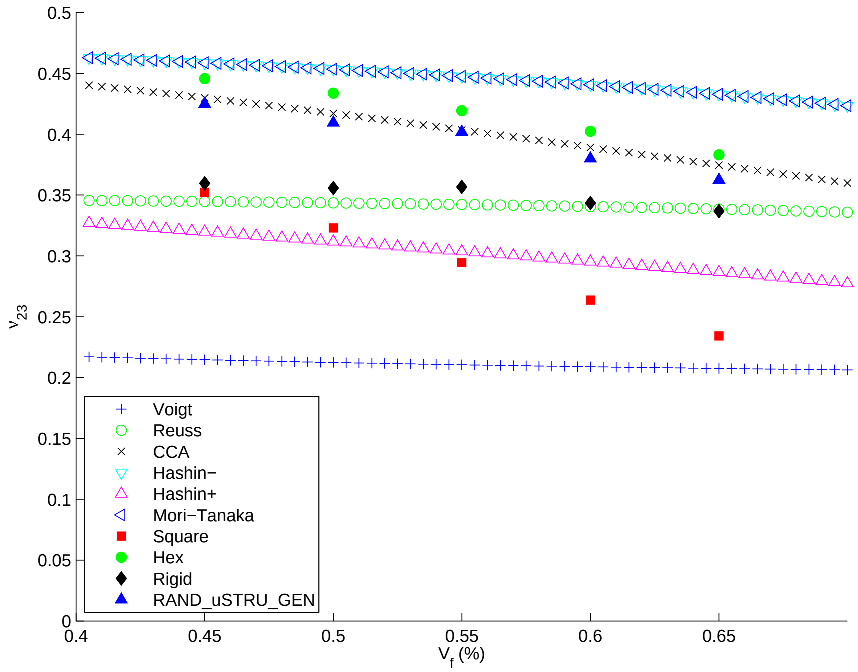

Figure 3.23: Transverse Poisson's ratio for Silenka/MY750/HY917/DY063.

composite, the chosen size of the RVE for the last two mentioned numerical methods was 30× the fibre radius. Only one volume element was generated for each of these methods.

It can easily be seen that the longitudinal Young's modulus is always well approximated by the rule of mixtures in figures 3.12 and 3.18; it is however the only property that can be well estimated by such a simple method. All three longitudinal properties are well approximated by any of the given numerical methods or analytical methods which take into consideration the geometry of the microstructure, such as the composite cylinder assemblage model or the Mori-Tanaka method.

It is however in the transverse properties that the predictions disagree the most. The square unit cell has the tendency to overestimate the transverse properties, especially if there is a significant difference between the constituents' elastic properties as is the case of carbon fibre reinforced polymers (AS4/3502-6). The most notable difference between the different prediction methods can be seen in the transverse Poisson's ratio and shear modulus. Because the boundaries do not present material continuity and are considered fixed in the *Rigid* model, it is on these two properties that this prediction method fails the most, even providing estimates outside of the Hashin-Hill bounds for the AS4/3501-6 composite. Probably, a bigger size would be required for a volume element with these boundary conditions to provide more accurate estimates on the transverse properties.

On the other hand, both the hexagonal unit cell and the RVE generated by the algorithm presented in chapter 2 provide very close estimates for all engineering properties, always inside the Hashin-Hill bounds as predicted by Ostoja-Starzewski [57] and Terada [51] for volume elements which use periodic boundary conditions. From the analytical tools in study, the composite cylinder assemblage was the one which provided better estimates.

The next section will provide a different set of studies for the estimation of effective properties on composite materials with long fibres using the algorithm presented in chapter 2. A series of parametric studies will be conducted to study the influence of geometrical parameters on the final effective properties of these materials.

3.4 Parametric studies

This section studies the dependency of the elastic properties of the composite material on four different parameters: the RVE size, the fibre radius, the RVE thickness in the fibre direction, and the minimum gap between fibres.

3.4.1 RVE size

To study how the five independent engineering properties of transverse materials plus the transverse Poisson's ratio vary with the size of the volume element, five different RVE sizes were selected and analysed: 10, 20, 30, 40, and 50 times the fibre radius. For each size, fifty distributions were generated using the algorithm described in chapter 2. The same sets of constituents were chosen for these analyses as for the previous studies. The fibre volume for both materials is set to 60%. The other three parameters to be studied were kept constant with the following values:

- Fibre radius - $7.1\mu m$ for the AS4/3501-6 composite and $5\mu m$ for the Silenka-based composite.
- RVE thickness - $2\times$ the fibre radius.
- Minimum gap between fibres - $0.07\times$ the fibre radius.

Figures 3.24 and 3.25 show the evolution of the material properties with the RVE size. The represented curves are the average of the fifty distributions and the error bars represent the minimum and maximum value corresponding to each volume element size.

Generally speaking, it can be seen that each engineering property tends to converge with the increase of the size of the volume element for both materials. However, for the composite with the largest difference in the constituents' properties – AS4/3501-6 – despite convergence of the average value, the scatter of predictions for the longitudinal properties seems to be larger than for the Silenka-based composite. As Trias [34] noted (table 2.1), these plots also allow to confirm that a minimum of $30\times$ the fibre radius should be used for the prediction of the effective elastic properties. Bigger volume elements provide a better estimate, but they also require a much greater computational effort. For the remainder of the parametric studies, a volume element size of $30\times$ will be used.

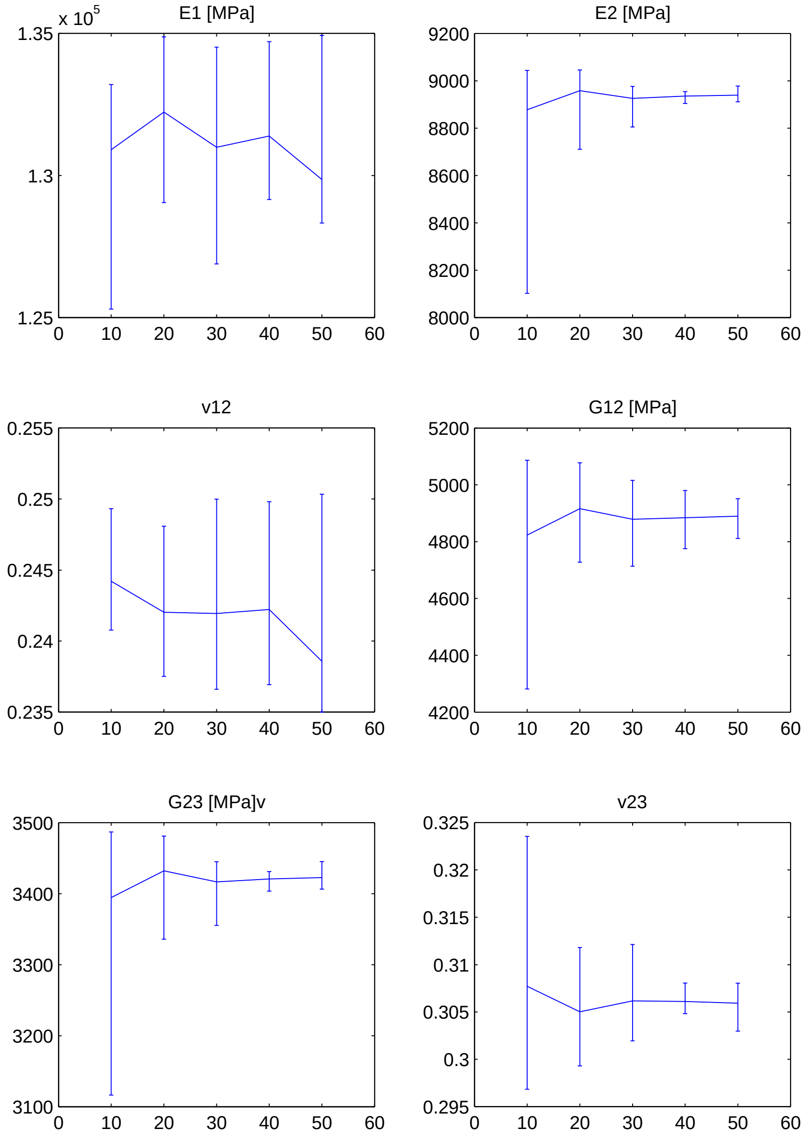

Figure 3.24: AS4's effective engineering properties as a function of RVE size.

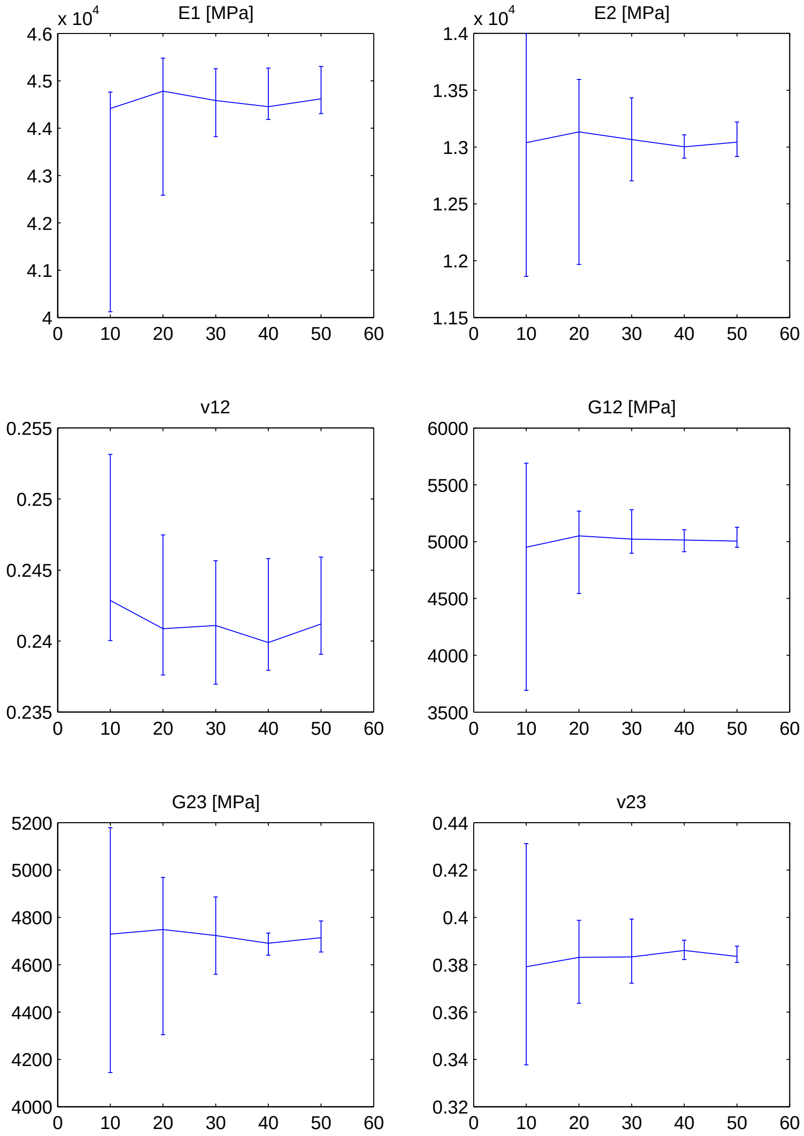

Figure 3.25: Silenka's effective engineering properties as a function of RVE size.

3.4.2 Fibre radius

Figures 3.26 and 3.27 show the evolution of the six engineering properties in study with the fibre radius. It can be seen that the fibre radius does not have an influence on the elastic properties of the composite for the two materials sets considered. The same result had been achieved by Gusev et al. [21].

3.4.3 RVE thickness

Figures 3.28 and 3.29 show the evolution of the six engineering material properties under study with the thickness of the representative volume element. The thickness is measured in the fibre direction, while the other two dimensions (transverse direction) maintain a constant 30× the fibre radius size. As can be seen, with the increase of the RVE thickness, the longitudinal properties, especially Young's modulus and Poisson's ratio, follow an increasing trend. Regarding the transverse Young's and shear moduli, only for the Silenka-based composite a slight decrease is registered.

3.4.4 Minimum gap between fibres

Figures 3.30 and 3.31 show the evolution of the six engineering properties being studied as a function of the minimum distance between any two neighbouring fibres. It can be seen that the Young's modulus and Poisson's ratio are not significantly affected by this parameter. However, for both composite-systems considered, the transverse Young's modulus and both longitudinal and transverse shear moduli suffer a considerable decrease.

3.5 Conclusions

The algorithm `RAND_uSTRU_GEN` presented in chapter 2 to generate a random distribution of fibres was used to perform a comparative study of the prediction of engineering material properties through analytical and numerical methods. It was demonstrated that the algorithm is capable of accurately predicting the elastic properties, when used in conjunction with a system of periodic boundary conditions.

A parametric study of the evolution of engineering properties with a number of different parameters used in the algorithm `RAND_uSTRU_GEN` was

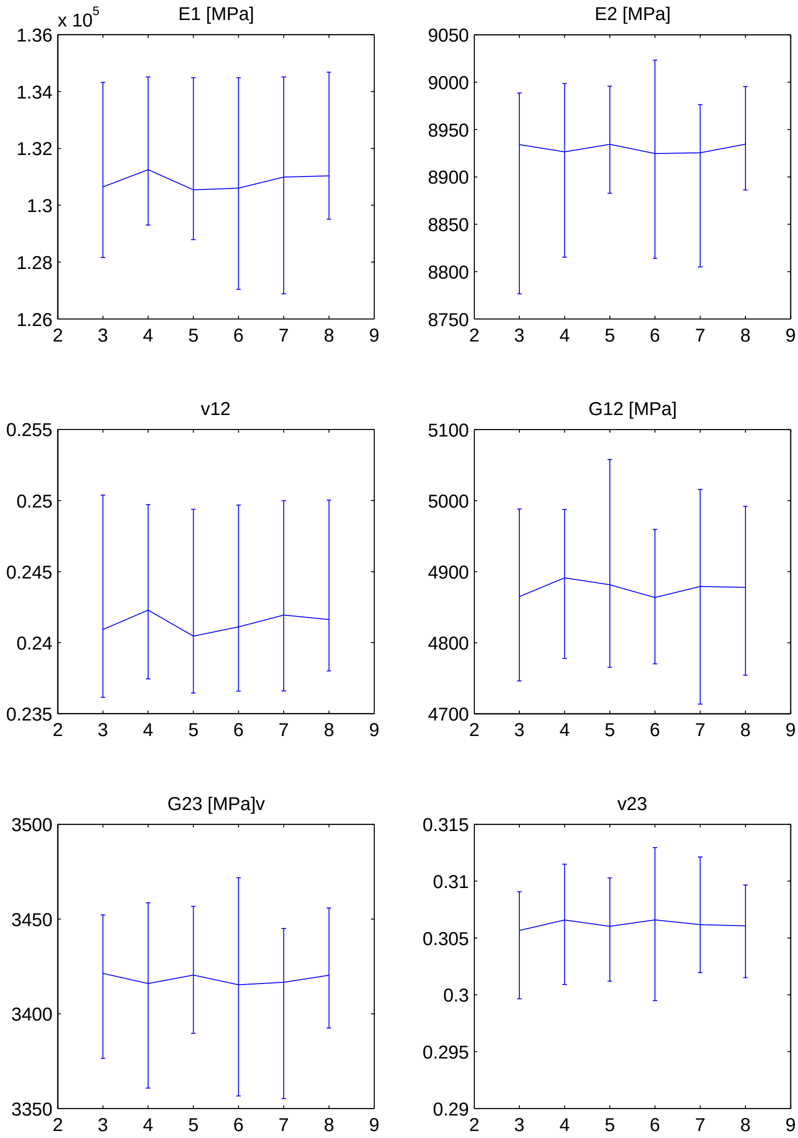

Figure 3.26: AS4's effective engineering properties as a function of fibre radius.

conducted. It was determined that the fibre radius does not have an influence on the mechanical properties of the composite. The same can not be said about the representative volume element dimensions (in both lon-

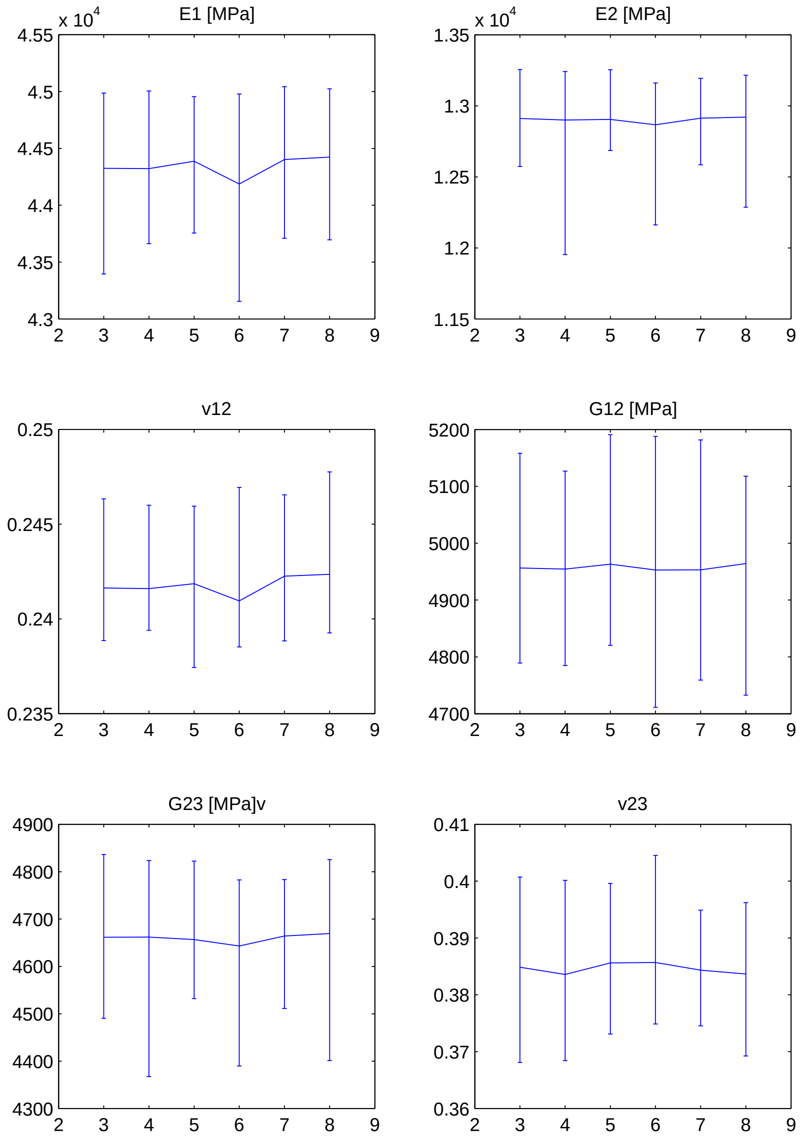

Figure 3.27: Silenka's effective engineering properties as a function of fibre radius.

gitudinal and transverse directions) and the minimum acceptable distance between any two neighbouring fibres.

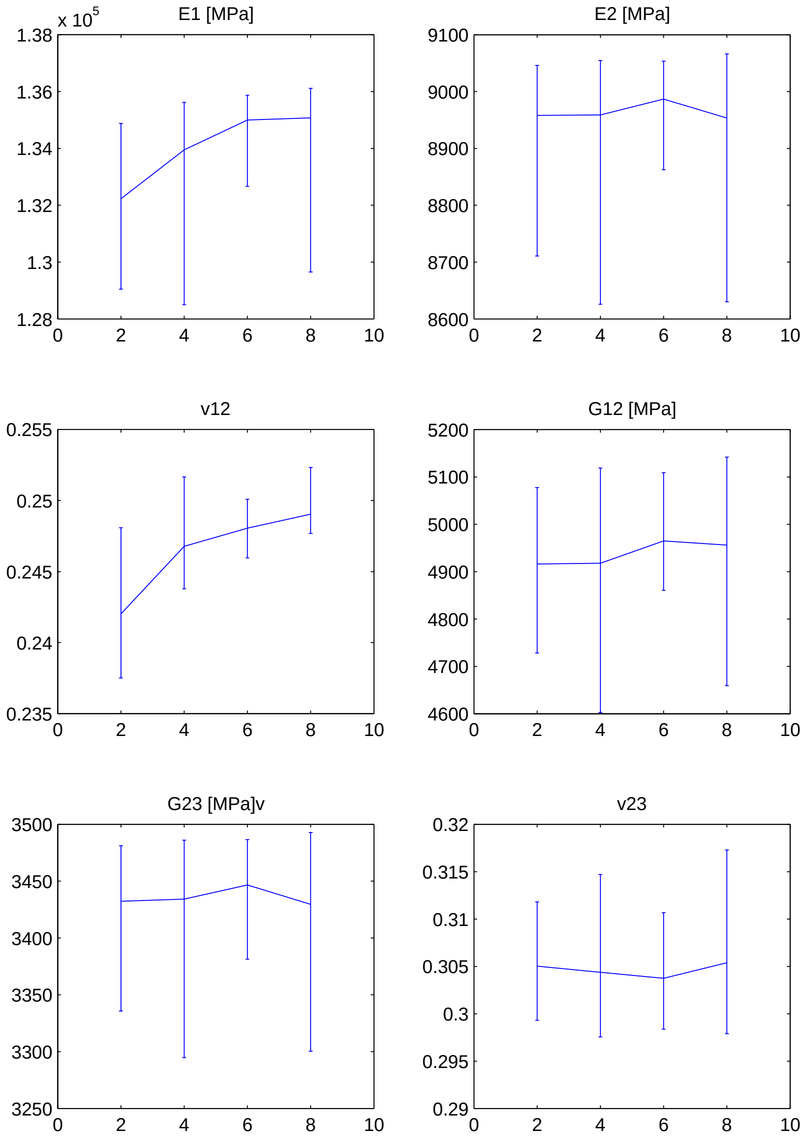

Figure 3.28: AS4's effective engineering properties as a function of RVE thickness.

The next chapter will present and include in the model an elasto-plastic constitutive model tailored to the typical mechanical behaviour of epoxy materials. This, together with the random distribution of fibres will allow

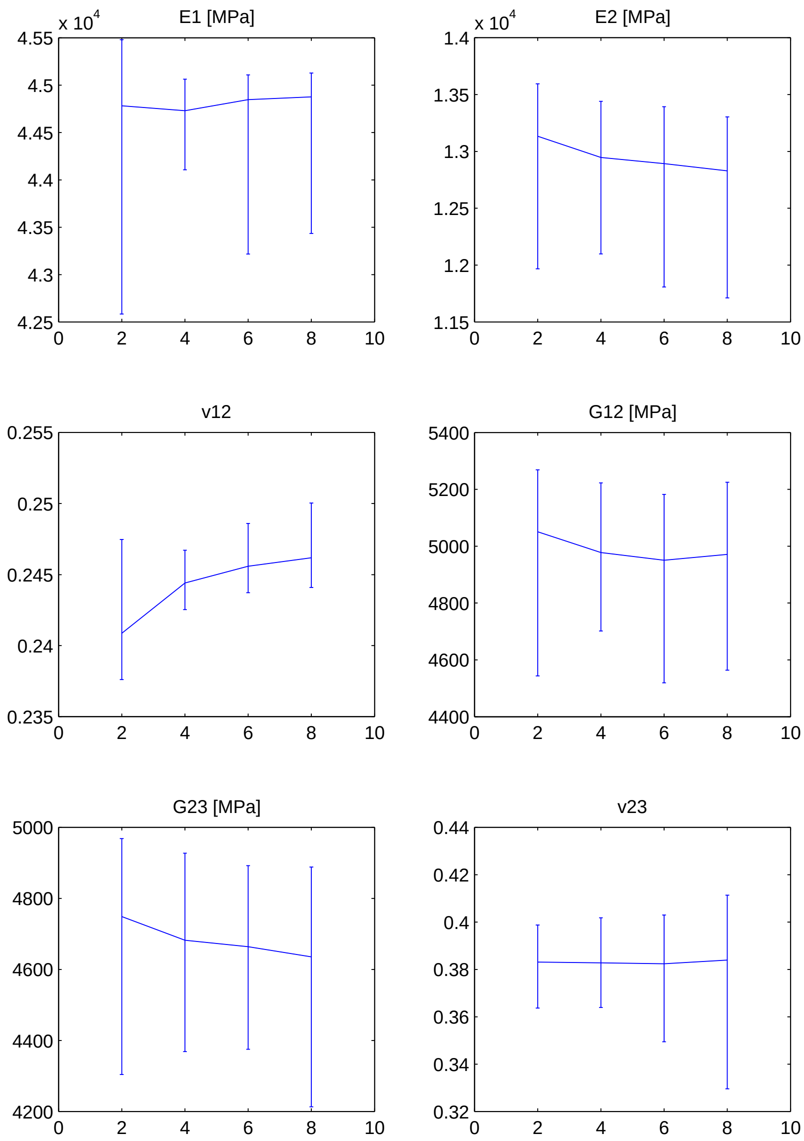

Figure 3.29: Silenka's effective engineering properties as a function of RVE thickness.

for a better understanding of the mechanical processes in action at the micro-scale level.

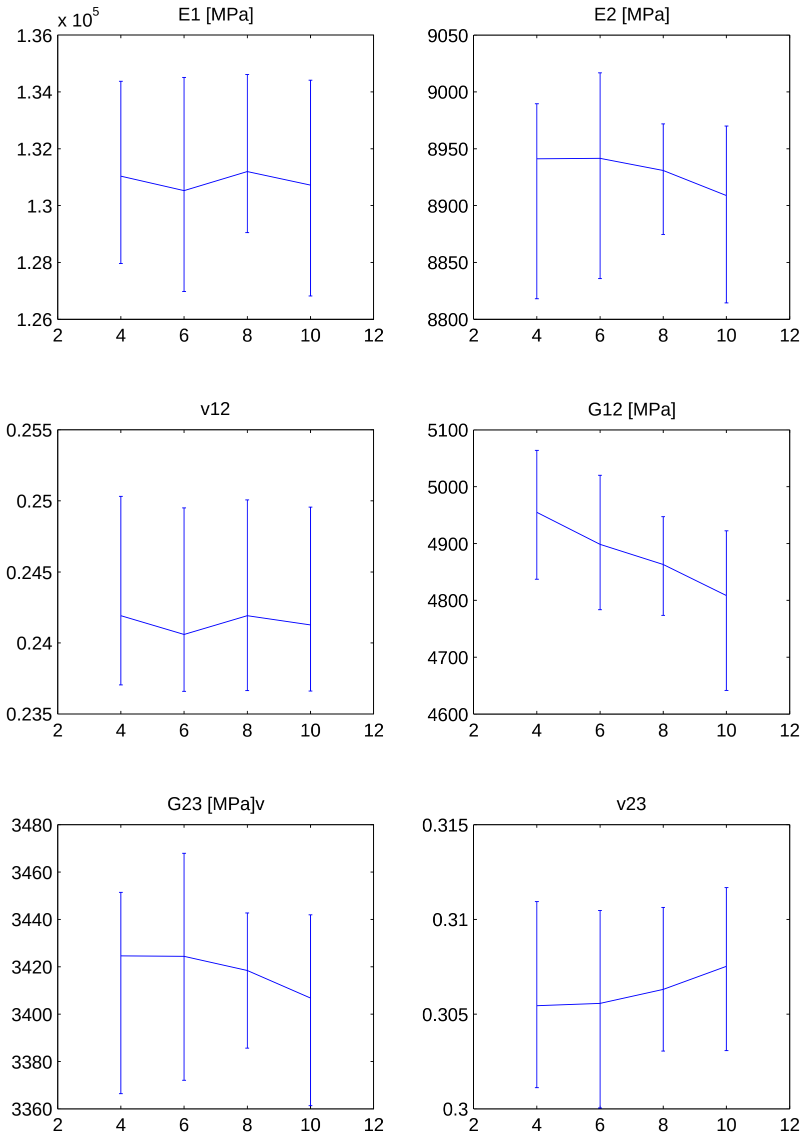

Figure 3.30: AS4's effective engineering properties as a function of minimum fibre gap.

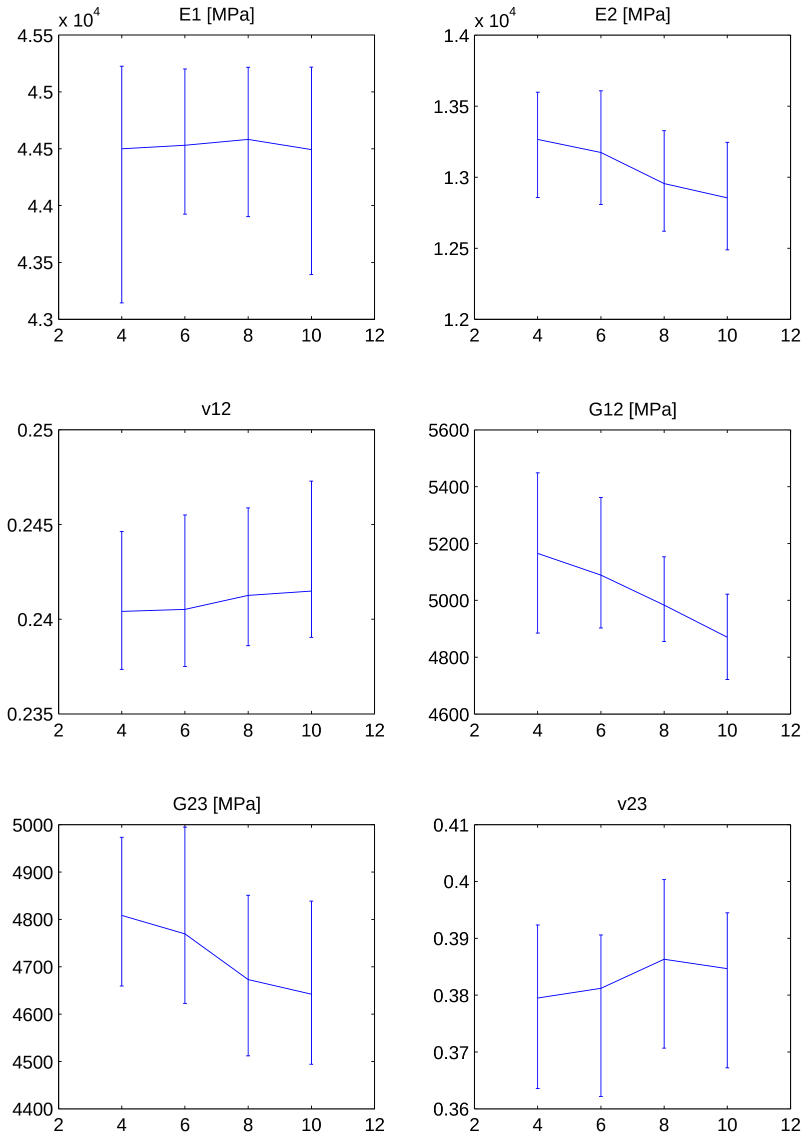

Figure 3.31: Silenka's effective engineering properties as a function of minimum fibre gap.

Chapter 4

Plasticity model for epoxy resins

My nature is to be linear, and when I'm not, I feel really proud of myself.

Cynthia Weil

After studying the elastic behaviour of the random reinforcement distributions generated by the algorithm of chapter 2, it is now time to enhance its simulation capabilities. The first improvement to be developed is the simulation of non-linear behaviour of the matrix material in advanced composites, namely epoxy matrices.

First, a brief introduction to the mathematical theory of plasticity is performed followed by a survey of the methods for the numerical implementation of plasticity models. A review of the current knowledge on non-linear material behaviour of epoxies based on experimental data is performed next. The implementation of a plasticity model which accounts for the specificities of epoxy materials is conducted. Finally, a few simple examples are presented demonstrating the plasticity model in action when applied to an epoxy matrix reinforced with unidirectional, continuous fibres.

4.1 Plasticity theory

The current section provides an overview on the theoretical aspects of plasticity. The books by Hill [59], Kachanov [60], Lubliner [61] or Souza Neto [62] provide a more detailed and broader perspective on the general theory of plasticity as well as its phenomenological aspects. In this thesis, only small deformations will be considered. This assumption is justified by the presence of cracking for small deformations. Considering only small-strains will also allow to simplify the model's definition and implementation.

4.1.1 Additive decomposition of the strain tensor

Figure 4.1 shows the mathematical idealisation of a typical stress-strain curve of an uniaxial tensile test on an elastoplastic material.

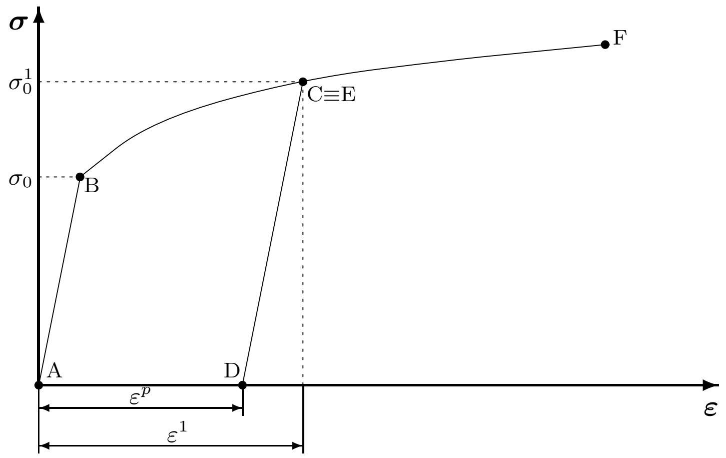

Figure 4.1: Mathematical model of uniaxial tensile test.

The segment $A - B$ represents the elastic domain of the material behaviour. The initial Young's modulus is given by the slope of this segment and remains constant in the elastic domain. Under elastic behaviour, it is considered that there are no permanent deformations and all strains can be recovered upon unloading. This elastic behaviour ends when the yield stress σ_0 is met (point B). From this moment on, the material begins suffering permanent plastic strains. The material can also suffer hardening, i.e. the yield stress increases as the plastic strains accumulate. This can be seen in figure 4.1 in segment $B - F$. At point C, for example, the accumulated plastic strain is given by ε^p and the increase of the yield stress from σ_0 to σ_0^1. This increase continues until the material reaches the ultimate strength (point F) and fails.

If the material is unloaded from point C, it will recover some of the accumulated strain, ε^1. In other words, at any given point of the loading curve under plastic domain, the strain tensor can be decomposed in two components: one elastic (and thus recoverable) component, and one plastic (or permanent) component. For the uniaxial example in figure 4.1, the recovered elastic strain after unloading (segment $C - D$) is given by:

$$\varepsilon^e = \varepsilon^1 - \varepsilon^p \tag{4.1}$$

In the most general case, the strain tensor is decomposed according to

$$\boldsymbol{\varepsilon} = \boldsymbol{\varepsilon}^e + \boldsymbol{\varepsilon}^p \tag{4.2}$$

where $\boldsymbol{\varepsilon}^e$ is the elastic strain tensor and $\boldsymbol{\varepsilon}^p$ is the plastic strain tensor.

4.1.2 Elastic law

Assuming that the material is isotropic with linear elastic behaviour, the stress tensor is defined by:

$$\begin{aligned} \boldsymbol{\sigma} &= \boldsymbol{D}^e : \boldsymbol{\varepsilon}^e \\ &= 2G\boldsymbol{\varepsilon}_d^e + K\varepsilon_v^e \boldsymbol{I} \end{aligned} \tag{4.3}$$

where G and K are respectively the shear and bulk moduli, $\boldsymbol{\varepsilon}_d^e$ is the deviatoric component of the elastic strain tensor, $\varepsilon_v^e \equiv tr\left[\boldsymbol{\varepsilon}^e\right]$ is the volumetric elastic strain, and $\boldsymbol{I}$ is the second order identity tensor.

4.1.3 Yield function

In an uniaxial test, the yield stress is nothing but a scalar (figure 4.1). However, in a general three dimensional case, the elastic domain is bounded by a yield surface instead. This surface is defined in the most general case by:

$$\Phi\left(\boldsymbol{\sigma}, \boldsymbol{q}\right) = 0 \tag{4.4}$$

where $\boldsymbol{q}$ represent a set of variables affected by the hardening (or softening) process. This scalar function delimits the region in the stress space where any point inside the surface, $\Phi < 0$, is in the elastic domain and any point on the surface, $\Phi = 0$, corresponds to plastic yielding.

As the hardening variables increase in value (or decrease), so will the yield surface expand (or shrink). This effect is known as isotropic hardening (or softening). In the most general case, the surface can even change its shape or translate in the stress space (kinematic hardening or softening).

4.1.4 Plastic flow and loading/unloading conditions

The dissipative plastic phenomenon is represented by the plastic strain tensor. Other internal variables related with the plastic deformation, the hardening variables, will be defined in the next subsection. The plastic flow rule (to be described in detail in subsection 4.1.6) can generically be defined as:

$$\dot{\boldsymbol{\varepsilon}}^p = \dot{\gamma}\boldsymbol{N}\left(\boldsymbol{\sigma}, \boldsymbol{q}\right) \tag{4.5}$$

where γ is known as the plastic multiplier, and $\boldsymbol{N}$ is the flow tensor which defines the direction of the plastic flow.

The plastic multiplier, along with the yield function, define whether a specific stress state is in the elastic or plastic domains. The plastic domain condition is expressed by the condition:

$$\dot{\gamma}\Phi\left(\boldsymbol{\sigma}, \boldsymbol{q}\right) = 0 \tag{4.6}$$

If the material is in the elastic state ($\Phi < 0$), equation (4.6) forces $\dot{\gamma} = 0$, which according with equation (4.5) forces the plastic strain to remain constant. But if the material is in the plastic state ($\Phi = 0$), then equation (4.6) does not impose any limit on the plastic multiplier. However, we know that γ can not be negative since the direction of the plastic flow is determined by the flow tensor $\boldsymbol{N}$. This leads to yet another condition in plasticity:

$$\dot{\gamma} \geqslant 0 \tag{4.7}$$

In total, there are three conditions known as the Kuhn-Tucker conditions, or simply the loading/unloading conditions, which define the evolution of dissipative plastic phenomena:

$$\Phi \leqslant 0, \qquad \dot{\gamma} \geqslant 0, \qquad \dot{\gamma}\Phi = 0 \tag{4.8}$$

During plastic flow, the yield function must remain equal to zero, i.e. the rate of its change must be zero. This leads to the consistency condition:

$$\dot{\gamma} = 0 \wedge \Phi = 0 \Rightarrow \dot{\Phi} = 0 \tag{4.9}$$

4.1.5 Hardening law

In the most general case, the hardening law is defined by two relations: the definition of the hardening variables, which in general is presented in rate form

$$\dot{\boldsymbol{\alpha}} = \dot{\gamma} \boldsymbol{H} \left(\boldsymbol{\sigma}, \boldsymbol{\alpha} \right) \tag{4.10}$$

where $\boldsymbol{H}$ is the generalised hardening modulus which defines the evolution of the hardening variables, $\boldsymbol{\alpha}$, and the dependency of the $\boldsymbol{q}$ variables in equation (4.4) on the hardening variables:

$$\boldsymbol{q} = k \left(\boldsymbol{\alpha} \right) \tag{4.11}$$

The variables $\boldsymbol{q}$ could be eliminated by substitution of equation (4.11) in equations (4.4) and (4.5). However, these variables often contain a clear physical meaning which helps to better understand and define the complete elastoplastic model.

4.1.6 Plastic flow rule

In the most general case, the flow tensor is defined in terms of a flow potential. Considering that such flow potential exists and is defined by

$$\Psi = \Psi \left(\boldsymbol{\sigma}, \boldsymbol{q} \right) \tag{4.12}$$

the flow tensor, $\boldsymbol{N}$, is obtained as:

$$\boldsymbol{N} = \frac{\partial \Psi}{\partial \boldsymbol{\sigma}} \tag{4.13}$$

For this approach to be valid, the flow potential must be a non-negative convex function of both $\boldsymbol{\sigma}$ and $\boldsymbol{q}$ and zero-valued at the origin. In the case of ductile materials and other pressure-independent materials, it is usual to consider the yield function as the potential function that defines the flow vector. The flow rule obtained this way is called an associative flow rule or normality rule:

$$\dot{\boldsymbol{\varepsilon}}^p = \dot{\gamma} \frac{\partial \Phi}{\partial \boldsymbol{\sigma}} \tag{4.14}$$

In the case of pressure-dependent materials, associative flow rules often yield unrealistic results, and the flow potential must be replaced by a more general one, different from the yield function. The flow rules obtained in this way are called non-associative and are generally described by

$$\dot{\boldsymbol{\varepsilon}}^p = \dot{\gamma}\frac{\partial g}{\partial \boldsymbol{\sigma}} \tag{4.15}$$

where g is the new flow potential.

4.1.7 Plastic multiplier

If plastic flow occurs ($\dot{\gamma} \neq 0$), then the plastic multiplier can be determined from the consistency condition in equation (4.9), since

$$\dot{\Phi} = 0 \tag{4.16}$$

By applying the chain rule, one can rewrite this condition:

$$\dot{\Phi} = \frac{\partial \Phi}{\partial \boldsymbol{\sigma}} : \dot{\boldsymbol{\sigma}} + \frac{\partial \Phi}{\partial \boldsymbol{q}} \cdot \dot{\boldsymbol{q}} = 0 \tag{4.17}$$

Combining the concepts of strain decomposition, plastic flow rule, and the elastic stress-strain law in rate form, the following equation is derived:

$$\dot{\boldsymbol{\sigma}} = \boldsymbol{D}^e : (\dot{\boldsymbol{\varepsilon}} - \dot{\gamma}\boldsymbol{N}) \tag{4.18}$$

Differentiating equation (4.11) and using equation (4.10):

$$\dot{\boldsymbol{q}} = \frac{\partial k}{\partial \boldsymbol{\alpha}} \cdot \dot{\boldsymbol{\alpha}} = \dot{\gamma}\frac{\partial k}{\partial \boldsymbol{\alpha}} \cdot \boldsymbol{H} \tag{4.19}$$

Substituting equations (4.18) and (4.19) into equation (4.17), a general equation for $\dot{\gamma}$ is obtained as:

$$\dot{\gamma} = \frac{\dfrac{\partial \Phi}{\partial \boldsymbol{\sigma}} : \boldsymbol{D}^e : \dot{\boldsymbol{\varepsilon}}}{\dfrac{\partial \Phi}{\partial \boldsymbol{\sigma}} : \boldsymbol{D}^e : \boldsymbol{N} - \dfrac{\partial \Phi}{\partial \boldsymbol{q}} \cdot \dfrac{\partial k}{\partial \boldsymbol{\alpha}} \cdot \boldsymbol{H}} \tag{4.20}$$

4.1.8 Elastoplastic tangent operator

Under plastic flow, especially if hardening is present, the slope of the uniaxial stress-strain curve varies as loading progresses. The tangent relation between stress and strain can be defined, in rate form, by

$$\dot{\sigma} = E^{ep}\dot{\varepsilon} \tag{4.21}$$

where E^{ep} is the elastoplastic tangent modulus. Generalising to the three dimensional case, the rate constitutive equation for stress is

$$\dot{\boldsymbol{\sigma}} = \boldsymbol{D}^{ep} : \dot{\boldsymbol{\varepsilon}} \tag{4.22}$$

where $\boldsymbol{D}^{ep}$ is a fourth-order tensor known as the elastoplastic tangent operator. By substituting the plastic multiplier defined in equation (4.20) into equation (4.18) and rearranging terms, the most general form of the elastoplastic tangent operator is defined by

$$\boldsymbol{D}^{ep} = \boldsymbol{D}^{e} - \frac{\boldsymbol{D}^{e} : \boldsymbol{N} \otimes \boldsymbol{D}^{e} : \partial\Phi/\partial\boldsymbol{\sigma}}{\partial\Phi/\partial\boldsymbol{\sigma} : \boldsymbol{D}^{e} : \boldsymbol{N} - \partial\Phi/\partial\boldsymbol{q} \cdot \partial k/\partial\boldsymbol{\alpha} \cdot \boldsymbol{H}} \tag{4.23}$$

The elastoplastic tangent operator is, in general, non-symmetric except for the particular case of associative flow rules.

For the sake of simplicity, we summarise here the basic equations of a general elastoplastic constitutive model:

1. Additive decomposition of the strain tensor
$$\boldsymbol{\varepsilon} = \boldsymbol{\varepsilon}^{e} + \boldsymbol{\varepsilon}^{p}$$
2. Elastic constitutive law
$$\boldsymbol{\sigma} = 2G\boldsymbol{\varepsilon}_d^{e} + K\varepsilon_v^{e}\boldsymbol{I}$$
3. Yield function
$$\Phi = \Phi\left(\boldsymbol{\sigma}, \boldsymbol{q}\right)$$
4. Plastic flow rule and hardening law
$$\dot{\boldsymbol{\varepsilon}}^{p} = \dot{\gamma}\boldsymbol{N}\left(\boldsymbol{\sigma}, \boldsymbol{q}\right) \qquad \dot{\boldsymbol{\alpha}} = \dot{\gamma}\boldsymbol{H}\left(\boldsymbol{\sigma}, \boldsymbol{\alpha}\right)$$
5. Kuhn-Tucker conditions
$$\Phi \leqslant 0, \qquad \dot{\gamma} \geqslant 0, \qquad \dot{\gamma}\Phi = 0$$

4.2 Computational plasticity

This section describes the required steps to implement the previously discussed plasticity theory in an implicit displacement-driven finite element solution.

When implementing the mathematical theory of plasticity in a numerical form, it is required to provide the following information:

- Stress return algorithm - if the stress state is known for a given moment t_n, we can fully determine the stress tensor at an instant t_{n+1}, upon definition of a strain increment. In other words, the stresses at the end of a strain increment are calculated based on the stresses, strains, and hardening variables at the beginning of the increment.

- Consistent tangent modulus - whenever the solution of the non-linear finite element equilibrium equations require the computation of a new tangent stiffness matrix.

Starting with the additive decomposition of the strain tensor and the elastic law, we derive the following equation:

$$\left.\begin{array}{c}\boldsymbol{\varepsilon} = \boldsymbol{\varepsilon}^e + \boldsymbol{\varepsilon}^p \\ \boldsymbol{\sigma} = \boldsymbol{D}^e : \boldsymbol{\varepsilon}^e\end{array}\right\} \Longrightarrow \boldsymbol{\sigma} = \boldsymbol{D}^e : (\boldsymbol{\varepsilon} - \boldsymbol{\varepsilon}^p) \tag{4.24}$$

Rewriting equation (4.24) at the end of the increment, t_{n+1}:

$$\boldsymbol{\sigma}_{n+1} = \boldsymbol{D}^e : \left(\boldsymbol{\varepsilon}_{n+1} - \boldsymbol{\varepsilon}^p_{n+1}\right) \tag{4.25}$$

Considering now the discretised form of the flow rule in equation (4.5):

$$\boldsymbol{\varepsilon}^p_{n+1} - \boldsymbol{\varepsilon}^p_n = (\gamma_{n+1} - \gamma_n)\, \boldsymbol{N}_{n+1} \tag{4.26}$$

Notice that the flow direction given by tensor $\boldsymbol{N}$ is determined at the end of the increment, t_{n+1}, which means that the backward Euler scheme is being used. Applying this same method to the loading/unloading conditions (4.8):

$$\begin{aligned} \Phi\left(\boldsymbol{\sigma}_{n+1}, \boldsymbol{q}_{n+1}\right) &\leqslant 0 \\ \gamma_{n+1} - \gamma_n &\geqslant 0 \\ (\gamma_{n+1} - \gamma_n) \cdot \Phi\left(\boldsymbol{\sigma}_{n+1}, \boldsymbol{q}_{n+1}\right) &= 0 \end{aligned} \tag{4.27}$$

The given strain increment can be decomposed in an elastic and a plastic component, and the following relation allows to determine the plastic strain at the end of the time increment, t_{n+1}:

$$\boldsymbol{\varepsilon}^p_{n+1} = \boldsymbol{\varepsilon}^p_n + \Delta\boldsymbol{\varepsilon} - \Delta\boldsymbol{\varepsilon}^e \tag{4.28}$$

According to the loading/unloading conditions in equations (4.27), one of two scenarios can take place when the strain increment is applied:

- The increment of the plastic multiplier, $\Delta\gamma$ is null, which means that there is no plastic flow in the time interval $[t_n, t_{n+1}]$. The stress tensor is given by:
$$\boldsymbol{\sigma}_{n+1} = \boldsymbol{D}^e : (\boldsymbol{\varepsilon}_n + \Delta\boldsymbol{\varepsilon} - \boldsymbol{\varepsilon}^p_n) \tag{4.29}$$
- The increment of the plastic multiplier is positive, which implies from the loading/unloading constraints that:
$$\Phi\left(\boldsymbol{\sigma}_{n+1}, \boldsymbol{q}_{n+1}\right) = 0 \tag{4.30}$$
Recalling that $\boldsymbol{\varepsilon}^e_{n+1} = \boldsymbol{\varepsilon}^e_n + \Delta\boldsymbol{\varepsilon} - \Delta\boldsymbol{\varepsilon}^p$, and replacing in the elastic law, and making use of the definition of flow rule in equation (4.5), the following relation for determining the stress tensor is derived:
$$\boldsymbol{\sigma}_{n+1} = \boldsymbol{D}^e : (\boldsymbol{\varepsilon}^e_n + \Delta\boldsymbol{\varepsilon}) - (\gamma_{n+1} - \gamma_n)\, \boldsymbol{D}^e : \boldsymbol{N}_{n+1} \tag{4.31}$$
Combining equations (4.30) and (4.31) and solving them for $\boldsymbol{\sigma}_{n+1}$ and γ_{n+1}, one obtains the final solution to the elastoplastic problem when there is plastic flow.

Although presented separately, the two possibilities mentioned above can be implemented into one single algorithm. This procedure is called the elastic predictor/plastic corrector algorithm and derives from equation (4.31). The first term on the second member of equation (4.31) is the elastic predictor, i.e. the stresses at the end of the increment are estimated assuming the step to be elastic. The second term represents the plastic corrector, which is null if the step is elastic and greater than zero if there is plastic flow in the step, thus correcting the initial elastic estimate.

In order to determine the plastic corrector, the following set of equations must be solved, in a process known as return mapping scheme:

$$\begin{aligned}
\Delta\boldsymbol{\varepsilon}^p &= \Delta\gamma \boldsymbol{N}\left(\boldsymbol{\sigma}_{n+1}, \boldsymbol{q}_{n+1}\right) \\
\Delta\boldsymbol{\alpha} &= \Delta\gamma \boldsymbol{H}\left(\boldsymbol{\sigma}_{n+1}, \boldsymbol{\alpha}_{n+1}\right) \\
\boldsymbol{\sigma}_{n+1} &= \boldsymbol{\sigma}_{n+1}^{tr} - \boldsymbol{D}^e : \Delta\boldsymbol{\varepsilon}^p \\
\Phi\left(\boldsymbol{\sigma}_{n+1}, \boldsymbol{q}_{n+1}\right) &= 0 \\
\boldsymbol{q}_{n+1} &= k\left(\boldsymbol{\alpha}_{n+1}\right)
\end{aligned} \tag{4.32}$$

where σ_{n+1}^{tr} corresponds to the elastic predictor above mentioned. The return mapping scheme can be better understood with the help of figure 4.2.

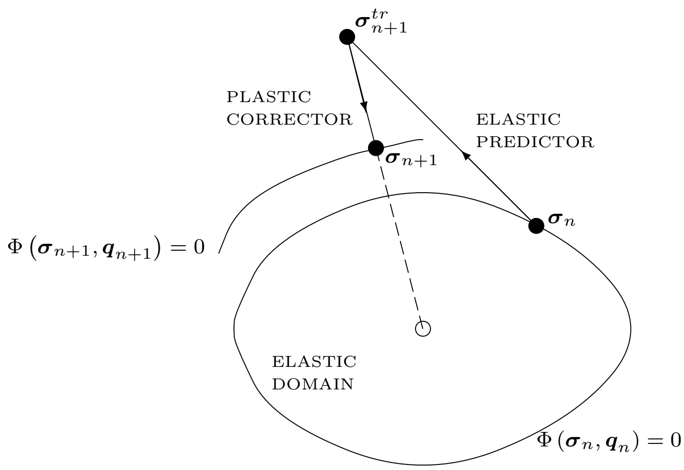

Figure 4.2: Return mapping scheme.

Starting at point $\boldsymbol{\sigma}_n$, which lies on the yield surface $\Phi\left(\boldsymbol{\sigma}_n, \boldsymbol{q}_n\right)$, a given strain increment is applied to the material. First, an elastic trial step is performed, leading to the result marked with point $\boldsymbol{\sigma}_{n+1}^{tr}$. This is the elastic predictor mentioned before. This result must satisfy the consistency condition, i.e. the point must be positioned on the yield surface, $\Phi\left(\boldsymbol{\sigma}_{n+1}, \boldsymbol{q}_{n+1}\right) = 0$. If the point is inside this surface, the trial stress, $\boldsymbol{\sigma}_{n+1}^{tr}$, is accepted as the solution to the problem and the increment is considered elastic. However, as represented in figure 4.2, if the point lies outside the yield surface, it is necessary to *return* it to the surface. If there was no hardening, the return would take place to the same yield surface; if hardening takes place, then the new surface will be different from the initial.

There are multiple algorithms to perform the return to the yield surface. The one used on this thesis and represented in figure 4.2 is the *radial return* *algorithm*. Radial, because the return is processed perpendicular to the flow potential Ψ (not represented in figure 4.2). In the particular case of an associative flow rule, the yield surface is the same as the flow potential, which means that the return will take place in a perpendicular direction to the yield surface, and the final point $\boldsymbol{\sigma}_{n+1}$, is also the closest point of the new yield surface to the trial stress point. This method is called the *closest-point projection*.

As can be seen in equations (4.32), the algebraic system of equations that needs to be solved in order to determine the increment of the plastic multiplier, $\Delta\gamma$, is generally non-linear. In order to circumvent this problem, the standard Newton-Raphson scheme is often an optimal choice and will be adopted throughout this thesis. This scheme provides a quadratic rate of convergence, thus increasing the computational efficiency of the material model implementations.

However, the Newton-Raphson method still depends on the first guess for the variable to be determined, and care should be taken regarding this. One other disadvantage of the Newton-Raphson is that it requires the exact definition of the associated residual functions. Especially in complex material models, these can become a tedious endeavour if performed manually. Albeit difficult to obtain by hand, computer software such as MATLAB® [29] or Maxima [63] allow for a quick and painless deduction of those residual functions thanks to their capabilities for symbolic calculus.

Determining the residual functions for the Newton-Raphson scheme applied to the return mapping algorithm also proves to be very useful from one other point of view: if the full Newton-Raphson iterative scheme is going to be used in the global finite element analysis, and not just in the return mapping algorithm, the derivatives are still needed to compute the consistent tangent operator, used to assemble the global tangent stiffness matrix.

There are other methods to implement the return mapping algorithm, such as the generalised trapezoidal or midpoint rules, or the generalised cutting plane algorithm which is a purely explicit method, not requiring the solution of any system of equations, but those were not used in this thesis and are thus out of the scope of the present review.

4.3 Plastic response of epoxy polymers

In order to properly define the constitutive model which will represent the mechanical behaviour of an epoxy matrix in long-fibre composite materials, a review over the most relevant findings in the literature regarding this class of materials is performed. Most of the data collected and presented in this section originates from experimental work on different types of epoxy polymers with application to composite materials.

Polymers in general are known to exhibit rate- and temperature-dependent behaviour with non-linear responses during loading and unloading. A significant permanent deformation is also observed, even at small deformation levels. In the current work, rate and temperature effects will not be considered, and focus will be given to the non-linear response and small-strain deformation.

Asp et al. [64] developed an interesting experimental set-up which allows to simulate the triaxial stress state experienced by the matrix when in a composite loaded in the transverse direction. This triaxial stress state happens due to the random distribution of fibres in the transverse cross-section which create a non-uniform stress state around the fibres, i.e. in the matrix. The experimental set-up consisted in using the poker-chip test concept and applying it to glassy epoxies. Four different epoxy systems were chosen: the epoxy component was the same for three systems (DGEBA), but the curing agents different (DETA, MHPA, APTA); the fourth system is an aromatic epoxy, TGDDM, cured with DDS.

Under uniaxial tests, all epoxies but the aromatic based TGDDM present highly non-linear behaviour. The aromatic epoxy TGDDM actually presents brittle failure at low strain. For the poker-chip configuration, all four systems presented linear stress/strain relationship until failure.

In a subsequent work, Asp et al. [65] conducted more experimental work in the same epoxy systems. Biaxial tension, uniaxial compression and plane strain compression demonstrated the sensitive behaviour of polymers to hydrostatic pressure, i.e. different yield strengths in tension and compression. It also showed that under all these test conditions the material behaviour for all epoxy systems tested is non-linear, and each system has a different yield behaviour. Assuming that the level of distortional energy density is low under the above mentioned loading schemes, Asp et al. proposed the use of the dilatational energy density criterion to predict failure of polymers under multiaxial tensile loads. However, the criterion is not completely general as it can not predict the material's behaviour under more complex stress-states such as the combined effect of shear and normal stresses.

Duncan et al. [66] conducted an experimental investigation to obtain material data for the numerical methods that predict the performance of adhesive bonded joints under impact loading. Although polymers present dependency on hydrostatic pressure, thus ensuing different yield strengths in tension and compression, Duncan and colleagues characterized the yield behaviour using tensile and pure shear experimental data. This was motivated by the difficulty in conducting compressive tests on epoxy materials. It was found that there is a strong influence of the strain rate on the yield behaviour of epoxy adhesives. The higher the strain rate, the higher the yield stress and Young's modulus.

Duncan et al. [66] and Charalambides and Dean [67] also introduced the concept of *plastic Poisson's ratio*. It is defined as the symmetric of the ratio between the plastic transverse strain and the plastic longitudinal strain in an uniaxial tensile test. In the Von Mises yield criterion, for example, this quantity is equal to 0.5, i.e. plastic deformation is assumed to take place without change of volume. However, in the most general case, the plastic Poisson's ratio varies as hardening progresses. Duncan et al. [66] showed that the plastic Poisson's ratio can vary between 0.5 and 0.3, thus indicating that the volume increases during yielding. However, as hardening increases, the plastic Poisson's ratio tends to converge to a value of 0.3, and this convergence is quite rapid. Taking this in consideration, Guild and colleagues [68] considered that the plastic Poisson's ratio is constant and equal to 0.32 for the numerical simulation of an epoxy adhesive behaviour in a bonded double-lap joint. Duncan et al. [66] also determined that the ratio of the yield compressive stress to the yield tensile stress is independent of the strain rate.

Charalambides et al. [69] studied the mechanical behaviour of adhesively-bonded repairs to fibre composite materials. Tensile and shear tests were conducted in order to fully characterise the mechanical behaviour of the adhesive. It was found that for both tests the epoxy adhesive has a non-linear behaviour. The shear test in particular provides an interesting result. While under tension the epoxy hardens until failure, under shear the hardening stops at one point and the epoxy behaves as a perfectly plastic material.

Fiedler et al. [70] conducted a more vast study on the behaviour of epoxy materials by performing tensile, compressive and shear tests to fully characterise the yield and failure behaviour of epoxies used in composites. Figures 4.3 to 4.5 show the main results obtained by Fiedler et al. [70].

For the tensile tests, two types of dog-bone shaped specimens were used with different thicknesses. The thinner specimens provide a more accurate simulation of a plane strain test as the ratio of surface to volume is smaller. This favours the deformation and the reduction of cross-section during elon-

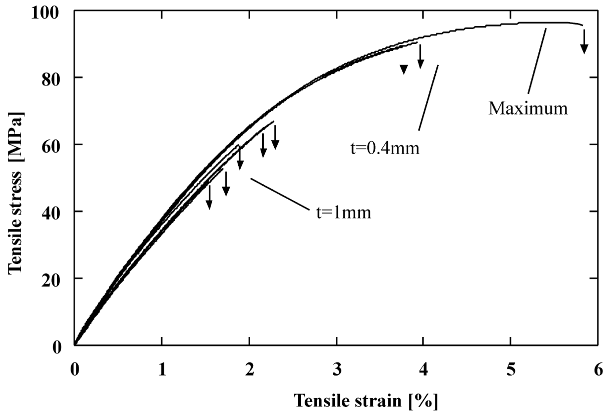

Figure 4.3: Results of tensile tests by Fiedler et al. [70].

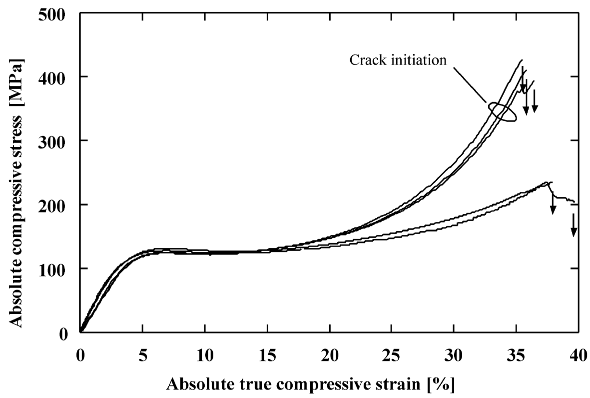

Figure 4.4: Results of compression tests by Fiedler et al. [70].

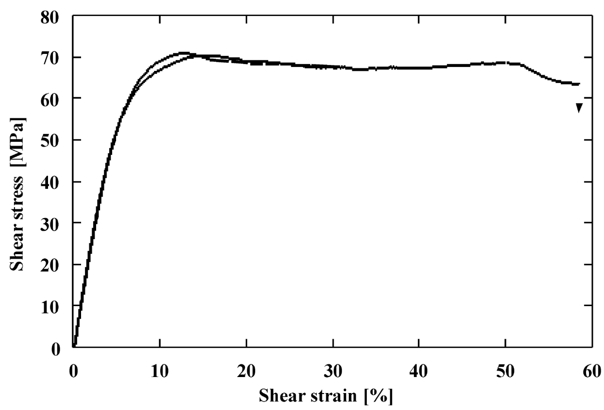

Figure 4.5: Results of torsion tests by Fiedler et al. [70].

gation. The results (figure 4.3) show the non-linearity of these specimens under such loading conditions, while the thicker specimens behave in a brittle manner.

The compressive tests were also conducted on two different specimens, both cubes but with different volumes. The larger specimens achieved lower maximum stress in figure 4.4. The curious aspect is that the cracks that appeared in the specimen are parallel to the loading direction. This took place for both sizes, although in the case of the larger specimens, the cracks were contained in the centre of the cube, mostly due to the barrel effect typical of this experimental procedure. The yielding process is similar for both geometries for small strains, but as the strains increase, the small specimens suffer a much stronger hardening. This was caused by undeformed regions at the top and bottom of the specimen, in the areas close to the test rig, with multi-axial stress states. The higher probability of defects in the larger volume also plays a role in the lower stress values achieved.

The torsion test provided interesting results as some of the specimens did not fail at all as the material revealed a high ductile capacity under a pure shear load. Upon a small non-linear behaviour with hardening for lower strains, the material behaved as an elastic-perfectly-plastic material. Despite the shown ductility, the final type of failure was that of a brittle material, along a plane inclined 45° with the plane of maximum shear stress.

Table 4.1 summarises the mechanical properties measured from the three tests performed. Table 4.2 presents the points that can be extracted from the plots in figures 4.3 and 4.4 which define the hardening behaviour of the epoxy matrix under tension and compression, respectively.

Table 4.1: Mechanical properties measured by Fiedler et al. [70].

Tension test		
	t=1 mm	t=0.4 mm
E(GPa)	3.9	3.9
$\sigma_{0.05}$ (MPa)	29	29
σ_S (MPa)	59 ± 8	93 ± 3
ε_S (%)	2 ± 0.3	4.9 ± 0.6
Compression test		
	V=1 cm^3	V=0.125 cm^3
E (GPa)	3.6	3.6
$\sigma_{0.05}$ (MPa)	-67	-67
σ_S (MPa)	-135 ± 1	-117 ± 1
ε_S (%)	-7 ± 1	-6.7 ± 0.4

Fiedler et al. [70]–[72] concluded that the best yield criterion to repre-

Table 4.2: Hardening data measured by Fiedler et al. [70].

Tension		Compression	
ε_p^e (%)	σ_T (MPa)	ε_p^e (%)	σ_C (MPa)
0.00	29.0	0.00	67.0
0.03	37.0	0.17	80.0
0.06	45.0	0.59	105.0
0.13	52.0	1.47	120.0
0.19	58.5	2.50	125.0
0.30	65.0	3.75	125.0
0.39	70.0	5.00	125.0
0.53	74.0	6.25	125.0
0.69	78.0	7.50	125.0
0.85	81.5	8.75	125.0
1.02	84.5	10.00	125.0
1.20	87.0		
1.41	89.0		
1.62	91.0		
1.82	92.5		
2.04	93.5		
2.27	94.5		
2.50	95.0		

sent the yield behaviour up to and including failure of epoxy materials is the paraboloidal criterion, represented in figure 4.6 in the octahedral stress plane. The white circles represent the yield stresses from the three experimental tests, while the black circles represent the failure stresses.

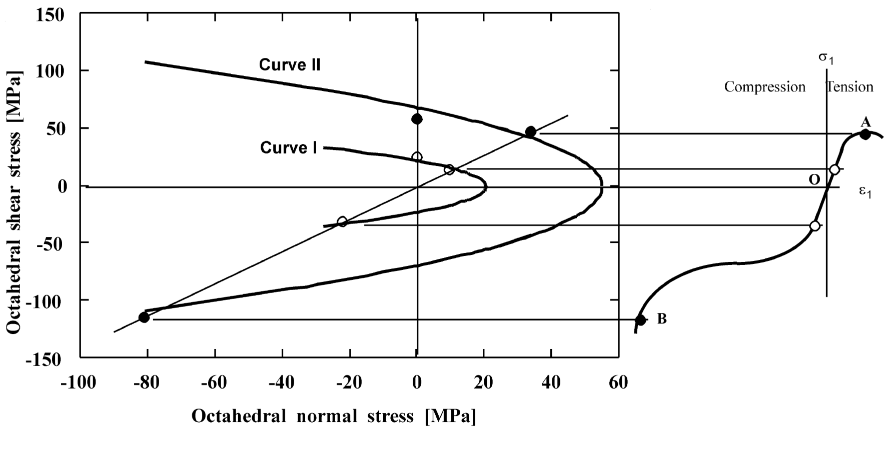

Figure 4.6: Paraboloidal criterion with experimental data by Fiedler et al. [70].

Ghorbel [73] conducted a comparative study of different yield criteria with experimental results for different polymers. It was concluded that there was no scattering of the experimental data provided by different authors and that between the standard Drucker-Prager and a paraboloidal variant, the latter provided better estimates for yield strengths, especially for high values of hydrostatic pressure.

With the above experimental results, one can conclude that a good yield criterion for epoxy polymers must have the following characteristics:

- Pressure dependency - the yield criterion must account for any dependency of yielding on the hydrostatic component of the applied stress state.
- Different yield strengths - epoxy polymers present a greater yield strength in compression than in tension. The ratio of these strengths is independent of temperature and strain rate.
- Strain rate - increasing strain rates lead to greater yield strengths and greater Young's modulus.

Other authors present the same conclusions when searching for a good yield criterion. Mascarenhas et al. [74] consider that both conic and parabolic criteria are best suited for the yield behaviour of polymers. The above mentioned work of Charalambides et al. [69] was followed by a numerical implementation and comparison with the obtained experimental results. Charalambides et al. [75] considered that in order to accurately simulate the epoxy adhesive yield behaviour, a paraboloidal yield criterion should be used.

This paraboloidal yield criterion was first defined by Tschoegl [76]. In the principal stress space, it is represented by a paraboloid whose axis coincides with the hydrostatic axis. A cylindrical surface corresponds to the Von Mises yield criterion and an hexagonal prism represents the Tresca criterion, both applicable to materials whose plastic flow is independent of hydrostatic pressure such as some metals. An hexagonal pyramid is a modified version of the Tresca criterion and represents the Mohr-Coulomb yield criterion. A modified Von Mises gives origin to the Drucker-Prager criterion represented by a conical surface. A quadratic modified version of the Von Mises criterion leads to the paraboloidal criterion, as it is represented in figure 4.7.

In his contribution, Tschoegl [76] considers failure in the broadest sense possible, including yield, fracture, etc. In that sense, figure 4.7 represents the yield (inner) surface, and the failure (outer) surface. This surface is particularly attractive because, unlike Tresca, Drucker-Prager or Mohr-Coulomb,

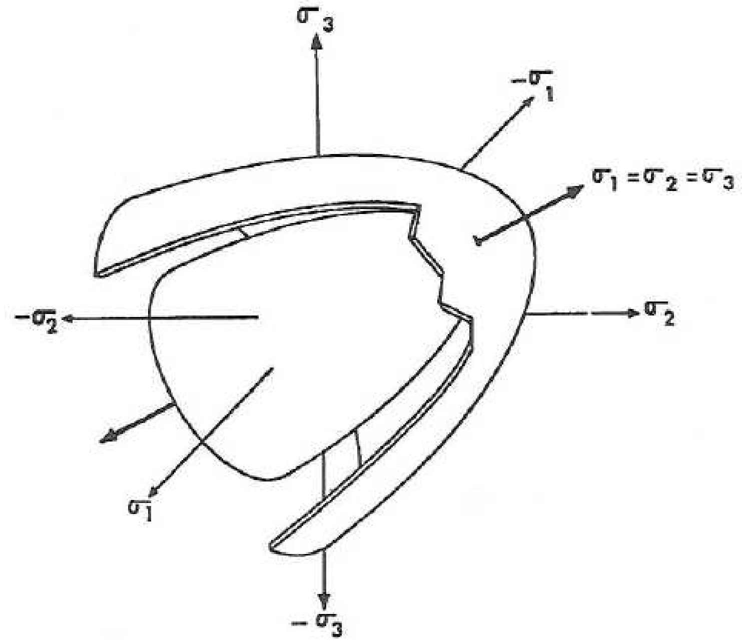

Figure 4.7: Paraboloidal yield surface (from [76]).

it does not contain any geometrical features such edges or vertices. This makes the surface differentiable in all of its domain, simplifying the process of implementation into a constitutive model.

Mathematically, the paraboloidal yield criterion is defined by

$$6J_2 + 2I_1 (\sigma_c - \sigma_t) - 2\sigma_c\sigma_t = 0 \tag{4.33}$$

where J_2 is the second invariant of the deviatoric stress tensor, I_1 is the first invariant of the stress tensor, and σ_c and σ_t are the compressive and tensile yield strengths, respectively. It can be seen that this criterion respects the above mentioned dependency on the hydrostatic pressure and different yield strengths. In the limit case that the yield strengths are equal, equation (4.33) reverts to the original Von Mises criterion.

Raghava et al. [77] were probably the first to use this criterion to study the yield behaviour of polymers. They concluded that if the ratio of compressive to tensile strengths is greater than 1.5, then the paraboloidal criterion yields better estimates than the Drucker-Prager criterion.

4.4 Elasto-plastic model for epoxy resins

After presenting the general characteristics of the yield behaviour of epoxy resins, an elasto-plastic constitutive model based on the paraboloidal yield criterion will be developed. The resulting model is implemented in an UMAT subroutine for inclusion in ABAQUS® [30] analyses. This subroutine can be found in appendix C. First, a quick survey on the mathematical theory behind yield surfaces is presented.

4.4.1 Yield surface formulation

Assuming an initial isotropic behaviour for the polymer, the most general quadratic yield surface can be written as [78]

$$\Phi = \boldsymbol{\sigma}^T \boldsymbol{F} \boldsymbol{\sigma} + \boldsymbol{B} \boldsymbol{\sigma} + F_0 \leqslant 0 \tag{4.34}$$

where $\boldsymbol{F}$ and $\boldsymbol{B}$ are second order tensors defined as (in Voigt notation):

$$\boldsymbol{F} = \begin{bmatrix} F_{11} & F_{12} & F_{12} & 0 & 0 & 0 \\ F_{12} & F_{11} & F_{12} & 0 & 0 & 0 \\ F_{12} & F_{12} & F_{11} & 0 & 0 & 0 \\ 0 & 0 & 0 & F_{44} & 0 & 0 \\ 0 & 0 & 0 & 0 & F_{44} & 0 \\ 0 & 0 & 0 & 0 & 0 & F_{44} \end{bmatrix} \quad \boldsymbol{B} = \begin{bmatrix} F_1 & 0 & 0 & 0 & 0 & 0 \\ 0 & F_1 & 0 & 0 & 0 & 0 \\ 0 & 0 & F_1 & 0 & 0 & 0 \\ 0 & 0 & 0 & 0 & 0 & 0 \\ 0 & 0 & 0 & 0 & 0 & 0 \\ 0 & 0 & 0 & 0 & 0 & 0 \end{bmatrix} \tag{4.35}$$

and $\boldsymbol{\sigma}$ is the stress tensor. A number of restrictions apply to the coefficients above derived from the definition of a yield surface. There must exist a stress-free state inside the yield surface, which leads to

$$F_0 \leqslant 0 \tag{4.36}$$

The equivalence of pure shear and biaxial tension/compression require the following relation to be satisfied

$$F_{44} = 2\left(F_{11} - F_{12}\right) \tag{4.37}$$

resulting in only four independent coefficients in equation (4.34). Without any loss of generality, the coefficients can be multiplied by a constant, thus reducing to only three independent coefficients in equation (4.34). The general equation for the yield surface can also be rewritten in terms of the hydrostatic pressure (p) and Von Mises stress (σ_{vm}) invariants:

$$\Phi = \sigma_{\mathrm{vm}}^2 - A_0 - A_1 p - A_2 p^2 \leqslant 0 \tag{4.38}$$

The A_i coefficients relate to the F_i coefficients of equation (4.34) by:

$$A_0 = -F_0,\ A_1 = 3F_1,\ A_2 = 9\,(1 - F_{11}) \tag{4.39}$$

The three independent coefficients, A_0, A_1, and A_2 can be determined from three uniaxial experiments: tension, compression and shear. From the three tests, three yield strengths are obtained, one for each test: σ_t, σ_c, and σ_s. Their relations with the coefficients in equation (4.38) can be demonstrated to be [79]:

$$A_0 = 3\sigma_s^2,\ A_1 = 9\sigma_s^2\left(\frac{\sigma_c - \sigma_t}{\sigma_c\sigma_t}\right),\ A_2 = 9\left(\frac{\sigma_c\sigma_t - 3\sigma_s^2}{\sigma_c\sigma_t}\right) \tag{4.40}$$

The yield function of an elastoplastic material must satisfy the convexity condition as well. A sufficient condition [78] for function Φ to be convex is that matrix $\boldsymbol{F}$ must be positive semi-definite. This condition is satisfied if the eigenvalues of $\boldsymbol{F}$ are all non-negative. There are three independent eigenvalues:

$$\begin{cases} F_{11} + 2F_{12} \geqslant 0 \\ F_{11} - F_{12} \geqslant 0 \\ F_{44} \geqslant 0 \end{cases} \tag{4.41}$$

Using relations (4.39) and (4.40), the final necessary and sufficient condition to satisfy convexity of the yield surface is achieved:

$$\sigma_s \geqslant \sqrt{\frac{\sigma_c\sigma_t}{3}} \tag{4.42}$$

Following from section 4.3, only two yield strengths are used to define the paraboloidal yield criterion. Considering only the tensile and compressive yield strengths, the coefficient A_2 in equation (4.38) is set to zero, forcing the equality in the convexity condition (4.42). Coefficients A_0 and A_1 are then redefined

$$A_0 = \sigma_c \sigma_t \,, \quad A_1 = 3\,(\sigma_c - \sigma_t) \tag{4.43}$$

thus resulting in the final definition of the paraboloidal yield criterion:

$$\Phi = 6J_2 + 2\,(\sigma_c - \sigma_t)\,I_1 - 2\sigma_c\sigma_t = 0 \tag{4.44}$$

4.4.2 Flow rule

Associative flow rule

As discussed in section 4.1, an associative flow rule leads to a flow vector that is normal to the yield surface. The flow tensor, $\boldsymbol{N}$, is defined by the derivative of the yield function to the stress tensor:

$$\boldsymbol{N} = 6\boldsymbol{S} + 2\,(\sigma_c - \sigma_t)\,\boldsymbol{I} \tag{4.45}$$

where $\boldsymbol{S}$ is the deviatoric stress tensor, and $\boldsymbol{I}$ is the second order identity tensor. A flow rule based on this flow tensor does not provide any control over the volumetric plastic straining. This leads to uncontrollable and sometimes even physically nonsensical values of the plastic Poisson's ratio. For example, under hydrostatic pressure, the stress tensor and corresponding deviatoric stress tensor are given by:

$$\boldsymbol{\sigma} = \begin{bmatrix} -\sigma & 0 & 0 \\ 0 & -\sigma & 0 \\ 0 & 0 & -\sigma \end{bmatrix} , \quad \boldsymbol{S} = \begin{bmatrix} 0 & 0 & 0 \\ 0 & 0 & 0 \\ 0 & 0 & 0 \end{bmatrix} \tag{4.46}$$

The flow rule would then be defined by:

$$\Delta\boldsymbol{\varepsilon}^p = 2\Delta\gamma\,(\sigma_c - \sigma_t)\,\boldsymbol{I} \tag{4.47}$$

Since the compressive yield strength is always greater than the tensile yield strength, and from the loading/unloading conditions in equations (4.8) the parameter $\Delta\gamma$ is positive, the increment of plastic strain in any direction is always positive. This leads to a positive volumetric plastic strain, even though the material is under hydrostatic pressure. In order to provide a better accountability for the plastic Poisson's ratio and the volumetric plastic straining, it is decided to use a non-associative flow rule.

Non-associative flow rule

Following the work of Rolfes et al. [80], Kolling et al. [79] and Zhang et al. [81], the following non-associative flow potential is used:

$$g = \sigma_{\mathrm{vm}}^2 + \alpha p^2 \tag{4.48}$$

where α is a parameter that controls the plastic volumetric flow. Its relation with the plastic Poisson's ratio will be deduced next. Using the flow potential defined in equation (4.48), the flow rule is defined by:

$$\Delta \boldsymbol{\varepsilon}^p = \Delta\gamma \frac{\partial g}{\partial \boldsymbol{\sigma}} = \Delta\gamma \left[2\sigma_{\mathrm{vm}} \frac{\partial \sigma_{\mathrm{vm}}}{\partial \boldsymbol{\sigma}} + 2\alpha p \frac{\partial p}{\partial \boldsymbol{\sigma}} \right] = \Delta\gamma \left[3\boldsymbol{S} + \frac{2}{3}\alpha p \boldsymbol{I} \right] \tag{4.49}$$

Under an uniaxial tensile load along the longitudinal direction, the deviatoric stress tensor is defined by:

$$\boldsymbol{S} = \begin{bmatrix} 2p & 0 & 0 \\ 0 & -p & 0 \\ 0 & 0 & -p \end{bmatrix} \tag{4.50}$$

Substituting in equation (4.49):

$$\Delta \boldsymbol{\varepsilon} = \Delta\gamma \frac{p}{3} \begin{bmatrix} 18 + 2\alpha & 0 & 0 \\ 0 & 2\alpha - 9 & 0 \\ 0 & 0 & 2\alpha - 9 \end{bmatrix} \tag{4.51}$$

From equation (4.51), the volumetric and longitudinal plastic strains are given by:

$$\Delta\varepsilon_{\mathrm{v}}^p = 2\Delta\gamma p \alpha \, , \quad \Delta\varepsilon_1^p = \Delta\gamma \frac{p}{3} \left(18 + 2\alpha\right) \tag{4.52}$$

In a uniaxial tension test, the transverse plastic strain is defined by:

$$\Delta\varepsilon_{22}^p = \Delta\varepsilon_{33}^p = -\nu_p \Delta\varepsilon_{11}^p \tag{4.53}$$

where ν_p is the plastic Poisson's ratio. Using equation (4.53), the volumetric plastic strain can also be defined by:

$$\Delta\varepsilon_{\mathrm{v}}^{p} = (1 - 2\nu_p)\, \Delta\varepsilon_{11}^{p} \tag{4.54}$$

Replacing equations (4.52) into equation (4.54), a relation between the parameter α and the plastic Poisson's ratio is obtained:

$$\begin{aligned} 2\Delta\gamma p\alpha = (1 - 2\nu_p)\, \Delta\gamma\frac{p}{3}\, (18 + 2\alpha) \Leftrightarrow \\ \Leftrightarrow 3\alpha = (1 - 2\nu_p)\, (9 + \alpha) \Leftrightarrow \\ \alpha = \frac{9}{2}\frac{1 - 2\nu_p}{1 + \nu_p} \end{aligned} \tag{4.55}$$

If the parameter ν_p is determined from a standard tension test, the material parameter α is fully defined. Notice that, if this flow potential was to be applied to a metal, the plastic Poisson's ratio would be equal to 0.5, and the parameter α would be null, thus reaching the standard Von Mises flow potential. Recall that the same happened with the yield surface definition. The flow rule is now fully characterised and the increment of plastic strain can now be defined, in tensorial notation:

$$\begin{aligned} \Delta\boldsymbol{\varepsilon}^{p} &= \Delta\gamma\boldsymbol{N} = \Delta\gamma\frac{\partial g}{\partial\boldsymbol{\sigma}} \\ &= \Delta\gamma\left(3\boldsymbol{S} + \frac{2}{9}\alpha I_1\boldsymbol{I}\right) \end{aligned} \tag{4.56}$$

The increment of plastic deformation can be decomposed in its deviatoric and volumetric components:

$$\Delta\boldsymbol{\varepsilon}_{d}^{p} = \Delta\gamma\boldsymbol{N}_d = 3\Delta\gamma\boldsymbol{S}\,, \qquad \Delta\varepsilon_{v}^{p} = \Delta\gamma N_v = \frac{2}{3}\Delta\gamma\alpha I_1 \tag{4.57}$$

As can be seen from the above equations, the flow tensor is not dimensionless. This is due to the quadratic nature of the flow potential. This forces a slight modification to the definition of the plastic multiplier as it is normally used. In this case, the plastic multiplier has the dimension of $\left[\mathrm{MPa}^{-1}\right]$. This situation is acceptable since the plastic multiplier functions only as a scaling quantity which affects the length of the flow tensor, which by its turn, is not dimensionless in the present model.

4.4.3 Hardening law

Following the experimental results obtained by Fiedler et al. [70], and since only tension and compression yield strengths are being explicitly used to define the yield surface, hardening will be considered to affect both of these yield strengths. Hardening is considered dependent of the equivalent plastic strain:

$$\sigma_t = \sigma_t\left((\varepsilon_e^p)_{n+1}\right) \ , \quad \sigma_c = \sigma_c\left((\varepsilon_e^p)_{n+1}\right) \tag{4.58}$$

These two hardening functions are provided by two piece-wise functions. The increment of equivalent plastic strain is defined by:

$$\Delta\varepsilon_e^p = \sqrt{k\Delta\boldsymbol{\varepsilon}^p : \Delta\boldsymbol{\varepsilon}^p} \tag{4.59}$$

The constant k depends on which yield criterion is being used. For the Von Mises case, where the plastic Poisson's ratio is 0.5, the parameter k is equal to 2/3. To determine the value of k, one can consider a simple uniaxial tensile case. In that situation, the equivalent plastic strain is defined by:

$$\varepsilon_e^p = \sqrt{k\left({\varepsilon_{11}^p}^2 + {\varepsilon_{22}^p}^2 + {\varepsilon_{33}^p}^2 + 2{\varepsilon_{12}^p}^2 + 2{\varepsilon_{13}^p}^2 + 2{\varepsilon_{23}^p}^2\right)} \tag{4.60}$$

The transverse plastic strain is defined per equation (4.53). Substitution into (4.60) leads to:

$$\varepsilon_e^p = \sqrt{k\left({\varepsilon_{11}^p}^2 + 2\nu_p^2{\varepsilon_{11}^p}^2\right)} = \varepsilon_{11}^p\sqrt{k\left(1+2\nu_p^2\right)} \tag{4.61}$$

To enforce the equality $\varepsilon_e^p = \varepsilon_{11}^p$, the parameter k must be defined by:

$$k = \frac{1}{1+2\nu_p^2} \tag{4.62}$$

Again, if the material under analysis is a metal, or other pressure-independent material, the parameter k is equal to 2/3.

4.4.4 Return mapping algorithm

The integration of the paraboloidal criterion is simpler than many other existing criteria. This simplicity originates from the fully differentiable yield function, unlike other criteria such as Tresca, Mohr-Coulomb or Drucker-Prager. One other aspect is the symmetry of both yield surface and flow potential about the hydrostatic axis.

Consider the general return mapping update formula for the stress tensor given by equation (4.32.3)

$$\boldsymbol{\sigma}_{n+1} = \boldsymbol{\sigma}^{tr}_{n+1} - \boldsymbol{D}^e : \Delta\boldsymbol{\varepsilon}^p \tag{4.63}$$

where the last term corresponds to the plastic corrector. As a consequence of the symmetry about the hydrostatic axis, equation (4.63) leads to a return vector always parallel to the plane that contains $\boldsymbol{\sigma}^{tr}_{n+1}$ and the hydrostatic axis. Thus, without any loss of generality, the return mapping algorithm can be formulated in such a plane of the stress space, leading to a simplification of the mathematical treatment of the elasto-plastic constitutive model being demonstrated here.

Replacing the increment of plastic strain defined in equation (4.56) in equation (4.63), the following stress update formula is obtained:

$$\boldsymbol{\sigma}_{n+1} = \boldsymbol{\sigma}^{tr}_{n+1} - 6G\Delta\gamma\boldsymbol{S}_{n+1} - \frac{2}{9}K\alpha\left(I_1\right)_{n+1}\boldsymbol{I} \tag{4.64}$$

Splitting equation (4.64) in its deviatoric and volumetric components (the subscript "$n+1$" corresponding to values at the end of the increment will be dropped from now on for the sake of clarity):

$$\boldsymbol{S} = \boldsymbol{S}^{tr} - 6G\Delta\gamma\boldsymbol{S} \Leftrightarrow \boldsymbol{S} = \frac{\boldsymbol{S}^{tr}}{1+6G\Delta\gamma} \tag{4.65}$$

$$p = p^{tr} - \frac{2}{3}\Delta\gamma K\alpha I_1 \Leftrightarrow p = \frac{p^{tr}}{1+2K\alpha\Delta\gamma} \tag{4.66}$$

It should be noted that both deviatoric and volumetric stresses at the end of the increment are obtained by simply scaling down the trial deviatoric and volumetric stresses by a factor which depends on $\Delta\gamma$.

For simplification of writing, lets redefine the denominators in equations (4.65) and (4.66):

$$\zeta_s = 1 + 6G\Delta\gamma\,, \quad \zeta_p = 1 + 2K\alpha\Delta\gamma \tag{4.67}$$

The consistency condition defined by the yield surface equation (4.44) is given by:

$$\begin{aligned}
& 6J_2 + 2\left(\sigma_c - \sigma_t\right) I_1 - 2\sigma_c\sigma_t = 0 \Leftrightarrow \\
\Leftrightarrow \quad & 3\boldsymbol{S} : \boldsymbol{S} + 6\left(\sigma_c - \sigma_t\right) p - 2\sigma_c\sigma_t = 0 \Leftrightarrow \\
\Leftrightarrow \quad & \frac{3}{\zeta_s^2}\boldsymbol{S}^{tr} : \boldsymbol{S}^{tr} + \frac{6}{\zeta_p}\left(\sigma_c - \sigma_t\right) p^{tr} - 2\sigma_c\sigma_t = 0 \Leftrightarrow \\
\Leftrightarrow \quad & \frac{6J_2^{tr}}{\zeta_s^2} + \frac{2\left(\sigma_c - \sigma_t\right) I_1^{tr}}{\zeta_p} - 2\sigma_c\sigma_t = 0
\end{aligned} \tag{4.68}$$

The two yield stresses in equation (4.68) are a function of the equivalent plastic strain defined in equation (4.59). Applying equations (4.56) and (4.62), the equivalent plastic strain is defined for the present model by

$$\begin{aligned}
\Delta\varepsilon_e^p &= \sqrt{\frac{1}{1+2\nu_p^2}}\Delta\gamma\sqrt{\boldsymbol{N}_d : \boldsymbol{N}_d + 3N_v^2} = \\
&= \sqrt{\frac{1}{1+2\nu_p^2}}\Delta\gamma\sqrt{\frac{9}{\zeta_s^2}\boldsymbol{S}^{tr} : \boldsymbol{S}^{tr} + \frac{4}{27}\alpha^2 I_1^2} = \\
&= \sqrt{\frac{1}{1+2\nu_p^2}}\Delta\gamma\sqrt{\frac{18J_2^{tr}}{\zeta_s^2} + \frac{4}{3}\alpha^2 p^2} \\
&= \sqrt{\frac{1}{1+2\nu_p^2}}\Delta\gamma\sqrt{\frac{18J_2^{tr}}{\zeta_s^2} + \frac{4\alpha^2}{27\zeta_p^2}\left(I_1^{tr}\right)^2}
\end{aligned} \tag{4.69}$$

where the radicand under the second square root will be defined from now on by the parameter A, which is a function of the increment of the plastic multiplier, $\Delta\gamma$.

$$A = \frac{18J_2^{tr}}{\zeta_s^2} + \frac{4\alpha^2}{27\zeta_p^2}\left(I_1^{tr}\right)^2 \;\Rightarrow\; \Delta\varepsilon_e^p = \Delta\gamma\sqrt{\frac{A}{1+2\nu_p^2}} \tag{4.70}$$

Equations (4.70) and (4.68) can now be written in function only of $\Delta\gamma$. However, this is not a closed form solution. In order to determine $\Delta\gamma$, the

Newton-Raphson iteration scheme [82] will be used. For that, it is required to differentiate the consistency condition with relation to $\Delta\gamma$:

$$\begin{aligned}
\frac{\partial \Phi}{\partial \Delta\gamma} &= 6J_2^{tr}\frac{\partial}{\partial \Delta\gamma}\left(\frac{1}{\zeta_s^2}\right) + 2I_1^{tr}\frac{\partial}{\partial \Delta\gamma}\left(\frac{\sigma_c - \sigma_t}{\zeta_p}\right) - \\
&\quad -2\sigma_c\frac{\partial \sigma_t}{\partial \Delta\gamma} - 2\sigma_t\frac{\partial \sigma_c}{\partial \Delta\gamma} = \\
&= 2I_1^{tr}\left[\frac{1}{\zeta_p}\left(\frac{\partial \sigma_c}{\partial \Delta\gamma} - \frac{\partial \sigma_t}{\partial \Delta\gamma}\right) - \frac{2K\alpha\left(\sigma_c - \sigma_t\right)}{\zeta_p^2}\right] - \\
&\quad -\frac{72GJ_2^{tr}}{\zeta_s^3} - 2\left(\sigma_c\frac{\partial \sigma_t}{\partial \Delta\gamma} + \sigma_t\frac{\partial \sigma_c}{\partial \Delta\gamma}\right) = \\
&= \frac{2I_1^{tr}}{\zeta_p}\left(\frac{\partial \sigma_c}{\partial \Delta\gamma} - \frac{\partial \sigma_t}{\partial \Delta\gamma}\right) - \frac{4K\alpha I_1^{tr}\left(\sigma_c - \sigma_t\right)}{\zeta_p^2} - \\
&\quad -\frac{72GJ_2^{tr}}{\zeta_s^3} - 2\left(\sigma_c\frac{\partial \sigma_t}{\partial \Delta\gamma} + \sigma_t\frac{\partial \sigma_c}{\partial \Delta\gamma}\right) = 0 \qquad (4.71)
\end{aligned}$$

The two derivatives of the yield strengths with relation to $\Delta\gamma$ can be determined by applying the chain rule,

$$\frac{\partial \sigma_c}{\partial \Delta\gamma} = \frac{\partial \sigma_c}{\partial \Delta\varepsilon_e^p}\frac{\partial \Delta\varepsilon_e^p}{\partial \Delta\gamma} = H_c\frac{\partial \Delta\varepsilon_e^p}{\partial \Delta\gamma} \qquad (4.72)$$

$$\frac{\partial \sigma_t}{\partial \Delta\gamma} = \frac{\partial \sigma_t}{\partial \Delta\varepsilon_e^p}\frac{\partial \Delta\varepsilon_e^p}{\partial \Delta\gamma} = H_t\frac{\partial \Delta\varepsilon_e^p}{\partial \Delta\gamma} \qquad (4.73)$$

where parameters H_c and H_t represent the hardening modulus of the two yield strengths being considered here – compressive and tensile – obtained from the two piece-wise functions in equations (4.58). To be able to solve equations (4.72) and (4.73), the derivative of the equivalent plastic strain must be determined:

$$\begin{aligned}
\frac{\partial \Delta\varepsilon_e^p}{\partial \Delta\gamma} &= \sqrt{\frac{A}{1+2\nu_p^2}} + \sqrt{\frac{1}{1+2\nu_p^2}}\frac{\Delta\gamma}{2\sqrt{A}}\frac{\partial A}{\partial \Delta\gamma} = \\
&= \sqrt{\frac{1}{1+2\nu_p^2}}\left[\sqrt{A} - \frac{\Delta\gamma}{2\sqrt{A}}\left(\frac{216GJ_2^{tr}}{\zeta_s^3} + \frac{16\alpha^3KI_1^{tr}}{27\zeta_p^3}\right)\right] \qquad (4.74)
\end{aligned}$$

Now the increment of plastic multiplier, $\Delta\gamma$ can be determined by applying the Newton-Raphson scheme to equation (4.68).

4.4.5 Consistent tangent operator

The elasto-plastic tangent modulus associated with a particular return mapping algorithm is defined as the derivative:

$$\boldsymbol{D}^{ep} = \frac{d\boldsymbol{\sigma}_{n+1}}{d\boldsymbol{\varepsilon}^{e}_{n+1}} \tag{4.75}$$

where $\boldsymbol{\sigma}_{n+1}$ is the outcome of the return mapping previously detailed. Since the input to the elasto-plastic integration procedure is the elastic trial strain, $\boldsymbol{\varepsilon}^{e\,tr}_{n+1}$, instead of the total strain, $\boldsymbol{\varepsilon}_{n+1}$, and they both relate by $\boldsymbol{\varepsilon}^{e\,tr}_{n+1} = \boldsymbol{\varepsilon}^{e}_{n} + \Delta\boldsymbol{\varepsilon}$, straightforward differentiation results in:

$$\boldsymbol{D}^{ep} = \frac{d\boldsymbol{\sigma}_{n+1}}{d\boldsymbol{\varepsilon}^{e}_{n+1}} = \frac{d\boldsymbol{\sigma}_{n+1}}{d\boldsymbol{\varepsilon}^{e\,tr}_{n+1}} \tag{4.76}$$

To determine the tangent operator corresponding to the present paraboloidal yield criterion, the derivatives of the two stress update formulas in equations (4.65) and (4.66) must be determined. Again, the subscript "n+1" is not being used for sake of clarity. Note that the derivatives are not partial, but global.

$$d\boldsymbol{S} = \frac{d\boldsymbol{S}^{tr}}{\zeta_s} - \frac{6Gd\Delta\gamma\boldsymbol{S}^{tr}}{\zeta_s^2} \tag{4.77}$$

$$dp = \frac{dp^{tr}}{\zeta_p} - \frac{2K\alpha d\Delta\gamma p^{tr}}{\zeta_p^2} \tag{4.78}$$

Differentiation of the consistency condition yields:

$$\begin{aligned} & d\left(\frac{6J_2^{tr}}{\zeta_s} + \frac{2\left(\sigma_c - \sigma_t\right) I_1^{tr}}{\zeta_p} - 2\sigma_c\sigma_t\right) = 0 \Leftrightarrow \\ \Leftrightarrow \quad & \frac{2dI_1^{tr}\left(\sigma_c - \sigma_t\right) + 2I_1^{tr}\left(\frac{\partial\sigma_c}{\partial\Delta\gamma} - \frac{\partial\sigma_t}{\partial\Delta\gamma}\right)d\Delta\gamma}{\zeta_p} + \frac{6dJ_2^{tr}}{\zeta_s^2} - \\ & -\frac{72J_2^{tr}Gd\Delta\gamma}{\zeta_s^3} - \frac{2\left(\sigma_c - \sigma_t\right) I_1^{tr} \cdot 2K\alpha d\Delta\gamma}{\zeta_p^2} - \\ & -2\left(\sigma_c\frac{\partial\sigma_t}{\partial\Delta\gamma} + \sigma_t\frac{\partial\sigma_c}{\partial\Delta\gamma}\right)d\Delta\gamma = 0 \end{aligned} \tag{4.79}$$

Isolating the terms which multiply by $d\Delta\gamma$:

$$\begin{aligned}
&\frac{6dJ_2^{tr}}{\zeta_s^2} + \frac{2dI_1^{tr}\left(\sigma_c - \sigma_t\right)}{\zeta_p} = \\
&\quad = d\Delta\gamma \left[\frac{72GJ_2^{tr}}{\zeta_s^3} - \frac{2I_1^{tr}}{\zeta_p}\left(\frac{\partial \sigma_c}{\partial \Delta\gamma} - \frac{\partial \sigma_t}{\partial \Delta\gamma}\right) + \right. \\
&\qquad \left. + \frac{4K\alpha\left(\sigma_c - \sigma_t\right) I_1^{tr}}{\zeta_p^2} + 2\left(\sigma_c \frac{\partial \sigma_t}{\partial \Delta\gamma} + \sigma_t \frac{\partial \sigma_c}{\partial \Delta\gamma}\right)\right]
\end{aligned} \tag{4.80}$$

The terms between square brackets are all constants for a given time increment and were already determined during the return mapping integration scheme. The character η will be used from now on to represent that term. Rearranging equation (4.80) in order to $d\Delta\gamma$:

$$d\Delta\gamma = \frac{1}{\eta}\left[\frac{6dJ_2^{tr}}{\zeta_s^2} + \frac{2\left(\sigma_c - \sigma_t\right)}{\zeta_p} dI_1^{tr}\right] \tag{4.81}$$

We can use the definition of the two invariants in equation (4.81), J_2^{tr} and I_1^{tr}, to determine their respective derivatives in function of the deviatoric and volumetric trial strains:

$$dJ_2^{tr} = 2G\boldsymbol{S}^{tr} : d\boldsymbol{\varepsilon}_d^{tr} \ , \quad dI_1^{tr} = 3K d\varepsilon_v^{tr} \tag{4.82}$$

Substituting equations (4.82) into equation (4.81), the following explicit equation for determining $d\Delta\gamma$ is obtained:

$$\begin{aligned}
d\Delta\gamma &= \frac{1}{\eta}\left[\frac{12G}{\zeta_s^2}\boldsymbol{S}^{tr} : d\boldsymbol{\varepsilon}_d^{tr} + \frac{6K\left(\sigma_c - \sigma_t\right)}{\zeta_p} d\varepsilon_v^{tr}\right] = \\
&= \frac{1}{\eta}\left[\frac{12G}{\zeta_s^2}\boldsymbol{S}^{tr} : d\boldsymbol{\varepsilon}^{tr} + \frac{6K\left(\sigma_c - \sigma_t\right)}{\zeta_p}\boldsymbol{I} : d\boldsymbol{\varepsilon}^{tr}\right]
\end{aligned} \tag{4.83}$$

Replacing equation (4.83) in equation (4.77):

$$\begin{aligned}
d\boldsymbol{S} &= \frac{d\boldsymbol{S}^{tr}}{\zeta_s} - \frac{1}{\eta}\frac{6G}{\zeta_s^2}\frac{12G}{\zeta_s^2}\boldsymbol{S}^{tr} \cdot \boldsymbol{S}^{tr} : d\boldsymbol{\varepsilon}^{tr} - \\
&\quad - \frac{1}{\eta}\frac{6G}{\zeta_s^2}\frac{6K\left(\sigma_c - \sigma_t\right)}{\zeta_p}\boldsymbol{S}^{tr} \cdot \boldsymbol{I} : d\boldsymbol{\varepsilon}^{tr} \Leftrightarrow
\end{aligned}$$

$$\begin{aligned}\Leftrightarrow \quad d\boldsymbol{S} = & \frac{2G}{\zeta_s}d\boldsymbol{\varepsilon}^{tr} - \frac{2G}{3\zeta_s}\boldsymbol{I}\cdot\boldsymbol{I} : d\boldsymbol{\varepsilon}^{tr} - \frac{72G^2}{\eta\zeta_s^4}\boldsymbol{S}^{tr}\cdot\boldsymbol{S}^{tr} : d\boldsymbol{\varepsilon}^{tr} - \\ & - \frac{36KG\left(\sigma_c - \sigma_t\right)}{\eta\zeta_s^2\zeta_p}\boldsymbol{S}^{tr}\cdot\boldsymbol{I} : d\boldsymbol{\varepsilon}^{tr}\end{aligned} \tag{4.84}$$

Performing the same way regarding equation (4.78):

$$\begin{aligned} dp &= \frac{dp^{tr}}{\zeta_p} - \frac{2K\alpha I_1^{tr}}{3\zeta_p^2}d\Delta\gamma = \\ &= \frac{K}{\zeta_p}d\varepsilon_v^{tr} - \frac{1}{\eta}\frac{4K^2\alpha I_1^{tr}}{\zeta_p^3}\left(\sigma_c - \sigma_t\right)\boldsymbol{I} : d\boldsymbol{\varepsilon}^{tr} - \\ &\qquad - \frac{1}{\eta}\frac{2K\alpha I_1^{tr}}{3\zeta_p^2}\frac{12G}{\zeta_s}\boldsymbol{S}^{tr} = \\ &= \left[\frac{K}{\zeta_p} - \frac{4K^2\alpha I_1^{tr}}{\eta\zeta_p^3}\left(\sigma_c - \sigma_t\right)\right]\boldsymbol{I} : d\boldsymbol{\varepsilon}^{tr} - \\ &\qquad - \frac{8K\alpha G I_1^{tr}}{\eta\zeta_p^2\zeta_s}\boldsymbol{S} : d\boldsymbol{\varepsilon}^{tr}\end{aligned} \tag{4.85}$$

Composing the two stress components, deviatoric and hydrostatic, the following is obtained:

$$d\boldsymbol{\sigma} = d\boldsymbol{S} + dp\boldsymbol{I} = \boldsymbol{D}^{ep} : d\boldsymbol{\varepsilon}^{tr} \tag{4.86}$$

Replacing equations (4.84) and (4.85) in (4.86), the final equation for the consistent tangent operator is achieved:

$$\boldsymbol{D}^{ep} = \beta\boldsymbol{I}_4 + \left(\varphi - \frac{\beta}{3}\right)\boldsymbol{I}\cdot\boldsymbol{I} - \rho\boldsymbol{S}^{tr}\cdot\boldsymbol{I} - \chi\boldsymbol{S}^{tr}\cdot\boldsymbol{S}^{tr} - \psi\boldsymbol{I}\cdot\boldsymbol{S}^{tr} \tag{4.87}$$

where $\boldsymbol{I}_4$ represent a fourth-order identity tensor and the constants β, φ, ρ, χ, and ψ are given by:

$$\begin{gathered}\beta = \frac{2G}{\zeta_s}\ , \quad \varphi = \frac{K}{\zeta_p} - \frac{4K^2\alpha}{\eta\zeta_p^3}I_1^{tr}\left(\sigma_c - \sigma_t\right)\ , \\ \rho = \frac{36KG\left(\sigma_c - \sigma_t\right)}{\eta\zeta_s^2\zeta_p}\ , \quad \chi = \frac{72G^2}{\eta\zeta_s^4}\ , \quad \psi = \frac{8KG\alpha}{\eta\zeta_p^2\zeta_s}I_1^{tr}\end{gathered} \tag{4.88}$$

4.5 Computational implementation

The overall integration algorithm as it was implemented in an `UMAT` subroutine of commercial finite element software ABAQUS® [30] is presented in the flowchart of figure 4.8. It follows a typical implicit elastic predictor/return mapping procedure used by, for example, Souza-Neto [62]. It begins by computing an elastic trial stress state and up-to-date hardening variables. The consistency condition in equation (4.68) is verified against a numerical tolerance value. If the trial stress state is still inside the paraboloidal yield surface, then the increment is considered to be fully elastic; otherwise, the algorithm for the return mapping is executed. Upon convergence of the plastic multiplier, all state variables, stress tensor and plastic strain tensor are updated accordingly.

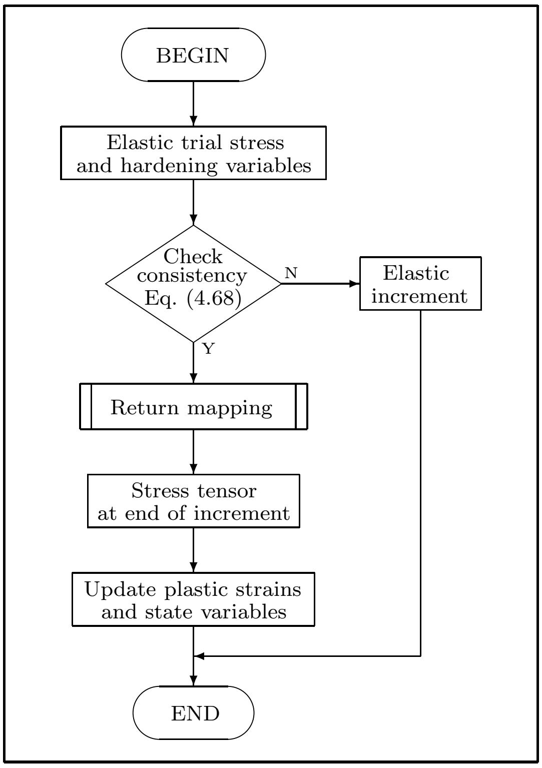

Figure 4.8: Flowchart of implicit elastic predictor/return mapping algorithm.

The flowchart for the return mapping algorithm is presented in figure 4.9. The objective of this algorithm is to determine the value of the plastic multiplier defined in subsection 4.1.7 using the iterative Newton-Raphson method [82]. It begins by providing an initial value for the plastic multiplier,

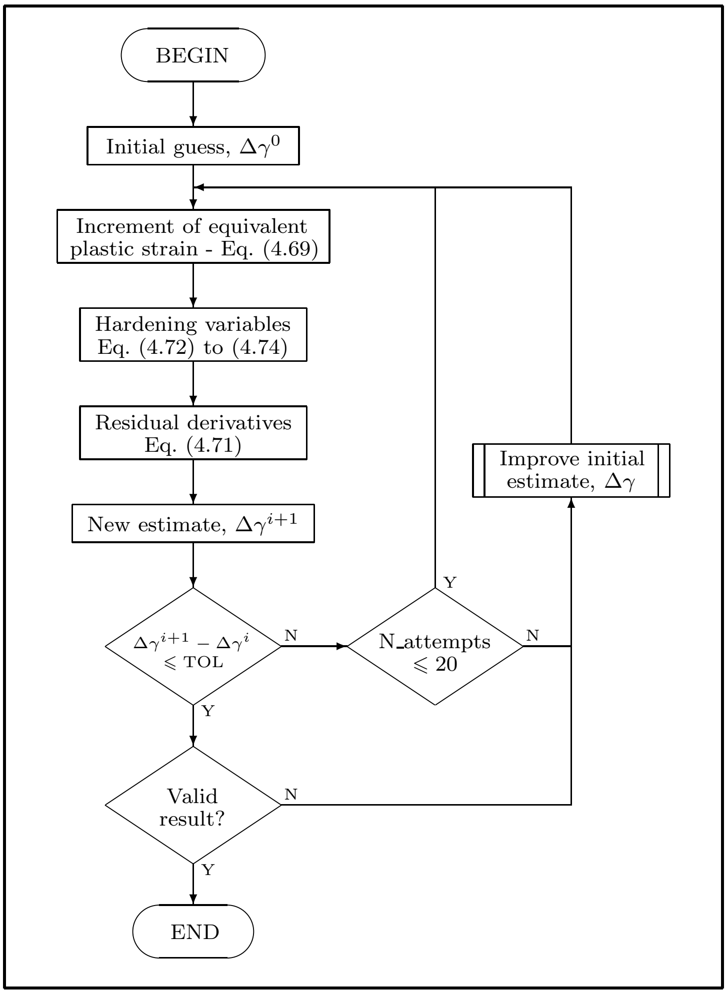

Figure 4.9: Flowchart of return mapping algorithm.

$\Delta\gamma^0$. According to this initial value, the increment of equivalent plastic strain and hardening variables are updated as per equations (4.69) and (4.73) to (4.74).

The Newton-Raphson method requires the calculation of the residual derivative as per equation (4.71) updated to the initial value of the plastic multiplier. With this and the consistency condition, the Newton-Raphson method can now be applied:

$$\Delta\gamma^{i+1} = \Delta\gamma^{i} - \frac{\Phi\left(\Delta\gamma^{i}\right)}{\dfrac{\partial\Phi}{\partial\Delta\gamma}\left(\Delta\gamma^{i}\right)} \tag{4.89}$$

The method will run for as many iterations as required to converge to the value of the plastic multiplier, with a maximum of twenty iterations. Upon convergence, the result is checked for validity. This is necessary since the shape of the consistency condition function is irregular at some points of its domain and the plastic multiplier might erroneously converge to absurd values such as towards infinite or even negative values. If the result is valid, the return mapping algorithm ends.

If the Newton-Raphson method did not converge after twenty iterations or if the validity checks determined that the obtained value was improper, then a secondary function is executed which will improve the initial guess of the plastic multiplier. The Newton-Raphson method is then restarted but using this improved initial guess. Figure 4.10 illustrates this auxiliary function.

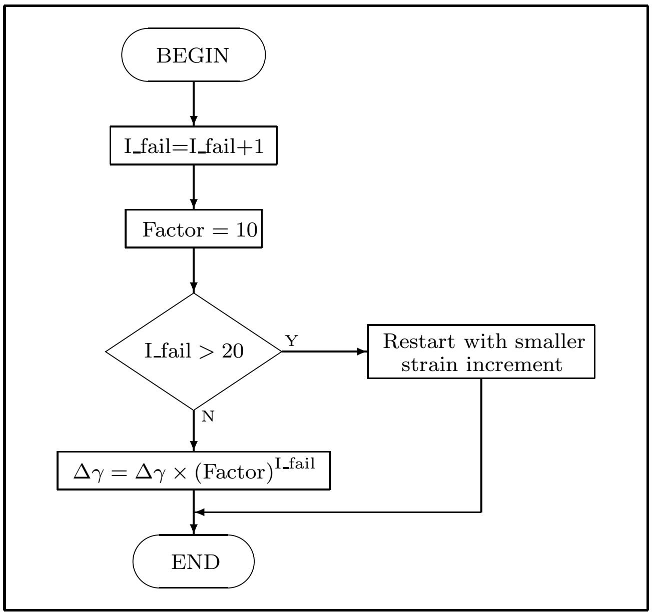

Figure 4.10: Flowchart for improving plastic multiplier's initial estimate.

The algorithm to improve the initial estimate of the plastic multiplier presented in figure 4.10 simply takes the default value of the initial estimate and multiples it by a power of 10. The exponent is the number of failed attempts at convergence performed by the return mapping algorithm in figure 4.9.

4.6 Verification of elasto-plastic model

The elasto-plastic constitutive model was implemented in an user subroutine `UMAT` in ABAQUS® [30]. In this section, a serious of tests will be performed to verify the correlation of the algorithm with the available experimental data.

4.6.1 One-element testing

Three different unidirectional analysis were performed on a simple three dimensional one-element mesh – tension, compression and shear. In figure 4.11 the results are compared with the experimental data from Fiedler et al. [70]. Considering that both tension and compression results are in good agreement by default with the experimental data, since it is based on these values that the plastic behaviour of the matrix is modelled, the shear curve becomes the most important factor of comparison. The numerical results for shear agree very well with the available experimental data, despite some under-prediction of the maximum stress.

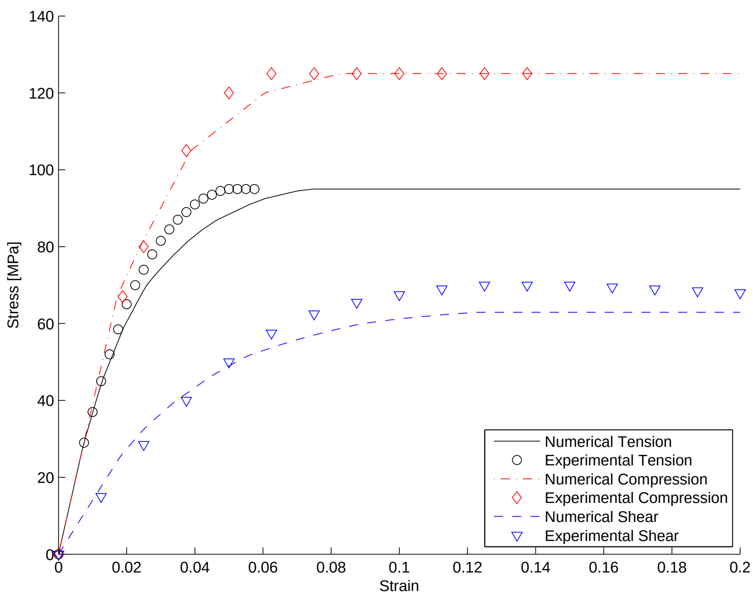

Figure 4.11: Comparison of experimental data [70] with numerical results from one-element mesh.

4.7 Application to composite volume elements

This section presents a few examples of representative volume elements under different loading conditions and provides a better insight to the matrix material behaviour defined by the present elasto-plastic constitutive model. Five loading conditions are presented: transverse tension, longitudinal shear, transverse shear, transverse compression, and a combination of transverse compression and shear. The elastic properties and plastic evolution data from Fiedler et al. [70] were used to model the epoxy mechanical behaviour. The fibres are considered elastic and transversely isotropic with the engineering constants given by table 3.1 for Silenka glass fibres.

Since the goal of the current section is to provide an overview of the deduced elasto-plastic constitutive model, a smaller volume element is chosen. Thus, the volume element has 10× the fibre radius in the transverse direction and a thickness of only two elements in the longitudinal direction. One volume element with a size of 20× the fibre radius in the transverse direction was also generated for comparing results obtained with different volume element sizes. The minimum interval between any two neighbouring fibres is set to 2.07× the fibre radius, and the fibre volume fraction is set to 60%.

Five different fibre distributions were generated, and one of them was given a lower fibre volume fraction (50%) for comparison purposes. The different loading conditions mentioned above were applied on each distribution independently, making a total of twenty five different analyses to be computed on the smaller volume elements plus five analyses on the larger volume element. Each case will be analysed in detail in the following.

4.7.1 Transverse tension

Figure 4.12 shows the results from an applied transverse tension load to a volume element. Figure 4.12a shows the spatial distribution of the equivalent plastic strain as defined in equation (4.69) for one of the generated fibre spatial distributions. It can be seen that the regions of the matrix where the equivalent plastic strain is greater are located between those neighbouring fibres aligned with the load direction (horizontal, in this case). Figure 4.12b shows the transverse stress-strain curves obtained after volumetric homogenisation for all fibre distributions. It can be seen that even for a small volume element ($10 \times R$), there is almost no scatter between all four curves. Increasing the size of the volume element leads to negligible differences between the stress-strain curves. Obviously, a lower fibre volume fraction leads to a lower stiffness as can be seen in figure 4.12b.

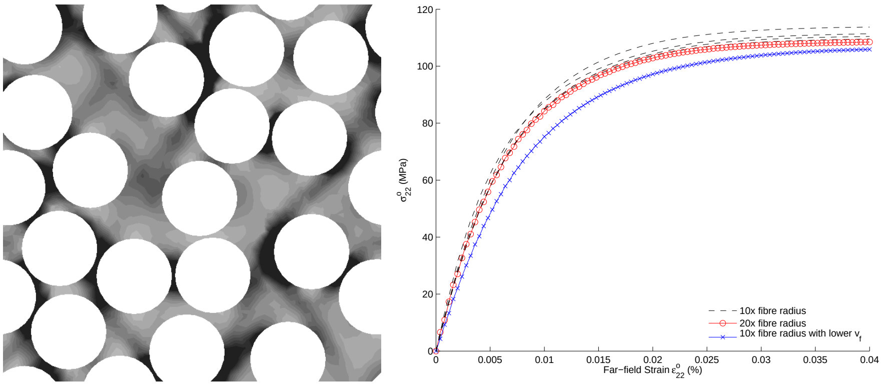

(a) Equivalent plastic strain (b) Stress-strain curves

Figure 4.12: Results for transverse tension example.

4.7.2 Longitudinal shear

Figure 4.13 shows the results from an applied longitudinal shear load to a volume element. Figure 4.13a shows the spatial distribution of the equivalent plastic strain as defined in equation (4.69) for one of the fibre spatial distributions. A band of plasticised material has formed in the matrix-rich region of the volume element. In the small strips of matrix material between neighbouring fibres there is also a tendency to develop plastic strains. Figure 4.13b shows the longitudinal shear stress-strain curves obtained after volumetric homogenisation for each fibre distribution. Again, no visible scatter is seen between the four curves from the smaller volume element. The stress-strain curve from the larger volume element fits very well with its smaller counterparts.

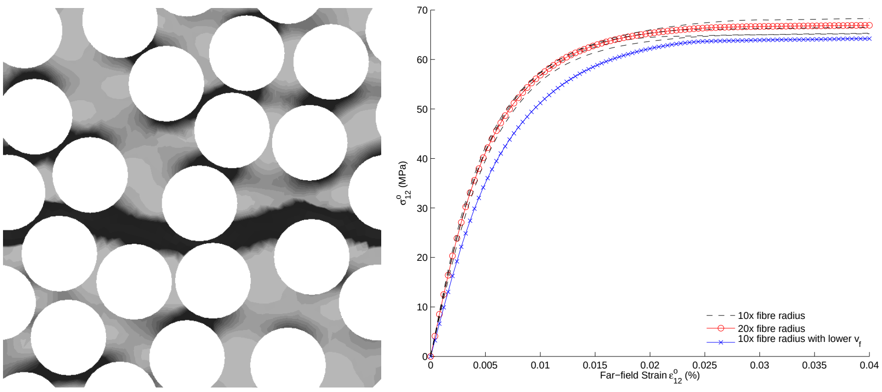

(a) Equivalent plastic strain (b) Stress-strain curves

Figure 4.13: Results for longitudinal shear example.

4.7.3 Transverse shear

Figure 4.14 shows the results from an applied transverse shear load to a volume element. Figure 4.14a represents the distribution of equivalent plastic strain as defined in equation (4.69) for one of the fibre spatial distributions. It can be seen that a vertical band of plasticised material has formed in the right side of the volume element. Figure 4.14b shows the transverse shear stress-strain curves obtained after volumetric homogenisation of all fibre distributions. A slight increase in the scatter between the curves is registered but without significance. The stress-strain curve for the larger volume element fits well with all four curves from the smaller volume elements.

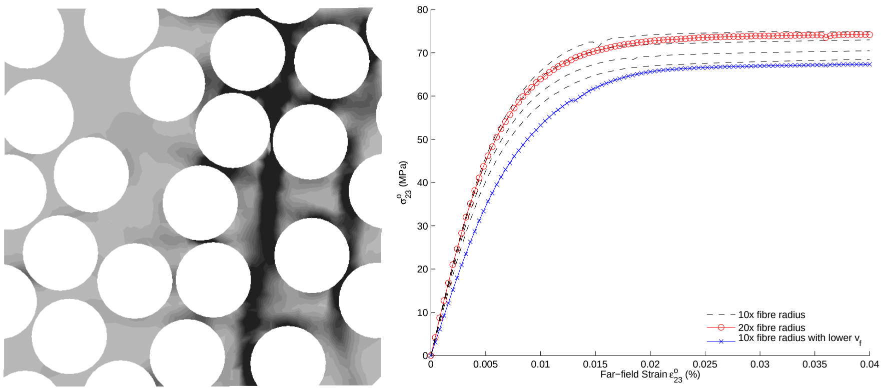

(a) Equivalent plastic strain (b) Stress-strain curves

Figure 4.14: Results for transverse shear example.

4.7.4 Transverse compression

Figure 4.15 shows the results from an applied transverse compression load to a volume element. Figure 4.15a shows the spatial distribution of the equivalent plastic strain as defined in equation (4.69) for one of the generated spatial distributions. The bands of plasticised matrix material follow an inclined orientation of approximately 53° measured from the vertical, leading to the conclusion that it is a shear effort and not the compressive load that is causing the material to plasticise. Figure 4.15b shows the compressive stress-strain curves obtained after volumetric homogenisation of all fibre distributions. The scatter is not significant between the curves for the smaller volume elements. The larger volume element again fits in between the curves from its smaller counterparts. The curves show some irregular behaviour due to convergence difficulties. It was noted that the transverse compression loading scenario is the one which presents more difficulty in converging to a final result.

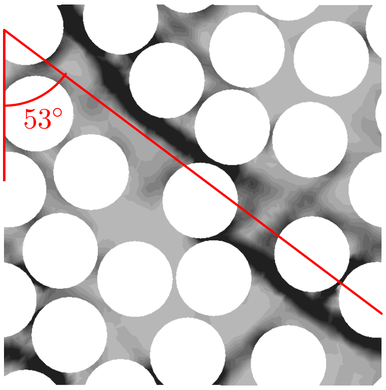

(a) Equivalent plastic strain

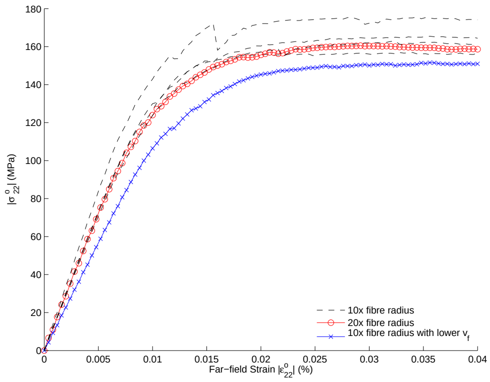

(b) Stress-strain curves

Figure 4.15: Results for transverse compression example.

4.7.5 Combined transverse compression and shear

Figure 4.16 shows the results from applying a combined transverse compression and transverse shear loads to a volume element. Both loads are of equal magnitudes. Figure 4.16a represents the distribution of equivalent plastic strain as defined in equation (4.69) for one of the generated spatial distributions. The distribution of equivalent plastic strain differs from both isolated loading conditions. There are more areas in the matrix material where plasticity has been activated, but the orientation of the band of plasticised material is more similar to the transverse shear case. Figure 4.16b shows the transverse compressive stress-strain curves obtained after volumetric homogenisation of all fibre distributions. As in all other loading cases, no significant scattering is visible.

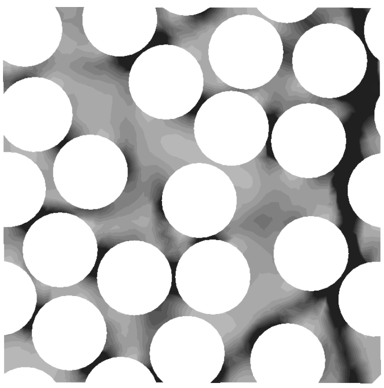

(a) Equivalent plastic strain

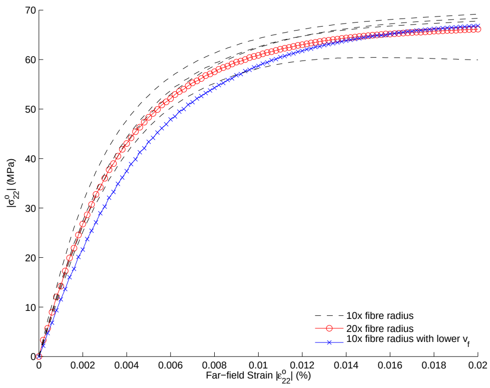

(b) Compressive stress-strain curve

Figure 4.16: Results for combined transverse shear / compression example.

4.8 Conclusions

The original paraboloidal yield criterion as proposed by Tschoegl [76] was implemented in an user material subroutine in ABAQUS® [30]. The good agreement with experimental data and the simple mathematics involved in its implementation were the deciding factors for its choice. The paraboloidal criterion is also capable of accounting for different tensile and compressive yield strengths and exhibits pressure dependency. The paraboloidal yield criterion requires the experimental determination of both tensile and compressive yield strengths of the bulk matrix material, as well as their evolution with relation to the equivalent plastic strain. The numerical model was implemented following a return mapping algorithm strategy. This strategy is based on an elastic predictor-plastic corrector scheme. For a faster convergence rate, the consistent tangent operator was also determined.

A set of analyses were conducted to confirm the model's numerical implementation and agreement with available experimental data. A few basic loading cases were applied to different volume elements, each of them generated according with the algorithm presented in chapter 2. It was demonstrated that the use of periodic boundary conditions as defined in chapter 3 allows for the use of smaller volume elements – unlike what had been proposed by Trias et al. [15] for different boundary conditions – when attempting to model the non-linear behaviour of the matrix material without loosing generality and saving considerable computational efforts at the same time.

The conducted analyses also provided some insight into the most sensitive areas of the matrix at a micromechanical level for plasticity to take place and what is the preferable orientation for a band of plasticised material to form depending on the loading scenario being applied. The results obtained with this numerical procedure are similar to what can be observed from experimental testing.

Next chapter will upgrade the constitutive model presented so far with a damage formulation being implemented. The damage model will comply with the presets of thermodynamics regarding the energy released by the material upon damage activation and consequent propagation. A damage formulation will be developed for each constituent of the composite according with the experimental data available in the literature regarding the mechanical behaviour of each constituent.

Chapter 5

Damage models

> The eternal quest of the individual human being is to shatter his loneliness.
>
> Norman Cousins

The present chapter will provide the final step for the implementation of the constitutive model for the matrix. After characterising the non-linear plastic behaviour, it is now required to define how damage will be activated and propagate in the material. The reinforcing material is considered linear elastic up to damage, and this chapter will also address the application of a damage model for the reinforcing material.

An introduction to damage and a brief review of how damage has been dealt with over the years in composite materials will first be performed. Then, the general theory used to describe the damage activation and propagation will be outlined. The analytical derivation and computational implementation of the damage model will then be performed for both materials – matrix and fibre. Finally, a quick verification of the presented elasto-plastic with damage constitutive model and some examples will be presented.

5.1 Damage in composites

Structural components are dimensioned according with all the events they will have to withstand during their lifetime – static and/or dynamic loading, environmental conditions, damage threats and propagation, just to name a few. All these events can cause material degradation of some sort, affecting the ability of the structure to perform its mission. This degradation has a completely different meaning for composite materials than it does for metallic materials, for example.

In broad terms, *fracture* refers to the opening of internal surfaces, or cracks. Fracture mechanics studies the conditions that might lead to crack growth. *Damage*, however, refers to all the irreversible changes in the material due to energy dissipation mechanisms, of which crack growth is one example. These changes are normally considered to be distributed through the material. Damage mechanics deals fundamentally with the conditions for initiation and propagation of these irreversible changes, as well as its consequences for the mechanical behaviour of the structure.

Damage can be studied at different scale levels. In general, there is an initiation of local damage in a lamina which, by itself, does not lead to catastrophic failure, and is distant from the final fracture of the laminate. Normally, the progression of these damage mechanisms is stopped by adjacent layers of material with different orientations. But the damage appearance at the lamina level is basically due to the intricacy of composite materials at a very small scale. With this in mind, the study of damage in composite materials can be split in three different scale levels, described in the next subsections.

5.1.1 Macro-scale

This refers to the structural level where the whole structure is considered an homogeneous continuum and the material behaviour is described by an anisotropic constitutive law. Finite element analyses are easily performed at this level and effective material properties are used.

Damage at this scale level is seen to lead to catastrophic failure of the structural component. It is mainly influenced by interlaminar stresses present along the free edges of the material. The finite dimension of structural components force the existence of a stress state along the edge that is different from the rest of the component. Interlaminar tensile and shear stresses appear which lead to delamination. The stacking sequence of the individual layers that give form to the laminate also has a significant effect on the component's capacity to resist initiation and propagation of delamination. Stacking sequence has also an influence on which mode of failure the component will suffer.

5.1.2 Meso-scale

At this intermediate scale level, it is the lamina, and not the laminate, that is seen as an homogeneous continuum. This obviously leads to a very different interpretation of damage initiation and propagation. Normally, a *first-ply* failure theory is followed, i.e. the laminate fails when damage is activated at any given ply. This is somewhat distant from reality since it is normal for multiple transverse cracks to develop in internal layers not oriented with the principal loading direction before ultimate laminate strength is achieved.

Because of this, many authors prefer to specify a *first-ply* failure and an *ultimate* failure, thus distinguishing the end of the elastic regime from the maximum strength the laminate can bear. An example of this approach was presented by Camanho and Lambert [83].

However, determining the exact strength of a lamina is not a trivial endeavour due to its anisotropic nature. Many failure theories were proposed throughout the years. Some of the most used ones are briefly presented in next points.

Maximum stress theory

The maximum stress failure criterion assumes that failure occurs whenever any of the stress components attains its limiting value, without any interaction with the other stress components. This condition can be mathematically written by:

$$\begin{aligned}
X_C < \sigma_{11} < X_T \\
Y_C < \sigma_{22} < Y_T \\
Z_C < \sigma_{33} < Z_T \\
|\sigma_{12}| < Q \\
|\sigma_{13}| < R \\
|\sigma_{23}| < S
\end{aligned} \tag{5.1}$$

where the subscripts T and C represent tension and compression respectively, X, Y and Z are the maximum normal stresses in the fibre direction and the two transverse directions respectively, and Q, R, and S represent the maximum shear stresses.

Maximum strain theory

The maximum strain theory is the strain equivalent to the maximum stress theory. Equations are written in a similar form to equations (5.1), but replacing the maximum stresses by the maximum strains:

$$
\begin{aligned}
\varepsilon_{11}^{C} < \varepsilon_{11} < \varepsilon_{11}^{T} \\
\varepsilon_{22}^{C} < \varepsilon_{22} < \varepsilon_{22}^{T} \\
\varepsilon_{33}^{C} < \varepsilon_{33} < \varepsilon_{33}^{T} \\
|\varepsilon_{12}| < \Gamma_{12} \\
|\varepsilon_{13}| < \Gamma_{13} \\
|\varepsilon_{23}| < \Gamma_{23}
\end{aligned}
\tag{5.2}
$$

Tsai-Hill

The Tsai-Hill theory [84] is an attempt to provide a quadratic criterion which would better fit the experimental observations. Thus the criterion is not based on physical aspects of failure mechanisms. It makes use of Hill's anisotropic plasticity theory [59] and applies it to failure of anisotropic and homogeneous materials. The failure surface is given by

$$
\begin{aligned}
(G+H)\,\sigma_{11}^2 + (F+H)\,\sigma_{22}^2 + (F+G)\,\sigma_{33}^2 - 2H\sigma_{11}\sigma_{22} - \\
-2G\sigma_{11}\sigma_{33} - 2F\sigma_{22}\sigma_{33} + 2L\tau_{23}^2 + 2M\tau_{13}^2 + 2N\tau_{12}^2 = 1
\end{aligned}
\tag{5.3}
$$

where F, G, H, L, M, and N are material strength parameters. Stress states on or outside this surface correspond to failure. The strength parameters are expressed in terms of the failure stresses obtained from unidirectional experimental tests:

$$
\begin{aligned}
2N &= 1/S^2 \\
2L &= 1/Q^2 \\
2M &= 1/R^2 \\
2H &= 1/X^2 + 1/Y^2 - 1/Z^2 \\
2G &= 1/X^2 - 1/Y^2 + 1/Z^2 \\
2F &= -1/X^2 + 1/Y^2 + 1/Z^2
\end{aligned}
\tag{5.4}
$$

One obvious limitation of this failure criterion is that since all normal strengths are squared in equations (5.4), there is no distinction between positive and negative strengths, which are generally different in composite materials.

Tensor polynomial failure criterion

To overcome this problem in a purely mathematical way, failure criteria based on polynomials of strength tensors were proposed. The most well known and used is probably the Tsai-Wu failure criterion [85]. It is a complete quadratic tensor polynomial and assumes that there is a function $f(\sigma_i)$ of the form:

$$f(\sigma_i) = F_i\sigma_i + F_{ij}\sigma_i\sigma_j \tag{5.5}$$

The reduced form – after simplifications due to tensorial symmetry and the normal/shear coupling terms being null – of the $f(\sigma_i)$ scalar function is:

$$\begin{aligned} f(\sigma_i) \;=\; & F_1\sigma_{11} + F_2\sigma_{22} + F_3\sigma_{33} + F_{11}\sigma_{11}^2 + F_{22}\sigma_{22}^2 + F_{33}\sigma_{33}^2 + \\ & + F_{44}\sigma_{12}^2 + F_{55}\sigma_{13}^2 + F_{66}\sigma_{23}^2 + 2F_{12}\sigma_{11}\sigma_{22} + \\ & + 2F_{13}\sigma_{11}\sigma_{33} + 2F_{23}\sigma_{22}\sigma_{33} \end{aligned} \tag{5.6}$$

The strength tensors F_i and F_{ij} can be determined from a series of thought experiments with one-dimensional loadings. The coefficients F_{12}, F_{13}, and F_{23} correspond to interaction terms involving two out of three normal stress components. Although difficult to obtain, these are generally very small and are normally considered null.

Hashin's criteria

Hashin was the first to establish the need for a real physical-based failure criterion. Hashin [86] proposed two different criteria, one for fibre failure and other for matrix failure. Later [87], Hashin updated his own criteria in order to distinguish tensile from compressive failure. The criteria for a plane stress state are summarised next:

- Matrix failure
  - Matrix tension, $\sigma_{22} \geqslant 0$

$$FI_M = \left(\frac{\sigma_{22}}{Y_T}\right)^2 + \left(\frac{\tau_{12}}{S_L}\right)^2 \tag{5.7}$$

– Matrix compression, $\sigma_{22} < 0$

$$FI_M = \left(\frac{\sigma_{22}}{2S_T}\right)^2 + \left[\left(\frac{Y_C}{2S_T}\right)^2 - 1\right]\frac{\sigma_{22}}{Y_C} + \left(\frac{\tau_{12}}{S_L}\right)^2 \tag{5.8}$$

- Fibre failure

– Fibre tension, $\sigma_{11} \geqslant 0$

$$FI_F = \left(\frac{\sigma_{11}}{X_T}\right)^2 + \left(\frac{\tau_{12}}{S_L}\right)^2 \tag{5.9}$$

– Fibre compression, $\sigma_{11} < 0$

$$FI_F = \frac{\sigma_{11}}{X_C} \tag{5.10}$$

where FI denotes Failure Index, with the subscripts M and F indicating matrix and fibre, respectively, and with S_L and S_T being the longitudinal and transverse shear strengths, respectively. If FI is greater than 1, then the corresponding failure criterion is activated.

Puck's action plane criterion

Hashin's criteria contain several limitations, especially in the cases of matrix or fibre compression, and the stress interactions proposed do not always fit the experimental data. In order to overcome some of these difficulties, many authors have proposed modifications to Hashin's criteria. One of them was Puck [88], who proposed a criterion based on an action plane, the plane of matrix failure under transverse compression. The matrix failure criteria are based on the brittle failure behaviour of composites. The beneficial influence of transverse compression on matrix shear strength is represented by a term that is proportional to the normal stress acting on that plane (figure 5.1). The matrix failure criterion under transverse compression is thus given by

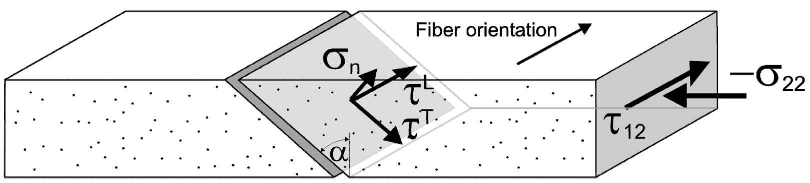

Figure 5.1: Puck's action plane (image from Dávila and Camanho [89]).

$$\left(\frac{\tau_T}{S_T - \eta_T \sigma_n}\right)^2 + \left(\frac{\tau_L}{S_L - \eta_L \sigma_n}\right)^2 = 1 \tag{5.11}$$

where τ_T and τ_L are the shear stresses acting on the fracture plane and σ_n is the normal stress to the fracture plane (figure 5.1). Internal material friction is characterised by the coefficients η_L and η_T, which are determined experimentally. The fracture angle α is determined according with the ratio of compression stress to in-plane shear stress. For matrix failures dominated by in-plane shear, the fracture plane is normal to the ply. For increasing amounts of transverse compression, the angle of the fracture plane changes to about 40°, and increases with compression to 53° for pure transverse compression.

LaRC's criterion

Although very well ranked in the World Wide Failure Exercise (WWFE) [31], Puck's criterion depends on a good number of material parameters which are not always easy to obtain experimentally. Dávila and Camanho [89] proposed a set of criteria for plane stress entirely based on the physical aspects of the different fracture mechanisms. Later, the criteria were expanded by Pinho et al. [90] to three dimensional stress states.

For the case of transverse compression, the Mohr-Coulomb effective stress concept is used to determine the fracture angle α. The model also distinguishes the application of the failure criteria to thick and thin plies, as well as inner and outer plies in a laminate, by taking into account the in-situ strengths of these plies instead of their unidirectional counterparts.

Failure due to compression in the fibre direction happens due to the collapse of the fibres as a result of shear kinking and damage to the supporting matrix, which leads to the formation of a kink band. The misalignment angle of the kink band can be determined and the failure criterion for longitudinal compression is a function of the stress components in the misaligned coordinate frame, i.e parallel to the kink band's orientation.

LaRC's failure criteria is one of the few that attempts to incorporate in its genesis some of the micro-scale failure mechanisms observed in long-fibre composite materials, as is the case of the formation of a kink band an example. Many other failure mechanisms occur at the micro-scale level and, for all of them, it is possible to establish a direct connection with the different features observed at the meso- and macro-scale level in experimental work at the failure moment. As a matter of fact, some of the failure mechanisms observed at the micro-scale do not lead directly to failure of the entire structural component, but accumulate with increasing load until a limit is achieved and the part collapses. The different failure mechanisms of the micro-scale are presented next.

5.1.3 Micro-scale

When analysed at the micro-scale level, composite materials present a high degree of anisotropy, randomness of fibre distribution (see chapter 2), and inhomogeneities. This leads to a variety of damage mechanisms that can appear in composite materials. Each damage mechanism has its own triggering event and several mechanisms can take place at the same time or be influenced by each other. A review of each of these damage mechanisms is presented next.

Matrix cracking

Being the weakest phase in the composite, the matrix is normally the first material to suffer some form of damage in composite materials. The most common one is cracking. Cracks are normally transverse to the load direction and traverse the thickness of the ply, running parallel to the fibres. At the meso-scale level, when using a first-ply failure theory, it is the start of this damage mechanism that is attempted to predict. An example of a matrix crack which has propagated through an entire layer on a laminate is visible in figure 5.2.

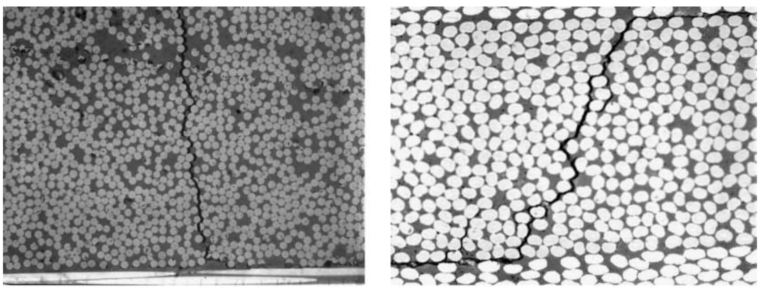

a $\{\ldots 0°/90°_2/0°\ldots\}$ b $\{\ldots +45°/90°/-45°\ldots\}$

Figure 5.2: Example of matrix cracks (from [91]).

Interfacial debonding

With the increase of the applied load, cracks on the matrix will propagate until they reach the interface region between the matrix and fibres. Also, it is quite common for the crack to initiate at this interface. This is a sensitive region for composite materials as the adhesion between the two materials has a strong effect on the macroscopic mechanical properties. In a composite with a weak interface, interfacial cracks will accumulate and grow with the increase of applied loads, and will tend to connect with each other and form a macro-crack. This is visible in figure 5.3.

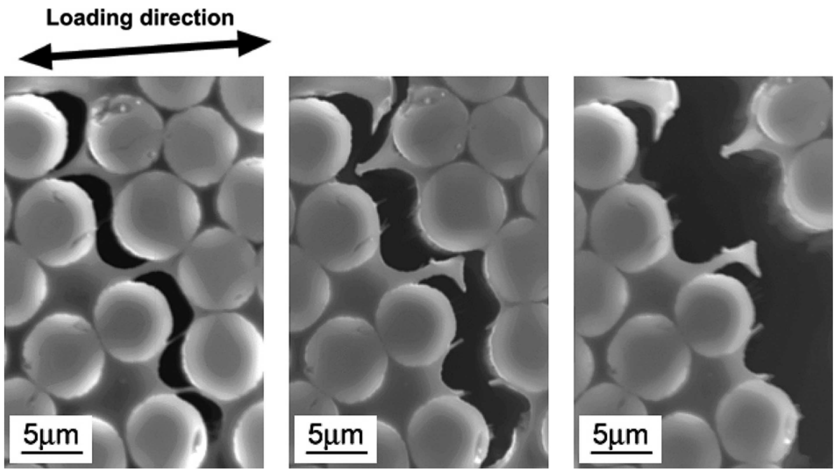

Figure 5.3: Interfacial debonding in a HTA/L135i composite (from [92]).

One other possibility for interfacial cracks to appear is when the propagation of a matrix crack is halted by the presence of a fibre. If the stress is not high enough to cause damage to the fibre, the crack will propagate around the fibre. The different Poisson's ratios between fibre and matrix will force the existence of shear stresses on the interface. When the shear stresses exceed the interfacial shear strength, interfacial debonding will occur which will extend along the length of the fibre as well as around it.

Fibre pull-out

Fibre pull-out, or interfacial sliding can occur when different displacement fields are imposed on the different constituents. This is the case of thermal loadings; due to different thermal expansion coefficients, the fibres (especially carbon fibres) and the matrix will be under different loading conditions. Also here, the interfacial strength plays a very important role for the existence of this kind of damage mechanism. The sliding of the fibre against the matrix can cause further damage due to frictional wear. Figure 5.4 shows an example of some fibres belonging to a bundle of fibres which have been pulled out of their composite sockets.

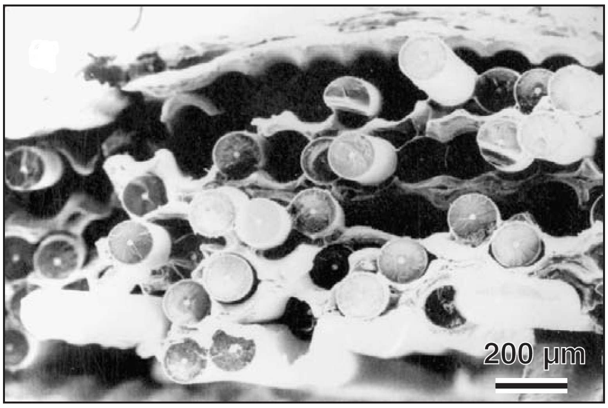

Figure 5.4: Micrograph showing the fibre pull-out effect on a B/Al composite (from [93]).

Fibre kinking

When a unidirectional composite is loaded in longitudinal compression, there is a phenomenon of local instability caused by failure of the matrix that supports the fibres, which leads to the formation of a kink band. With the lack of lateral support, fibres start buckling (figure 5.5b). As the load increases, the fibres will reach a critical buckling load and initial fibre fracture in the

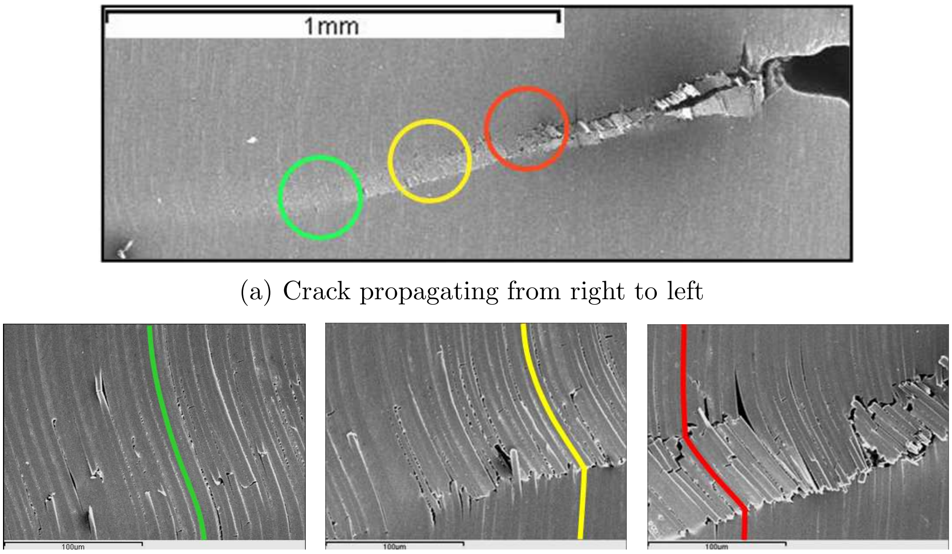

(a) Crack propagating from right to left

(b) Initial fibre buckling (c) Cracking at lower edge (d) Full kink band

Figure 5.5: Formation of a kink band (from [94]).

compression side [94] is registered (figure 5.5c). Finally, the kink band is fully formed when fibres fail at the top side of the kink band (figure 5.5d). The critical buckling load is thus a function of the properties of both the fibre and the matrix.

Fibre fracture

Fibre fracture occurs when the longitudinal tensile or compressive strength of the fibre is achieved. As the previously mentioned damage mechanisms appear and the stress field becomes even more complex due to the presence of material discontinuities (cracks) in both constituents and their interface, the accumulated damage compromises the structural integrity of the component. Damage progression becomes catastrophic and the ultimate strength of the material is achieved. Fibre fracture is predicted at the meso-scale by *ultimate ply failure* theories.

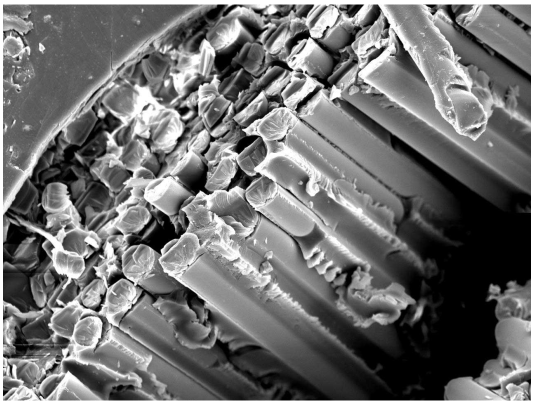

Figure 5.6: Fibre fracture (from [95]).

Fibre splitting

Although a rare situation, fibres can also suffer transverse fracture if the transverse or hoop stresses in the fibre surpass the transverse strength of the fibre. This situation gives origin to radial interface cracks which propagate to the matrix. Conversely, fibre splitting can also be caused by already existing matrix cracks which, instead of propagating around the fibre and creating interfacial debonding, propagate straight through the fibre.

Having presented the different damage mechanisms visible at the micro-scale level, some numerical and analytical attempts to predict the activation of those damage mechanisms are presented next.

5.1.4 Damage prediction at the micro-level: state of the art

Several authors have tried to predict the damage activation and propagation for the composite as an homogenised material or for each of the individual constituents.

Asp et al. [64]-[65] conducted several experimental tests on an epoxy matrix material. The results suggest that under a purely dilatational tension load, or with a very low deviatoric load component, microcavitation begins forming inside the epoxy, leading to a highly brittle behaviour with reduction of the strain to failure. Under these conditions (low distortional energy density), Asp and colleagues proposed the use of the dilatational energy density criterion as a failure criterion for epoxies. The criterion can be summarised in the following equation:

$$U_v = \frac{1-2\nu}{6E}\left(\sigma_1 + \sigma_2 + \sigma_3\right)^2 \tag{5.12}$$

Trias et al. [50] applied the dilatational energy criterion for matrix cracking prediction in a two-scale probabilistic method. At the micro-scale, the material possesses random distribution of the reinforcements, with the elastic properties of both constituents considered constants. At the macro-scale, the elastic properties of the material are known from either experimental tests or by means of a statistical representative volume element, while the failure properties are random. These are obtained from the microstructure models: a micro-scale model represents a solution point in the macro-scale and as long as the micro-scale model is statistically representative of the material, the results are valid for the macro-scale. Trias obtained a set of probability density functions of the dilatational energy density for three different composite materials. The results can then be used for reliability studies or to analyse scaling effects.

There are two fundamental limitations to the dilatational energy density criterion. The first, is that it can only be applied if the deviatoric component of the stress tensor is low. This is not the case of the matrix material in a composite medium with a random distribution of the reinforcements. The second limitation is that it does not account for damage propagation, but only for damage initiation.

In order to circumvent some of these limitations, Gosse [96] proposed a failure criterion based on strain invariants which is capable of predicting not only the initiation of damage in the matrix, but also its propagation until failure. The criterion makes use of the first invariant of strain tensor (or volumetric strain), I_1', and the equivalent strain, ε_{eq}, defined by:

$$\varepsilon_{eq} = \sqrt{\frac{1}{2}\left((\varepsilon_1 - \varepsilon_2)^2 + (\varepsilon_2 - \varepsilon_3)^2 + (\varepsilon_3 - \varepsilon_1)^2\right)} \tag{5.13}$$

The criteria is based in a set of material constants determined from experimental tests performed on the composite material. In order to define the matrix behaviour, the properties required are the critical first invariant of strain, $I_1'^{\,cr}$, the critical equivalent strain, $\varepsilon_e{}^{cr}$, the critical initial second invariant of strain, $I_2'^{\,i}$, and the critical final second invariant of strain, $I_2'^{\,f}$. The first invariant is responsible for controlling the volumetric straining; under low or null deviatoric conditions, the matrix material will fail by microcavitation or crazing (only microcavitation in the case of epoxies). This means that $I_1'^{\,cr}$ represents damage initiation.

The second invariant of strain tensor can be determined from the first invariant and the equivalent strain by:

$$I_2' = \frac{\left(I_1'^{\,2} - \varepsilon_{eq}{}^2\right)}{3} \tag{5.14}$$

In this model, Gosse [97] considers that the second invariant is a measure of damage propagation in the matrix and the equivalent strain is the dominant factor in it. This is demonstrated because the extracted values for I_2' from the experimental tests at the initiation of damage and ultimate failure are always negative (as per equation (5.14)).

Although the objective is to predict the initiation and propagation of damage in the matrix, this method is closer to a meso-scale method of damage modelling than of micro-scale modelling because there is no influence of the individual constituents' properties.

Swaminathan and Ghosh [13] attempted to determine the representative volume element size for composite microstructures undergoing fibre-matrix interfacial debonding. The interfacial debonding was simulated using a bilinear cohesive zone law in a Voronoi cell finite element model. No other damage mechanism was modelled.

Ghosh et al. [98] proposed an adaptive multi-level computational model for multi-scale analysis of composite structures undergoing damage initiation and growth at the micro-structural level. The damage was considered to be induced by debonding at the fibre-matrix interface. The same Voronoi cell finite element model was used to simulate damage initiation and propagation as before [13]. The inclusion of other damage mechanisms is envisaged in a future work.

Barbero et al. [99] have proposed a model for damage evolution in polymer composites based in a combination of two constituent-level models and an interphase model. The damage models are based in continuum damage mechanics, i.e. the damage evolution in each phase is represented by a state variable, in the form of a second-order damage tensor. The failure surface chosen corresponds to the Tsai-Wu criterion. However, to completely define the constitutive model, especially the evolution of damage segment, it is necessary to determine experimentally a total of nine parameters, three per phase. The parameters are then adjusted to experimental data from standard tensile and shear tests.

Lubineau et al. [100] presented a very pragmatic approach on multi-scale modelling of the degradation of laminated composites. The continuous damage mechanics theory was used for progressive mechanisms on the ply's scale, whereas finite fracture mechanisms were used for discrete mechanisms, through minimum cracking surfaces introduced a priori on the composite.

Bulsara et al. [48] performed a numerical analysis on a volume element with a random distribution of fibres to study the initiation of interfacial damage and consequent progression into the matrix following a radial direction relatively to the fibre (i.e. its interface) where damage initiated. The activation criterion was a simple maximum normal stress criterion, applied to each of the damage mechanisms modelled.

Wang and Yan [101] studied the matrix tensile failure in unidirectional composites with a V-notch. The distribution of fibres was considered regular. The first form of the inter-scale theory is presented in [101], where an homogenisation/localisation algorithm is presented. The model aims at simulating a macro-scale failure mode, but with a formulation of the theory taking place at the micro-scale. The theory adequately mimics the linear elastic fracture mechanics for a large notch and provides qualitatively interesting results for small notches. As is mentioned by the authors, the theory is still in an embryonic status as it only allows for the study of transverse tension in the matrix.

Grufman and Ellyin [102] expanded a study previously performed [103] in order to analyse the influence of damage in the matrix caused by a transverse tension load in the size of the representative volume element. The idea was to apply a Kolmogorov goodness-of-fit test, with a low significance level, at which samples of the real micro-distribution of fibres in the material are deemed representative of the global population, i.e. the lamina. It was concluded that a 300×300 μm RVE size was necessary to properly study the initiation and propagation of damage in the matrix. Considering the radius of the fibre as reference, the volume element should be $50\times$ the fibre radius, a result which is in agreement with Trias et al. [15].

París et al. [104], using a Boundary Element Model (BEM), studied the interface damage mechanism on a single fibre under the effect of transverse biaxial tension. París and co-workers assumed that there existed an initial crack in the interface between the fibre and the matrix, which would progress around the fibre up to a critical limit, from which the crack would kink towards the matrix and progress in a radial direction. The crack would merge with other cracks around other fibres, thus forming a macro-crack which would lead the material to final fracture. Correa et al. [105] organised a follow up study using the same concepts and techniques, but applied to a transverse compression load case. Correa and colleagues determined that an initial separation on the interface was likely to appear close to an angle approximately equal to 135° to a perpendicular plane to the load (figure 5.7a). Correa demonstrated that, for a single fibre model, this crack would propagate unstably up to the position at 206° downwards and upwards to 130° as per figure 5.7a.

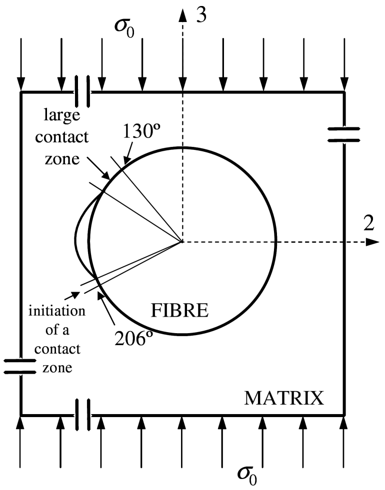

(a) Configuration of the crack at the interface

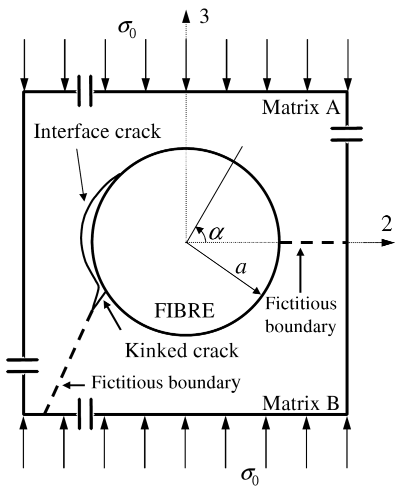

(b) Interface crack after kinking

Figure 5.7: Single fibre model under transverse compression (from [106]).

In a follow up study of [105], Correa et al. [106] studied the further evolution of the interfacial crack after this unstable growth. One of two things could happen: either the crack would continue along the interface, or it would change its direction and progress to the matrix. Correa demonstrated that the last would be the case for a single fibre loaded in compression (figure 5.7b). The inclination of the kinked crack with relation to the perpendicular to the loading direction is determined to be between 50° and 58°. This is in agreement with experimental observations which show that the fracture plane in a composite under transverse compression is approximately 53°. It should be noted however that the 53° fracture angle is a macro-angle, i.e. it is measured at the lamina, or even laminate, level. At the micro-scale, there is no strong evidence that the fracture angle will be of 53° for all fibres in a high fibre volume reinforced composite.

Canal et al. [52] performed a study on an epoxy matrix with circular voids under transverse tension. The epoxy was modelled with a modified Drucker-Prager model to account for damage [107] and pressure sensitiveness of a porous material. Viscoplastic regularisation was implemented in order to control mesh dependency effects. Canal and colleagues concluded that an increase in the percentage of voids leads to a decrease in the overall elastic limit of the material and to a faster progression of damage through the matrix.

In a follow up contribution, Canal et al. [108] analysed the behaviour of a ductile rubber-toughened epoxy matrix in a composite under a biaxial load of transverse tension and transverse shear. The matrix was modelled with an elasto-viscoplastic constitutive model, while the fibre is considered isotropic in the transverse plane. The influence of the interface between matrix and fibre was also studied. The results were compared with two classical phenomenological failure criteria – Puck [109] and Hashin [87]. It was found that the lack of interface representation in these failure criteria represented a considerable drawback for these theories, especially in the case of a weak interface.

González and Llorca [110] performed a micromechanical study on a representative volume element with randomly distributed reinforcements. The matrix was modelled with an elasto-plastic constitutive model, where the Mohr-Coulomb plasticity criterion was chosen. The fracture plane required to completely define the criterion was considered to be equal to 53°. The interface between matrix and fibres was also modelled using cohesive elements and two different failure strengths for the interface were used: weak and strong. The volume element was subjected to a pure transverse compression load. It was determined that the failure mechanism activated was different depending on the strength of the interface – interfacial decohesion in the case of weak interface or localisation on a shear band on the matrix if the strength of the interface was equal to the strength of the matrix.

In a follow up study, Totry et al. [111] applied a combination of transverse compression and transverse shear to the volume element. Similar results were obtained regarding the influence of the interface strength. The failure locus obtained from the micromechanical model was also extracted from the results of this multi-axial load and compared with predictions from three lamina failure models – Hashin [87], Puck [88], and LaRC [90]. Because these lamina failure models are also based on the Mohr-Coulomb model to predict matrix failure under compressive loads, results for the strong interface case are in very good agreement with the predictions from these models. However, for the weak interface case, the results do not agree very well, especially for the case where shear stresses are dominant since it is the interface decohesion and not a localised shear band on the matrix that dominates failure. Totry et al. [56] also concluded that the loading path was not important for the activation and evolution of damage in a composite under transverse compression and shear.

Later, Totry et al. [112] performed a comparative analysis between a representative volume element loaded in a multiaxial state of transverse compression and longitudinal shear, and the experimental data available from Vogler and Kyriakides [113]. This time, a three-dimensional representative volume element was used to account for the longitudinal shear stresses. The results obtained from the micromechanical analysis are in excellent agreement with the experimental data demonstrating the usefulness of micromechanical analyses. Still, there was no damage model implemented for the epoxy matrix, but only for the interface between matrix and fibre.

Rolfes et al. [80] performed micromechanical analyses on a unit cell made of voxel elements, simulating a weft-knitted fabric. The matrix was modelled with an elasto-plastic with damage constitutive model. The plasticity criterion chosen was the paraboloidal criterion detailed in chapter 4. The damage activation criterion is defined on the positive side of hydrostatic stresses by a paraboloidal built from the uniaxial tensile and shear ultimate strengths, while on the compressive side of the hydrostatic stresses, a straight line defined by the uniaxial compressive and shear ultimate strengths is used. Hardening of the matrix is obtained from standard experimental tests of the matrix. Stiffness degradation is controlled by only one scalar variable and the damage evolution law is defined by a linear relation with the effective stresses (undamaged material). The fibres were modelled using a transversely isotropic yield surface while the damage activation function was defined in the fibre direction as well as in the transverse direction. Comparing the homogenised results from the unit cell with test data available from WWFE [31], a good agreement is obtained although there was a need to tweak some of the parameters of the resin's constitutive model since they were not given in WWFE [31].

Rolfes et al. [114] have also performed a study in which the same strain energy damage variable and fracture energy formulations were used. A viscoelastic regularisation was also implemented in order to control mesh dependency and to provide numerical stabilisation.

Fiedler et al. [70] performed a set of experimental tests on epoxy material in order to fully characterise the tensile, compressive and shear behaviours of these materials. The results can be summarised in figure 5.8. The open circles represent the beginning of non-linear behaviour for each of the three tests, while the closed circles represent the points of final failure. Each set of three points can be approximated by a parabola (curves I and II) in the octahedral stress space. These are the yield and failure surfaces of the tested epoxy material.

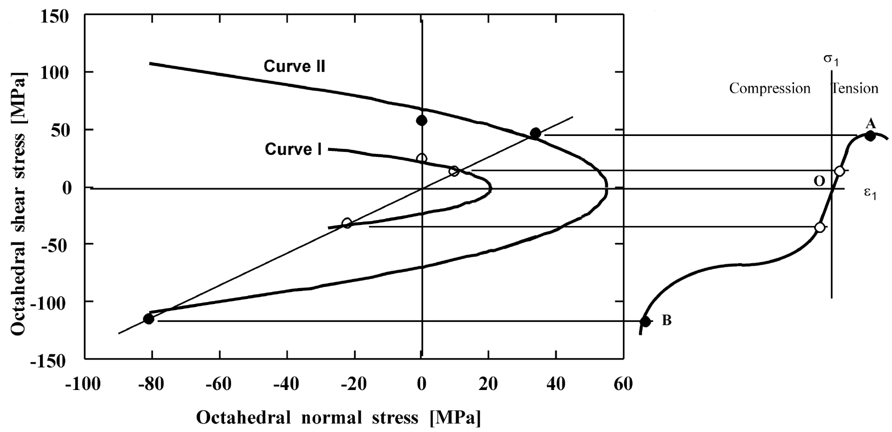

Figure 5.8: Parabolic yield and failure criterion (from Fiedler et al. [70]).

Fiedler and colleagues then performed a series of numerical analyses [71]-[72] in order to study the influence of thermal stresses on the onset of damage on the matrix for a composite under transverse tensile loads. An hexagonally periodic distribution of the reinforcements was used and the hoop, longitudinal and radial stresses around the fibres were studied as a function of the fibre volume fraction and temperature. It is concluded that the residual thermal stresses have a strong influence on the initiation of damage on the matrix. The increase of fibre volume fraction leads to the same effect, meaning that the transverse tensile strength of composites is always lower than the strength of the pure resin.

The parabolic failure criterion is identical to the yield criterion already mentioned in chapter 4, but simply substituting the yield strengths by the failure strengths. It is a very simple to implement criterion, and provides good agreement with experimental data [70] available for epoxy materials.

This is the chosen criterion to be applied for an epoxy matrix material throughout this thesis. The next section will provide some insight on the different strategies to analyse and study damage onset and evolution using numerical simulation tools. Section 5.3 will present the analytical definition of the two constitutive damage models for each constituent.

5.2 Numerical simulation of damage

As reviewed in the previous section, many strength-based failure criteria have been developed through the years that can be used to predict damage initiation and, under specific conditions, may also predict ultimate structural collapse of the material. For composite structures, which are capable of accumulating damage before ultimate failure, these failure criteria might not be capable of providing adequate information regarding the different failure mechanisms in action and their extension and severeness.

The numerical simulation of damage and structural collapse of composite materials using finite element analyses is normally performed under the concepts of either fracture mechanics or continuum damage mechanics, or even a combination of the two theories. Fracture mechanics is dependent on the existence of a pre-crack. Using linear elastic fracture mechanics, crack propagation can be predicted by comparing the energy release rate (or stress intensity factors), with the corresponding critical values determined by experimentation. Several techniques exist to determine the stress intensity factors or the energy release rates, notably the VCCT (Virtual Crack Closure Technique), J-integral and collapsed finite elements.

On the other hand, continuum damage mechanics does not require the existence of a pre-crack in the material, or even any hint on the location of crack initiation. The theory is based on the standard continuum mechanics framework with continuous displacement fields, which allows for an easy numerical implementation. The progressive loss of material integrity is modelled by a degradation of the material stiffness, leading to greater strains in the damaged area, but without disrupting the continuity of the displacement field. The only drawback of this technique is that as soon as damage begins to localise, the problem becomes ill-posed. From a numerical point of view, the problem manifests itself by a strong sensitivity of the solution to the size of finite elements. The problem is illustrated in figure 5.9.

Consider a beam of constant cross-section, A, clamped on one end and with a longitudinal force applied on the other end, as per figure 5.9a. The length of the beam is given by L. Let us assume that damage will first manifest in a central section of the beam with length l^e and that the material's constitutive law is given by the curve in figure 5.9b. Up to a strain of ε_i, all sections of the beam behave linearly elastic and at that moment, the beam is withstanding the maximum force it can bear. After that, the strength of the beam starts decreasing. Stresses can decrease either by elastic unloading (decreasing strain) or softening (increasing strain). The equation of equilibrium of this problem forces the stress profile to remain constant throughout

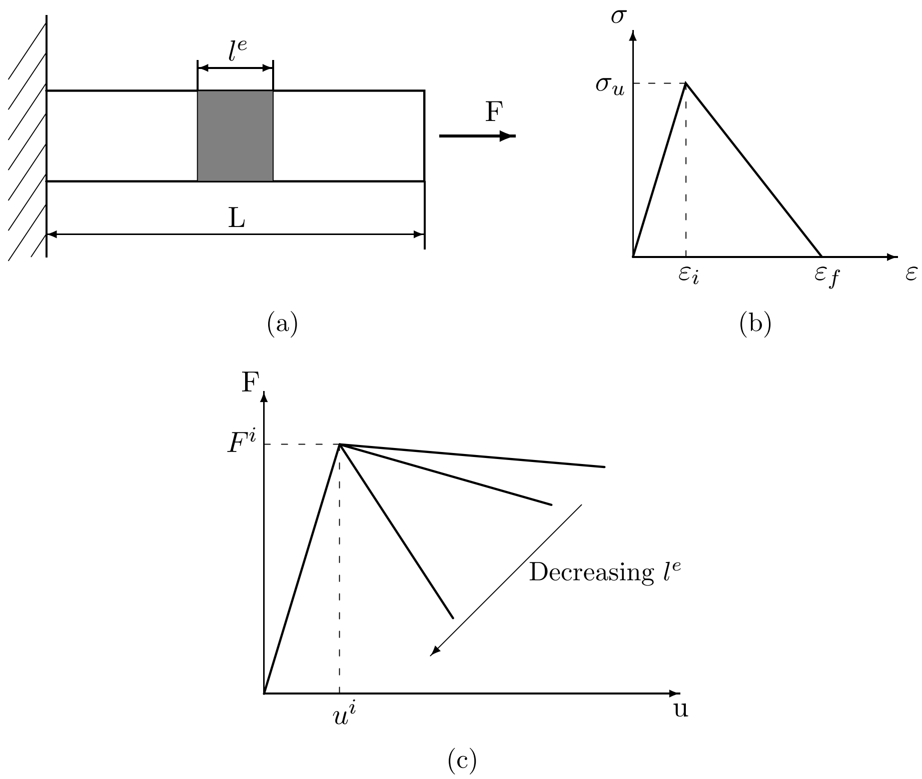

Figure 5.9: Mesh-dependency caused by ill-posedness of CDM.

the entire length of the beam, but the same can not be said regarding the strain profile, since for each stress level, there are two possible values of the strain – one corresponding to elastic unloading and the other to softening (figure 5.9b).

When stress reaches zero, the strain in the damage section of the beam (the material suffers softening) is given by ε_f, while the strains everywhere else will be zero (elastic unloading). The displacement, however, is given by $l^e\varepsilon_f$, since the strains are only different from zero in the damaged (softened) section of the beam. In other words, the displacement field depends on the size l^e of the damaged region. This means that the problem has infinite solutions after the maximum stress is achieved.

Considering now that the beam is discretised in finite elements, it becomes clear that it will be the size of the elements which will dictate the size of the section where the strains localise, i.e. the damaged area. The smaller the finite elements are, the steeper the inclination of the descending curve in figure 5.9c will be. In the limit, when the element length tends to zero, the energy dissipated in the section where strains have localised is given by

$$\lim_{l^e \to 0} \int_V \int_0^{\varepsilon_f} \sigma d\varepsilon dV = \lim_{l^e \to 0} \frac{1}{2} \sigma_u \varepsilon_f A l^e = 0 \tag{5.15}$$

which is obviously a physically impossible scenario.

Sensitivity of finite element solutions to the element size compromises the validity of the results obtained, and is thus not acceptable. There are two main procedures to assure the objectivity of the solution: methods acting at the constitutive model level, or the definition of the material response as a function of the characteristic element length in the computational model. The second method was chosen for this thesis and it will be described next.

5.2.1 Crack band model

A simple methodology to impose the objectivity of the solution after the maximum strength of the material has been achieved was proposed by Bažant and Oh [115]. The proposal is known as *the crack band model* and consists in the use of one more variable in the definition of the constitutive model – the characteristic element length – which leads to the assurance that the computed dissipated energy due to the creation of two new surfaces after fracture is constant. The theory was first applied to concrete which exhibits a gradual strain-softening due to micro-cracking. Fracture is modelled as a blunt smeared crack band, which is justified by the random nature of the micro-structure of concrete which leads to a crack propagation around its aggregates instead of in a straight line. The technique assumes that the crack band is one-element thick.

Material fracture properties are characterised by only three parameters – the fracture energy, the maximum uniaxial strength and the width of the crack band which defines the fracture process zone ahead of a crack tip, and is represented in the model by the characteristic element length. The fracture energy, G_{fe}, is the energy necessary for the creation of two fracture surfaces. It can be related with the characteristic element length by

$$\Psi = \frac{G_{fe}}{l^e} \tag{5.16}$$

where Ψ is the energy dissipated per unit volume and l^e is the characteristic element length of the finite element. Ψ is obtained by integrating the rate of energy dissipation due to damage which, in its turn, can be obtained from the derivative of the complimentary free energy density. A deeper insight on this point will be given in the discussion of the damage models implemented in this thesis.

In the next subsection, the damage mechanics theory applied to a transversely isotropic material and an isotropic material will be outlined. This theory will serve as basis for the development of the damage models implemented on this thesis.

5.2.2 Damage mechanics theory

The damage mechanics basic theory will be outlined in the present subsection. This will serve as a basis of work for the development of the damage models to be implemented on this thesis. The theory will be presented for the most general material case and posteriorly simplified to the transversely isotropic and isotropic cases.

The goal of damage mechanics is to predict the material response in the presence of damage that initiates at some stress state and propagates as the applied loads increase the stresses in the material. All materials exhibit some level of damage at a very small scale. Damage can manifest itself in the form of voids or micro-cracks, so the expression *damage-free* is a function of the scale under study. Here, it will be considered that a damage-free state exists at the beginning of an analysis for the size of the representative volume elements that will be used. The materials under consideration will be considered to suffer only an increase in the damage level, i.e. there exists a progressive deterioration of the stiffness of the material.

Kachanov [116] presented a very simple way to represent the loss of stiffness under a creep failure load. It consisted in using a single scalar variable, d, to represent the decrease in stiffness. Generalising the concept to the different material stiffness properties, the following relations can be written

$$\begin{aligned} E &= (1-d_E)E_o \\ G &= (1-d_G)G_o \\ K &= (1-d_K)K_o \\ \nu &= (1-d_\nu)\nu_o \end{aligned} \tag{5.17}$$

where d_E, d_G, d_K, and d_ν represent the different scalar damage variables associated with the loss of Young's modulus E_o, shear modulus G_o, bulk modulus K_o, and Poisson's ratio ν_o. The subscript o indicates the stiffness values while the material is still in a damage-free condition. The value of each of the damage variables is obviously smaller than one and greater than zero. It is clear that these scalar variables are not independent from one another, especially if one considers that the material becomes anisotropic after damage initiation. Under such circumstances, the number of damage variables necessary to fully characterise damage initiation and progression becomes difficult to define. With this in mind, Cauvin and Testa [117] attempted to identify a fundamental set of damage variables which would take in account the symmetry or lack of symmetry in damage, independently of the initial material symmetries.

A tensorial representation of damage is the most general and formal way to represent the direction of formed cracks depending on the load history, boundary conditions and initial material and geometrical properties. Like a fourth-order tensor is necessary to fully characterise the elastic behaviour of a material, also only a fourth-order tensor can fully capture all the effects that can take place after damage initiation – loss of material symmetry, loss of stiffness, etc. Considering that the relation between the elastic response of the virgin material, $\boldsymbol{C_o}$, and the damaged elastic moduli, $\boldsymbol{C}$, is linear, then the two fourth-order tensors can be related by

$$\boldsymbol{C} = \boldsymbol{R_8} :: \boldsymbol{C_o} \tag{5.18}$$

where $\boldsymbol{R_8}$ is an eighth-order tensor representing the level of damage affecting the stiffness of the material. In the absence of damage, $\boldsymbol{R_8}$ must reduce itself to the eighth-order identity tensor, $\boldsymbol{I_8}$. This definition can be used to rewrite equation (5.18):

$$\boldsymbol{C} = (\boldsymbol{I_8} - \boldsymbol{D_8}) :: \boldsymbol{C_o} \tag{5.19}$$

A schematic of this relation for an uniaxial tensile load is presented in figure 5.10. Considering that the material does not suffer any permanent deformations and that damage is the only cause of stiffness reduction, the stress increases linearly up to the ultimate stress, σ_u. At that point, damage starts accumulating in the material and the damage variable, d, associated with the reduction of the Young's modulus, increases. At point C, the material is unloaded (returns to point A). Because the material has accumulated some percentage of damage in the form of micro-cracks or similar, upon reloading the new material stiffness will be given by $(1 - d)\,E_o$, less than the original. At the stress level given by point C, damage will resume its propagation until the material is no longer capable of supporting any stress (point D).

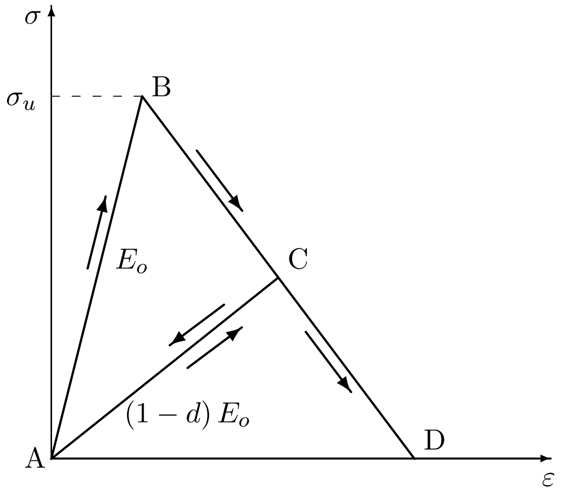

Figure 5.10: Idealised elastic response of damaged material under uniaxial load.

In 1968, Rabotnov [118] introduced the concept of *effective stresses*, $\tilde{\boldsymbol{\sigma}}$, as the stress tensor to be applied to a virgin representative volume element in order to obtain the same elastic strain tensor produced by applying the actual stress tensor, $\boldsymbol{\sigma}$, to the damaged volume element. The principle of strain equivalence is thus applied here since the same elastic strain is considered in both damaged and undamaged cases, and it can be written as:

$$\begin{aligned} \boldsymbol{\sigma} &= \boldsymbol{C} : \boldsymbol{\varepsilon} \\ \tilde{\boldsymbol{\sigma}} &= \boldsymbol{C_o} : \boldsymbol{\varepsilon} \end{aligned} \tag{5.20}$$

Application of the principle of strain equivalence allows the reduction of the eighth-order tensor $\boldsymbol{R_8}$ to a fourth-order tensor, $\boldsymbol{R_4} = \boldsymbol{I_4} - \boldsymbol{D_4}$ [117]. Considering that an arbitrary load history can lead to an anisotropic damaged material, even if the virgin material is isotropic, and taking in consideration the general symmetry conditions imposed by the stress and strain tensors, the fourth-order tensor $\boldsymbol{D_4}$, which defines the presence or not of damage, contains 21 independent elements, just like the fourth-order elastic modulus tensor $\boldsymbol{C_o}$ of the pristine material. If the material is originally isotropic, a series of fifteen constraints can be determined which describe general anisotropic damage [117]. However, the damage tensor does not possess the full symmetry typical of elastic modulus tensors, $\boldsymbol{C_o}$ and $\boldsymbol{C}$.

The consideration of additional symmetries in the damaged material further reduces the number of independent elements of the fourth-order damage tensor, $\boldsymbol{D_4}$. In this thesis, two kinds of symmetries will be considered, one for each of the composites' constituents: isotropy for the matrix, and transverse isotropy for the reinforcement. These two possible situations will be considered next in more detail.

Transverse isotropy of damaged material

Considering that the material acquires (or maintains) transverse isotropy, both $\boldsymbol{C}$ and $\boldsymbol{D}$ tensors can be reduced to only five independent variables. The damage tensor can be defined by:

$$\boldsymbol{D} = \begin{bmatrix} D_1 & D_2 & D_2 & 0 & 0 & 0 \\ D_2^* & D_3 & D_4 & 0 & 0 & 0 \\ D_2^* & D_4 & D_3 & 0 & 0 & 0 \\ 0 & 0 & 0 & (D_3 - D_4)/2 & 0 & 0 \\ 0 & 0 & 0 & 0 & D_5 & 0 \\ 0 & 0 & 0 & 0 & 0 & D_5 \end{bmatrix} \tag{5.21}$$

where the value of D_2^* is given as a function of the remaining damage parameters by:

$$D_2^* = \frac{1}{1-\nu_{12}} \left[D_2 + \nu_{12} \left(D_1 - D_3 - D_4\right)\right] \tag{5.22}$$

The different values for D_2 and D_2^* is the reason for the lack of symmetry on the damage tensor. Deduction of these equations can be followed in Cauvin and Testa [117].

Isotropic damage

If one assumes that the material is isotropic in its pristine state, and remains isotropic even after damage has started to coalesce, then the tractability of the damage tensor becomes significantly simplified as there are only two independent variables – one affecting the Young's modulus, and the other affecting the Poisson's ratio. The variable related with the shear modulus can be determined by [117]:

$$D_{1212} = \left(D_{1111} - D_{1122}\right)/2 \tag{5.23}$$

The damage tensor becomes defined by the following:

$$\boldsymbol{D} = \begin{bmatrix} D_1 & D_2 & D_2 & 0 & 0 & 0 \\ D_2 & D_1 & D_2 & 0 & 0 & 0 \\ D_2 & D_2 & D_1 & 0 & 0 & 0 \\ 0 & 0 & 0 & \dfrac{(D_1 - D_2)}{2} & 0 & 0 \\ 0 & 0 & 0 & 0 & \dfrac{(D_1 - D_2)}{2} & 0 \\ 0 & 0 & 0 & 0 & 0 & \dfrac{(D_1 - D_2)}{2} \end{bmatrix} \tag{5.24}$$

It is possible to establish a relation between the original material properties, namely the Young's modulus, the shear modulus, the bulk modulus, and the Poisson's ratio, and the two independent damage variables in the damage tensor. This allows for a better understanding of the physical meaning behind each of the two parameters and the influence each one has on the damaged material properties. The relations are given by the following set of equations [119]:

$$E = (1 - D_E)\, E_o \quad \Rightarrow \quad D_E = 1 - \frac{(D_1 - 2D_2)\,(1 - D_1 + D_2)}{(1 - D_1) - (1 + 2\nu)\, D_2} \tag{5.25}$$

$$G = (1 - D_S)\, G_o \quad \Rightarrow \quad D_S = D_1 - D_2 \tag{5.26}$$

$$K = (1 - D_K)\, K_o \quad \Rightarrow \quad D_K = D_1 + 2D_2 \tag{5.27}$$

$$\nu = (1 - D_\nu)\, \nu_o \quad \Rightarrow \quad D_\nu = 1 - \frac{(1 - D_1)\, \nu - D_2}{(1 - D_1) - (1 + 2\nu)\, D_2} \tag{5.28}$$

With equations (5.26) and (5.27), a damage domain can be defined as a function of the two damage parameters as can be seen in figure 5.11a [119]. D_1 varies between 0 and 1, while D_2 varies between $-1/3$ and $1/3$. Excluding the values of D_2 for which the Poisson's ratio becomes negative, then the maximum value for D_2 becomes $\nu/\,(1+\nu)$. The domain $ABCO$ in figure 5.11a bounds all the possible paths that damage can follow during its progression. Point O represents a virgin material, while segments BC and BA correspond to a fully damaged material.

Some particular cases of damage paths can be seen in figure 5.11b. These paths have the common characteristic of forcing a specific value to the damage parameter D_2. Of these, the only path that starts in the origin O and finishes in B is the path that enforces a constant Poisson's ratio throughout the damage progression, i.e. $D_2 = 0$. This situation provides a further simplification of the damage tensor, reducing it to $(1-d)\,\boldsymbol{I_4}$. The damaged moduli are thus simply calculated by multiplying $(1-d)$ by the undamaged material moduli.

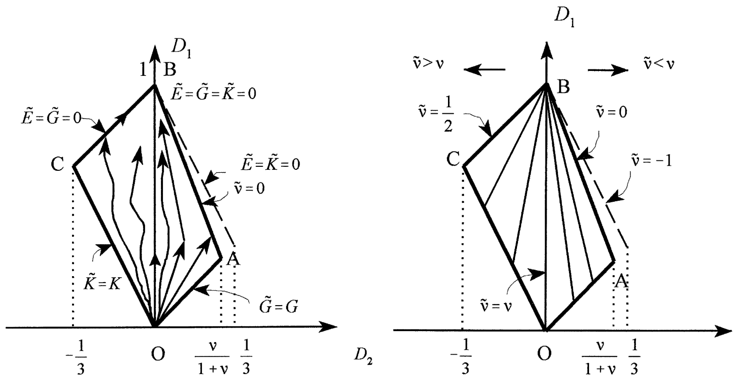

(a) Different damage paths (b) Lines of constant Poisson's ratio

Figure 5.11: Damage domain for isotropic damaged materials (from [119]).

Ladevèze et al. [120] was the first to introduce this simplification into a meso-scale damage model and apply it to composite materials. Ladevèze's theory considers a composite to be a laminated structure consisting of two elementary constituents – layers of composite and interface in between the layers. The theory is based upon the mean value of stress in each layer and allows the damage to appear independently on each layer.

Lemaître and Chaboche [121] proposed a damage model using only one variable to define the damage path and assuming that the Poisson's ratio would remain constant.

Maimí et al. [122] performed an identical consideration for the non-variation of the Poisson's ratio. A thermodynamically consistent damage model in plane stress was presented assuming only three independent damage variables, two related with the longitudinal and transverse Young's moduli, and the third affecting the shear modulus. Later, Maimí et al. [123] expanded the model to three dimensions considering that the material is initially transverse isotropic and remains as such during damage progression. The model now requires four independent parameters in the damage tensor – three parameters affecting the longitudinal and both transverse Young's moduli, and the fourth related with the longitudinal shear modulus.

The theories presented thus far were applied to composite materials at the meso-scale level assuming equal stress and strains along the thickness of a layer. The constitutive model developed in this thesis will apply the concepts described in this chapter to the two constituents of the composite – matrix and fibre. The next section will describe the analytical deduction of the damage model for both matrix and fibre.

5.3 Definition of damage model

This section will be dedicated to the analytical definition of the damage models, one for the reinforcing material and another to be added to the already existing constitutive elasto-plastic model for the matrix. Each of the two constituents of a composite material – matrix and fibre – will be considered separately.

The two constitutive damage models will be developed in the framework of the thermodynamics of irreversible processes. This framework allows to establish the necessary constitutive equations to completely define the mechanical behaviour of the material before and after damage onset. It also avoids a number of physical incompatibilities which can occur during implementation.

5.3.1 Matrix

The damage model developed for the matrix is based on the works by Fiedler et al. [70], where an epoxy material was tested in uniaxial tension, uniaxial compression, and pure shear. The results suggest that both yield stress and ultimate stress can be predicted by a paraboloidal surface (as per figure 5.8).

In the light of the thermodynamics approach to be followed here, it is necessary to first define the complementary free energy density in the material. This is a scalar function, positive definite, and it must be zero at the origin with respect to the stresses [124]. In order to achieve an isotropic damage model, the following definition for the complementary free energy density is proposed:

$$\begin{aligned} \mathscr{G}_m &= \frac{\sigma_{11}^2+\sigma_{22}^2+\sigma_{33}^2}{2E_m\left(1-d_m\right)} - \frac{\nu_m}{E_m}\left(\sigma_{11}\sigma_{22}+\sigma_{22}\sigma_{33}+\sigma_{33}\sigma_{11}\right) + \\ & \quad + \frac{1+\nu_m}{E_m\left(1-d_m\right)}\left(\sigma_{12}^2+\sigma_{13}^2+\sigma_{23}^2\right) + \mathscr{G}_m^P \end{aligned} \tag{5.29}$$

where E_m and ν_m are the Young's modulus and Poisson's ratio of the matrix, respectively. Only one damage variable, d_m, is being considered here, and it affects only the Young's modulus of the material. It thus shall be assumed that the Poisson's ratio of the material is not to be affected by a second damage variable as discussed in section 5.2. $\mathscr{G}_m^P$ represents the contribution of plastic flow to the stored energy. This contribution, although not explicitly defined, has been considered in chapter 4. To ensure the irreversibility of the damage process, the rate of change of the complementary free energy must be greater than the externally applied stresses:

$$\dot{\mathscr{G}}_m - \dot{\boldsymbol{\sigma}} : \boldsymbol{\varepsilon} \geqslant 0 \tag{5.30}$$

Equation (5.30) represents the positiveness of the dissipated energy required by any constitutive model [124]. Expanding the equation after application of the chain rule of derivation and recalling the symmetry of both stress and strain tensors:

$$\left(\frac{\partial \mathscr{G}_m}{\partial \boldsymbol{\sigma}} - \boldsymbol{\varepsilon}\right) : \dot{\boldsymbol{\sigma}} + \frac{\partial \mathscr{G}_m}{\partial d_m} \cdot \dot{d}_m \geqslant 0 \tag{5.31}$$

Ensuring positive dissipation of the mechanical energy requires the expression in between brackets in equation (5.31) to be equal to zero. In other words, the strain tensor is given by the derivative of the complementary free energy density with respect to the stress tensor,

$$\begin{aligned} \boldsymbol{\varepsilon} &= \frac{\partial \mathscr{G}_m}{\partial \boldsymbol{\sigma}} = \\ &= \frac{\boldsymbol{\sigma}}{2G_m\left(1-d_m\right)} - \frac{\nu_m d_m}{E_m\left(1-d_m\right)} \boldsymbol{I} \cdot \boldsymbol{I} : \boldsymbol{\sigma} - \frac{\nu_m}{E_m} I_1 \boldsymbol{I} \end{aligned} \tag{5.32}$$

where G_m is the shear stiffness of the matrix. For easiness of implementation, the strain tensor will be defined using engineering shear strains. The terms in equation (5.32) can be rearranged in order to obtain the compliance tensor of the material:

$$\boldsymbol{H_m} = \frac{\partial^2 \mathscr{G}_m}{\partial \boldsymbol{\sigma}^2} =$$
$$= \begin{bmatrix} \frac{1}{E_m(1-d_m)} & -\frac{\nu_m}{E_m} & -\frac{\nu_m}{E_m} & 0 & 0 & 0 \\ -\frac{\nu_m}{E_m} & \frac{1}{E_m(1-d_m)} & -\frac{\nu_m}{E_m} & 0 & 0 & 0 \\ -\frac{\nu_m}{E_m} & -\frac{\nu_m}{E_m} & \frac{1}{E_m(1-d_m)} & 0 & 0 & 0 \\ 0 & 0 & 0 & \frac{1}{G_m(1-d_m)} & 0 & 0 \\ 0 & 0 & 0 & 0 & \frac{1}{G_m(1-dm)} & 0 \\ 0 & 0 & 0 & 0 & 0 & \frac{1}{G_m(1-d_m)} \end{bmatrix} \tag{5.33}$$

Inverting the compliance tensor, $\boldsymbol{H_m}$, the stiffness tensor, $\boldsymbol{C_m}$, can be defined:

$$\boldsymbol{C_m} = \begin{bmatrix} G_d & \lambda_d & \lambda_d & 0 & 0 & 0 \\ \lambda_d & G_d & \lambda_d & 0 & 0 & 0 \\ \lambda_d & \lambda_d & G_d & 0 & 0 & 0 \\ 0 & 0 & 0 & G\left(1-d_m\right) & 0 & 0 \\ 0 & 0 & 0 & 0 & G\left(1-d_m\right) & 0 \\ 0 & 0 & 0 & 0 & 0 & G\left(1-d_m\right) \end{bmatrix} \tag{5.34}$$

where the parameters G_d and λ_d are given by:

$$G_d = \frac{E_m\left(1-d_m\right)\left(1-\nu_m\left(1-d_m\right)\right)}{\left(1+\nu_m\left(1-d_m\right)\right)\left(1-2\nu_m\left(1-d_m\right)\right)} \tag{5.35}$$

$$\lambda_d = \frac{E_m\nu_m\left(1-d_m\right)^2}{\left(1+\nu_m\left(1-d_m\right)\right)\left(1-2\nu_m\left(1-d_m\right)\right)} \tag{5.36}$$

The stiffness tensor in equation (5.34) will allow to perform the stress update based on the increment of elastic strain and on the damage progression. Before that, damage onset needs to be defined. A similar equation to the paraboloidal yield criterion used in chapter 4 is used here, simply replacing the yield strengths with the failure strengths of the matrix.

A damage activation function defines the elasto-plastic domain under a general stress state. The elasto-plastic domain is involved by the paraboloidal surface defined by the tensile and compressive ultimate strengths of the matrix material. The damage activation function becomes thus defined by equation 5.37,

$$F_m^d = \phi_m^d - r_m \leqslant 0 \tag{5.37}$$

where r_m is an internal variable controlled by the damage evolution law and ϕ_m^d is the loading function defined by:

$$\phi_m^d = \frac{3\tilde{J}_2}{X_m^c X_m^t} + \frac{\tilde{I}_1\left(X_m^c - X_m^t\right)}{X_m^c X_m^t} \tag{5.38}$$

In equation (5.38), X_m^t and X_m^c represent the tensile and compressive ultimate strengths of the matrix material, respectively. The two invariants $\tilde{J}_2$ and $\tilde{I}_1$ are determined using the concept of effective stresses. The effective stress tensor, $\tilde{\boldsymbol{\sigma}}$, is computed as:

$$\tilde{\boldsymbol{\sigma}} = \boldsymbol{H_m^o}^{-1} : \boldsymbol{\varepsilon} \tag{5.39}$$

where $\boldsymbol{H_m^o}$ is the undamaged compliance tensor obtained from equation (5.33) by forcing the damage variable equal to zero, $d_m = 0$. Hence, $\tilde{J}_2$ represents the second invariant of the deviatoric effective stress tensor, while $\tilde{I}_1$ represents the first invariant of the effective stress tensor.

After damage onset, the evolution of damage can be measured by the rate of energy dissipation per unit volume:

$$\Xi_m = \frac{\partial \mathscr{G}_m}{\partial d_m} \dot{d}_m = Y_m \dot{d}_m \geqslant 0 \tag{5.40}$$

The complementary free energy definition presented in equation (5.29) assures that the thermodynamic force, Y_m, is always positive:

$$Y_m = \frac{\partial \mathscr{G}_m}{\partial d_m} = \frac{\sigma_{11}^2 + \sigma_{22}^2 + \sigma_{33}^2}{2E_m \left(1 - d_m\right)^2} + \frac{\sigma_{12}^2 + \sigma_{13}^2 + \sigma_{23}^2}{2G_m \left(1 - d_m\right)^2} \geqslant 0 \tag{5.41}$$

It can be concluded that the condition of irreversibility of damage, $\dot{d}_m \geqslant 0$, is sufficient to fulfill the second law of thermodynamics.

In the elasto-plastic regime, the damage activation function is negative, $F_m^d < 0$. When the damage criterion is activated, the condition $F_m^d = 0$ must be satisfied. Just like in the plastic regime, there is also the need here to apply Kuhn-Tucker conditions in order to distinguish loading and unloading situations. These are written in function of the internal variable and the damage activation function:

$$\dot{r}_m \geqslant 0; \quad F_m^d \leqslant 0; \quad \dot{r}_m F_m^d = 0 \tag{5.42}$$

In order to distinguish loading from unloading situations and determine if there is damage evolution or not, the gradient of the loading function, $\dot{\phi}_m^d$ must be determined. If $\dot{\phi}_m^d \leqslant 0$, the state is one of unloading; if the gradient is positive, then there is damage evolution, and the following consistency condition must be satisfied:

$$\dot{F}_m^d = \dot{\phi}_m^d - \dot{r}_m = 0 \tag{5.43}$$

Under the conditions that the internal variable depends exclusively of the damage variable and that the loading function is defined in terms of the strain tensor, the constitutive model can be explicitly integrated [125]–[126]. From the consistency condition in equation (5.43), it can be demonstrated that the internal variable is given by:

$$r_m = \max\left\{1, \max_{t\to\infty}\left\{\phi^d_{m,t}\right\}\right\} \tag{5.44}$$

In order to complete the definition of the damage model, the relation between the internal variable, r_m, and the damage variable, d_m, must be given. This relation is called the damage evolution law and will establish the rate of evolution of damage. While the material is in an undamaged condition, $r_m = 1$, which leads to $d_m = 0$. Equation (5.44) imposes that when damage progresses in the material, $\dot{r}_m \geqslant 0$ and condition (5.40) for positive dissipation is satisfied if $\dot{d}_m \geqslant 0$. This last condition can be fulfilled if the damage evolution law satisfies the condition

$$\frac{\partial d_m}{\partial r_m} \geqslant 0, \text{ since } \quad \dot{d}_m = \frac{\partial d_m}{\partial r_m}\dot{r}_m \geqslant 0 \tag{5.45}$$

When the material is completely damaged, the damage variable will assume the value of 1 while the internal variable r_m will tend to infinity. As discussed in the previous section, when the tangent stiffness tensor is not positive definite, damage localises in a narrow band with the same thickness as the element where damage was activated. Therefore, there is a dependency of the structural response on the mesh size – the smaller the element is in the band of localised damage, the lesser the computed dissipated energy will be.

In order to circumvent this problem, Bažant's crack band model [115] was implemented along with the definition of the damage evolution law. By making use of the characteristic length of the finite element and the fracture toughness, it is possible to regularise the computed dissipated energy,

$$\Psi_m = \int_0^\infty Y_m \dot{d}_m \mathrm{dt} = \int_1^\infty \frac{\partial \mathscr{G}_m}{\partial d_m}\frac{\partial d_m}{\partial r_m}\mathrm{d}r_m = \frac{G_{fm}}{l^e} \tag{5.46}$$

where Ψ_m is the energy dissipated per unit volume, G_{fm} is the energy release rate of the matrix and l^e is the characteristic element length.

The damage evolution law considered here that respects the two boundaries imposed by the value of the damage variable, d_m, when the damage criterion has not been activated yet and when the material is fully damaged, is given by equation 5.47,

$$d_m = 1 - \frac{e^{A_m\left(3-\sqrt{7+2r_m^2}\right)}}{\sqrt{7+2r_m^2}-2} \tag{5.47}$$

where the parameter A_m needs to be computed from solving equation (5.46) as a function of the characteristic element length. In other words, the parameter A_m will be unique for each finite element in the mesh. This damage evolution law has been chosen in order to force damage localisation and strain softening on the material under a tensile load.

The energy dissipated per unit volume for an uniaxial stress condition is obtained by integrating the rate of energy dissipation given by equation (5.40). But first, the relation between the effective stress and the real stress in a uniaxial case must be established. This is achieved by imposing the principle of strain equivalence:

$$\left.\begin{array}{l} \boldsymbol{\sigma} = \boldsymbol{C_m} : \boldsymbol{\varepsilon} \\ \tilde{\boldsymbol{\sigma}} = \boldsymbol{C_m^o} : \boldsymbol{\varepsilon} \end{array}\right\} \boldsymbol{\sigma} = \boldsymbol{C_m} : \boldsymbol{C_m^o}^{-1} : \tilde{\boldsymbol{\sigma}} = \boldsymbol{C_m} : \boldsymbol{H_m^o} : \tilde{\boldsymbol{\sigma}} \tag{5.48}$$

where $\boldsymbol{C_m^o}$ is the undamaged stiffness tensor. For the isotropic material in analysis, the relation between the stress tensor and the effective stress tensor is:

$$\boldsymbol{\sigma} = (1-d_m)\,\tilde{\boldsymbol{\sigma}} + \frac{d_m\,(1-d_m)\,\nu_m}{1+\nu_m\,(1-d_m)}\boldsymbol{I_4} : \left(\tilde{\boldsymbol{\sigma}} - \frac{\tilde{\boldsymbol{I_1}}}{1-2\nu_m\,(1-d_m)}\boldsymbol{I}\right) \tag{5.49}$$

where the fourth-order tensor $\boldsymbol{I_4}$ is defined in Voigt notation by:

$$\boldsymbol{I_4} = \begin{bmatrix} 1 & 0 & 0 & 0 & 0 & 0 \\ 0 & 1 & 0 & 0 & 0 & 0 \\ 0 & 0 & 1 & 0 & 0 & 0 \\ 0 & 0 & 0 & 0 & 0 & 0 \\ 0 & 0 & 0 & 0 & 0 & 0 \\ 0 & 0 & 0 & 0 & 0 & 0 \end{bmatrix} \tag{5.50}$$

Defining now the particular case of an uniaxial tensile load applied to the material, where the effective stress tensor is defined by:

$$\tilde{\boldsymbol{\sigma}} = \begin{bmatrix} \tilde{\sigma}_{11} \\ 0 \\ 0 \\ 0 \\ 0 \\ 0 \end{bmatrix} \tag{5.51}$$

the three normal components of the real stress tensor are given by:

$$\sigma_{11} = \frac{(1-d_m)\left[1-\nu_m(1-d_m)(1+2\nu_m)\right]}{\left[1+\nu_m(1-d_m)\right]\left[1-2\nu_m(1-d_m)\right]}\tilde{\sigma}_{11} \tag{5.52}$$

$$\sigma_{22} = \sigma_{33} = \frac{-\nu_m d_m(1-d_m)}{\left[1+\nu_m(1-d_m)\right]\left[1-2\nu_m(1-d_m)\right]}\tilde{\sigma}_{11} \tag{5.53}$$

while the three shear components are null, $\sigma_{12} = \sigma_{13} = \sigma_{23} = 0$. The rate of energy dissipation per unit volume for the uniaxial tensile case is obtained by replacing equations (5.52) and (5.53) in equation (5.41):

$$\frac{\partial \mathscr{G}_m}{\partial d_m}^{UN} = \frac{1}{2E_m}\frac{2\nu_m^2 d_m^2 + \left[1-\nu_m(1-d_m)(1+2\nu_m)\right]^2}{\left[1+\nu_m(1-d_m)\right]^2\left[1-2\nu_m(1-d_m)\right]^2}\tilde{\sigma}_{11}^2 \tag{5.54}$$

The derivative of the damage evolution law in order to the internal variable, r_m, is given by:

$$\frac{\partial d_m}{\partial r_m} = \frac{2r_m e^{A_m\left(3-\sqrt{7+2r_m^2}\right)}}{\sqrt{7+2r_m^2}\left(\sqrt{7+2r_m^2}-2\right)}\left(A_m + \frac{1}{\sqrt{7+2r_m^2}-2}\right) \tag{5.55}$$

Finally, the damage activation function defined for the uniaxial tensile case is given by:

$$F_m^{d\,UN} = \frac{\tilde{\sigma}_{11}^2}{X_m^c X_m^t} + \frac{X_m^c - X_m^t}{X_m^c X_m^t}\tilde{\sigma}_{11} - r_m \leqslant 0 \tag{5.56}$$

For damage progression to occur, the Kuhn-Tucker conditions in equations (5.42) impose that the damage activation function must equal zero. Solving equation (5.56) in order to the applied effective stress $\tilde{\sigma}_{11}$:

$$\tilde{\sigma}_{11} = \frac{X_m^t - X_m^c + \sqrt{(X_m^c - X_m^t)^2 + 4X_m^t X_m^c r_m}}{2} \tag{5.57}$$

Substituting now equations (5.54), (5.55) and (5.57) into equation (5.46) the following is finally obtained:

$$\begin{aligned}
&\int_1^\infty \frac{1}{2E_m}\left(\frac{X_m^t - X_m^c + \sqrt{(X_m^c - X_m^t)^2 + 4X_m^t X_m^c r_m}}{2}\right)^2 \times \\
&\times \frac{2\nu_m^2 d_m^2 + [1 - \nu_m (1 - d_m)(1 + 2\nu_m)]^2}{[1 + \nu_m (1 - d_m)]^2 [1 - 2\nu_m (1 - d_m)]^2} \times \\
&\times \frac{2r_m e^{A_m\left(3 - \sqrt{7 + 2r_m^2}\right)}}{\sqrt{7 + 2r_m^2}\left(\sqrt{7 + 2r_m^2} - 2\right)}\left(A_m + \frac{1}{\sqrt{7 + 2r_m^2} - 2}\right) \mathrm{d}r_m = \frac{G_{fm}}{l^e}
\end{aligned} \tag{5.58}$$

This equation must now be solved numerically using the secant method for non-linear equations, along with the definition of the damage evolution law in equation (5.47), in order to solve it for the parameter A_m. A more detailed description of the implementation of the secant method will be presented in the next section.

Constitutive tangent operator

In order to obtain a faster convergence rate of the solution for the non-linear damage model presented here, it is necessary to provide the correct constitutive tangent operator, $\boldsymbol{C_m^T}$, defined by:

$$\dot{\boldsymbol{\sigma}} = \boldsymbol{C_m^T} : \dot{\boldsymbol{\varepsilon}} \tag{5.59}$$

To determine the general form of the constitutive tangent operator, equation (5.59) must be transformed into its rate form:

$$\begin{aligned}
&\boldsymbol{\varepsilon} = \boldsymbol{H_m} : \boldsymbol{\sigma} \Rightarrow \dot{\boldsymbol{\varepsilon}} = \boldsymbol{H_m} : \dot{\boldsymbol{\sigma}} + \dot{\boldsymbol{H}}_{\boldsymbol{m}} : \boldsymbol{\sigma} \Leftrightarrow \\
&\Leftrightarrow \boldsymbol{H_m}\dot{\boldsymbol{\sigma}} = \dot{\boldsymbol{\varepsilon}} - \dot{\boldsymbol{H}}_{\boldsymbol{m}} : \boldsymbol{\sigma} \Leftrightarrow \dot{\boldsymbol{\sigma}} = \boldsymbol{C_m} : \dot{\boldsymbol{\varepsilon}} - \boldsymbol{C_m} : \dot{\boldsymbol{H}}_{\boldsymbol{m}} : \boldsymbol{\sigma} \Leftrightarrow \\
&\Leftrightarrow \dot{\boldsymbol{\sigma}} = \boldsymbol{C_m} : \dot{\boldsymbol{\varepsilon}} - \boldsymbol{C_m} : \boldsymbol{M_m} : \dot{\boldsymbol{\varepsilon}} \Leftrightarrow \dot{\boldsymbol{\sigma}} = \boldsymbol{C_m} : (\boldsymbol{I} - \boldsymbol{M_m}) : \dot{\boldsymbol{\varepsilon}}
\end{aligned} \tag{5.60}$$

The constitutive tangent operator is thus defined by:

$$\boldsymbol{C}_{\boldsymbol{m}}^{\boldsymbol{T}} = \boldsymbol{C}_{\boldsymbol{m}} : (\boldsymbol{I} - \boldsymbol{M}_{\boldsymbol{m}}) \tag{5.61}$$

where the fourth-order tensor, $\boldsymbol{M}_{\boldsymbol{m}}$, is given by:

$$\boldsymbol{M}_{\boldsymbol{m}} = \frac{1}{(1-d_m)^2} \begin{bmatrix} \frac{\sigma_{11}}{E_m}\frac{\partial d_m}{\partial \varepsilon_{11}} & \frac{\sigma_{11}}{E_m}\frac{\partial d_m}{\partial \varepsilon_{22}} & \frac{\sigma_{11}}{E_m}\frac{\partial d_m}{\partial \varepsilon_{33}} & \frac{\sigma_{11}}{E_m}\frac{\partial d_m}{\partial \gamma_{12}} & \frac{\sigma_{11}}{E_m}\frac{\partial d_m}{\partial \gamma_{13}} & \frac{\sigma_{11}}{E_m}\frac{\partial d_m}{\partial \gamma_{23}} \\ \frac{\sigma_{22}}{E_m}\frac{\partial d_m}{\partial \varepsilon_{11}} & \frac{\sigma_{22}}{E_m}\frac{\partial d_m}{\partial \varepsilon_{22}} & \frac{\sigma_{22}}{E_m}\frac{\partial d_m}{\partial \varepsilon_{33}} & \frac{\sigma_{22}}{E_m}\frac{\partial d_m}{\partial \gamma_{12}} & \frac{\sigma_{22}}{E_m}\frac{\partial d_m}{\partial \gamma_{13}} & \frac{\sigma_{22}}{E_m}\frac{\partial d_m}{\partial \gamma_{23}} \\ \frac{\sigma_{33}}{E_m}\frac{\partial d_m}{\partial \varepsilon_{11}} & \frac{\sigma_{33}}{E_m}\frac{\partial d_m}{\partial \varepsilon_{22}} & \frac{\sigma_{33}}{E_m}\frac{\partial d_m}{\partial \varepsilon_{33}} & \frac{\sigma_{33}}{E_m}\frac{\partial d_m}{\partial \gamma_{12}} & \frac{\sigma_{33}}{E_m}\frac{\partial d_m}{\partial \gamma_{13}} & \frac{\sigma_{33}}{E_m}\frac{\partial d_m}{\partial \gamma_{23}} \\ \frac{\sigma_{12}}{G_m}\frac{\partial d_m}{\partial \varepsilon_{11}} & \frac{\sigma_{12}}{G_m}\frac{\partial d_m}{\partial \varepsilon_{22}} & \frac{\sigma_{12}}{G_m}\frac{\partial d_m}{\partial \varepsilon_{33}} & \frac{\sigma_{12}}{G_m}\frac{\partial d_m}{\partial \gamma_{12}} & \frac{\sigma_{12}}{G_m}\frac{\partial d_m}{\partial \gamma_{13}} & \frac{\sigma_{12}}{G_m}\frac{\partial d_m}{\partial \gamma_{23}} \\ \frac{\sigma_{13}}{G_m}\frac{\partial d_m}{\partial \varepsilon_{11}} & \frac{\sigma_{13}}{G_m}\frac{\partial d_m}{\partial \varepsilon_{22}} & \frac{\sigma_{13}}{G_m}\frac{\partial d_m}{\partial \varepsilon_{33}} & \frac{\sigma_{13}}{G_m}\frac{\partial d_m}{\partial \gamma_{12}} & \frac{\sigma_{13}}{G_m}\frac{\partial d_m}{\partial \gamma_{13}} & \frac{\sigma_{13}}{G_m}\frac{\partial d_m}{\partial \gamma_{23}} \\ \frac{\sigma_{23}}{G_m}\frac{\partial d_m}{\partial \varepsilon_{11}} & \frac{\sigma_{23}}{G_m}\frac{\partial d_m}{\partial \varepsilon_{22}} & \frac{\sigma_{23}}{G_m}\frac{\partial d_m}{\partial \varepsilon_{33}} & \frac{\sigma_{23}}{G_m}\frac{\partial d_m}{\partial \gamma_{12}} & \frac{\sigma_{23}}{G_m}\frac{\partial d_m}{\partial \gamma_{13}} & \frac{\sigma_{23}}{G_m}\frac{\partial d_m}{\partial \gamma_{23}} \end{bmatrix} \tag{5.62}$$

The scalar terms $\partial d_m / \partial \boldsymbol{\varepsilon}$ in tensor $\boldsymbol{M}_{\boldsymbol{m}}$ are given by

$$\frac{\partial d_m}{\partial \boldsymbol{\varepsilon}} = \frac{\partial d_m}{\partial r_m}\frac{\partial r_m}{\partial \boldsymbol{\varepsilon}} \tag{5.63}$$

The first term in equation (5.63) is given by equation (5.55), while the second term can be easily achieved differentiating equation (5.37) in order to the strain tensor:

$$\begin{aligned} \frac{\partial r_m}{\partial \boldsymbol{\varepsilon}} &= \frac{3}{X_m^c X_m^t}\frac{\partial \tilde{J}_2}{\partial \boldsymbol{\varepsilon}} + \frac{X_m^c - X_m^t}{X_m^c X_m^t}\frac{\partial \tilde{I}_1}{\partial \boldsymbol{\varepsilon}} = \\ &= \frac{6G_m}{X_m^c X_m^t}\tilde{\boldsymbol{S}} + \frac{3K_m\left(X_m^c - X_m^t\right)}{X_m^c X_m^t}\boldsymbol{I} \end{aligned} \tag{5.64}$$

where the tensor $\tilde{\boldsymbol{S}}$ is the deviatoric component of the effective stress tensor, $\boldsymbol{I}$ is a second-order identity tensor, and K_m is the elastic bulk modulus of the matrix. Substituting equations (5.64) and (5.55) in equation (5.63), and recalling that engineering shear strains are being used in the implementation of the constitutive model, the scalar parameters are all given by (in Voigt notation):

$$\frac{\partial d_m}{\partial \varepsilon} = \frac{2r_m e^{A_m\left(3-\sqrt{7+2r_m^2}\right)}}{\sqrt{7+2r_m^2}\left(\sqrt{7+2r_m^2}-2\right)} \cdot \left(A_m + \frac{1}{\sqrt{7+2r_m^2}-2}\right) \cdot$$
$$\cdot \left\{ \frac{6G_m}{X_m^c X_m^t} \begin{bmatrix} \tilde{S}_{11} \\ \tilde{S}_{22} \\ \tilde{S}_{33} \\ \tilde{S}_{12} \\ \tilde{S}_{13} \\ \tilde{S}_{23} \end{bmatrix} + 3K_m \frac{X_m^c - X_m^t}{X_m^c X_m^t} \begin{bmatrix} 1 \\ 1 \\ 1 \\ 0 \\ 0 \\ 0 \end{bmatrix} \right\} \tag{5.65}$$

The elasto-plastic with damage constitutive model for the matrix thus becomes completely defined.

5.3.2 Fibrous reinforcements

A damage law has also been implemented for the reinforcing material. It is considered that the reinforcing material possesses transverse isotropy. Due to the lack of experimental data regarding the transverse mechanical behaviour of a fibre in terms of damage activation and evolution, it was decided to implement a damage model which is activated solely by the longitudinal stress component. Thus, only one damage variable will be used.

Following the same procedure here that was used for the implementation of the matrix damage model, the complimentary free energy density of the fibre, $\mathscr{G}_f$, is defined by:

$$\begin{aligned} \mathscr{G}_f \;=\; & \frac{\sigma_{11}^2}{2E_1(1-d_f)} + \frac{\sigma_{22}^2+\sigma_{33}^2}{2E_2(1-d_f)} - \frac{\nu_{12}}{E_1}(\sigma_{11}\sigma_{22}+\sigma_{11}\sigma_{33}) - \\ & -\frac{\nu_{23}}{E_2}\sigma_{22}\sigma_{33} + \frac{\sigma_{12}^2+\sigma_{13}^2}{2G_{12}(1-d_f)} + \frac{\sigma_{23}^2}{2G_{23}(1-d_f)} \end{aligned} \tag{5.66}$$

where E_1 and E_2 are the Young's moduli in the longitudinal and transverse directions, G_{12} and G_{23} represent the longitudinal and transverse shear moduli, and d_f is the damage variable. Unlike for the matrix material, it is considered here that there is no plastic flow. To ensure the irreversibility of the damage process, the rate of change of the complimentary free energy density must be greater than the externally applied stress:

$$\dot{\mathscr{G}}_f - \dot{\boldsymbol{\sigma}} : \boldsymbol{\varepsilon} \geqslant 0 \tag{5.67}$$

Equation (5.67) represents the positiveness of the dissipated energy. Expanding the equation, the following is obtained:

$$\left(\frac{\partial \mathscr{G}_f}{\partial \boldsymbol{\sigma}} - \boldsymbol{\varepsilon}\right) : \dot{\boldsymbol{\sigma}} + \frac{\partial \mathscr{G}_f}{\partial d_f}\dot{d}_f \geqslant 0 \tag{5.68}$$

The strain tensor is defined by the derivative of the complementary free energy density with respect to the stress tensor (in engineering notation):

$$\boldsymbol{\varepsilon} = \frac{\partial \mathscr{G}_f}{\partial \boldsymbol{\sigma}} = \begin{bmatrix} \dfrac{\sigma_{11}}{E_1\left(1-d_f\right)} - \dfrac{\nu_{12}}{E_1}\left(\sigma_{22}+\sigma_{33}\right) \\ \dfrac{\sigma_{22}}{E_2\left(1-d_f\right)} - \dfrac{\nu_{12}}{E_1}\sigma_{11} - \dfrac{\nu_{23}}{E_2}\sigma_{33} \\ \dfrac{\sigma_{33}}{E_2\left(1-d_f\right)} - \dfrac{\nu_{12}}{E_1}\sigma_{11} - \dfrac{\nu_{23}}{E_2}\sigma_{22} \\ \dfrac{\sigma_{12}}{G_{12}\left(1-d_f\right)} \\ \dfrac{\sigma_{13}}{G_{12}\left(1-d_f\right)} \\ \dfrac{\sigma_{23}}{G_{23}\left(1-d_f\right)} \end{bmatrix} \tag{5.69}$$

The terms in equation (5.69) can be rearranged in order to obtain the compliance tensor of the reinforcing material:

$$\boldsymbol{H_f} = \frac{\partial^2 \mathscr{G}_f}{\partial \boldsymbol{\sigma}^2} = $$
$$= \begin{bmatrix} \frac{1}{E_1\left(1-d_f\right)} & -\frac{\nu_{12}}{E_1} & -\frac{\nu_{12}}{E_1} & 0 & 0 & 0 \\ -\frac{\nu_{12}}{E_1} & \frac{1}{E_2\left(1-d_f\right)} & -\frac{\nu_{23}}{E_2} & 0 & 0 & 0 \\ -\frac{\nu_{12}}{E_1} & -\frac{\nu_{23}}{E_2} & \frac{1}{E_2\left(1-d_f\right)} & 0 & 0 & 0 \\ 0 & 0 & 0 & \frac{1}{G_{12}\left(1-d_f\right)} & 0 & 0 \\ 0 & 0 & 0 & 0 & \frac{1}{G_{12}\left(1-d_f\right)} & 0 \\ 0 & 0 & 0 & 0 & 0 & \frac{1}{G_{23}\left(1-d_f\right)} \end{bmatrix} \tag{5.70}$$

Inverting equation (5.70), the stiffness tensor, $\boldsymbol{C_f}$ is obtained:

$$
\boldsymbol{C_f} = \frac{1-d_f}{\Delta}\begin{bmatrix} E_1(1-\beta^2) & E_2\nu_{12}(1-d_f)(1+\beta) & E_2\nu_{12}(1-d_f)(1+\beta) & 0 & 0 & 0 \\ & E_2\left[1-\gamma(1-d_f)\right] & E_2(1-d_f)(\nu_{23}+\gamma) & 0 & 0 & 0 \\ & & E_2\left[1-\gamma(1-d_f)\right] & 0 & 0 & 0 \\ & & & G_{12}\Delta & 0 & 0 \\ & & & & G_{12}\Delta & 0 \\ SYM. & & & & & \frac{E_2\Delta}{2(1+\nu_{23})} \end{bmatrix} \tag{5.71}
$$

where the parameters β, γ and Δ are defined as:

$$\beta = \nu_{23}\,(1-d_f) \tag{5.72}$$

$$\gamma = \nu_{12}\nu_{21}\,(1-d_f) \tag{5.73}$$

$$\Delta = (1+\beta)\left[1-\beta-2\gamma\,(1-d_f)\right] \tag{5.74}$$

The damage activation function is generically defined the same way as for the matrix material:

$$F_f^d = \phi_f^d - r_f \leqslant 0 \tag{5.75}$$

with the loading function, ϕ_f^d, defined as:

$$\phi_f^d = \frac{\tilde{\sigma}_{11}}{X_f^t} \tag{5.76}$$

and the internal variable, r_f generically defined as:

$$r_f = \max\left\{1, \max_{t\to\infty}\left\{\phi_{f,t}^d\right\}\right\} \tag{5.77}$$

As it can be seen in equation (5.76), the damage is activated when the maximum stress criterion is satisfied in the longitudinal direction only. Also in equation (5.76), the effective stress value along the longitudinal direction is used. The effective stress tensor is defined by:

$$\tilde{\boldsymbol{\sigma}} = \boldsymbol{H_f^o}^{-1} : \boldsymbol{\varepsilon} \tag{5.78}$$

where $\boldsymbol{H_f^o}$ is the undamaged compliance tensor obtained from equation (5.70) by forcing the damage variable to be null. In order to avoid mesh dependency problems and control the amount of dissipated energy due to the fracture process, Bažant's crack band model [115] was implemented along with the definition of the damage evolution law. The computed dissipated energy for the reinforcing material is defined by:

$$\Psi_f = \int_0^\infty Y_f \dot{d}_f \mathrm{dt} = \int_1^\infty \frac{\partial \mathscr{G}_f}{\partial d_f} \frac{\partial d_f}{\partial r_f} \mathrm{d}r_f = \frac{G_{ff}}{l^e} \tag{5.79}$$

where G_{ff} represents the energy release rate of the fibre, l_e is the characteristic element length, and Y_f represents the thermodynamic force associated with the damage variable d_f:

$$\Xi_f = \frac{\partial \mathscr{G}_f}{\partial d_f} \dot{d}_f = Y_f \dot{d}_f \geqslant 0 \tag{5.80}$$

The complimentary free energy density presented in equation (5.66) enforces the thermodynamic force, Y_f, to be always positive:

$$Y_f = \frac{\partial \mathscr{G}_f}{\partial d_f} = \frac{1}{(1-d_f)^2} \left[\frac{\sigma_{11}^2}{2E_1} + \frac{\sigma_{22}^2 + \sigma_{33}^2}{2E_2} + \frac{\sigma_{12}^2 + \sigma_{13}^2}{2G_{12}} + \frac{\sigma_{23}^2}{2G_{23}} \right] \geqslant 0 \tag{5.81}$$

The damage evolution law established here is slightly different from the one used for the matrix material:

$$d_f = 1 - \frac{e^{A_f \left(1-r_f\right)}}{r_f} \tag{5.82}$$

where the parameter A_f must be determined after solving equation (5.79) as a function of the characteristic element length, i.e. there will be a unique value of the parameter A_f for each element in the mesh. The energy dissipated per unit volume for an uniaxial stress condition is obtained after integration of the rate of energy dissipation given by equation (5.81). Before, the relation between the effective stress tensor and the real stress tensor must be established by imposing the principle of strain equivalence:

$$\left.\begin{aligned} \boldsymbol{\sigma} &= \boldsymbol{C_f} : \boldsymbol{\varepsilon} \\ \tilde{\boldsymbol{\sigma}} &= \boldsymbol{C_f^o} : \boldsymbol{\varepsilon} \end{aligned}\right\} \boldsymbol{\sigma} = \boldsymbol{C_f} : \boldsymbol{C_f^{o}}^{-1} : \tilde{\boldsymbol{\sigma}} = \boldsymbol{C_f} : \boldsymbol{H_f^o} : \tilde{\boldsymbol{\sigma}} \tag{5.83}$$

where $\boldsymbol{C_f^o}$ is the undamaged stiffness tensor. Considering the particular case of an uniaxial tensile load applied to the material, where the effective stress tensor is defined by equation (5.51), the three normal components of the real stress tensor are given by:

$$\sigma_{11} = \frac{1-d_f}{\Delta}\left[1-\beta^2-2\gamma\left(1+\beta\right)\right]\tilde{\sigma}_{11} \tag{5.84}$$

$$\sigma_{22} = \sigma_{33} = -\frac{1-d_f}{\Delta}\nu_{21}\left(1+\beta\right)d_f\tilde{\sigma}_{11} \tag{5.85}$$

while the three shear components are null, $\sigma_{12}=\sigma_{13}=\sigma_{23}=0$. The rate of energy dissipation per unit volume for the uniaxial tensile case is obtained by replacing equations (5.84) and (5.85) in equation (5.81):

$$\frac{\partial \mathscr{G}_f{}^{UN}}{\partial d_f} = \frac{\left(1+\beta\right)^2}{2E_1\Delta^2}\left[\left(1-\beta-2\gamma\right)^2+2\nu_{12}\nu_{21}d_f^2\right]\tilde{\sigma}_{11}^2 \tag{5.86}$$

The derivative of the damage evolution law in order to the internal variable, r_f, is given by:

$$\frac{\partial d_f}{\partial r_f} = \frac{e^{A_f\left(1-r_f\right)}}{r_f}\left(A_f+\frac{1}{r_f}\right) \tag{5.87}$$

Finally, the damage activation function defined for the uniaxial tensile case is given by:

$$F_f^{dUN} = \frac{\tilde{\sigma}_{11}}{X_f^t} - r_f \leqslant 0 \tag{5.88}$$

For damage to propagate, equation (5.88) must be equal to zero. Solving it in order to the applied effective stress, $\tilde{\sigma}_{11}$:

$$\tilde{\sigma}_{11} = X_f^t r_f \tag{5.89}$$

Substituting now equations (5.86), (5.87) and (5.89) into equation (5.79) the following equation is obtained:

$$\int_1^{\infty}\frac{{X_f^t}^2 r_f^2\left(1+\beta\right)^2}{2E_1\Delta^2}\left[\left(1-\beta-2\gamma\right)^2+2\nu_{12}\nu_{21}d_f^2\right]\frac{\partial d_f}{\partial r_f}dr_f = \frac{G_{ff}}{l^e} \tag{5.90}$$

This equation must now be solved numerically using the secant method for non-linear equations, along with the definition of the damage evolution law in equation (5.82) in order to determine the parameter A_f. The next section will describe the numerical implementation of these equations.

Constitutive tangent operator

In order to obtain a faster convergence rate of the solution for the non-linear damage model presented here, it is necessary to provide the correct constitutive tangent operator, $\boldsymbol{C_f^T}$, defined by:

$$\dot{\boldsymbol{\sigma}} = \boldsymbol{C_f^T} : \dot{\boldsymbol{\varepsilon}} \tag{5.91}$$

To determine the general form of the constitutive tangent operator, equation (5.91) must be transformed into its rate form:

$$\begin{aligned}
&\boldsymbol{\varepsilon} = \boldsymbol{H_f} : \boldsymbol{\sigma} \Rightarrow \dot{\boldsymbol{\varepsilon}} = \boldsymbol{H_f} : \dot{\boldsymbol{\sigma}} + \dot{\boldsymbol{H}}_{\boldsymbol{f}} : \boldsymbol{\sigma} \Leftrightarrow \\
&\Leftrightarrow \boldsymbol{H_f}\dot{\boldsymbol{\sigma}} = \dot{\boldsymbol{\varepsilon}} - \dot{\boldsymbol{H}}_{\boldsymbol{f}} : \boldsymbol{\sigma} \Leftrightarrow \dot{\boldsymbol{\sigma}} = \boldsymbol{C_f} : \dot{\boldsymbol{\varepsilon}} - \boldsymbol{C_f} : \dot{\boldsymbol{H}}_{\boldsymbol{f}} : \boldsymbol{\sigma} \Leftrightarrow \\
&\Leftrightarrow \dot{\boldsymbol{\sigma}} = \boldsymbol{C_f} : \dot{\boldsymbol{\varepsilon}} - \boldsymbol{C_f} : \boldsymbol{M_f} : \dot{\boldsymbol{\varepsilon}} \Leftrightarrow \dot{\boldsymbol{\sigma}} = \boldsymbol{C_f} : (\boldsymbol{I} - \boldsymbol{M_f}) : \dot{\boldsymbol{\varepsilon}}
\end{aligned} \tag{5.92}$$

The constitutive tangent operator is thus defined by:

$$\boldsymbol{C_f^T} = \boldsymbol{C_f} : (\boldsymbol{I} - \boldsymbol{M_f}) \tag{5.93}$$

where the fourth-order tensor, $\boldsymbol{M_f}$, is given by, in Voigt notation:

$$\boldsymbol{M_f} = \frac{1}{\left(1-d_f\right)^2}\begin{bmatrix}
\frac{\sigma_{11}}{E_1}\frac{\partial d_f}{\partial \varepsilon_{11}} & \frac{\sigma_{11}}{E_1}\frac{\partial d_f}{\partial \varepsilon_{22}} & \frac{\sigma_{11}}{E_1}\frac{\partial d_f}{\partial \varepsilon_{33}} & \frac{\sigma_{11}}{E_1}\frac{\partial d_f}{\partial \gamma_{12}} & \frac{\sigma_{11}}{E_1}\frac{\partial d_f}{\partial \gamma_{13}} & \frac{\sigma_{11}}{E_1}\frac{\partial d_f}{\partial \gamma_{23}} \\
\frac{\sigma_{22}}{E_2}\frac{\partial d_f}{\partial \varepsilon_{11}} & \frac{\sigma_{22}}{E_2}\frac{\partial d_f}{\partial \varepsilon_{22}} & \frac{\sigma_{22}}{E_2}\frac{\partial d_f}{\partial \varepsilon_{33}} & \frac{\sigma_{22}}{E_2}\frac{\partial d_f}{\partial \gamma_{12}} & \frac{\sigma_{22}}{E_2}\frac{\partial d_f}{\partial \gamma_{13}} & \frac{\sigma_{22}}{E_2}\frac{\partial d_f}{\partial \gamma_{23}} \\
\frac{\sigma_{33}}{E_2}\frac{\partial d_f}{\partial \varepsilon_{11}} & \frac{\sigma_{33}}{E_2}\frac{\partial d_f}{\partial \varepsilon_{22}} & \frac{\sigma_{33}}{E_2}\frac{\partial d_f}{\partial \varepsilon_{33}} & \frac{\sigma_{33}}{E_2}\frac{\partial d_f}{\partial \gamma_{12}} & \frac{\sigma_{33}}{E_2}\frac{\partial d_f}{\partial \gamma_{13}} & \frac{\sigma_{33}}{E_2}\frac{\partial d_f}{\partial \gamma_{23}} \\
\frac{\sigma_{12}}{G_{12}}\frac{\partial d_f}{\partial \varepsilon_{11}} & \frac{\sigma_{12}}{G_{12}}\frac{\partial d_f}{\partial \varepsilon_{22}} & \frac{\sigma_{12}}{G_{12}}\frac{\partial d_f}{\partial \varepsilon_{33}} & \frac{\sigma_{12}}{G_{12}}\frac{\partial d_f}{\partial \gamma_{12}} & \frac{\sigma_{12}}{G_{12}}\frac{\partial d_f}{\partial \gamma_{13}} & \frac{\sigma_{12}}{G_{12}}\frac{\partial d_f}{\partial \gamma_{23}} \\
\frac{\sigma_{13}}{G_{12}}\frac{\partial d_f}{\partial \varepsilon_{11}} & \frac{\sigma_{13}}{G_{12}}\frac{\partial d_f}{\partial \varepsilon_{22}} & \frac{\sigma_{13}}{G_{12}}\frac{\partial d_f}{\partial \varepsilon_{33}} & \frac{\sigma_{13}}{G_{12}}\frac{\partial d_f}{\partial \gamma_{12}} & \frac{\sigma_{13}}{G_{12}}\frac{\partial d_f}{\partial \gamma_{13}} & \frac{\sigma_{13}}{G_{12}}\frac{\partial d_f}{\partial \gamma_{23}} \\
\frac{\sigma_{23}}{G_{23}}\frac{\partial d_f}{\partial \varepsilon_{11}} & \frac{\sigma_{23}}{G_{23}}\frac{\partial d_f}{\partial \varepsilon_{22}} & \frac{\sigma_{23}}{G_{23}}\frac{\partial d_f}{\partial \varepsilon_{33}} & \frac{\sigma_{23}}{G_{23}}\frac{\partial d_f}{\partial \gamma_{12}} & \frac{\sigma_{23}}{G_{23}}\frac{\partial d_f}{\partial \gamma_{13}} & \frac{\sigma_{23}}{G_{23}}\frac{\partial d_f}{\partial \gamma_{23}}
\end{bmatrix} \tag{5.94}$$

The scalar terms $\partial d_f / \partial \boldsymbol{\varepsilon}$ in tensor $\boldsymbol{M_f}$ are given by

$$\frac{\partial d_f}{\partial \boldsymbol{\varepsilon}} = \frac{\partial d_f}{\partial r_f}\frac{\partial r_f}{\partial \boldsymbol{\varepsilon}} \tag{5.95}$$

The first term in equation (5.95) is given by equation (5.87), while the second term can be easily achieved by establishing a relation between the internal variable, r_f, and the strain tensor, using the definition of effective stress:

$$\begin{aligned} r_f &= \frac{\tilde{\sigma}_{11}}{X_f^t} = \\ &= \frac{1}{X_f^t}\left[\frac{E_1\left(1-\nu_{23}\right)}{1-\nu_{23}-2\nu_{21}\nu_{12}}\varepsilon_{11} + \frac{E_2\nu_{12}}{1-\nu_{23}-2\nu_{21}\nu_{12}}\left(\varepsilon_{22}+\varepsilon_{33}\right)\right] = \\ &= \frac{E_1}{X_f^t}\cdot\frac{1}{1-\nu_{23}-2\nu_{21}\nu_{12}}\cdot\left[\left(1-\nu_{23}\right)\varepsilon_{11}+\nu_{21}\left(\varepsilon_{22}+\varepsilon_{33}\right)\right] \end{aligned} \tag{5.96}$$

Differentiating equation (5.75) in order to the strain tensor (in Voigt notation), the following is obtained:

$$\frac{\partial r_f}{\partial \boldsymbol{\varepsilon}} = \frac{E_1}{X_f^t}\cdot\frac{1}{1-\nu_{23}-2\nu_{21}\nu_{12}}\cdot\begin{bmatrix} 1-\nu_{23} \\ \nu_{21} \\ \nu_{21} \\ 0 \\ 0 \\ 0 \end{bmatrix} \tag{5.97}$$

Substituting equations (5.97) and (5.87) in equation (5.95) and recalling that engineering shear strains are being used in the implementation of the constitutive model, the scalar parameters are all given by (in Voigt notation):

$$\frac{\partial d_f}{\partial \boldsymbol{\varepsilon}} = \frac{e^{A_f\left(1-r_f\right)}}{r_f}\left(A_f+\frac{1}{r_f}\right)\frac{E_1}{X_f^t}\cdot\frac{1}{1-\nu_{23}-2\nu_{21}\nu_{12}}\begin{bmatrix} 1-\nu_{23} \\ \nu_{21} \\ \nu_{21} \\ 0 \\ 0 \\ 0 \end{bmatrix} \tag{5.98}$$

And this concludes the definition of the two constitutive damage models to be used in this thesis. In the next section, a detailed description of the numerical implementation of the two constitutive models will be presented.

5.4 Computational implementation of the damage models

This section will describe the numerical implementation of the two damage models defined in section 5.3. The final version of the UMAT subroutine that was programmed for the commercial finite element analysis software ABAQUS® [30] can be found in appendix D.

5.4.1 Matrix

Figure 5.12 shows the flowchart of the algorithm corresponding to the numerical implementation of the constitutive model for the matrix material.

The damage parameter A_m used in the definition of the damage evolution law as per equation (5.47) is set to a negative value in the beginning of the analysis. In the first increment, this parameter must be computed for each element in the mesh. In the following increments this parameter remains constant and does not need to be re-calculated.

Just like for the return mapping algorithm already described in chapter 4, each increment begins with the computation of an elastic trial stress and update of hardening variables associated with the plastic flow that the matrix material endures. Since there is no coupling between the plastic and damage dissipative processes, it is considered that an element will follow the sequence elastic-plastic-damage during the loading process. Due to this, if damage has been activated (IF condition $d_m < TOL$), the plastic formulation is skipped; else the return mapping algorithm already described in chapter 4 is executed.

Independently of the plastic mechanism being activated or not in the current increment, the damage activation function defined in equation (5.37) is checked using the updated stress tensor. If damage is propagating, damage variables r_m and d_m are updated according with equations (5.37) and (5.47). This update is not performed if under a situation of unloading/loading after damage has been activated, as per the Kuhn-Tucker conditions defined in equations (5.42). The damaged stiffness tensor is then computed according with equation (5.34) and the new damaged stress tensor is determined. All state and energy variables are computed at the end of the increment.

Energy variables do not have an influence in the constitutive model by themselves, but they provide a useful way to check if the energy dissipated by both plastic and damage mechanisms along with the elastic energy stored in the element are coincident with the work performed by external forces.

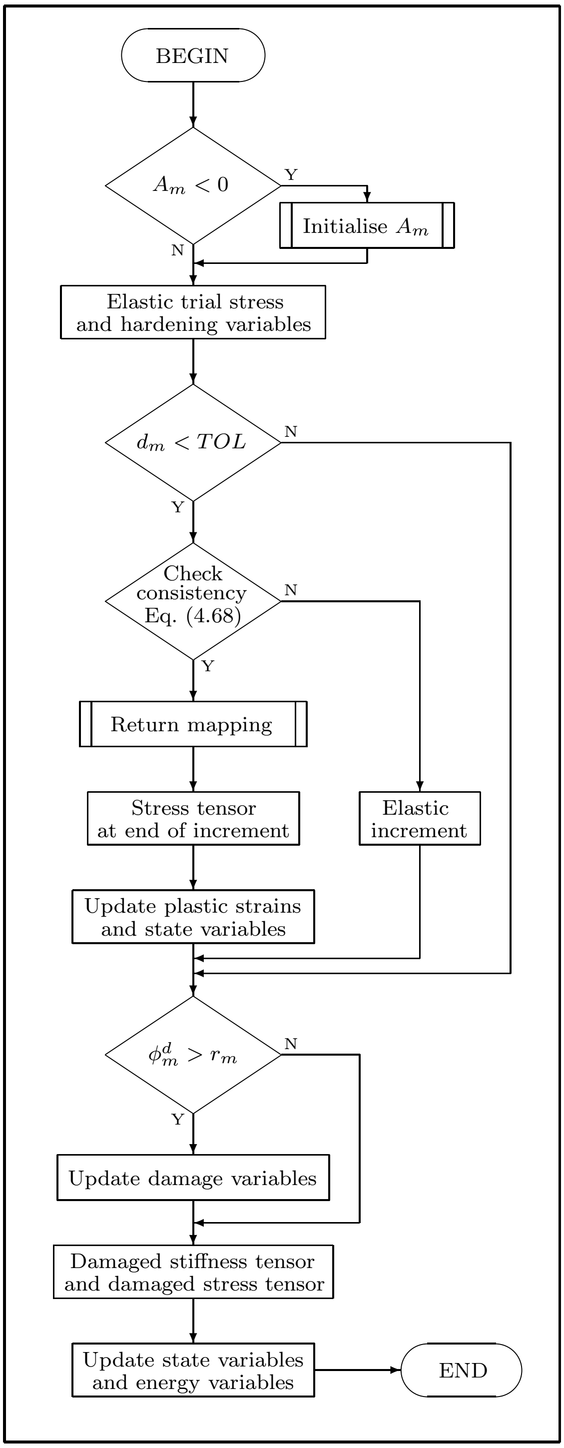

Figure 5.12: Flowchart of constitutive model for matrix material.

5.4.2 Fibrous reinforcements

Figure 5.13 shows the flowchart corresponding to the algorithm of the constitutive model for the reinforcement material.

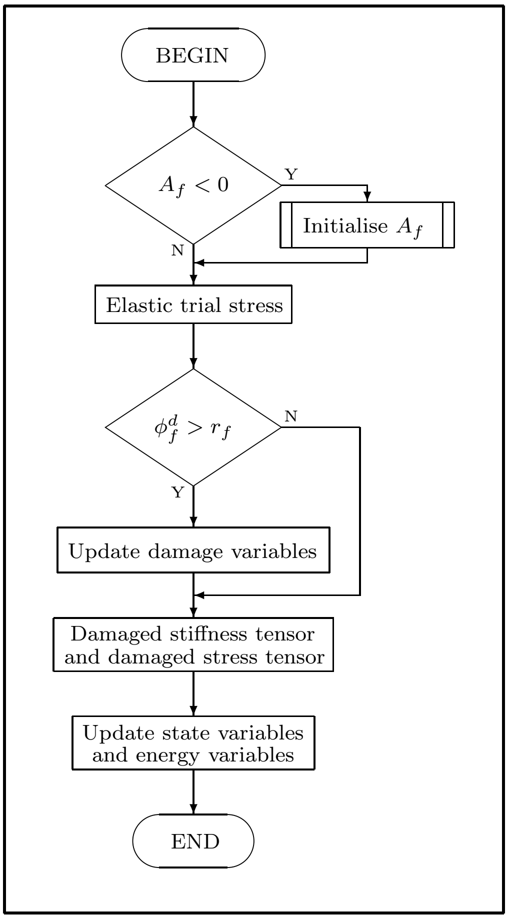

Figure 5.13: Flowchart of constitutive model for reinforcement material.

The algorithm implemented for the constitutive model of the fibrous reinforcements is exactly equal to the constitutive model for the matrix material except for the absence of the return mapping algorithm and the remaining plasticity-related formulation.

Also here the damage parameter A_f used in the definition of the damage evolution law as per equation (5.82) must be initialised at the beginning of the first increment. An elastic trial stress is computed and the resulting stress state is checked according with the damage activation function defined by equation (5.75). If damage is propagating, damage variables are updated;

else, if an unloading/loading condition is detected, the Kuhn-Tucker conditions must be satisfied and the damage variables are not updated.

The damaged stiffness tensor and the damaged stress tensor are then calculated and finally the state and energy variables are updated. All that remains to be defined is the initialisation procedure of the damage parameters A_m and A_f.

5.4.3 Determining the damage parameters

The procedure to determine the damage parameters A_f and A_m is almost equal since both damage evolution laws have a similar formulation. The main difference is in the integrand function of equations (5.58) and (5.90). Without loss of generality, both equations can be written in the form

$$f_x\left(A_x\right) - \frac{G_{fx}}{l^e} = 0 \tag{5.99}$$

where the subscript x represents the energy dissipated by either matrix or fibre material. Function f_x represents the improper integral of equations (5.58) and (5.90). Solving equation (5.99) will allow to determine the damage parameter A_x. This requires two more numerical procedures, one for solving the improper integral and one iterative procedure for non-linear equations. Given the difficulty in calculating the derivative of equation (5.99), the secant method was chosen. Figure 5.14 shows the flowchart to implement the secant method.

The first two parameters to give start to the iterative process are chosen according to [122]:

$$A_x^1 = \frac{2l^e X_x^{t^2}}{2E_x G_{fx} - l^e X_x^{t^2}} \qquad A_x^0 = 0.5 A_x^1 \tag{5.100}$$

Care must be taken in implementing the secant method since the damage parameters A_x only have a physical meaning if greater than zero. Hence the minimization function is defined by:

$$\begin{aligned} \ln\left(A_x^{i+1}\right) &= \ln\left(A_x^i\right) - \left[\ln\left(f_x\left(A_x^i\right)\right) - \ln\left(\frac{G_{fx}}{l^e}\right)\right] \cdot \\ &\quad \cdot \frac{\ln\left(A_x^i\right) - \ln\left(A_x^{i-1}\right)}{\ln\left(f_x\left(A_x^i\right)\right) - \ln\left(f_x\left(A_x^{i-1}\right)\right)} \end{aligned} \tag{5.101}$$

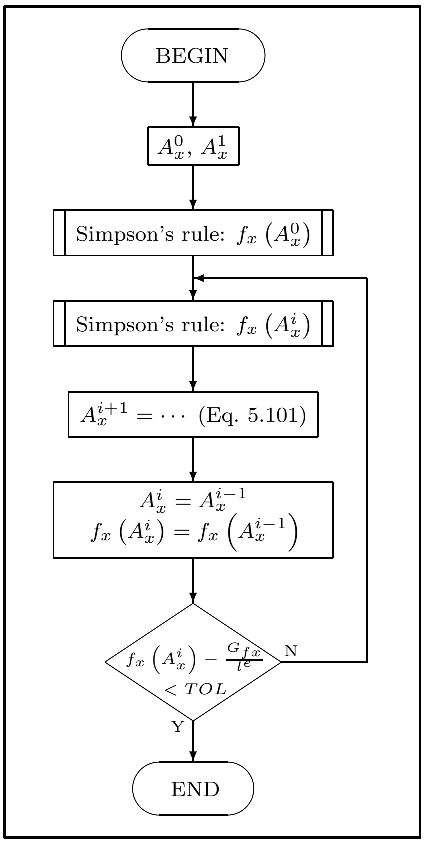

Figure 5.14: Flowchart of secant method to determine damage parameters.

In the flowchart shown in figure 5.14, the improper integral of equations (5.58) and (5.90) is calculated using Simpson's rule with a stopping limit defined by the ratio of real stresses in the longitudinal direction – defined in equations (5.52) and (5.84) – with a small percentage of the tensile fracture strength. This is possible since the damage evolution laws chosen tend to zero. Simpson's rule can be expressed according to:

$$f_x \approx \frac{h}{3}\left(F_x^0 + \cdots + 4F_x^{odd} + 2F_x^{even} + \cdots + F_x^n\right) \tag{5.102}$$

where F_x^i is the integrand function of f_x and is defined between $r = 1$ and $r \to \infty$, and h is the step increment. When the stress becomes less than K times the tensile fracture strength, the remaining energy can be neglected. The increment h can be defined as a function of the number of steps by:

$$h = -\frac{1}{nA_x} \ln\left(\frac{1}{K}\right) \tag{5.103}$$

Figure 5.15 shows the flowchart of the algorithm that implements Simpson's rule.

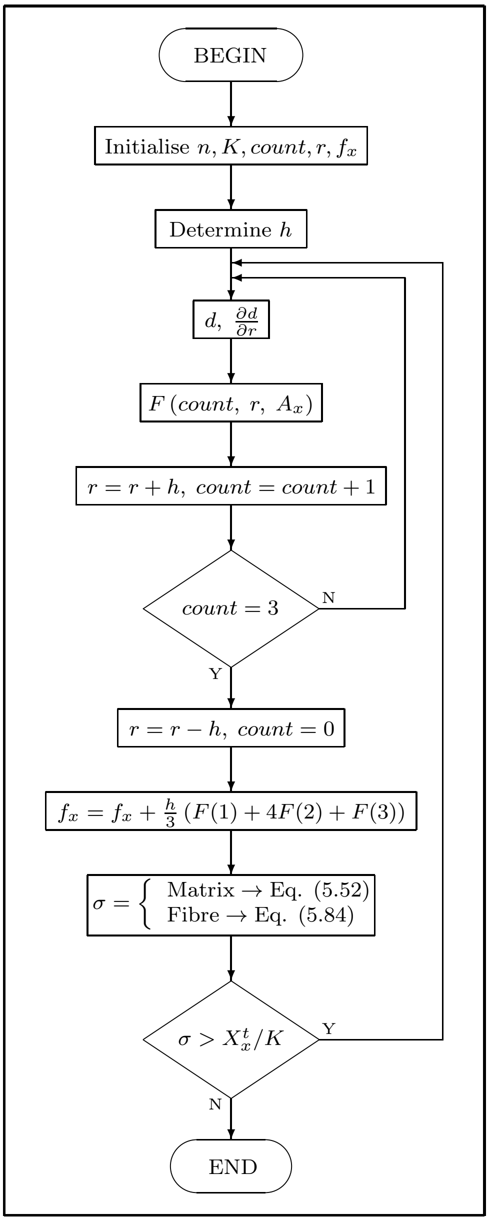

Figure 5.15: Flowchart of Simpson's rule.

5.5 Verification of the damage models

After their numerical implementation, both constitutive models need to be verified for consistency and for mesh dependency. The models were first verified for one-element tensile cases. Afterwards, a series of localisation tests were performed using open-hole tension models which allow to validate the implementation of Bažant's crack band model [115] and assess the mesh dependency of both constitutive models.

Material properties are the same as used in section 4.6 adding the fracture related ones provided in table 5.1 for the different materials under consideration.

Table 5.1: Fracture properties. Values marked with $^{(a)}$ were estimated.

Material	X^t [MPa]	X^c [MPa]	G_f [N/mm]
Fibres			
AS4	3350	-	$90^{(a)}$
Silenka E-glass	2150	-	$60^{(a)}$
Matrix			
Fiedler [70]	93	124	$0.09^{(a)}$

5.5.1 One-element testing

For this test, three one-element analyses were run. Each element has a cubic shape with the side length varying. The smallest measured 0.01 mm, the intermediate, 0.02 mm, and the biggest measured 0.05 mm.

For the case of one-element analyses, the energy absorbed by the element after complete failure, U, is given by:

$$U = L^3 \cdot \frac{X^t \varepsilon^f}{2} \tag{5.104}$$

where L is the element side length, X^t is the fracture stress, and ε^f is the maximum strain. Figure 5.16 shows an example of a simple material law. The shadowed area below the curve represents the energy absorbed by the element, U. In order to avoid snap-back effects, the maximum strain ε^f must be greater than ε^0. Defining G_f as the fracture per unit area of the material, it is possible to relate G_f with the energy absorbed U by

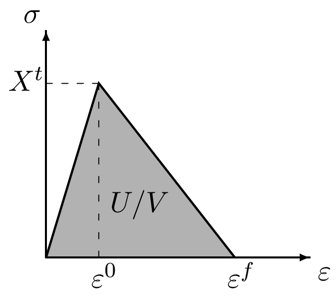

Figure 5.16: Example of material law.

$$U = G_f \frac{V}{l^e} \tag{5.105}$$

where V is the volume of the element, and l^e is the element length in the loading direction. Relating equations (5.104) and (5.105) the following can be obtained:

$$G_f \frac{V}{l^e} = \frac{X^t \varepsilon^f}{2} V \Leftrightarrow l^e = \frac{2G_f}{X^t \varepsilon^f} \tag{5.106}$$

In the limit, the maximum strain ε^f must be equal to $\varepsilon^0 = X^t/E$. Substituting in equation (5.106) the following relation for the maximum element size is obtained:

$$l^e < \frac{2G_f E}{X^{t^2}} \tag{5.107}$$

This condition must be verified for one-element tests but also for all analyses performed in this thesis involving damage in the constitutive models of the materials being used. The limit values were checked and the element sizes confer with this condition.

Matrix

Since the portion of the code involving plasticity was already validated in chapter 4, it was decided to turn off this sequence and use only the initial elastic behaviour with damage. Figure 5.17 shows the stress-strain curves for the three one-element meshes.

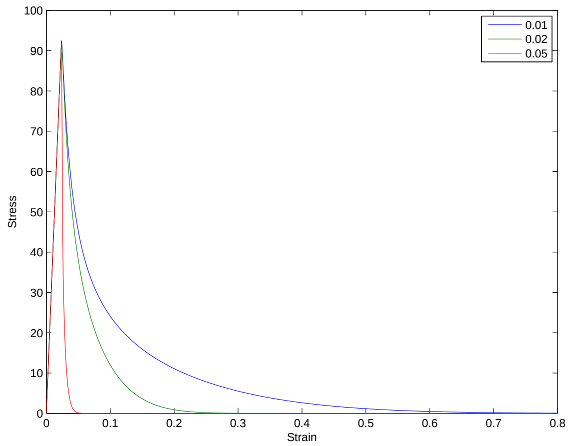

Figure 5.17: Stress-strain curves for one-element tests of matrix material.

It can be seen that as the element size increases, the area under the curve is reduced by a factor equal to the ratio of element sizes, i.e. the ratio of areas under the curves for any two element sizes is equal to the ratio of element size.

Fibrous reinforcement

Similar results are obtained for the reinforcement material as can be seen in figure 5.18.

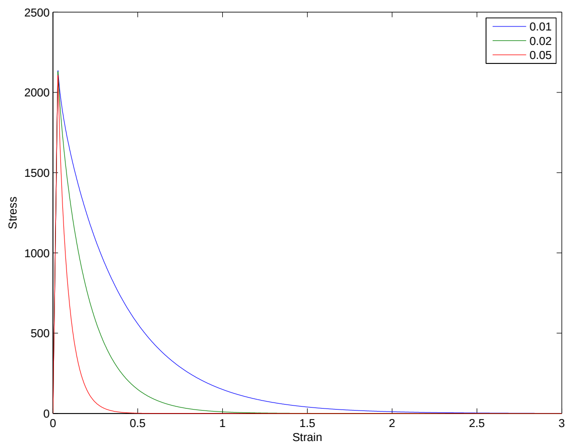

Figure 5.18: Stress-strain curves for one-element tests of fibre material.

5.5.2 Open-hole tensile tests

In order to verify damage propagation and localisation, a series of analyses were performed using the geometry of an open-hole tension specimen shown in figure 5.19.

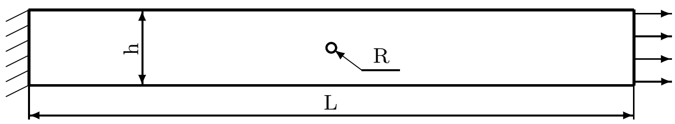

Figure 5.19: Geometry of open-hole tension specimen.

In order to reduce computational cost, the dimensions in figure 5.19 were chosen for the two different material models in study according with table 5.2.

Table 5.2: Dimensions of open-hole tension specimen.

Dimension	L [mm]	h [mm]	R [mm]
Fibres	320	40	5
Matrix	8	1	0.125

A detail of the mesh used for the analyses is shown in figure 5.20. In order to verify the influence of the element size, three different meshes were generated with different sizes of element in the region where damage is expected to localise. This region is marked with l^e in figure 5.20.

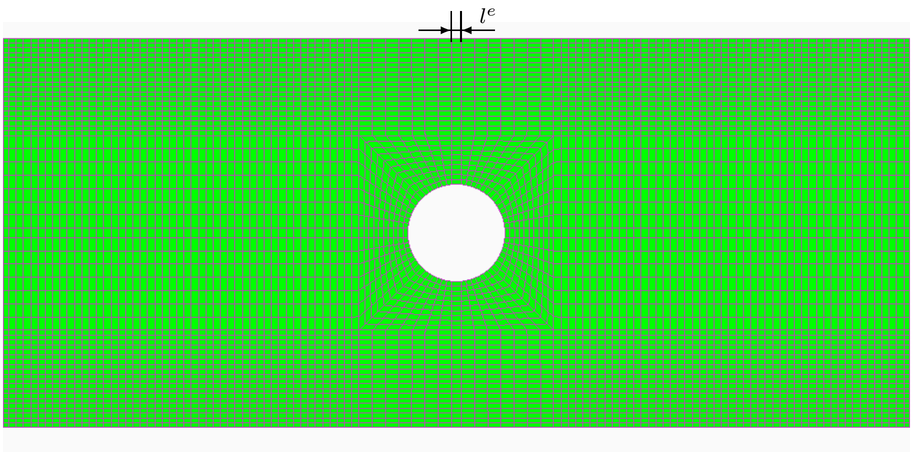

Figure 5.20: Detail of mesh for open-hole tension analyses.

Matrix

Six different analyses were run, in two groups of three. In the first group a parametric study was conducted varying only the fracture toughness of the material while the second group aimed at studying the influence of the element length in the fracture zone (l^e in figure 5.20). Table 5.3 clarifies the test scheme and provides the values used for each parameter in the analyses.

Table 5.3: Parameters used in matrix model verification.

Code	G_f [N/mm]	l^e [mm]	Code	G_f [N/mm]	l^e [mm]
OHT_M_1	0.5	0.02	OHT_M_7	0.09	0.005
OHT_M_2	5	0.02	OHT_M_8	0.09	0.01
OHT_M_3	50	0.02	OHT_M_9	0.09	0.02

Figures 5.21 and 5.22 show the results for each group of analyses. It can be seen that for the first group there is an increase of the area below the curve as the fracture toughness is increased. This increase is difficult to see in the plot due to the chosen damage evolution function which forces softening in an abrupt manner. On the second group, the independence of the constitutive model from the element size is clearly shown as all curves are overlapped. Plasticity was not considered in these analyses.

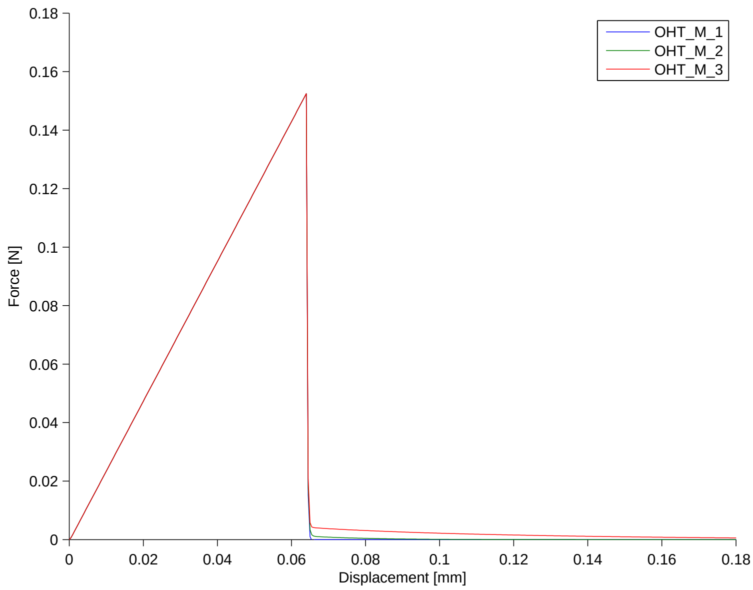

Figure 5.21: Dependence on toughness for epoxy material.

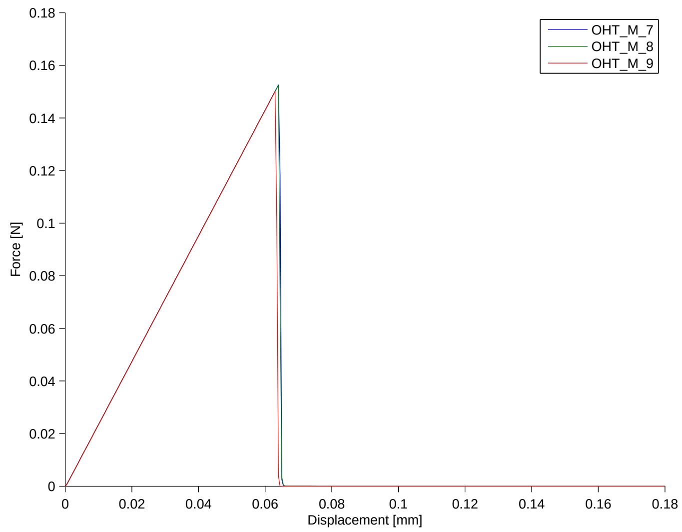

Figure 5.22: Dependence on element size for epoxy material.

Fibrous reinforcements

The same procedure used for the matrix material was adopted for the fibrous reinforcements. Two different kinds of reinforcing material were considered – Carbon and Glass fibres. Table 5.4 clarifies the test scheme and provides the values used for each parameter in the analyses for the Carbon fibres. Input data for the analyses with Glass fibres can be seen in Table 5.5.

It can be seen from figures 5.23 to 5.26 that there is complete independence from the mesh size and an increase in the value of the fracture toughness leads to a much slower crack propagation.

Table 5.4: Parameters used in Carbon fibre model verification.

Code	G_f [N/mm]	l^e [mm]
OHT_F_C_1	90	0.2
OHT_F_C_2	900	0.2
OHT_F_C_3	9000	0.2
OHT_F_C_7	90	0.2
OHT_F_C_8	90	0.5
OHT_F_C_9	90	1.0

Table 5.5: Parameters used in Glass fibre model verification.

Code	G_f [N/mm]	l^e [mm]
OHT_F_G_1	60	0.2
OHT_F_G_2	600	0.2
OHT_F_G_3	6000	0.2
OHT_F_G_7	60	0.2
OHT_F_G_8	60	0.5
OHT_F_G_9	60	1.0

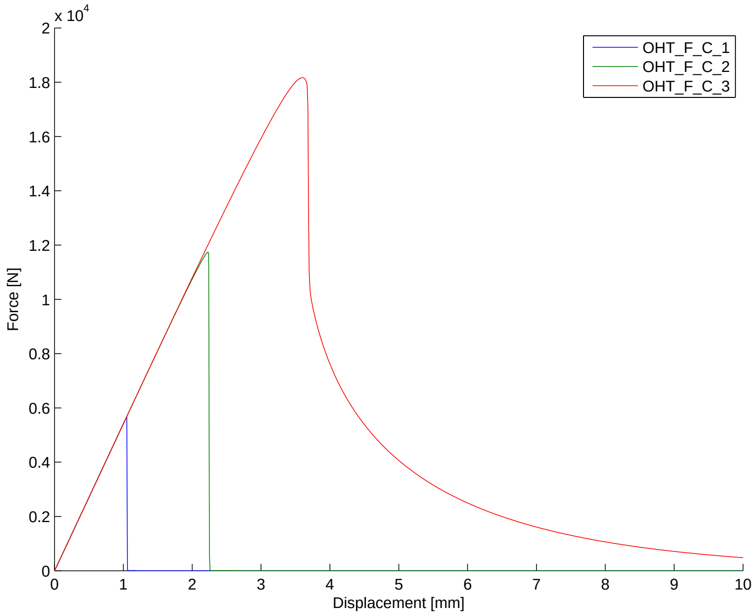

Figure 5.23: Dependence on toughness for Carbon fibres.

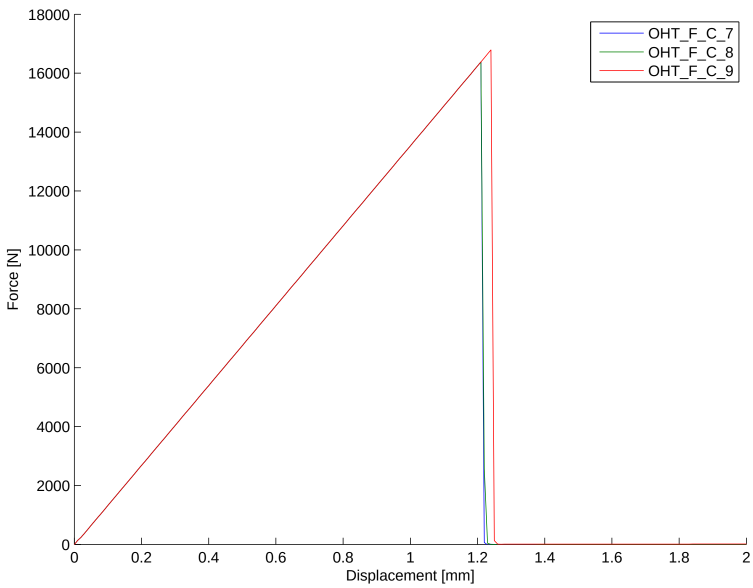

Figure 5.24: Dependence on element size for Carbon fibres.

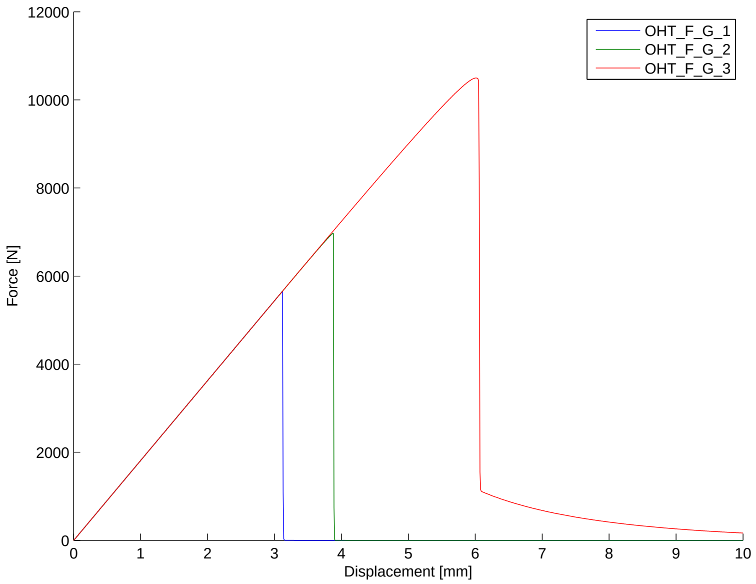

Figure 5.25: Dependence on toughness for Glass fibres.

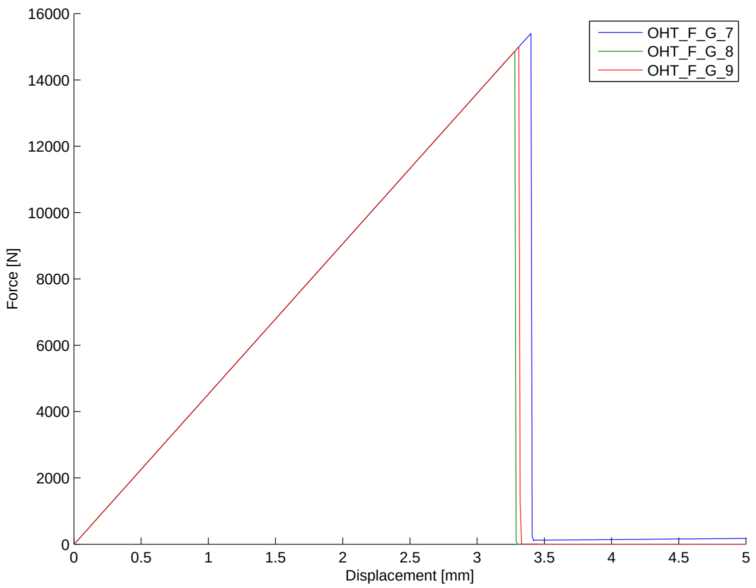

Figure 5.26: Dependence on element size for Glass fibres.

5.6 Application to composite volume elements

The same loading conditions which were used in section 4.7 will be applied to a set of five different volume elements with 10× the fibre radius of width. A bigger volume element with a width of 20× the fibre radius was generated and the results from all six volume elements were compared. The same material properties that had been used in section 4.7 were applied here adding the material strengths and toughnesses from table 5.1. Again, one of the smaller volume elements was given a lower fibre volume fraction for comparison purposes.

In addition to the five different loading conditions specified in section 4.7, one more type of loading was implemented in order to verify the application of the constitutive damage model for the fibrous reinforcements under longitudinal tension.

5.6.1 Transverse tension

Figure 5.27 shows the results from an applied transverse tension load to a volume element. Figure 5.27a shows the spatial distribution of the damage variable for the matrix material in one of the generated fibre spatial distributions, being the darker regions those where damage has been activated. As expected, a band of localised damage formed in a plane normal to the load direction (horizontal, in this case). Figure 5.27b shows the transverse stress-strain curves obtained after volumetric homogenisation for all fibre distributions. The greyed area on the top represents the range of fracture strengths for the volume elements with 60% of fibre volume fraction. Unlike

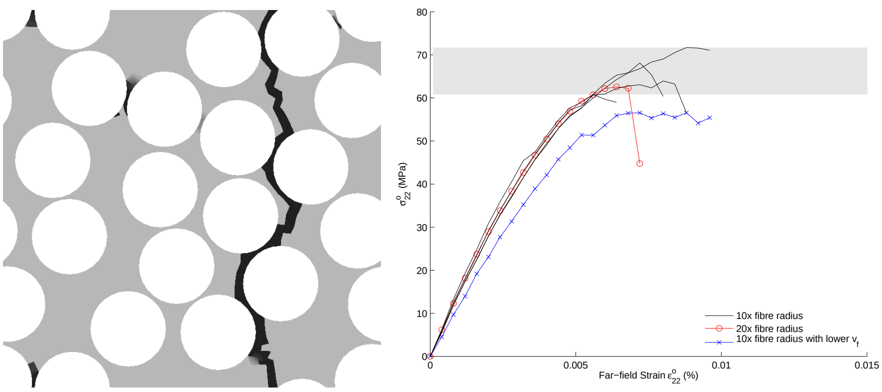

(a) Damage variable (b) Stress-strain curves

Figure 5.27: Results for transverse tension example.

what was registered in section 4.7 without the damage formulation included in the constitutive model, now there is a much greater scattering for the maximum stress achieved after homogenisation of results. This is a direct consequence of having different fibre distributions which may or may not favour the propagation of damage in the matrix and around the fibres.

5.6.2 Longitudinal shear

Figure 5.28 shows the results from an applied longitudinal shear load to a volume element. Figure 5.28a shows the spatial distribution of the damage variable for the matrix material in one of the generated fibre spatial distributions, being the darker regions those where damage has been activated. In section 4.7 it was revealed that for a longitudinal shear load, an horizontal band of plasticised material would form in the weaker region of the volume element (as per figure 4.13a). After including the damage formulation in the constitutive model of the matrix material, it is precisely along the band of plasticised material that the damage variable is activated. Figure 5.28b shows the longitudinal shear stress-strain curves obtained after volumetric homogenisation for all fibre distributions. The greyed area on the top represents the range of fracture strengths for the volume elements with 60% of fibre volume fraction. Some scatter is visible in the fracture strengths that can be extracted from these analyses but still in the realm of logical values that can be obtained when a series of random distributions are used. Interesting to observe the effect of the periodic boundary conditions on the band of damaged material. Although the band is primarily located in the bottom edge of the volume element, there is a small portion of the band which shows up in the top, along the interface boundary between the two constituents of

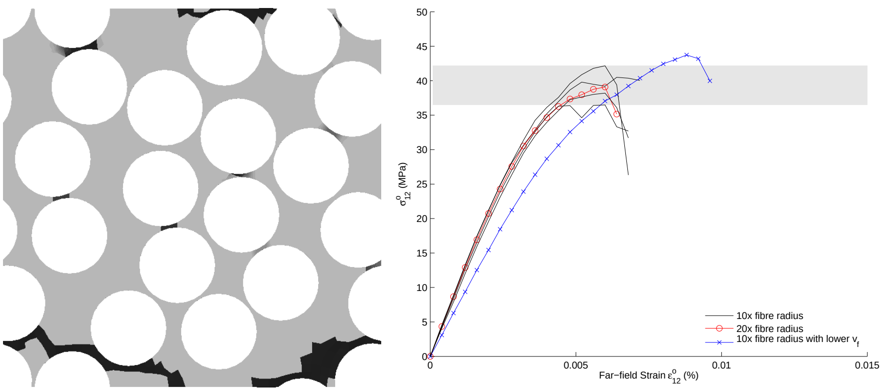

(a) Damage variable (b) Stress-strain curves

Figure 5.28: Results for longitudinal shear example.

the composite, due to the material and geometrical continuity imposed by the kinematic relations which define the periodic boundary conditions.

5.6.3 Transverse shear

Figure 5.29 shows the results from an applied transverse shear load to a volume element. Figure 5.29a shows the spatial distribution of the damage variable for the matrix material in one of the generated fibre spatial distributions, being the darker regions those where damage has been activated. An horizontal crack formed on the top of the volume element. A branch of this main crack is also visible. Figure 5.29b shows the transverse shear stress-strain curves obtained after volumetric homogenisation for all fibre distributions. The greyed area on the top represents the range of fracture strengths for the volume elements with 60% of fibre volume fraction. Scattering of fracture strength values is lesser than in previous load cases.

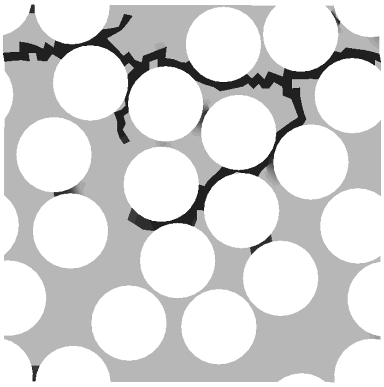

(a) Damage variable

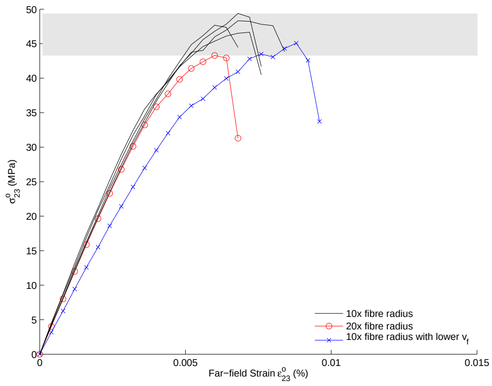

(b) Stress-strain curves

Figure 5.29: Results for transverse shear example.

5.6.4 Transverse compression

Figure 5.30 shows the results from an applied transverse compressive load to a volume element. Figure 5.30a shows the spatial distribution of the damage variable for the matrix material in one of the generated fibre spatial distributions, being the darker regions those where damage has been activated. The crack pattern follows a direction not aligned with the compressive load. The inclination of this angle varies between 45° and 55° with a vertical line. Two conclusions can be taken from this result. Firstly, it is not due to the compressive load but due to the shear stresses developing in the matrix that failure is bound to occur in a composite under transverse compression. This conclusion is supported by experimental data. Secondly, experimental data also reveals that the fracture angle under a transverse compression effort is approximately 53° for a Carbon fibre reinforced composite [109], [127]. Attention should be paid to the fact that this is a macro-measure, i.e. it does not need to be reproduced in a micro-analysis. However, a micro-analysis should provide a hint on the fact that fracture at the macro-scale is influenced by all micro-scale events and constituent properties. And this is perfectly achieved with the micro-mechanical analyses results being presented here.

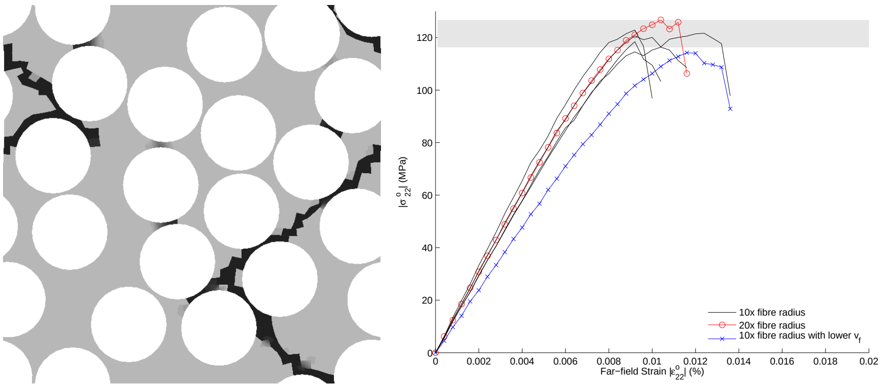

(a) Damage variable (b) Compressive stress-strain curves

Figure 5.30: Results for transverse compression example.

Figure 5.30b shows the compressive stress-strain curves obtained after volumetric homogenisation for all fibre distributions. The greyed area on the top represents the range of fracture strengths for the volume elements with 60% of fibre volume fraction. Very little scattering of the fracture strengths is found. There is however some tendency for a fast crack propagation. This most likely is due to the implementation of a damage evolution function defined from an uniaxial tensile case (as per section 5.3) which enforces a fast damage propagation.

5.6.5 Combined transverse compression and shear

Figure 5.31 shows the results from applying a combined transverse compression and transverse shear loads to a volume element. Both loads are of equal magnitudes. Figure 5.31a shows the spatial distribution of the damage variable for the matrix material in one of the generated fibre spatial distributions, being the darker regions those where damage has been activated. A different crack direction is visible in this load case when comparing with the individual crack patterns of figures 5.29a and 5.30a. Given the fact that the shear load applied to the volume element is of the same magnitude as the compressive load, shear stresses at the micro-scale acquire a much greater importance than normal stresses.

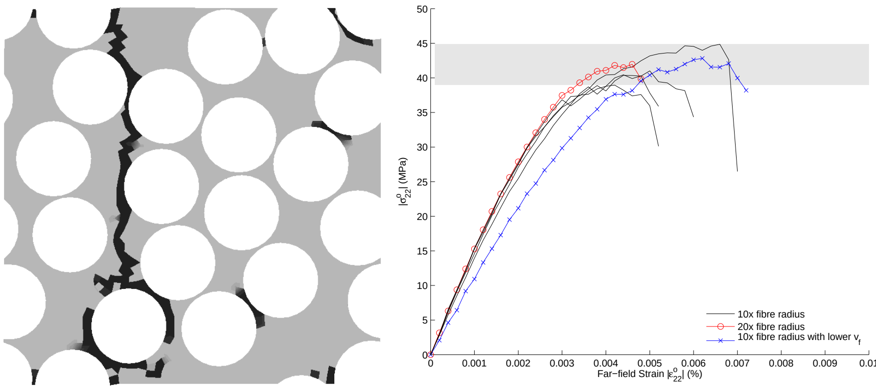

(a) Damage variable (b) Stress-strain curves

Figure 5.31: Results for combined transverse shear and compression example.

Figure 5.31b shows the transverse compressive stress-strain curves obtained after volumetric homogenisation of all fibre distributions. The greyed area on the top represents the range of fracture strengths for the volume elements with 60% of fibre volume fraction. The propensity that was registered in figures 5.29b and 5.30b for little scatter of fracture strengths is repeated here. However, there is greater non-linearity for this combined load case than had been registered in the isolated load cases.

5.6.6 Longitudinal tension

Figure 5.32a shows the longitudinal tensile stress-strain curves obtained after volumetric homogenisation of all fibre distributions. The greyed area on the top represents the range of fracture strengths for the volume elements with 60% of fibre volume fraction. A perfect linear behaviour is observed up until full fracture of the fibrous reinforcements and little scatter of results for tensile strengths is observed.

For these analyses, volume elements of greater thickness were used. Initially, this was done because of the little influence in the calculated elastic properties of a composite that the thickness parameter has (see section 3.4). However, after post-processing the results, one of the damage mechanisms mentioned in section 5.1.3 was detected in an unexpected way. Figure 5.32b shows a three dimensional image of the volume element, representing only those elements of the matrix where damage has been activated. It can be seen that damage does not concentrate along one fracture plane; instead, damage will propagate from one fibre to its neighbours along the matrix in a longitudinal direction. This phenomenon is observed in micrographs from longitudinal tensile tests (figure 5.4) and is known as fibre pull-out. It occurs when there is a separation of the fibre from the matrix due to failure along the interface between the two constituents and this mechanism is captured in these micro-mechanical analyses.

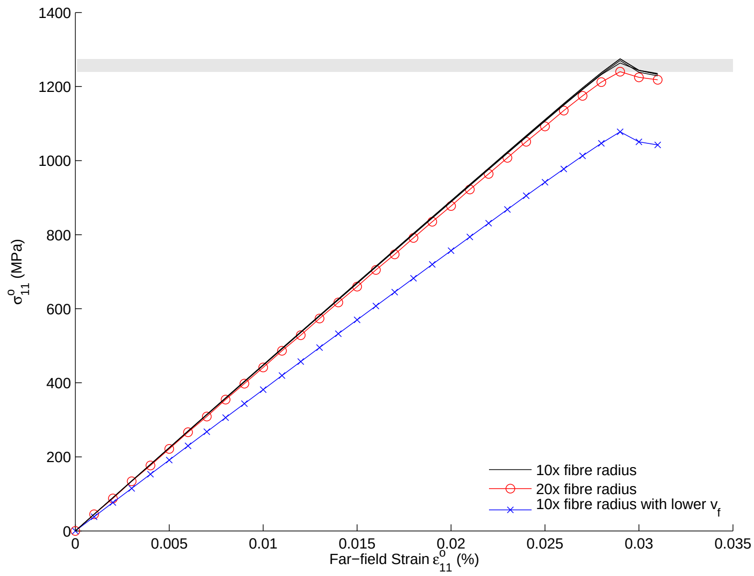

(a) Stress-strain curves

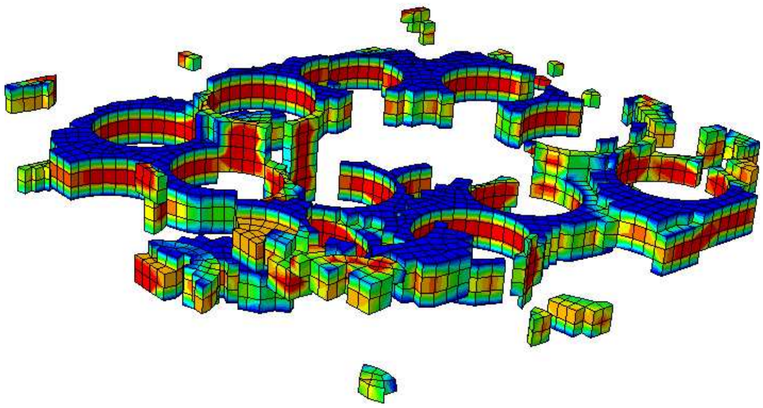

(b) Damage variable on the matrix

Figure 5.32: Results for longitudinal tension example.

5.7 Conclusions

The constitutive model developed for an epoxy matrix presented in chapter 4 has now been improved to include an isotropic damage law. Also for the fibrous reinforcement a constitutive damage model was developed and implemented considering damage only in the longitudinal direction. Both damage models were developed taking into consideration the effect of mesh size in the results. To tackle this problem, Bažant's crack band model [115] was used in order to properly account for the energy released upon fracture of the material.

The two constitutive models were implemented in a `UMAT` subroutine of the commercial finite element software package ABAQUS® [30]. The two models were validated making use of one-element tests and open-hole tension tests. It was verified that both models complied with varying toughness and mesh size adequately and shown that there is no mesh dependency of the results.

Using the procedures presented in chapter 2 for the generation of a representative volume element and the method presented in chapter 3 for the application of periodic boundary conditions to representative volume elements, a batch of representative volume elements were generated and an array of different loading conditions was applied to each volume element. The different micro-mechanical behaviour of each constituent was analysed for each load condition and a good agreement with experimental observations is achieved. Namely, the possibility of the damage model to predict fracture paths under uniaxial compressive loads along an angle between 45° and 55°, as well as the capability to capture the fibre pull-out failure mechanism typical of longitudinal tensile tests.

Having developed and implemented two constitutive damage models, one for each of the composite's constituents, and with the added advantage of having all the procedure of generating a representative volume element and implementing on it periodic boundary conditions fully automated, it is now possible to perform almost an infinite number of micro-mechanical analyses under all sorts of load combinations. In the next chapter, different failure envelopes for a glass-reinforced and a carbon-reinforced composite will be generated making use of the full possibilities provided by micro-mechanical analyses.

Chapter 6

Failure envelopes

> I'm going to do damage with it.
> I'll make sure that my work gets out.
>
> Michael Moore

Up to this moment, the main concern has been to provide a thorough presentation, validation and verification of the two constitutive material models developed and to assure a good geometrical representation of the cross-section of a long-fibre reinforced composite.
Now, with the certainty that the developed material models provide a close description of the mechanical behaviour of each constituent in a composite and with the software tool developed in chapter 2 to generate the required random distribution of fibres typically observed in composites, it is possible to begin using these concepts and start performing more complex and generic micro-mechanical analyses.
This chapter will present an array of failure envelopes obtained after running several finite element analyses with different loading conditions being applied to the generated representative volume elements. Composites reinforced with both glass and carbon fibre will be examined and differences will be scalped. A comparison with an analytical model recently proposed will be performed.

6.1 Analytical model

The predictions obtained from the micro-mechanical analyses performed in this chapter will be compared with those from an analytical model recently proposed by Catalanotti [128]. Catalanotti [128] developed a 3D analytical model capable of predicting the failure of composite materials. The model takes into consideration the different failure mechanisms observed in experimental analyses. In the longitudinal direction (i.e. aligned with the fibre direction), it is considered that the fibrous reinforcement is responsible for bearing the loads applied to the composite, while in the transverse direction this role is fundamentally portrayed by the matrix material.

As mentioned in chapter 5, composite materials exhibit considerably different mechanical behaviour whether a tensile or a compressive load is being applied. In the longitudinal direction, a tensile load will lead to a rupture of the reinforcements along a transverse plane. On the other hand, a compressive load gives origin to the formation of a kink band, i.e. due to failure of the matrix providing lateral support to the long fibres of reinforcement and/or due to initially misaligned fibres, a band of buckled fibres forms and gives origin to failure of the composite.

As per the transverse direction, the composite material exhibits an intricate mechanical behaviour. The available experimental data indicates that failure will occur in an inclined plane. Figure 6.1 illustrates the situation.

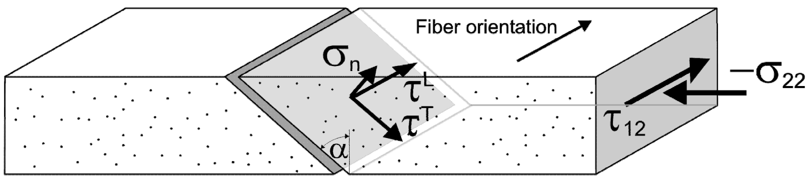

Figure 6.1: Puck's action plane (image from Dávila and Camanho [89]).

Puck [109] has introduced the concept of *action plane* to describe the phenomenon. This action plane is inclined by an angle α. The stress tensor acting on this plane can be decomposed in one normal stress perpendicular to the plane, σ_N, and two shear stresses, τ_T and τ_L, tangential and longitudinal, respectively. If the transverse stress σ_{22} applied to the composite is positive, then experimental data shows that $\alpha = 0°$. But if a compressive transverse stress is being applied instead, the inclination of the plane will be different. This is due to a greater capacity of the matrix material to resist compressive efforts instead of shear ones. The shear stresses acting on the action plane will weigh considerably in the strength of the composite under transverse compression and consequently cause a failure angle α different from zero. In Carbon reinforced composite materials, the fracture angle measured from experimental tests is approximately $\alpha = 53° \pm 2°$.

Due to all these intricacies in the fracture behaviour of a composite lamina, any analytical model attempting to predict its failure must be split in a number of failure activation functions, one function for each different failure mechanism. Catalanotti's analytical model [128] provides a set of four different activation functions:

- **Transverse tension**
  Matrix failure under a transverse tensile load is defined by the following equation,

$$FMT = \left(\frac{\tau_L}{S_L^{is}}\right)^2 + \left(\frac{\sigma_I}{Y_T^{is}}\right)^2 \tag{6.1}$$

  where the superscript ^{is} denotes *in-situ* strengths as defined by Dávila and Camanho [89], τ_L represents longitudinal shear stress and σ_I is the maximum principal stress on a transverse plane to the fibres. Fracture angle α is given by the direction of the maximum principal stress σ_I, i.e. a search is performed through all the possible failure angles and the one which maximises the failure index FMT is selected.

- **Transverse compression**
  Catalanotti [128] uses the same criterion for transverse compression which has been proposed by Dávila and Camanho [89], based on a modification of Puck's failure criterion [109]. The criterion is defined by the following equation:

$$FMC = \left(\frac{\tau_L}{S_L^{is} - \eta_L \sigma_N}\right)^2 + \left(\frac{\tau_T}{S_T^{is} - \eta_T \sigma_N}\right)^2 \tag{6.2}$$

  Definition of coefficients η_L and η_T can be found in [89] and are referred in the literature as the angles of internal friction related with longitudinal and transverse shear stresses, respectively. Mathematically, they represent the gradient of the function $\tau = f(\sigma_N)$ when $\sigma_N = 0$:

$$\eta_L = -\left.\frac{\partial \tau_L}{\partial \sigma_N}\right|_{\sigma_N = 0}, \quad \eta_T = -\left.\frac{\partial \tau_T}{\partial \sigma_N}\right|_{\sigma_N = 0} \tag{6.3}$$

  It is mainly due to this definition that a different orientation for the fracture angle can be obtained from this failure criterion as represented in figure 6.1.

- **Longitudinal tension**
  A tensile load applied on the longitudinal direction will be resisted almost solely by the fibrous reinforcements. The failure activation function is thus simply a function of the maximum longitudinal strain of the composite, ε_1^T:

$$FFT = \frac{\varepsilon_{11}}{\varepsilon_1^T} \tag{6.4}$$

- **Longitudinal compression**

  In theory, a kink band may form with the buckled fibres positioning themselves along an arbitrary plane. However, this plane can be defined using two angles, the first being the rotation of the kink plane relatively to a longitudinal cross-section of the composite, while the second being a rotation of the fibres themselves in the plane of kinking (figure 6.2).

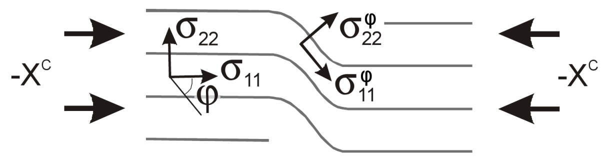

Figure 6.2: Misalignment of fibres.

Catalanotti's failure criterion for longitudinal compression [128] requires the use of the stress tensor defined in the rotated reference frame where the kink band is formed, i.e. it is required to perform two tensor transformations, one for each of the angles referenced above. Proper definition of the rotation angles can be found in Catalanotti [128]. Failure under longitudinal compression is formulated as the maximum failure index out of the two previously defined ones for transverse tension and compression of the composite, but computed now on the rotated reference frame. In other words, it is considered that longitudinal compressive failure is activated by failure of the matrix supporting the fibres which lead to the formation of a kink band of buckled fibres. The failure criterion can thus be defined by:

$$FFC = \max\left\{\max\left\{FK_{MC}\right\},\ \max\left\{FK_{MT}\right\}\right\} \tag{6.5}$$

where FK_{MC} and FK_{MT} represent the failure activation mechanism for matrix compression and matrix tension, respectively, in the rotated reference frame and are given by:

$$FK_{MC} = \left(\frac{\tau_L^{\varphi}}{S_L^{is} - \eta_L \sigma_N^{\varphi}}\right)^2 + \left(\frac{\tau_T^{\varphi}}{S_T^{is} - \eta_T \sigma_N^{\varphi}}\right)^2 \tag{6.6}$$

$$FK_{MT} = \left(\frac{\tau_L^{\varphi}}{S_L^{is}}\right)^2 + \left(\frac{\sigma_N^{\varphi}}{Y_T^{is}}\right)^2 \tag{6.7}$$

where the superscript $^{\varphi}$ represents the components of the stress tensor in the rotated reference frame.

6.2 Failure envelopes

Two different composite materials will be considered to generate the failure envelopes – one Glass fibre reinforced polymer and one Carbon fibre reinforced polymer. The elastic properties of each constituent are provided in table 6.1. The same matrix information that has been used in chapter 4 will be used for both composites.

Table 6.1: Elastic properties of constituents.

Material	E_1 [GPa]	E_2 [GPa]	G_{12} [GPa]	ν_{12}	G_{23} [GPa]
Fibres					
AS4	225	15	15	0.2	7
Silenka E-glass	74	74	30.8	0.2	30.8
Matrix					
Toho #113 [70]	3.76	3.76	1352	0.39	1352

Three different fibre distributions were generated for each composite system with 60% fibre volume fraction. Elastic and strength properties were determined after averaging results from the three distributions for each composite system. Table 6.2 shows the computed elastic properties while table 6.3 provides a summary of the strength properties calculated for each composite system.

Table 6.2: Elastic properties of composite systems.

Material	E_1 [GPa]	E_2 [GPa]	v_{12}	G_{12} [GPa]	G_{23} [GPa]
AS4/Toho#113	126.41	8.76	0.25	4.41	3.17
Silenka/Toho#113	43.73	14.65	0.25	5.37	5.02

Table 6.3: Strength properties of composite systems.

Material	Y_T [GPa]	S_L [GPa]	α [deg]	Y_C [GPa]	η_L
AS4/Toho#113	73.22	42.03	53	128.30	0.26
Silenka/Toho#113	62.30	40.57	53	118.70	0.25

Different loading schemes were applied to each distribution in order to generate failure envelopes for each composite system. What follows is a discussion on the applied far-field strain state for each loading scheme and a comparison of the results with the analytical model recently proposed by Catalanotti [128].

6.2.1 Biaxial transverse load

The far-field strain tensor applied in order to obtain biaxial transverse loading is generically defined by (in Voigt notation):

$$\boldsymbol{\varepsilon^o} = \begin{bmatrix} - & - & - \\ - & a & - \\ - & - & b \end{bmatrix} \tag{6.8}$$

Different values are given to parameters a and b in order to obtain different loading conditions. Table 6.4 shows the different combinations used.

Table 6.4: Definition of loading trajectories.

ID	a	b	ID	a	b
A	1	1	J	-3	2
B	1	2	L	-6	1
C	-	1	M	-6	2
D	-1	8	N	-1	-
E	-1	4	O	-6	-1
G	-1	2	P	-6	-2
H	-2	3	Q	-2	-1
I	-1	1	R	-2	-2

Figures 6.3 and 6.4 present the failure envelopes for the Carbon based and the Glass based composite systems, respectively. The dashed line represents the analytical results while the blue line represents the numerical results after averaging the three different distributions obtained from homogenisation of the stress fields in the representative volume element. It should be noted that the analytical model by Catalanotti [128] is not closed in the biaxial compression quadrant of the $\sigma_{22} - \sigma_{33}$ stress space.

Comparing the analytical model with the numerical results, and excluding the third quadrant, both methods provide almost equal predictions. Judging from the numerical results, the general shape of the failure envelope is close to one of an ellipse. None of the models predict a strength reduction under a biaxial tensile load; actually, the micromechanical analyses even predict failure at greater values for biaxial loading than for uniaxial loading. This could be due to the use of a non-linear model for the matrix with considerable plastic deformation before failure. It would require a greater number of experimental data for both the epoxy matrix and the composite in order to determine the influence of the constitutive model for the matrix material in the overall composite's mechanical behaviour.

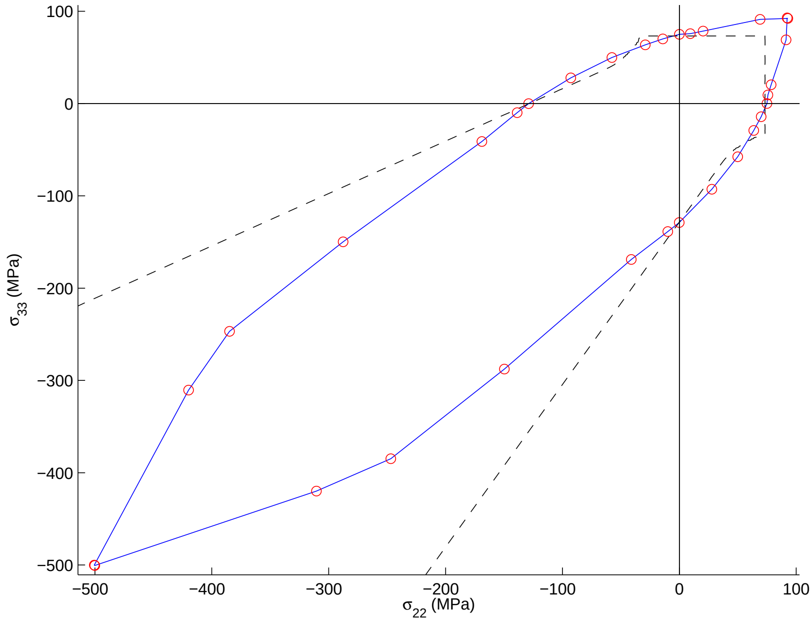

Figure 6.3: Failure envelope for biaxial transverse stresses for Carbon fibre composite.

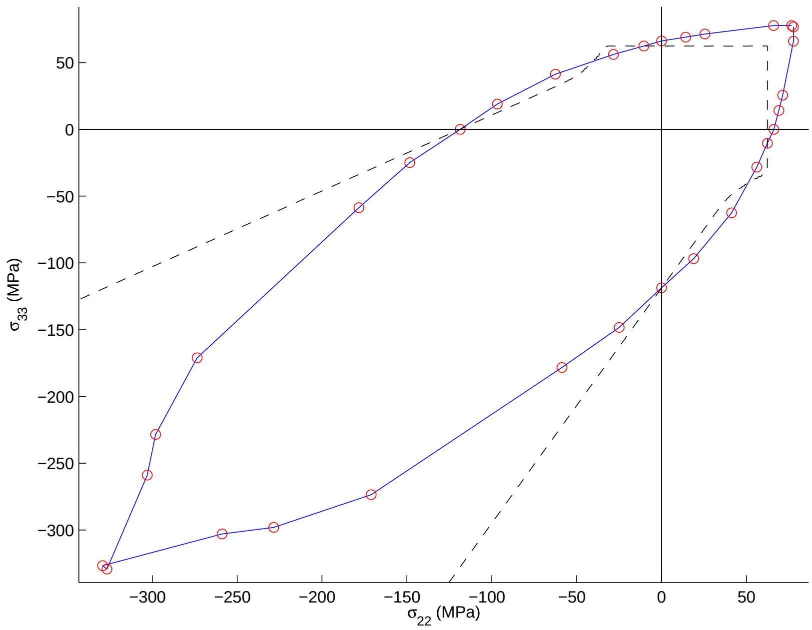

Figure 6.4: Failure envelope for biaxial transverse stresses for Glass fibre composite.

6.2.2 Transverse normal and longitudinal shear load τ_{12}

The far-field strain tensor applied in order to obtain a combination of transverse normal loading with longitudinal shear is generically defined by (in Voigt notation):

$$\varepsilon^o = \begin{bmatrix} - & b & - \\ b & a & - \\ - & - & - \end{bmatrix} \tag{6.9}$$

Different values are given to parameters a and b in order to obtain different loading conditions. Table 6.5 shows the different combinations used.

Table 6.5: Definition of loading trajectories.

ID	a	b	ID	a	b
A	2	-	I	-1	3
B	10	1	J	-2	3
C	3	1	K	-4	3
D	2	1	L	-4	2
E	4	3	M	-3	1
F	2	3	N	-10	1
G	1	3	O	-2	-
H	-	2			

Figures 6.5 and 6.6 present the failure envelopes for the Carbon based and the Glass based composite systems, respectively. The dashed line represents the analytical results while the blue line represents the numerical results after averaging the three different distributions obtained from homogenisation of the stress fields in the representative volume element.

On the tension side of the plots an excellent agreement between the analytical and the numerical approaches is achieved. However, the same can not be said for the compression side, especially if there is a strong presence of a shear load. For both composite systems, the micromechanical approach is considerably more conservative in the estimates it provides. This is probably due to the damage evolution function used in the constitutive model of the matrix material which enforces damage localisation in an abrupt manner.

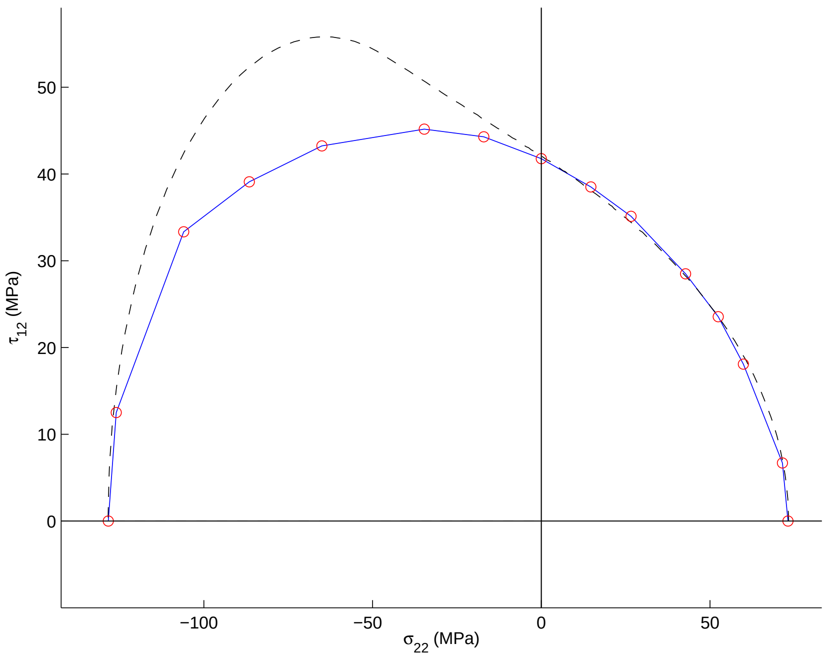

Figure 6.5: Failure envelope for transverse normal stress with longitudinal shear τ_{12} for Carbon fibre composite.

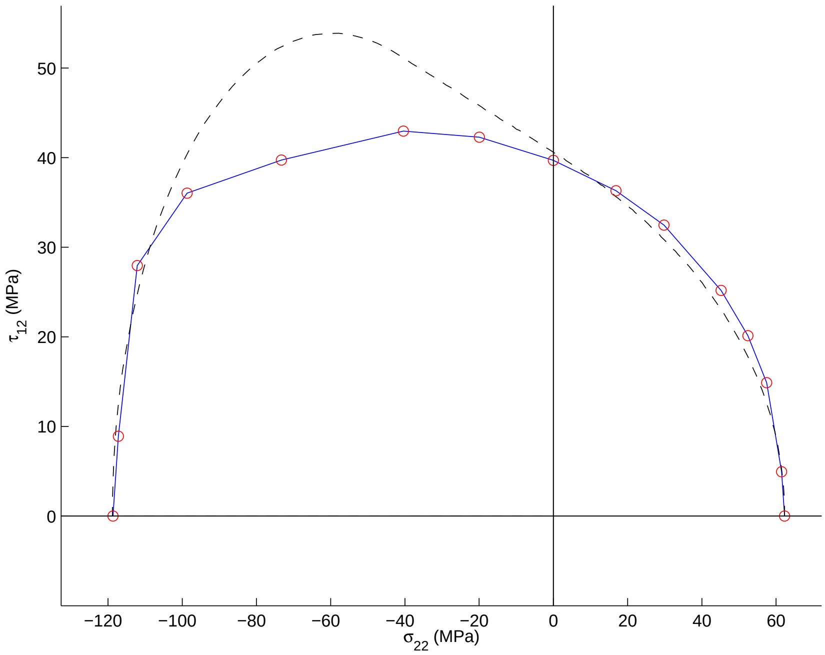

Figure 6.6: Failure envelope for transverse normal stress with longitudinal shear τ_{12} for Glass fibre composite.

6.2.3 Transverse normal and longitudinal shear load τ_{13}

The far-field strain tensor applied in order to obtain a combination of transverse normal loading with longitudinal shear is generically defined by (in Voigt notation):

$$\varepsilon^{o} = \begin{bmatrix} - & - & b \\ - & a & - \\ b & - & - \end{bmatrix} \tag{6.10}$$

Different values are given to parameters a and b in order to obtain different loading conditions. Table 6.6 shows the different combinations used.

Table 6.6: Definition of loading trajectories.

ID	a	b	ID	a	b
A	2	-	I	-1	3
B	10	1	J	-2	3
C	3	1	K	-4	3
D	2	1	L	-4	2
E	4	3	M	-6	2
F	2	3	N	-10	1
G	1	3	O	-2	-
H	-	2			

Figures 6.7 and 6.8 present the failure envelopes for the Carbon based and the Glass based composite systems, respectively. The dashed line represents the analytical results while the blue line represents the numerical results after averaging the three different distributions obtained from homogenisation of the stress fields in the representative volume element.

An excellent agreement between the analytical and numerical predictions can be found for the entire failure envelope. Exception only to the combination of tensile normal stress with high longitudinal shear stresses τ_{13} where the micromechanical curves follow a more smooth path and eliminate the sharp edge predicted by the analytical model. This result was expectable since the micromechanical model will provide a much closer result to reality eliminating singularities existent in the analytical approach. The longitudinal shear stress τ_{13} does not have such a strong influence on the compressive side of the curve as the stress component τ_{12} had (vide previous subsection).

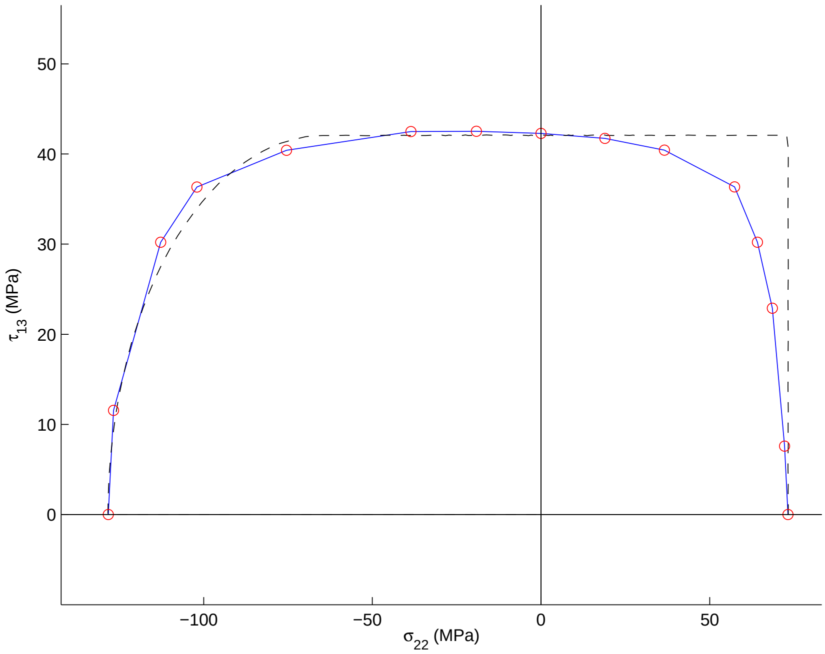

Figure 6.7: Failure envelope for transverse normal stress with longitudinal shear τ_{13} for Carbon fibre composite.

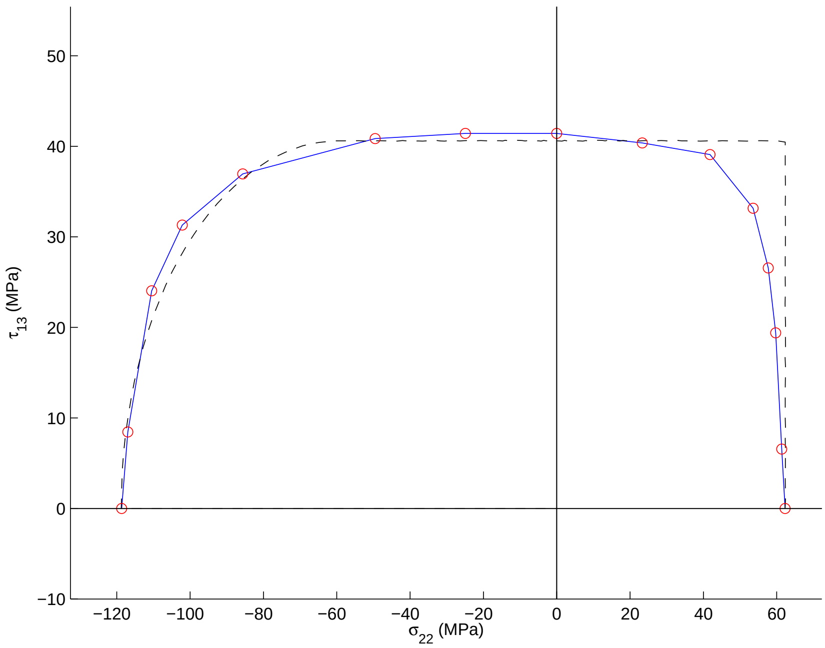

Figure 6.8: Failure envelope for transverse normal stress with longitudinal shear τ_{13} for Glass fibre composite.

6.2.4 Transverse normal and transverse shear load

The far-field strain tensor applied in order to obtain a combination of transverse normal loading with transverse shear is generically defined by (in Voigt notation):

$$\varepsilon^{o} = \begin{bmatrix} - & - & - \\ - & a & b \\ - & b & - \end{bmatrix} \tag{6.11}$$

Different values are given to parameters a and b in order to obtain different loading conditions. Table 6.7 shows the different combinations used.

Table 6.7: Definition of loading trajectories.

ID	a	b	ID	a	b
A	2	-	I	-1	3
B	10	1	J	-2	3
C	3	1	K	-4	3
D	2	1	L	-4	2
E	4	3	M	-6	2
F	2	3	N	-10	1
G	1	3	O	-2	-
H	-	2			

Figures 6.9 and 6.10 present the failure envelopes for the Carbon based and the Glass based composite systems, respectively. The dashed line represents the analytical results while the blue line represents the numerical results after averaging the three different distributions obtained from homogenisation of the stress fields in the representative volume element.

The general shape of the failure envelopes differs slightly between the analytical model and the numerical results. In the tension side, the analytical approach overshoots the micromechanical predictions, especially when a high transverse shear stress is present. Again, a sharp edge is visible from the analytical model which is eliminated by the numerical approach. On the compression side, the opposite scenario occurs: it is now the micromechanical approach that provides greater strengths than the analytical model. The numerical estimates suggest that the transverse shear stress τ_{23} has a somewhat similar effect on the strength of the composite under transverse compressive loading than the longitudinal shear stress τ_{12}.

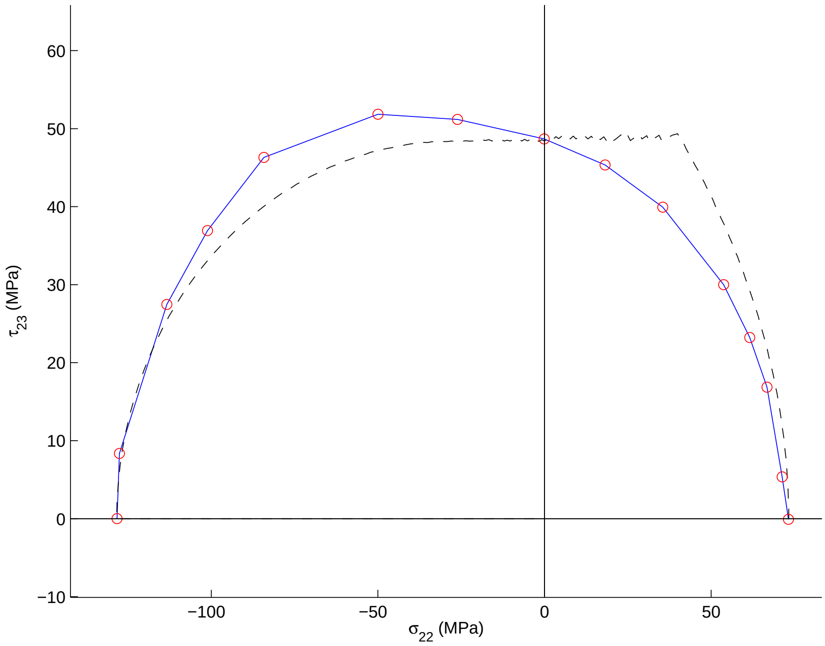

Figure 6.9: Failure envelope for transverse normal stress with transverse shear for Carbon fibre composite.

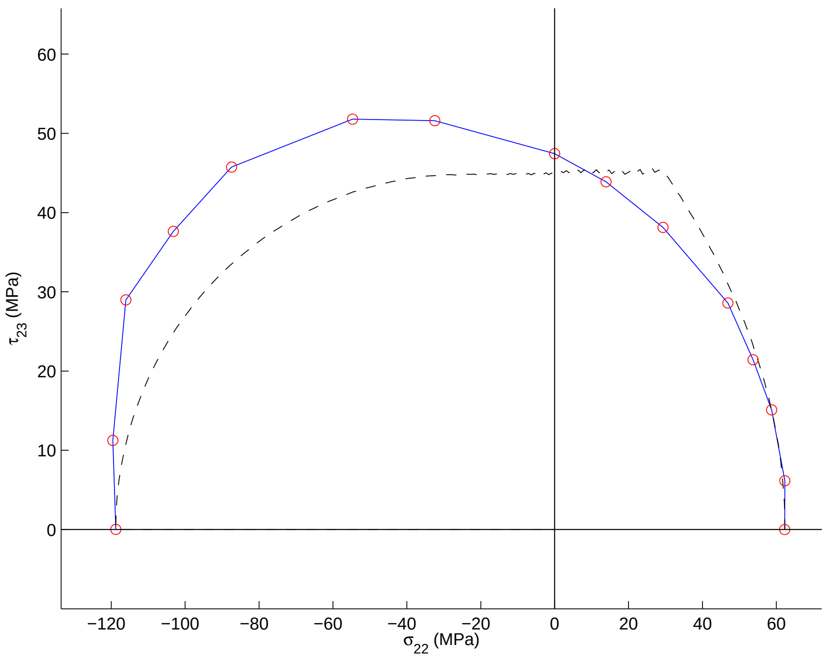

Figure 6.10: Failure envelope for transverse normal stress with transverse shear for Glass fibre composite.

6.3 Conclusions

Micromechanical analyses can provide a better insight on the constitutive behaviour of any composite material. The procedure can be used to determine not only the elastic constants of the composite starting from the properties of each constituent, but it can also provide the strength properties under a miscellanea of loading conditions, given the fact that each constituent is modelled with a physically sound constitutive model.

Both elastic and strength properties determined from micromechanics can be used in analytical failure criteria as input parameters, making no longer necessary to accept assumptions, sometimes arguable, so often the case in analytical models.

Three dimensional periodic boundary conditions allow for the application of any kind of far-field strain tensor. This possibility opens the door to the generation of any kind of two dimensional or even three dimensional failure envelope. These failure envelopes can lead to the creation of better analytical failure criteria whenever availability of experimental data is scarce or even nonexistent. The failure envelope for the transverse normal stress and transverse shear stress is an example of that.

Comparing the results from both micromechanics and a recently proposed analytical model, it can be concluded that the paths of these two methodologies do come close in many aspects, providing similar estimates for most of the loading conditions. Differences still exist, making it necessary for more experimental work to be performed for improvement and validation of both analytical and micromechanical approaches. Experimental data for the matrix material should be considered essential to achieve this goal.

Chapter 7

Application to textile composites

When weaving a blanket, an Indian woman leaves a flaw in the weaving of that blanket to let the soul out.

Martha Graham

The constitutive models developed and presented in previous chapters do not have their application limited to unidirectional composites. In this chapter, the elasto-plastic material model with damage developed for an epoxy matrix will be applied to a different class of composite materials – textile composites. Special attention will be given to a particular kind of textile – 5-harness satin.

A brief introduction will be provided describing the different presentations this kind of materials can have, their individual properties, advantages and drawbacks. Since this chapter will focus on 5-harness satin weaves, a state of the art on the existent numerical and experimental knowledge is presented. The sequential steps taken to generate a representative volume element of a satin weave is provided next and the modifications necessary for the application of periodic boundary conditions are given in detail.

Lastly, a sequence of numerical analyses on the generated representative volume element are performed under different types of loading conditions. A *wet* configuration is used, i.e. the tows that build up the textile are embedded in an epoxy matrix. The constitutive model developed for the matrix in previous chapters is applied here, while the tows are modelled with a previously published transversely isotropic damage model for an homogenised composite.

7.1 Different types of textile composites

Woven composite materials have provided several enhancements over traditional unidirectional and multi-directional composite layups. Substantial improvements in resisting delamination and better drape properties have been achieved by using woven composites. However, new challenges have been presented by this new type of materials, namely in terms of predicting damage initiation and propagation as the different internal geometry of the material leads to different stress concentration areas, crack propagation patterns and final failure scenarios.

Every woven fabric consists of two sets of interlacing yarns disposed in a perpendicular direction to each other. The idea behind this disposition comes from the wicker industry for the production of baskets, furniture and decorative pieces. Just like for wickers, a large number of combinations are possible for the weaving of the yarns. However, each different weaving pattern leads not only to a different visual aspect of the fabric, but also to different material properties. Hence when choosing a fabric for a given application, the designer must consider not only aesthetics but also mechanics.

There are three basic weave types: plain, twill, and satin. Figure 7.1 shows examples of each of these weave patterns. In this thesis, it will be considered that the yarn in an horizontal position is the warp yarn, while the yarn in a vertical position is the weft yarn. The plain weave is the simplest pattern; each odd warp operates over one and under the next weft, while each even warp follows the same sequence but in reverse order (under one and over the next).

Twill weaves repeat on three or more warp and weft yarns. In a 2x2 twill, each warp will pass over two weft yarns and then under two weft yarns; the following warp follows the same sequence but out of phase by one weft. Twill weaves are characterized by a distinctive diagonal line.

A satin weave provides the smoothest surface of all weaves as it is created by long warp yarns. Each warp will pass over a weft every X wefts. The name of the satin is given by the value of X; in a 5-harness satin, a warp will pass over a weft every 5^{th} weft. The locations where this crimp occurs repeat in an L-shaped pattern.

Figure 7.1 provides only four examples out of a multitude of possibilities for different arrangements for plain, twill and satin weaves. As mentioned before, each arrangement will originate a weave with not only different visual appearance, but also with different mechanical properties. One of the most important aspects influencing the mechanical behaviour of a weave is the number of intersections per area. In other words, the greater number of

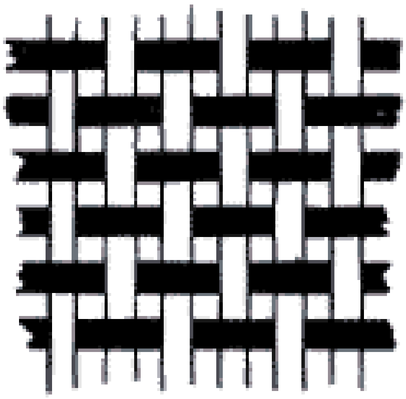

(a) Plain weave

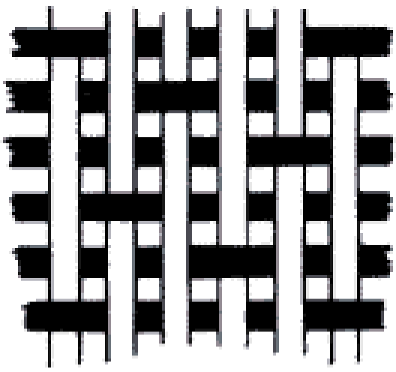

(b) 5-Harness satin weave

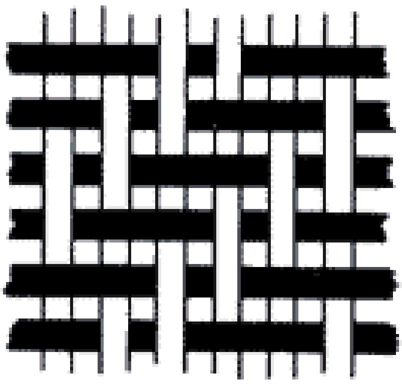

(c) 2x2 twill weave

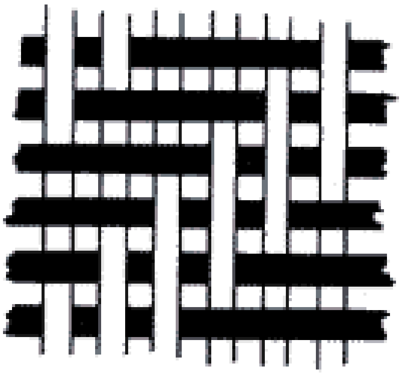

(d) 3x3 twill weave

Figure 7.1: Different types of weave patterns.

interlacings per area in a weave, the tighter the weave will be. A plain weave is the tightest weave of those presented in figure 7.1, followed by twill weaves. Satin weaves are the loosest.

The tighter a weave is, the less it will shrink during application and finishing processes. A satin weave will shrink the most as it possesses a much more loose configuration, allowing for the yarns to move more freely relatively to one another. However, the tighter a weave is, the greater propensity to tear it will exhibit. Because of its tightness, in a plain weave there is only one yarn bearing load when the weave is being torn.

Crimp is the degree of waviness or distortion of a yarn due to its interlacing with a perpendicular yarn. Since a plain weave has the highest number of intersections, it also possesses the highest degree of crimp. This leads to different extensibility properties. The highest the degree of crimp, the more extensible the weave is when under a tensile load. A satin weave having the lowest degree of crimp possesses the lowest extensibility of all three types of weave considered here.

The easier it is for the yarns to move freely relatively to each other provides a better resistance to wrinkling. In plain weaves, the yarns are so tight to each other, that it makes very difficult for the material to recover after deformation. Satin weaves provide better resistance to wrinkling due to their more loose construction pattern.

An important aspect for aesthetic reasons is draping. It is defined as the ability of the fabric to hang in a graceful manner. Again, the tighter the construction of the weave is, the more difficult it will be for the weave to drape. Satin weaves being the loosest provide better draping.

Satin weaves lose to plain weaves in terms of snagging resistance. The shorter the length between consecutive crimps, the more resistant the weave will be to snagging. However, this very same geometric characteristic of the construction pattern provides satin weaves with a smoother surface, while plain weaves are not so smooth. Twill weaves provide a middle term in between satin and plain weaves for these two properties.

As a final remark, it is noted that there are multiple constructions possible for twill and satin weaves, and even for plain weaves it is possible to group consecutive yarns instead of the most simple construction represented in figure 7.1. And as seen above, for each construction, the number of intersections per unit area will be one of the most influential aspects for aesthetics and material mechanical behaviour.

Out of the three main types of weaving – plain, twill, and satin – it was the latest that has caught the attention of automotive and aerospace industries due to their outstanding compromise between drape, crimp, and wet-out properties.

In the woven composites world, it is not possible to provide a general failure behaviour since each kind of weave pattern has a unique geometry leading to completely different stress-strain patterns, stress concentration regions, and failure circumstances. Hence, a review of the most widely used and potentially interesting satin weaves was made close to the automotive and aerospace industry. 5-harness satin revealed to be the most adequate choice for a careful and methodical study of its mechanical behaviour as it is the one which maximises the above mentioned properties. The next section will present a summary of the analytical, numerical and experimental data available for this kind of textile composite.

7.2 State of the art on 5-harness satins

Applying the concepts from the wicker industry to advanced composite materials is relatively recent. One of the first attempts to identify the elastic parameters of a textile composite was made by Ishikawa [129] in 1982. Ishikawa proposed the use of a mosaic which would represent in a very simplified manner the cross-section of a textile composite. Figure 7.2 represents this concept.

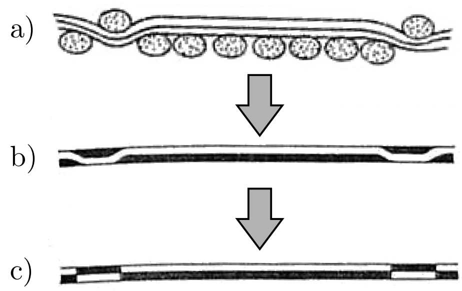

Figure 7.2: Ishikawa's idealised mosaic model (from [130]).

Figure 7.2a shows the most generic cross section of a satin weave, in this case an 8-harness satin, i.e. a warp yarn will pass under a weft yarn every 8^{th} weft yarn. After resin impregnation and curing process, the yarns will accommodate themselves better and form a flattened distribution in the matrix material (figure 7.2b). If the crimp angles and waviness are disregarded, then the cross-section can be reduced to the idealised mosaic model represented in figure 7.2c. The model was developed and applied to both non-hybrid [129] and hybrid [130] textile composites by Ishikawa.

As with most analytical models, the idealised mosaic model of Ishikawa leads to the definition of an upper and a lower bound on the stiffness and compliance properties of the textile composite in a closed form. The bounds are obtained by applying either an iso-stress or an iso-strain over the textile.

More advanced models have been proposed for determining the elastic constants of even more complex structural weaves, such as three dimensional textile composites. Yang et al. [131] developed a *Fibre Inclination Model* which models the unit cell of a textile composite as an assemblage of inclined unidirectional laminae (figure 7.3). The analysis is based on the classical theory for laminated plates. Whitney and Chou [132] extended this model for the prediction of elastic constants of textile composites with three-dimensional angle-interlock preforms. Figure 7.4 show an idealised angle interlock preform of a satin weave.

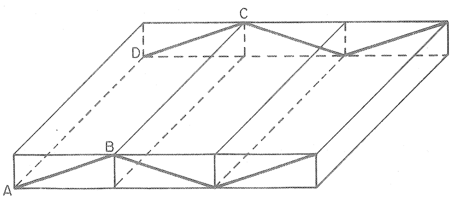

Figure 7.3: Schematic view of *Fibre Inclination Model* (from [131]).

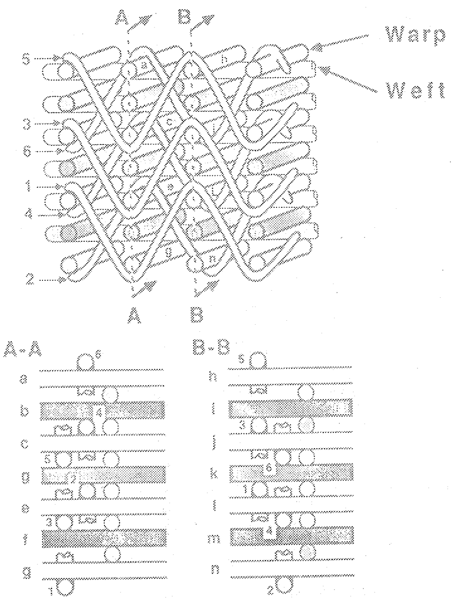

Figure 7.4: Idealised angle interlock preform of a satin weave (from [132]).

Many other models have been proposed, but all suffer from the same limitation: by ignoring the effect of the crimp regions and the waviness of the yarns in those regions, an important stress concentration region is ignored, and the results from these models tend to over predict the elastic moduli. These same conclusions were obtained by Byström et al. [133] when a comparison study of analytical, numerical and experimental results was performed.

King et al. [134] made an attempt to include the different geometric characteristics in a numerical model that simplified the shape of the textile to a beam-construction structure (figure 7.5). Each beam would have a constitutive model capable of modelling the yarn mechanical behaviour and the intersections between the different beams where crimp occurs were modelled using bending or crossover springs in an out-of-plane truss-like configuration. The model was numerically implemented and its results compared with experimental data. The model predicted well the behaviour under uniaxial and biaxial loading of a strip of textile composite in both failure estimate and deformation of the textile.

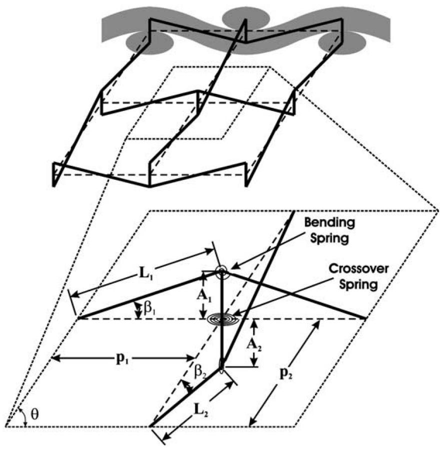

Figure 7.5: Model geometry proposed by King et al. [134].

Some attempts have been conducted to model a representative volume element of a textile composite making use of a unit cell and the repetitive geometry existing in weave patterns. Zako et al. [135] performed such analyses on plain weaves in a *wet* configuration (figure 7.6). An anisotropic damage model was used to model the yarns and an isotropic damage model was used for the matrix. The main advantage of performing a three dimensional finite element analysis on a representative volume element is that it becomes possible to adequately capture all of the events taking place in the crimp region, by far the most susceptible region to damage activation. The numerical results agreed well with the experimental data. Cracks initiated in the yarns perpendicular to the loading direction and propagated to the matrix till reaching the surface of the volume element and extending through its width causing a decrease on the longitudinal Young's modulus.

A similar discretisation was performed by Barbero et al. [136], but with a damage model developed in the framework of thermodynamics. Special care was taken in the definition of the material parameters of the yarns in order to account for the change in direction of material properties along a crimped yarn. Also here a good agreement with experimental data was found.

The main difficulty behind micro-mechanical analyses of textile composites is the correct definition of the geometry of the yarn, arrangement of neighbouring yarns and crimping regions where the weft and warp yarns cross each other. The geometry becomes even more complex to define if a three dimensional effect such as stitching is added to the composite. In or-

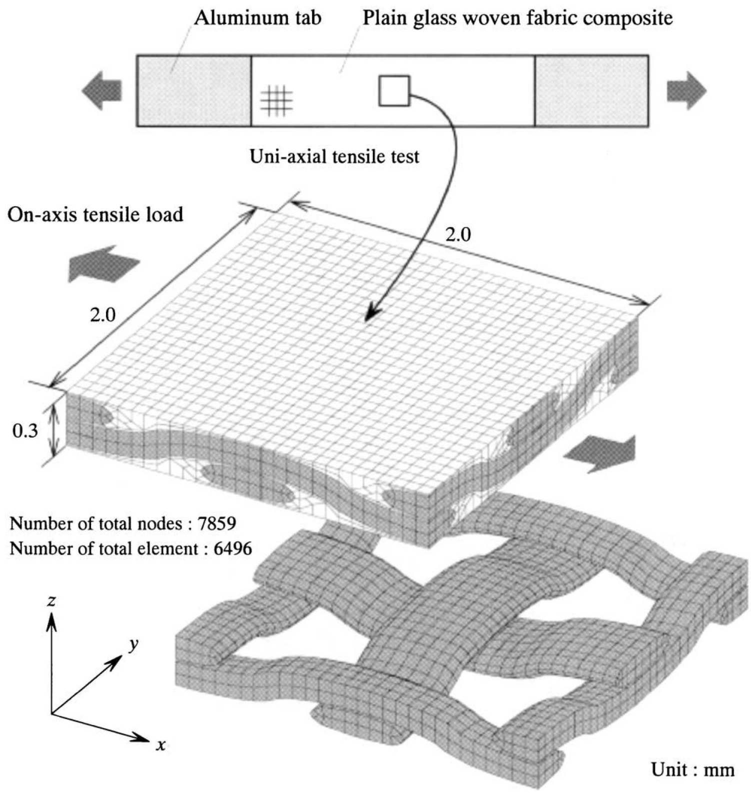

Figure 7.6: Three-dimensional model of plain weave by Zako et al. [135].

der to simplify the process of geometry specification and mesh generation for finite element analyses to be performed, Lomov and co-workers developed a set of algorithms compiled in a software package called *WiseTex* [137]-[138]. The geometry models generated can then be used in commercial finite element software packages such as ANSYS® [139] or ABAQUS® [30] along with the material definition the analyst sees more appropriate for the textile under study.

Making use of this software package, Daggumati et al. [140] performed a complete discretisation of a 5-harness satin weave (figure 7.7). The elastic constants and strength properties for the fibre bundle were calculated following Chamis' analytical formulas [141]. The damage model considered for the yarns is an extension of the Hoffman failure criteria [142] while for the matrix an isotropic damage formulation is applied. Depending on what kind of boundary conditions are specified, different predictions for damage activation are obtained. An infinite laminate will indicate that transverse damage occurs first at the edges of the crimped weft yarns, while in-plane periodic boundary conditions will concentrate transverse damage at the centre of the crimped weft yarns. The two different modelling approaches can be used for different regions of the laminate, being the first associated with the inner layers and the second with the surface layers of the laminate.

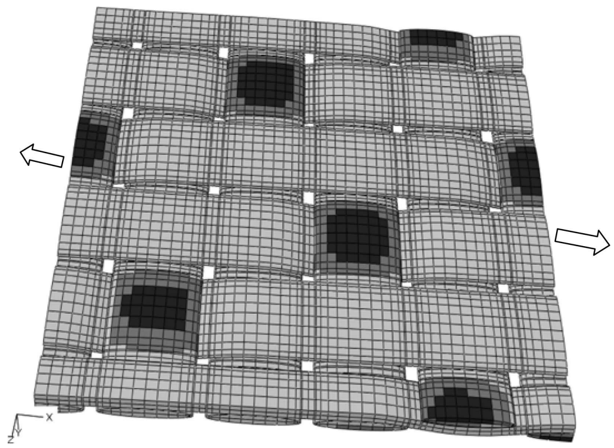

Figure 7.7: Three-dimensional model of 5-harness satin weave by Daggumati et al. [140].

Daggumati et al. [140] also performed experimental tests on a Carbon-PPS 5-harness satin under static tension. Acoustic emission techniques were involved in the capture of damage events during the tests. The load is applied in the direction of the warp yarns. Tests were performed on a laminate with eight layers of textile composite. Thanks to a methodical microscopic analysis it was possible to characterise damage evolution in the laminate and divide it in four easily identifiable steps:

- Damage is first detected along the edges of the weft yarns inside the laminate;
- As the load is increased isolated transverse cracks begin to appear in the nested yarns (i.e. weft yarns which are not in a crimp region) throughout all laminate;
- With the load building up, cracks propagate towards the matrix until they reach the outer surface of the laminate. By this time, most of the nested yarns have already developed transverse cracks which propagated to the intra-yarns region;
- Finally, damage is observed at the edges of those weft yarns which are closely packed by load carrying warp yarns. From this point, catastrophic failure of the composite becomes eminent.

7.3 Generation of representative volume element

This section will concentrate on the steps required in order to generate a unit-cell representative of the geometric pattern of a 5-harness satin. The geometric parameters were measured from micrographs taken of the real material and a three-dimensional model of the weave was generated using CAD software SolidWorks® [143]. The model was then exported to finite element pre-processing software FEMAP® [144] where a mesh with tetrahedra elements was generated.

7.3.1 Geometry of weave

In cooperation with Imperial College London, a series of micrographs were taken of a real 5-harness satin weave. Several measurements were performed in order to obtain the overall dimensions of the yarns, inter-yarn distance, inter-crimp distance and crimp angle. Figure 7.8 presents one of the micrographs taken. As can be seen, the geometry of the weave is extremely complex with overlapping yarns and shifted layers. As a first approach it was decided to model a simplified version of the satin's geometry, assuming that the yarns along same direction would remain parallel to each other and only one layer of the satin weave would be considered for the analyses.

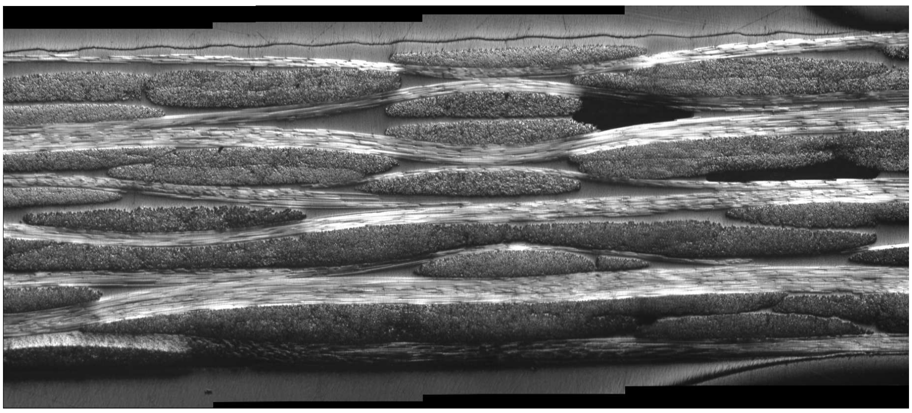

Figure 7.8: Micrograph of 5-harness satin.

Figure 7.9 provides a schematic representation of the simplified geometry used to build the three-dimensional model of the 5-harness satin. Table 7.1 provides the values used for the different dimensions represented in figure 7.9.

Regarding the crimp region, the yarn was modelled using a spline curve defined by nine points and imposing an horizontal tangent constraint on the first, middle and last points. Figure 7.10 shows a schematic with the location of the nine points which define the spline curve. Table 7.2 provides the coordinates of those nine points.

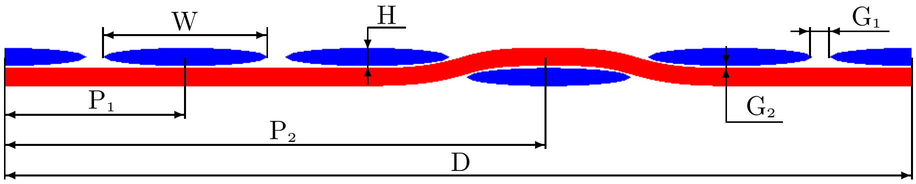

Figure 7.9: General dimensions of 5-harness satin weave.

Table 7.1: 5-harness satin dimensions.

Dimensions	[mm]
W	1.58
H	0.17
G_1	0.16
G_2	0.02
P_1	1.74
P_2	5.22
D	8.7

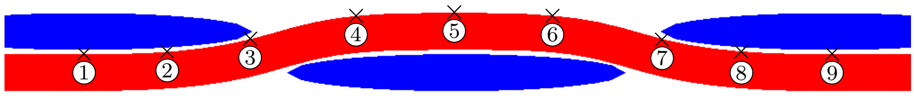

Figure 7.10: Crimp points of 5-harness satin weave.

Table 7.2: Geometry of the crimp region (in relative coordinates).

Point	x-coord.	y-coord
1	0.000	0.000
2	0.280	0.005
3	0.790	0.070
4	1.070	0.145
5	1.740	0.190
6	2.410	0.145
7	2.690	0.070
8	3.200	0.005
9	3.480	0.000

With the geometry of the satin completely defined, a three-dimensional model of the yarns was generated in SolidWorks® [143]. The final result can be seen in figure 7.11. It is considered that the yarns are embedded in epoxy matrix with a total layer thickness of 0.40 mm. Using a sequence of boolean operations, it is possible to obtain the three dimensional solid of the matrix surrounding the yarns. This solid is represented in figure 7.12 with the top surface transparent for better understanding of its interior geometry.

Figure 7.11: Three-dimensional model for the yarns.

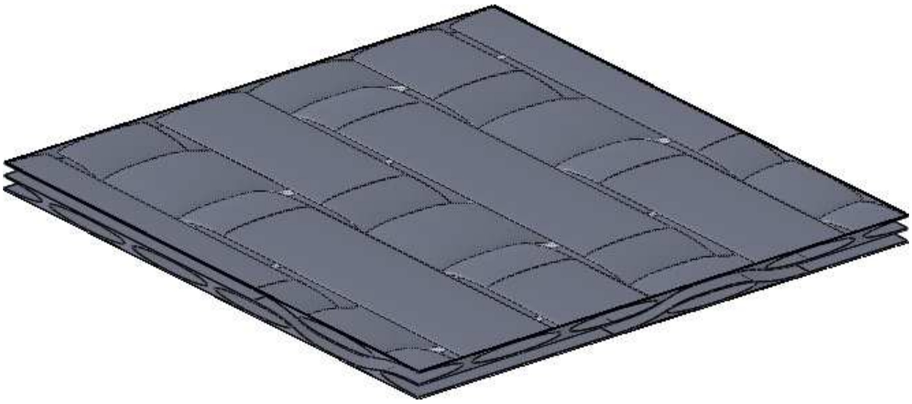

Figure 7.12: Three-dimensional model for the matrix.

The three-dimensional model was then exported to commercial pre-processing software FEMAP® [144] for mesh generation, always in accordance with the concept of periodic boundary conditions. Given the difficulty in generating a mesh using hexahedra elements due to the very complex geometry of the matrix solid, it was ultimately chosen to use tetrahedra elements. Figure 7.13 depicts the assembled solids – matrix and both warp and weft yarns – before being meshed. Figure 7.14 shows the model completely meshed and in figure 7.15 a detail of the mesh is presented for better understanding of the mesh geometry.

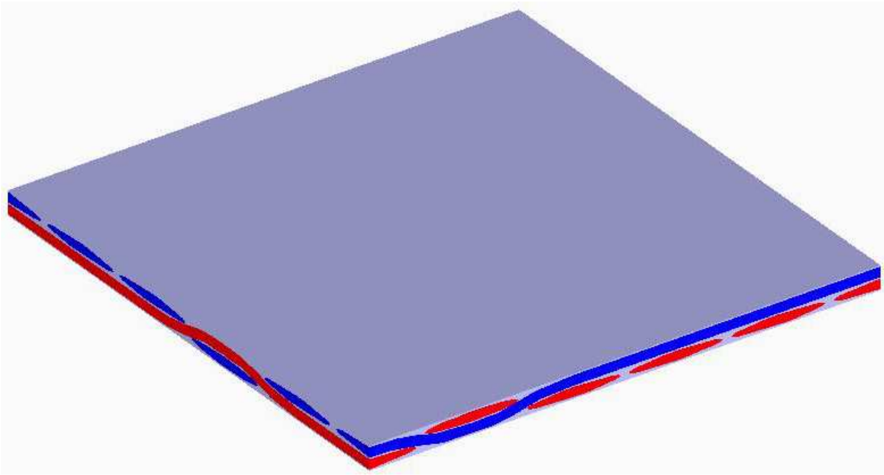

Figure 7.13: Assembled model prepared for meshing.

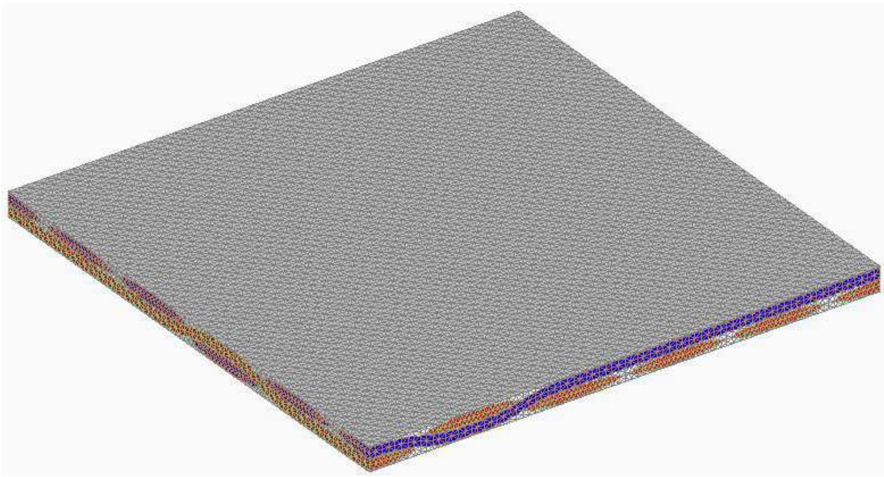

Figure 7.14: Meshed RVE with tetrahedra elements.

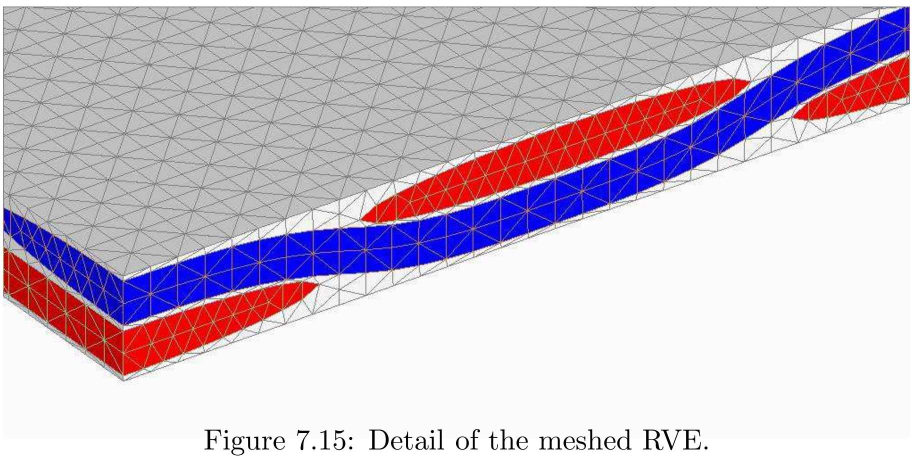

Figure 7.15: Detail of the meshed RVE.

7.4 Periodic boundary conditions

The concept of periodic boundary conditions has been introduced in chapter 3. The method was presented for a full three-dimensional case where the degrees of freedom of all nodes laying on faces, edges and vertices of a representative volume element had to be connected using kinematic equations. For the present case, since it is being considered only one layer of satin weave, there is no need to apply periodic boundary conditions along the off-plane axis. The set of kinematic equations thus becomes reduced to a simpler two-dimensional case. There is no longer a need to establish kinematic relations between the degrees of freedom of the nodes on the vertices of the representative volume element. Only the nodes along the four edges that define the lateral faces and those on the lateral faces themselves will be connected using kinematic equations.

Figure 7.16 represents the face numbering as defined for the application of two-dimensional periodic boundary conditions.

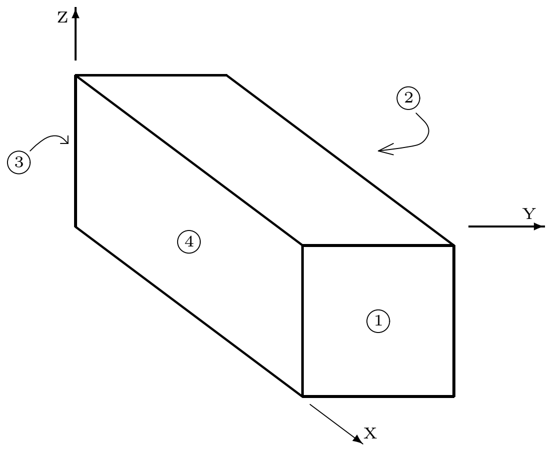

Figure 7.16: Face numbering of RVE for application of 2D PBC.

Each node positioned on one face will have its degrees of freedom combined with a node placed in the opposite face, abiding by the following sets of equations:

$$
\begin{aligned}
u_i^1 - u_i^3 - c\varepsilon_{i1}^o &= 0 \\
u_i^2 - u_i^4 - a\varepsilon_{i2}^o &= 0
\end{aligned}
\tag{7.1}
$$

where a and c are the dimensions of the representative volume element in the y and x directions, respectively. The number in superscript represents the face to which the node belongs to and ε^o_{ij} represents the ij-component of the far-field strain tensor.

Figure 7.17 shows the location and numbering used for the edges of the representative volume element to apply two-dimensional periodic boundary conditions.

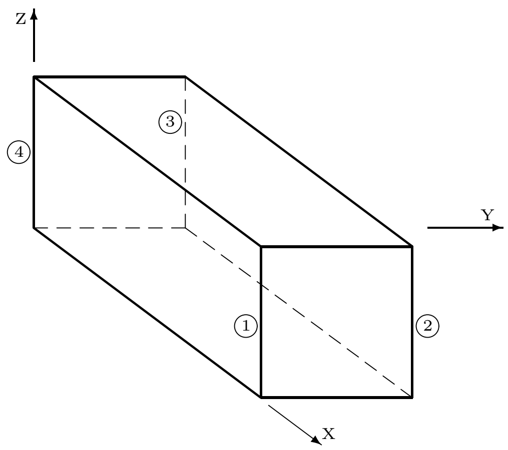

Figure 7.17: Edge numbering of RVE for application of 2D PBC.

Each node along one edge of the RVE combines with the node on the parallel but opposite edge, making a total of six possible edge combinations. Since only the vertical edges need to be considered for this particular case as there is no periodicity in the z direction, only two pairings are established. Although two faces converge on an edge, it is impossible to apply more than one kinematic constraint in the same degree of freedom. This justifies the need to develop different sets of equations for faces and edges. The numbering in superscript used in the following equations identifies the edge according with figure 7.17:

$$\begin{aligned} u_i^2 - u_i^4 - c\varepsilon^o_{i1} - a\varepsilon^o_{i2} &= 0 \\ u_i^1 - u_i^3 - c\varepsilon^o_{i1} + a\varepsilon^o_{i2} &= 0 \end{aligned} \tag{7.2}$$

The pre-processing MATLAB® [29] scripts required to implement two-dimensional periodic boundary conditions on the 5-harness satin weave here presented can be found in appendix E.

7.5 Constitutive models

The three dimensional model being considered contains two different materials, the yarns and the embedding matrix. The elasto-plastic with damage constitutive model presented in this thesis is used to model the mechanical behaviour of the epoxy matrix. Yarns will be regarded in this chapter as homogenised material. A thermodynamically consistent damage model recently proposed by Maimí et al. [123] will be used to model the mechanical behaviour of the yarns. The following is a short summary of Maimí's et al. damage model. Further details can be found in [123].

Both weft and warp yarns are considered as a transversely isotropic homogeneous material, similar to a uniaxial lamina of composite material. The model takes into consideration the transverse isotropy typical of composite materials and is capable of predicting both interlaminar and intralaminar failure mechanisms.

The ability to predict different failure mechanisms derives from its three different damage activation functions, defined as:

$$\begin{aligned} F_{L+} &= \phi_{L+} - r_{L+} \leqslant 0 \\ F_{L-} &= \phi_{L-} - r_{L-} \leqslant 0 \\ F_T &= \phi_T - r_T \leqslant 0 \end{aligned} \tag{7.3}$$

where F_{L+} defines the elastic domain for longitudinal tensile failure, F_{L-} defines the elastic domain for longitudinal compressive failure, and F_T defines the elastic domain for transverse failure. The loading functions ϕ_N are a function of the strain tensor, elastic and strength properties of the homogenised composite material. The internal variables r_N of the constitutive model are related to the damage variables by damage evolution laws and have an initial value of 1. Non-linear behaviour, such as plasticity, is not included in the present version of the transversely isotropic damage model.

The loading functions are defined by:

$$\begin{aligned} \phi_{L+} &= \frac{E_1}{X_T} \langle \varepsilon_{11} \rangle \\ \phi_{L-} &= \frac{E_1}{X_C} \langle -\varepsilon_{11} \rangle \\ \phi_T &= \sqrt{\left\langle \frac{Y_C - Y_T}{Y_C Y_T} \left(\tilde{\sigma}_{22} + \tilde{\sigma}_{33}\right) + \frac{1}{Y_C Y_T} \left(\tilde{\sigma}_{22} - \tilde{\sigma}_{33}\right)^2 + \frac{\tilde{\sigma}_{12}^2 + \tilde{\sigma}_{13}^2}{S_L^2} \right\rangle} \end{aligned} \tag{7.4}$$

where $\tilde{\sigma}$ represents the effective stresses, calculated using the undamaged stiffness tensor, Y_C and Y_T are the ultimate transverse strengths of the unidirectional lamina in compression and tension, respectively, X_C and X_T are the ultimate longitudinal strengths of the unidirectional lamina in compression and tension, respectively, S_L is the ultimate longitudinal shear strength, E_1 is the longitudinal Young's modulus and the operator $\langle\cdot\rangle$ is the McCauley operator defined as $\langle x\rangle := (x + |x|)/2$.

The equations for the damage evolution functions can be found in [123]. These equations have been deduced taking into account Bažant's crack band model [115] which allows for a proper definition of the energy dissipated during damage propagation. The energy release rate and the characteristic element length are used to compute parameters specific of each element which will control the pace at which damage evolves, thus guaranteeing mesh size independency.

The internal variables r_N are defined in such a way as to respect the Kuhn-Tucker loading/unloading conditions, $\dot{r}_N \geqslant 0$; $F_N \leqslant 0$; $\dot{r}_N F_N = 0$.

In order to improve convergence rate, and as it was done in chapters 4 and 5 for the matrix material surrounding the yarns, the tangent consistent matrix was analytically defined.

Both material constitutive models – yarns and epoxy matrix – were implemented in a user-defined material subroutine `UMAT` of the commercial finite element analysis software ABAQUS® [30]. The `UMAT` subroutine for the matrix presented in this thesis can be found in appendix D.

A second subroutine – `ORIENT` – needed to be implemented in order to define the different orientation for both weft and warp yarns as well as for those regions where a crimp occurs, i.e. where the two perpendicular yarns interlace each other and the principal direction of the yarn is slightly tilted relatively to the plane of the satin weave. This subroutine was created for the specific case of the geometry presented in section 7.3. Since care was taken during mesh generation in order to have sets of nodes and sets of elements for each material type, the definition of the correct material orientation becomes a straightforward task. The subroutine `ORIENT` can be found in appendix E. Both `ORIENT` and `UMAT` subroutines are coded in FORTRAN® programming language.

Post-processing of results is performed by a MATLAB® [29] script which takes into account the correct orientation of the material axes for each element as it was defined by the `ORIENT` subroutine. This script can also be found in appendix E.

7.6 Elastic and strength properties of yarns

Yarns are considered a transversely isotropic material and in this chapter will be modelled using Maimí's et al. [123] three dimensional damage model. As in any other situation, this damage model requires input variables such as the elastic properties of the homogenised material as well as the strength parameters which will be used in the definition of the damage activation functions.

The elastic properties of the homogenised material can be determined following the procedure outlined in chapter 3 using the concepts of representative volume elements along with periodic boundary conditions. Three different random fibre distributions were generated using the algorithm presented in chapter 2. The fibre volume fraction considered inside the yarns is of 65%. It is considered that the constituents of the yarns are a Carbon fibre, AS4, and an epoxy matrix, the same which was characterised by Fiedler et al. [70]. The material properties of these two constituents are summarised in table 7.3.

Table 7.3: Material properties of yarn constituents.

Elastic Properties	AS4 fibres	Epoxy
E_1 [MPa]	225000	3760
E_2 [MPa]	15000	-
G_{12} [MPa]	15000	-
G_{23} [MPa]	7000	-
v_{12}	0.2	0.39
Strength Properties		
X_T [MPa]	3350	93
X_C [MPa]	2500	124

Running similar analyses as in chapter 3, and after volumetric homogenisation of results, it is possible to obtain the elastic properties of the yarn material (table 7.4). Performing similar analyses to the ones in chapter 6, it was possible to determine the strength parameters for the yarn material. The values presented in table 7.4 are the average of the results obtained from the three different fibre distributions. These properties will be used as input parameters for Maimí's et al. transversely isotropic damage model [123].

The damage model proposed by Maimí et al. [123] requires an array of material properties which are not available for the composite system being simulated in this chapter for the yarns. Instead, approximate values taken from the literature and experience were used. Table 7.5 presents the values

Table 7.4: Material properties of yarns after homogenisation.

Elastic Properties	
E_1 [MPa]	138910
E_2 [MPa]	9380
G_{12} [MPa]	5080
v_{32}	0.350
v_{12}	0.245
Strength Properties	
X_T [MPa]	2056.5
Y_T [MPa]	67.7
Y_C [MPa]	122.5
S_L [MPa]	39.1
S_T [MPa]	47.9

used for the remaining necessary properties.

Table 7.5: Remaining material properties of yarns.

Property	
α_{11} [°C^{-1}]	-8.4×10^{-7}
α_{22} [°C^{-1}]	2.91×10^{-5}
X_{PO} [MPa]	400
X_C [MPa]	610
G_{IC}^{FL} [N/m]	40
G_{IC}^{FE} [N/m]	41
G_{IC}^{M} [N/m]	0.09
G_{IIC}^{M} [N/m]	1.55
G_{IC}^{FC} [N/m]	100

7.7 Numerical study of 5-harness satin

Having characterised both the matrix and the yarns, it is now possible to perform three dimensional numerical analyses on the representative volume element developed in section 7.3 using the constitutive damage models presented before.

A set of elastic runs was performed first in order to determine the elastic constants of the 5-harness satin weave under study. Although the model has been prepared in three dimensions, given the planar geometry of a satin, only the properties in the weave plane are important for its mechanical characterisation. Table 7.6 presents the two dimensional elastic properties of the 5-harness satin weave under consideration.

Table 7.6: Elastic properties of 5-harness satin.

Property	
E_1° [MPa]	37.58
E_2° [MPa]	37.58
G_{12}° [MPa]	3.31
v_{12}°	0.129

Using the concept of periodic boundary conditions as defined in section 7.4 for three dimensional models but where the periodicity does not apply along one of the directions, it is possible to perform several finite element analyses on the micromechanical unit cell developed for the 5-harness satin weave. Four different loading conditions will be considered here: uniaxial tension, in-plane shear, biaxial tension and a combination of uniaxial tension with in-plane shear. The next subsections will detail the results obtained for each of these loading scenarios.

Unfortunately, due to the fact that both constitutive models follow an implicit numerical implementation and the excessive time required for convergence that it leads to, it was not possible to run the analyses to final failure of the satin weave in a timely manner. Convergence was slightly improved with the use of implicit dynamic analyses instead of static implicit. However, the presence of inertia effects becomes visible in the plots to follow by the waviness of the stress-strain curves. This waviness is however within acceptable limits and does not jeopardise the quality and trustworthiness of the obtained results. Albeit incomplete, the achieved results from the micromechanical analyses performed allow for a qualitative analyses of the damage evolution on the satin weave and for a partial comparison with the scarce experimental data available.

7.7.1 Uniaxial tension

The far-field strain tensor applied in order to obtain an uniaxial tension load is generically defined by (in Voigt notation):

$$\boldsymbol{\varepsilon^{o}} = \begin{bmatrix} a & - & - \\ - & - & - \\ - & - & - \end{bmatrix} \tag{7.5}$$

Figure 7.18 shows the results for the uniaxial tensile load case. The load is applied along the warp (horizontal) yarns. Figure 7.18a shows the evolution of the normal stress in the direction of the applied load and figure 7.18b details the evolution of the Young's modulus in the loading direction. It is visible that as damage accumulates there is a strong decrease in the material stiffness. Figure 7.18c provides a field plot of the transverse damage variable showing where in the satin weave damage accumulates. It is clearly visible that damage first tends to accumulate in the crimp region where the yarns cross each other.

As loading progresses, damage begins to appear in the weft yarns along a direction almost perpendicular to the yarns (i.e. almost aligned with the loading direction) in the nested sections of the weft yarns. This damage evolution is in close agreement with the experimental results obtained by Daggumati et al. [140]. Damage in the matrix had not been activated yet. It is also visible in figure 7.18b that damage evolves in independent peaks, since the stiffness of the material tends to stabilise after an initial drop. Experimentally this is observed by Daggumati et al. [140] in uniaxial tension tests.

7.7.2 In-plane shear

The far-field strain tensor applied in order to obtain an in-plane shear load is generically defined by (in Voigt notation):

$$\boldsymbol{\varepsilon^{o}} = \begin{bmatrix} - & a & - \\ a & - & - \\ - & - & - \end{bmatrix} \tag{7.6}$$

Figure 7.19 shows the results for the in-plane shear load case. Figure 7.19a shows the evolution of the in-plane shear stress and figure 7.19b details the evolution of the in-plane shear modulus. It is visible that as damage accumulates there is a strong decrease in the material stiffness. Figure 7.19c

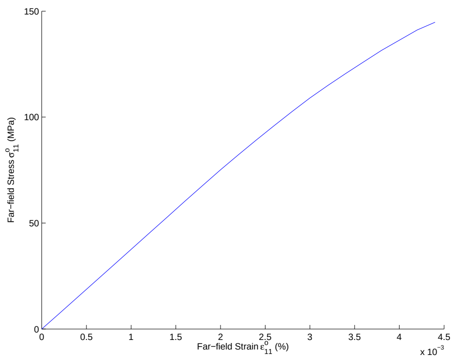

(a) Stress-strain curve

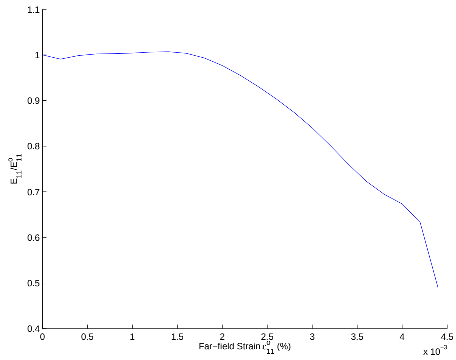

(b) Variation of Young's modulus

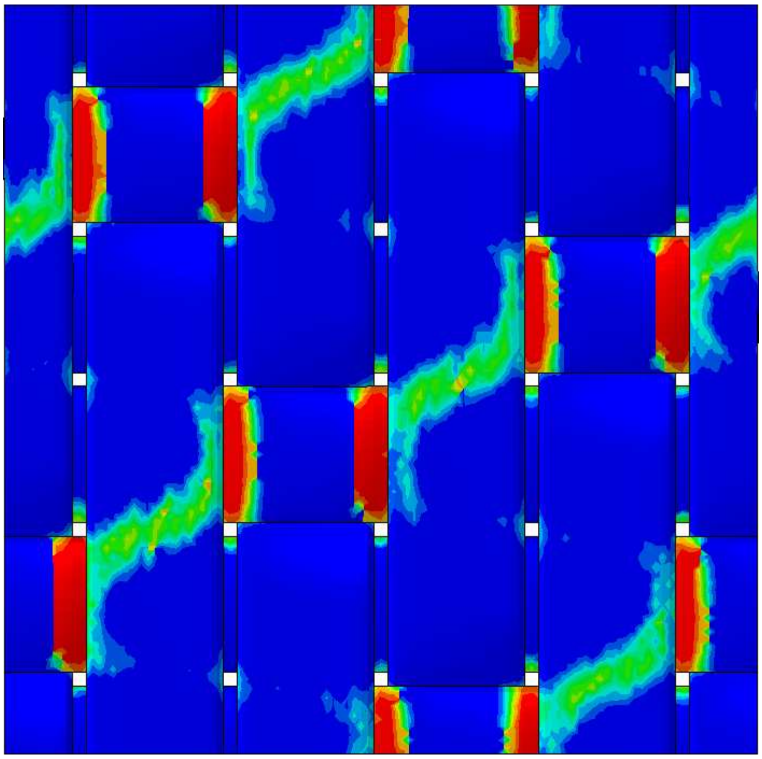

(c) Transverse damage variable in yarns

Figure 7.18: Results for uniaxial tensile load.

provides a field plot of the shear damage variable showing where in the satin weave damage accumulates.

Damage caused by shear tends to concentrate in the unloaded weft yarns. The transverse damage variable (not represented in figure 7.19) is active around the crimp regions where the yarns cross each other and from there propagate along the edges of both yarns. Damage in the matrix had not been activated yet. It can be concluded that under a pure in-plane shear load to the satin weave, it is close to the interface between the individual yarns and the matrix that surrounds them that the different shear moduli will create greater stress concentration. This makes this region the weakest of the material, particularly on the yarn side due to the presence of the fibrous reinforcements, hence the region where damage will tend to be first activated and propagate easily.

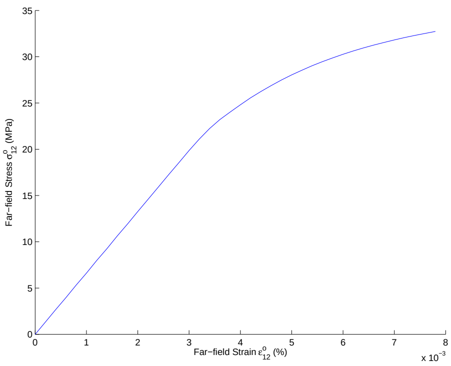

(a) Stress-strain curve

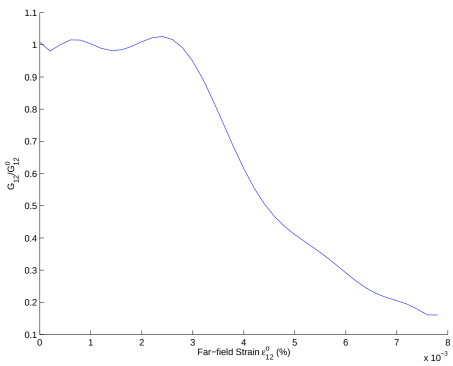

(b) Variation of shear modulus

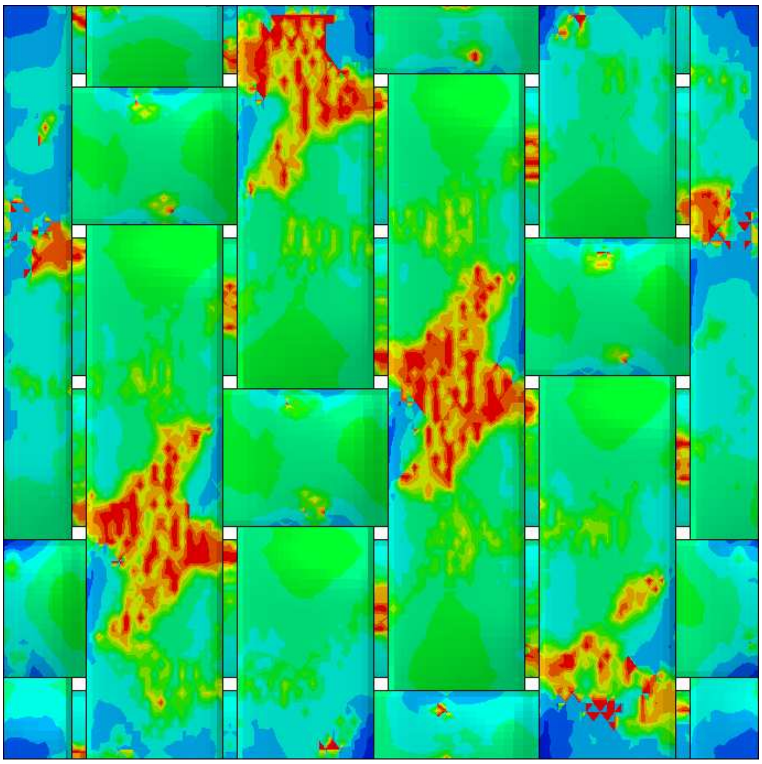

(c) Shear damage variable in yarns

Figure 7.19: Results for in-plane shear load.

7.7.3 Biaxial tension

The far-field strain tensor applied in order to obtain a biaxial tension load is generically defined by (in Voigt notation):

$$\boldsymbol{\varepsilon^o} = \begin{bmatrix} a & - & - \\ - & a & - \\ - & - & - \end{bmatrix} \tag{7.7}$$

Figure 7.20 shows the results for the biaxial tensile load case. Figure 7.20a shows the evolution of the normal stress in the direction of the warp yarns and figure 7.20b details the evolution of the Young's modulus in that same direction. It is visible that as damage accumulates there is a strong decrease in the material stiffness. Figure 7.20c provides a field plot of the transverse damage variable showing where in the satin weave damage accumulates. It is clearly visible that damage first tends to accumulate in the crimp region where the yarns cross each other. The difference to the uniaxial case is that damage accumulates on all four edges around the crimp regions.

As in the uniaxial case, damage will extend towards the weft yarns. By the time these plots were generated, damage was beginning to localise in the weft yarns and propagate to the matrix material. Also visible is the tendency for damage propagation to stabilise after an initial phase of propagation. Experimentally this is observed by Daggumati et al. [140] in uniaxial tension tests.

7.7.4 Uniaxial tension and in-plane shear

The far-field strain tensor applied in order to obtain a combination of uniaxial tension and in-plane shear load is generically defined by (in Voigt notation):

$$\boldsymbol{\varepsilon^o} = \begin{bmatrix} a & a & - \\ a & - & - \\ - & - & - \end{bmatrix} \tag{7.8}$$

Figure 7.21 shows the results for the combined uniaxial tensile and in-plane shear load case. The uniaxial tensile load is applied along the warp (horizontal) yarns. Figure 7.21a shows the evolution of the normal stress in the direction of the applied uniaxial tensile load and figure 7.21b details the evolution of the Young's modulus in that direction. It is visible that as damage accumulates there is a strong decrease in the material stiffness.

Figure 7.21c provides a field plot of the transverse damage variable showing where in the satin weave damage accumulates.

Damage first tends to accumulate in the crimp region where the yarns cross each other. Unlike the pure uniaxial tension case or pure in-plane shear case, damage evolves in a different pattern (compare figures 7.18c and 7.19c with figure 7.21c). After localising around the crimp regions, damage

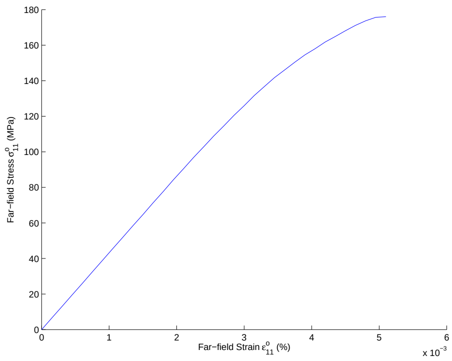

(a) Stress-strain curve

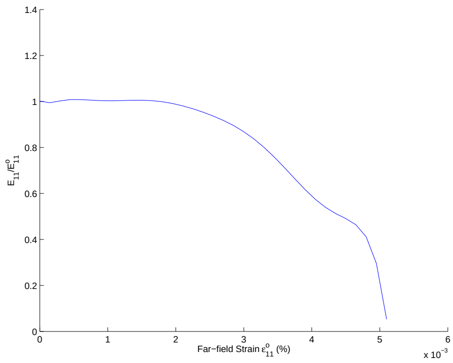

(b) Variation of Young's modulus

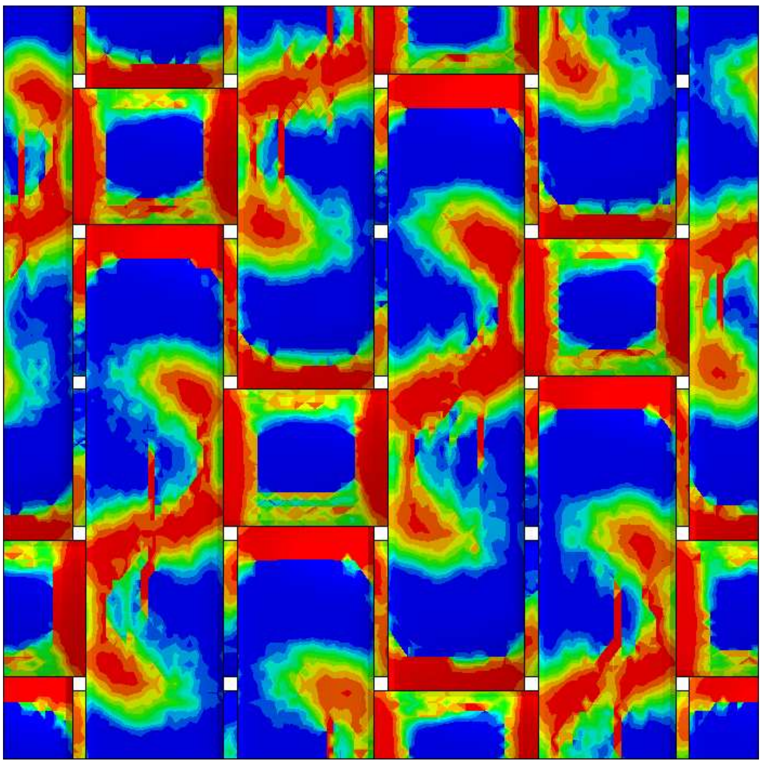

(c) Transverse damage variable in yarns

Figure 7.20: Results for biaxial tensile load.

will be activated along the weft yarns mainly due to the presence of shear stresses.

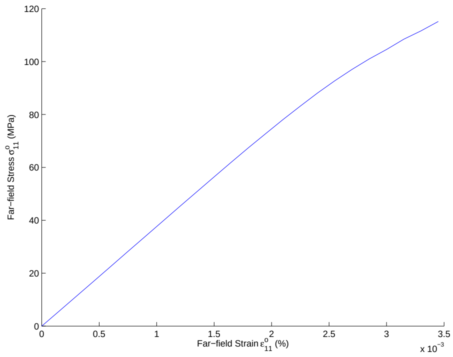

(a) Stress-strain curve

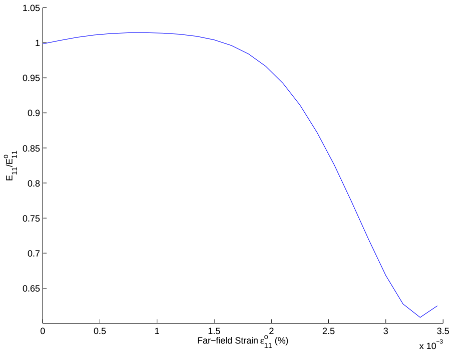

(b) Variation of Young's modulus

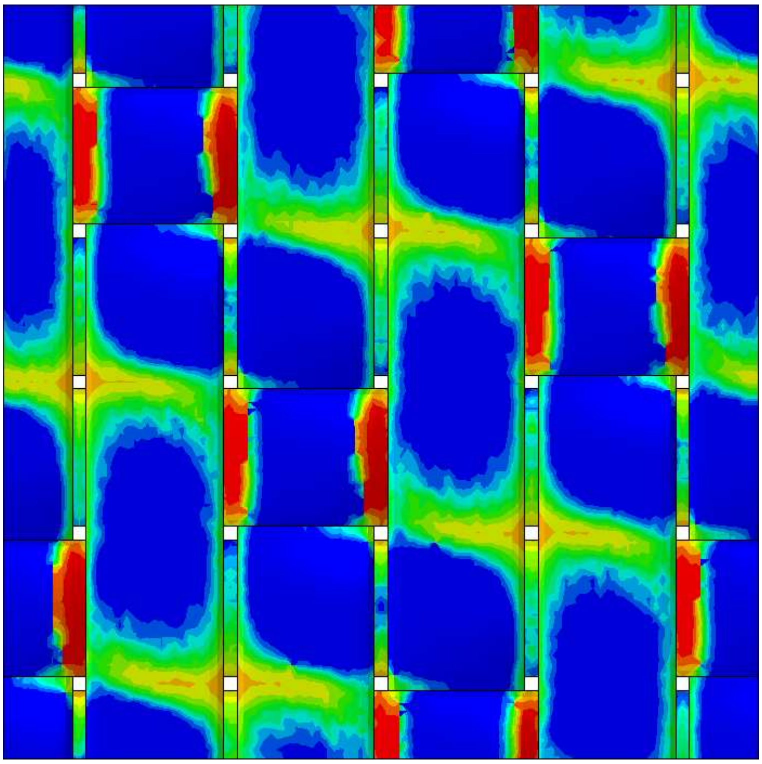

(c) Transverse damage variable in yarns

Figure 7.21: Results for combination of uniaxial tensile load with in-plane shear.

7.8 Conclusions

A representative volume element of a 5-harness satin weave was generated using as reference a series of micrographs taken of the real material. In the process, a batch of computer-aided design and finite element pre-processing software were used. The generated mesh was built making use of tetrahedra elements due to its extremely complex geometry. Periodic boundary conditions were applied to the representative volume element generated; however, due to the rather planar geometry of the satin weave, periodicity was considered only in two dimensions instead of the most general three-dimensional case.

The satin weave is modelled in its *wet* state, i.e. the yarns are immersed in an epoxy matrix material. For finite element analyses, the yarns are considered as a transversely isotropic homogenised material modelled by a recently proposed damage model while the epoxy matrix was modelled using the elasto-plastic with damage constitutive model developed in this thesis. Care was taken with regards to the material orientation of the elements in the volume element, especially in the crimp regions.

The required elastic and strength properties for the transversely isotropic damage model were determined using the procedures already described in chapters 3 to 5.

Four different loading conditions were applied to the representative volume element and results were compared with the scarcely available experimental data. For the uniaxial tensile case, a good qualitative agreement is obtained with experimental data regarding damage activation regions of the material as well as damage progression. In-plane shear, biaxial tension and a combination of uniaxial tension with in-plane shear analyses were also run and results provide an interesting insight on the triggering sequence of different damage mechanisms for this type of textile composite.

The analyses presented in this chapter demonstrate the usefulness of the damage models developed throughout this thesis. It also provides insight on the multiplicity of studies that can be performed thanks to micromechanics, providing answers which often not even experimental work is capable of.

Chapter 8

Conclusions and future work

> Not every rainbow has a pot of gold at the end; some just have a cloud!
>
> Unknown

The following chapter will provide a summary of the achievements of the present thesis. All the results and breakthroughs were achieved with little accumulated knowledge from the past at Faculdade de Engenharia da Universidade do Porto. The grounds for future work in the field of micromechanics are now laid down and now exists the possibility to not only perform such kind of numerical analyses, but also to evolve, mature, improve what has been presented in this thesis.
The doors are now wide open to a considerable number of possibilities. A list of future activities that can be performed, some easily achievable while others tantalising for the mind, will be presented. Possible solutions for the problems encountered throughout this endeavour will also be discussed.

8.1 Achievements

In chapter 2 a new algorithm capable of generating random spatial distributions of fibres with high fibre volume fractions is presented. The algorithm is capable of providing results much more quickly and efficiently than any of the algorithms proposed thus far. Geometrical periodicity is imposed so that periodic boundary conditions can be applied on the representative volume elements generated. The distributions generated by this algorithm were tested for real randomness of results using an array of statistical tools which proved the existence of real randomness and thus good agreement with a real distribution of fibres as seen in a composite material. Numerical analyses were performed in order to demonstrate the capacity of the algorithm to generate distributions capable of modelling the transverse isotropic behaviour of real composite materials.

Using this algorithm, it became possible to develop a sequential and automatic procedure to generate not only the random fibre distributions, but also a complete three-dimensional representative volume element of a long fibre advanced composite material. Chapter 3 describes this procedure, starting from the generated random distributions of reinforcements, application of three-dimensional periodic boundary conditions, and determination of the elastic mechanical parameters of a composite. The elastic parameters are determined after performing volumetric homogenisation on the results from finite element micromechanical analyses of the generated representative volume elements. A series of parametric studies was conducted in order to infer about the influence of the fibre radius, the volume element dimensions, and the minimum distance between any two fibres in the generated fibre spatial distribution. It was found that the thickness (dimension in the fibre direction) and the minimum distance between fibres can have a small influence in the elastic properties calculated.

Chapter 4 gave start to the numerical implementation of the constitutive material laws which will model the mechanical behaviour of each constituent. First, focus was placed on the plastic behaviour of the matrix. Based on the limited experimental data available for the matrix, the paraboloidal yield criterion was chosen as the one which can best describe the hardening process of the matrix. The criterion is capable of accounting for different yield stresses in tension and compression and exhibits pressure dependency. The criterion was deduced and implemented in a user subroutine of commercial finite element software ABAQUS® [30] following an implicit return mapping algorithm scheme.

The elasto-plastic model for the matrix was tested in a number of different loading situations using generated representative volume elements. A better insight is now possible on the most sensitive regions of the matrix constituent in a composite material. Since there is no access to a complete material characterisation of matrix, fibre, and the composite formed by them, only a qualitative analyses of the results can be made. After volumetric homogenisation of the micro-mechanical stress and strain fields obtained from finite element analyses on the representative volume elements generated it can be concluded that there is a good qualitative agreement of the numerical results with the experimental knowledge of composite materials.

The constitutive model of the matrix becomes complete after development and implementation of an isotropic damage law in chapter 5. The damage evolution laws were developed in the framework of the thermodynamics of admissible processes. A crack band model was also used in order to avoid mesh dependency of the results obtained and to properly account for the energy released upon fracture of the material. Also for the fibrous reinforcement a damage law was implemented, but considering only longitudinal failure of the fibres. The crack band model was also implemented for the fibres. In both materials, and since an implicit formulation is being used, the consistent tangent operator was deduced in order to improve convergence of results. Both damage models had their implementation validated using a series of one-element and open-hole tension tests.

The batch of analyses which had been applied in chapter 4, is now repeated using the full elasto-plastic with isotropic damage constitutive law for the matrix and the elastic with damage constitutive law for the fibre. Depending on the loading applied to the representative volume element, different crack patterns are visible at the micro-scale level. An important result achieved by these constitutive laws which provides good indications on their prediction capabilities is the crack orientation under a transverse compressive load. A very approximate result to the 53° measured in experimental procedures is achieved. This also provides an indication that fracture under a transverse compressive load in a composite occurs due to high shear stresses and not due to compressive normal stresses. Also worthy of reference is the possibility to capture the fibre-pull out damage mechanism visible in longitudinal tensile tests.

With the two constituents having their mechanical behaviour completely modelled by the constitutive laws developed in chapters 4 and 5, it is now possible to perform more complex micromechanical stress analyses. The first application is performed in chapter 6 for the definition of failure envelopes of a uniaxial lamina. Failure envelopes for four different loading schemes are generated: biaxial normal loading, transverse normal stress with each of the longitudinal shear stresses and transverse normal stress with transverse shear stress. The results were compared with a recently proposed analytical model for prediction of failure in composite materials and results are encouraging. However, it is necessary to perform more experimental work in order to better characterise the matrix behaviour under biaxial tension and biaxial compression.

An important detail should be mentioned: if given the proper input parameters, the plasticity and damage laws implemented for the matrix degenerate in the more simple Von Mises yield criterion with associative flow rule and Von Mises failure criterion. Given this, and although not an initial objective of this thesis, the constitutive model developed for the matrix can also be used in the study of metal matrix composites and not only polymer matrix composites.

The application of the constitutive damage models to the generation of any kind of failure envelopes shows not only the flexibility of the methodology presented in this thesis, but also the potential to provide information on the micro-mechanical behaviour of composite materials under any type of loading, even for loading conditions which are very difficult or even impossible to obtain experimentally.

In chapter 7 the developed models were applied to a different type of composite materials – textile composites. After development of a representative unit-cell of the weaving pattern using CAD software, the constitutive models can be applied to both yarns and matrix surrounding them. Again, thanks to the concept of periodic boundary conditions, any kind of loading can be applied to the representative volume element and the activation and propagation of damage can be studied. A study on the triggering sequence of damage mechanisms for different loading conditions was performed and good qualitative results were obtained with the scarcely available experimental data.

These two applications demonstrate the potential behind micromechanical analyses and the immense flexibility they provide along with the aid of periodic boundary conditions for the study of composite materials, their mechanical behaviour and damage activation and propagation.

8.2 Improvements

No technique is ever finished, and no model is ever perfect. A number of improvements and modifications can be made to the constitutive models developed in this thesis and to the modelling techniques used.

The constitutive damage model for the fibrous reinforcements implemented in this thesis considers only damage activation when the composite is under a longitudinal tensile load. More experimental data is required in order to properly characterise the transverse and shear mechanical properties and constitutive behaviour of a reinforcing fibre. Also for compressive longitudinal loading the model should be updated.

The matrix was modelled considering a yield criterion dependent only on the first invariant of the stress tensor, I_1, and on the second invariant of the deviatoric stress tensor, J_2. I_1 is responsible for dilation of the polymer while J_2 controls pure shear deformation mechanisms. However, some authors [73] consider that the third invariant of the deviatoric stress tensor, J_3, is responsible for a third deformation mechanism, rotation of the molecules relatively to each other. This effect is most visible under torsion. Again, more reliable and complete experimental data regarding the matrix hardening behaviour is required to determine its dependency on J_3.

The matrix mechanical behaviour under biaxial loading, both tension and compression, also needs to be experimentally characterised to more extent. The failure envelopes generated in chapter 6 for a biaxial loading denounce that there is still the need to investigate further the matrix yield and failure behaviour for such loading conditions.

Typical polymers used as matrix in advanced composite materials are known to exhibit strain rate effects [66]. A full experimental set-up for characterisation of the matrix polymer should also account for a definition of strain rate dependency. This dependency should be accounted for in future versions of the non-linear constitutive model of the matrix material.

One other important feature of composite materials is that during manufacture they are subjected to thermal variations which lead to the existence of residual stresses in the constituents given the different coefficients of thermal expansion each material has. Although programmed in the code available in the appendices of this thesis, there was no opportunity to study the influence of these residual thermal stresses on the mechanical constitutive behaviour of the composite from a micromechanical point of view. It is envisaged in the near future to study the influence of residual thermal stresses on the failure envelopes presented in chapter 6 as well as the influence in more complex geometries such as textile composites.

Up to this moment, it has been considered that there exists only two constituents in the composite – fibre and matrix. A third constituent can be considered in the micromechanical study of advanced composites. The interface between fibre and matrix can be regarded as a different material with different mechanical properties. Due to the difficulty in obtaining proper experimental data for this third phase, a possible simplification that can be considered is the use of the same material model as for the matrix, but with reduced strength and elastic properties. In other words, the interface would be regarded as a weaker part of the matrix material. Quantifying how week the interface should be compared with the matrix is the only difficulty in this simplification. One other alternative is the use of cohesive elements in the geometrical boundary between the fibre and the matrix. It is possible to include in the pre-processing scripts used in this thesis the possibility to add this type of elements to the model.

One other major difficulty throughout this thesis was the fact that an implicit formulation has been chosen to implement the developed constitutive damage models. Even though the consistent tangent operators were deduced and implemented, thus increasing the convergence speed of the numerical process, the random distribution of fibres and high number of degrees of freedom required by the three dimensional models make the entire process painfully slow. Just for reference, the models for the 5-harness satin weave in chapter 7 can take up to 2-3 months of computation time. It is envisaged to transpose the constitutive models developed from an implicit to an explicit formulation. This update will lower computational times and allow for the study of even more complex geometries and material laws that can be implemented and already discussed above. However, care must be taken in order not to compromise convergence to physically reasonable results.

8.3 Future Work

8.3.1 Multiscale analyses

Independently of any modifications that can be applied to the constitutive damage models presented in this thesis, the groundwork for full multiscale analyses has been setup. A real structure can be discretised using finite elements at the macroscale and the strain tensor, $\boldsymbol{\varepsilon}^{\circ}_{\boldsymbol{P}}$, in each integration point easily acquired. There is no need for a very refined mesh at this length scale.

Using the scripts developed in chapters 2 and 3 for the generation of representative volume elements of advanced composite materials and for the application of three-dimensional periodic boundary conditions, different volume elements can be generated for each integration point of the macroscale mesh. The global strain tensor, $\boldsymbol{\varepsilon}^{\circ}_{\boldsymbol{P}}$, for each integration point at the macroscale can be applied to the generated volume elements using the kinematic relations defining the periodic boundary conditions. The micromechanical analyses can then be run and its results go through the volumetric homogenisation script from which the global stress tensor, $\boldsymbol{\sigma}^{\circ}_{\boldsymbol{P}}$, in the integration point of the macroscale model can be obtained. One micromechanical analysis must be run for each integration point of the macroscale mesh. The obtained global stress field is a function of the damage variables defined in the micromechanical constitutive models. Hence, the results after homogenisation will be affected by the activation of damage or not at the microscale.

Two main difficulties arise from the application of this procedure. The first one is concerning the dependency of the homogenised stress tensor to the size of the representative volume element after damage localisation at the microscale. This could lead to erroneous results at the macroscale level if care is not taken to avoid this. Consideration of the fracture toughness of the composite in the homogenisation script might be required in order to eliminate this dependency.

The second difficulty is with the outstanding number of calculations required for this methodology. Even worse if a real component or complete structural item with complex geometry is under analyses. However, the power of distributed computing along with the good will of volunteers can help tackle this problem.

8.3.2 Distributed computing

Distributed computing is a form of network computing in which individual computers connected with each other share information but not system resources like CPU or physical memory. One particular type of distributed computing is volunteer computing in which individual computer owners donate their idle CPU time and system resources to one or more research projects.

The concept became world-wide spread when University of California, Berkeley released its first application in 1999 to analyse the data collected from radiotelescopes and scan it using Fourier techniques in hope to find evidence of extraterrestrial life. This application was named SETI@Home (Search for Extraterrestrial Intelligence) and was made available on the internet for volunteers to download and use freely. The application would connect with a dedicated server at Berkeley which would provide the volunteer computer with workunits (WUs), individual pieces of raw data, in which the volunteer computer would apply the search algorithm. The results of the scan would then be reported back to Berkeley and a new WU would be sent. This process repeated itself for as long as the owner of the computer would wish, as there was no legal or whatsoever binding between the volunteer and Berkeley. Nevertheless, the goal of the project revealed to be so attractive that caught media attention and seduced several hundred thousand volunteers.

For obvious reasons, some of the volunteers tried to hack into this application and provide erroneous results back to the servers. In order to overcome such problems, Berkeley launched in 2002 the software BOINC – Berkeley Open Infrastructure for Network Computing. This software changed the way volunteers interacted with the workunits and the research project servers. BOINC is a middleware system provided under the GNU

Lesser General Public License. It offers a platform for distributed applications to run, managing the interaction between the *server*, normally in the hands of the institute which developed the research application, and the *client* machine, i.e. the volunteer computer. BOINC inherited the general working procedure from the original SETI@Home application, but became independent from it, having its own development process separated from SETI@Home. Nowadays, SETI@Home is a research project which uses BOINC as a middle platform between the server and the client machines.

After 2004, many Universities and research institutes started realising the potential behind the possibility of harnessing the idle CPU time of individual desktop and laptop computers and started developing their own applications according to their own research areas and goals. Nowadays, BOINC is used in areas as diverse as medicine, climatology, astrophysics, pure mathematics and physics, cryptology, and engineering. It is particularly suited for applications which can be split in minor segments of data and distributed to individual volunteer computers and executed in parallel. It is estimated that there are about 530000 active volunteer machines processing on average $5,4$ PFLOPS (the fastest supercomputer on Earth grants only $2,5$ PFLOPS).

Multi-scale analysis has never been implemented in any distributed computing project to date. For it to be possible, several applications would have to be developed:

- An in-house finite element code. Commercial software can not be used in distributed computing since the application needs to be sent to random users across the globe for free.
- A parallelisation software capable of performing the splitting of a finite element model in different processes possible of running in parallel.
- A validation script to ensure that results sent by client machines have not been tempered.
- A workunits generator which would feed the BOINC server and, from there, the client machines.
- An homogenisation script to perform post-processing of results from the micromechanical model to the macro-scale.
- Material models which would represent adequately the constitutive behaviour of the constituents of the composite.

The last two items of the previous list have been developed in this thesis. Complete development of the remaining scripts would require about 2 man-years since knowledge from both mechanical and computer engineering is required. The BOINC platform itself should not require much development as it is distributed in an almost ready-to-use condition. Implementation of the system requires a server machine with free access to and from the internet for data transfer with the client machines. Although the system was designed to communicate with the outer world, it is also possible, if desirable, to limit communications to inside the research institute or university. Once set-up and running, the system is self regulatory and does not need any human intervention except to update applications as seen fit or other random events such as power cuts.

The BOINC system can be expanded to other branches of engineering or even other fields of research provided the server has the capability to handle all the processes running at any given time. Applications can be developed for any operative system (Windows, Linux, MacOS, Solaris, etc). More recently, the BOINC platform has been upgraded to be able to use not only the idle CPU time, but also both NVIDIA and ATI Graphics Processing Units (GPUs). GPUs can improve computational time up to a factor of $10\times$.

If such a system is implemented, the possibilities are unlimited with regards to the size, complexity, and type of analyses that any given design or research process requires.

Bibliography

[1] Carl T. Herakovich. *Mechanics of Fibrous Composites*. John Wiley & Sons, 1998.

[2] A.B. Strong. History of composite materials – opportunities and necessities. Brigham Young University.

[3] Clara Schuecker. *Mechanism based modeling of damage and failure in fiber reinforced polymer laminates*. PhD thesis, Technischen Universitt Wien, Wien, 2005.

[4] Robert M. Jones. *Mechanics of Composite Materials*. Taylor & Francis, Inc., 2nd edition edition, 1999.

[5] Ronald F. Gibson. *Principles of Composite Material Mechanics*. Engineering Mechanics Series. McGraw-Hill International Editions, 1994.

[6] F.L. Mathews, G.A.O. Davies, D. Hitchings, and C. Soutis. *Finite element modelling of composite materials and structures*. Woodhead Publishing Limited, 2000.

[7] Thomas E. Lacy, David L. McDowell, and Ramesh Talreja. Gradient concepts for evolution of damage. *Mechanics of Materials*, 31(12):831–860, 1999.

[8] R Hill. Elastic properties of reinforced solids: Some theoretical principles. *Journal of the Mechanics and Physics of Solids*, 11(5):357–372, 1963.

[9] W.J. Drugan and J.R. Willis. A micromechanics-based nonlocal constitutive equation and estimates of representative volume element size for elastic composites. *Journal of the Mechanics and Physics of Solids*, 44(4):497–524, 1996.

[10] Zhaohui Shan and Arun M. Gokhale. Representative volume element for non-uniform micro-structure. *Computational Materials Science*, 24(3):361–379, 2002.

[11] S. Yang, Asim Tewari, and Arun M. Gokhale. Modeling of non-uniform spatial arrangement of fibers in a ceramic matrix composite. *Acta Materialia*, 45(7):3059–3069, 1997 1997.

[12] Shriram Swaminathan, Somnath Ghosh, and N.J. Pagano. Statistically equivalent representative volume elements for unidirectional composite microstructures: Part I - without damage. *Journal of Composite Materials*, 40(7):583–604, 2006.

[13] Shriram Swaminathan and Somnath Ghosh. Statistically equivalent representative volume elements for unidirectional composite microstructures: Part II - with interfacial debonding. *Journal of Composite Materials*, 40(7):605–621, 2006.

[14] I.M. Gitman, M.B. Gitman, and H. Askes. Quantification of stochastically stable representative volumes for random heterogeneous materials. *Arch. Appl. Mech.*, 75(2-3):79–92, 2006.

[15] Daniel Trias, Josep Costa, Albert Turon, and J.E. Hurtado. Determination of the critical size of a statistical representative volume element (SRVE) for carbon reinforced polymers. *Acta Materialia*, 54(13):3471–3484, August 2006.

[16] J. R. Brockenbrough, S. Suresh, and H. A. Wienecke. Deformation of metal-matrix composites with continuous fibers: geometrical effects of fiber distribution and shape. *Acta metallurgica et materialia*, 39(5):735–752, 1991.

[17] B.F. Sørensen and R. Talreja. Effects of nonuniformity of fiber distribution on thermally-induced residual stresses and cracking in ceramic matrix composites. *Mechanics of Materials*, 16(4):351–363, 1993.

[18] R. Pyrz. Correlation of microstructure variability and local stress field in two-phase materials. *Materials Science and Engineering A*, 177(1-2):253–259, 1994.

[19] R. Pyrz. Quantitative description of the microstructure of composites. Part I: Morphology of unidirectional composite systems. *Composites Science and Technology*, 50(2):197–208, 1994.

[20] T. Matsuda, N. Ohno, H. Tanaka, and T. Shimizu. Effects of fibre distribution on elastic-viscoplastic behaviour of long fibre-reinforced laminates. *International Journal of Mechanical Sciences*, 45(10):1583–1598, 2003.

[21] Andrei A. Gusev, Peter J. Hine, and Ian M. Ward. Fiber packing and elastic properties of a transversely random unidirectional glass/epoxy composite. *Composites Science and Technology*, 60(4):535–541, 2000.

[22] V. A. Buryachenko, N. J. Pagano, R. Y. Kim, and J. E. Spowart. Quantitative description and numerical simulation of random microstructures of composites and their effective elastic moduli. *International Journal of Solids and Structures*, 40(1):47–72, 2003.

[23] Daniel Trias. *Analysis and Simulation of Transverse Random Fracture of Long Fibre Reinforced Composites*. PhD thesis, University of Girona, Girona, January 2005.

[24] A. Wongsto and S. Li. Micromechanical finite element analysis of unidirectional fibre-reinforced composites with fibres distributed at random over the transverse cross-section. *Composites: Part A*, 36(9):1246–1266, January 2005.

[25] Tetsuya Matsuda, Nobutada Ohno, Hiroki Tanaka, and Toshihiro Shimizu. Homogenized in-plane elastic-viscoplastic behavior of long fibre-reinforced laminates. *JSME International Journal, Series A*, 45(4):538–544, 2002.

[26] Philip M. Dixon. Ripley's K function. In Walter W. Piegorsch Abdel H. El-Shaarawi, editor, *Encyclopedia of Environmetrics*, volume 3, pages 1796–1803. John Wiley & Sons, Ltd, 2002.

[27] B.D. Ripley. The second-order analysis of stationary point processes. *Journal of Applied Probability*, 13(2):255–266, 1976.

[28] Wendy L. Martinez and Angel R. Martinez. *Computational Statistics Handbook with Matlab®*. Chapman & Hall/CRC, 2002.

[29] The MathWorks. *MATLAB & Simulink R2009a® Manual*, 2009.

[30] Hibbit, Karlsson & Sorensen, Inc. *ABAQUS® 6.6/Standard User's Manual*, 2006.

[31] PD Soden, MJ Hinton, and AS Kaddour. Lamina properties, lay-up configurations and loading conditions for a range of fibre-reinforced composites laminates. *Composites Science and Technology*, 58(7):1225–1254, 1998.

[32] O. van der Sluis, P. J. G. Schreurs, W. A. M. Brekelmans, and H. E. H. Meijer. Overall behaviour of heterogeneous elastoviscoplastic materials: effect of microstructural modelling. *Mechanics of Materials*, 32(8):449–462, 2000.

[33] R. J. M. Smit, W. A. M. Brekelmans, and H. E. H. Meijer. Prediction of the mechanical behavior of nonlinear heterogeneous systems by multi-level finite element modeling. *Computer Methods in Applied Mechanics and Engineering*, 155(1-2):181–192, 1998.

[34] D. Trias, J. Costa, J. A. Mayugo, and J. E. Hurtado. Random models versus periodic models for fibre reinforced composites. *Computational Materials Science*, 38(2):316–324, 2006.

[35] W. Voigt. Ueber die beziehung zwischen den beiden elasticitätsconstanten isotroper körper. *Annalen der Physik*, 274(12):573–587, 1889.

[36] A. Reuss. Berechnung der fließgrenze von mischkristallen auf grund der plastizitätsbedingung für einkristalle . *ZAMM - Zeitschrift für Angewandte Mathematik und Mechanik*, 9(1):49–58, 1929.

[37] B. Paul. Prediction of elastic constants of multiphase materials. *Transactions of the Metallurgical Society of AIME*, 218:36–41, 1960.

[38] Z. Hashin and S. Shtrikman. A variational approach to the theory of the elastic behaviour of multiphase materials. *Journal of the Mechanics and Physics of Solids*, 11(2):127–140, March 1963.

[39] Z. Hashin. On elastic behaviour of fibre reinforced materials of arbitrary transverse phase geometry. *Journal of the Mechanics and Physics of Solids*, 13(3):119–134, June 1965.

[40] R. Hill. Theory of mechanical properties of fibre-strengthened materials: I. elastic behaviour. *Journal of the Mechanics and Physics of Solids*, 12(4):199–212, September 1964.

[41] Z. Hashin and B.W. Rosen. The elastic moduli of fiber reinforced materials. *Journal of Applied Mechanics*, 31:223–232, 1964.

[42] Richard M. Christensen. *Mechanics of Composite Materials*. Dover Publications, Inc., Mineola, New York, 1979.

[43] R. M. Christensen and K. H. Lo. Solutions for effective shear properties in three phase sphere and cylinder models. *Journal of the Mechanics and Physics of Solids*, 27(4):315–330, August 1979.

[44] T. Mori and K. Tanaka. Average stress in matrix and average elastic energy of materials with misfitting inclusions. *Acta Metallurgica*, 21(5):571–574, May 1973.

[45] S. Li. General unit cells for micromechanical analyses of unidirectional composites. *Composites: Part A*, 32(6):815–826, 2001.

[46] M.M. Aghdam, M.J. Pavier, and D.J. Smith. Micro-mechanics of off-axis loading of metal matrix composites using finite element analysis. *International Journal of Solids and Structures*, 38(22-23):3905–3925, 2001 2001.

[47] L. E. Asp, L. A. Berglund, and R. Talreja. Prediction of matrix-initiated transverse failure in polymer composites. *Composites Science and Technology*, 56(9):1089–1097, 1996.

[48] V.N. Bulsara, R. Talreja, and J. Qu. Damage initiation under transverse loading of unidirectional composites with arbitrarily distributed fibers. *Composites Science and Technology*, 59:673–682, 1999.

[49] Je Hoon Oh, Kyo Kook Jin, and Sung Kyu Ha. Interfacial strain distribution of a unidirectional composite with randomly distributed fibers under transverse loading. *Journal of Composite Materials*, 40(9):759–778, May 2006.

[50] Daniel Trias, Josep Costa, Bodo Fiedler, Thomas Hobbiebrunken, and Jorge E. Hurtado. A two-scale method for matrix cracking probability in fibre-reinforced composites based on a statistical representative volume element. *Composites Science and Technology*, 66(11-12):1766–1777, 2006.

[51] Kenjiro Terada, Muneo Hori, Takashi Kyoya, and Noboru Kikuchi. Simulation of the multi-scale convergence in computational homogenization approaches. *International Journal of Solids and Structures*, 37(16):2285–2311, April 2000.

[52] L. Canal, J. Segurado, and J. Llorca. Modelización numérica del daño de la matriz en materiales compuestos de matriz polimérica. In *Materiales Compuestos '07*, pages 523–530, 2007.

[53] C. González, J. Segurado, and J. LLorca. Numerical simulation of elasto-plastic deformation of composites: evolution of stress microfields and implications for homogenization models. *Journal of the Mechanics and Physics of Solids*, 52(7):1573–1593, 2004.

[54] Javier Segurado and Javier LLorca. Computational micromechanics of composites: The effect of particle spatial distribution. *Mechanics of Materials*, 38(8-10):873–883, 2006.

[55] J. Segurado and J. LLorca. A numerical approximation to the elastic properties of sphere-reinforced composites. *Journal of the Mechanics and Physics of Solids*, 50(10):2107–2121, 2002.

[56] Essam Totry, Carlos González, and Javier LLorca. Influence of the loading path on the strength of fiber-reinforced composites subjected to transverse compression and shear. *International Journal of Solids and Structures*, 45(6):1663–1675, March 2008.

[57] Martin Ostoja-Starzewski. Material spatial randomness: From statistical to representative volume element. *Probabilistic Engineering Mechanics*, 21(2):112–132, April 2005.

[58] Ever J. Barbero. *Finite Element Analysis of Composite Materials*. CRC, 1 edition, Agugust 2008.

[59] R. Hill. *The Mathematical Theory of Plasticity*. Oxford University Press, 1998.

[60] L. M. Kachanov. *Fundamentals of the Theory of Plasticity*. Dover Publications, Inc., 2004.

[61] Jacob Lubliner. *Plasticity Theory*. Dover Publications, 2008.

[62] Eduardo de Souza Neto, Djordje Perić, and David Owen. *Computational Methods for Plasticity: Theory and Applications*. John Wiley & Sons Ltd, 2008.

[63] *Maxima Manual v5.20.1*, 2009.

[64] Leif E. Asp, Lars A. Berglund, and Peter Gudmundson. Effects of a composite-like stress state on the fracture of epoxies. *Composites Science and Technology*, 53(1):27–37, 1995.

[65] L. E. Asp, L. A. Berglund, and R. Talreja. A criterion for crack initiation in glassy polymers subjected to a composite-like stress state. *Composites Science and Technology*, 56(11):1291–1301, 1996.

[66] B.C. Duncan, Dean G.D., and B.E. Read. Prediction of the performance of adhesives under impact loading. Technical Report 4, NPL, January 1998.

[67] M.N. Charalambides and G.D. Dean. Constitutive models and their data requirements for use in finite element analysis of adhesives under impact loading. Technical Report 2, NPL, April 1997.

[68] F. J. Guild, K. D. Potter, J. Heinrich, R. D. Adams, and M. R. Winsom. Understanding and control of adhesive crack propagation in bonded joints between carbon fibre composite adherends II. finite element analysis. *International Journal of Adhesion and Adhesives*, 21(6):445–453, 2001.

[69] M. N. Charalambides, R. Hardouin, A. J. Kinloch, and F. L. Matthews. Adhesively-bonded repairs to fibre-composite materials I. experimental. *Composites Part A: Applied Science and Manufacturing*, 29(11):1371–1381, November 1998.

[70] B. Fiedler, M. Hojo, S. Ochiai, K. Schulte, and M. Ando. Failure behavior of an epoxy matrix under different kinds of static loading. *Composites Science and Technology*, 61(11):1615–1624, 2001.

[71] B. Fiedler, M. Hojo, S. Ochiai, K. Schulte, and M. Ochi. Finite-element modeling of initial matrix failure in CFRP under static transverse tensile load. *Composites Science and Technology*, 61(1):95–105, January 2001.

[72] B. Fiedler, M. Hojo, and S. Ochiai. The influence of thermal residual stresses on the transverse strength of CFRPI using FEM. *Composites Part A: Applied Science and Manufacturing*, 33(10):1323–1326, October 2002.

[73] Elhem Ghorbel. A viscoplastic constitutive model for polymeric materials. *International Journal of Plasticity*, 24(11):2032–2058, November 2008.

[74] W. N. Mascarenhas, C. H. Ahrens, and A. Ogliari. Design criteria and safety factors for plastic components design. *Materials & Design*, 25(3):257–261, May 2004.

[75] M. N. Charalambides, A. J. Kinloch, and F. L. Matthews. Adhesively-bonded repairs to fibre-composite materials II. finite element modelling. *Composites Part A: Applied Science and Manufacturing*, 29(11):1383–1396, November 1998.

[76] N. W. Tschoegl. Failure surfaces in principal stress space. *Journal of Polymer Science Part C: Polymer Symposia*, 32(1):239–267, 1971.

[77] R. Raghava, R. M. Caddell, and G. S. Y. Yeh. The macroscopic yield behavior of polymers. *Journal Of Materials Science*, 8(2):225–232, 1973.

[78] W.W. Feng and W.H. Yang. General and specific quadratic yield functions. *Journal of Composites Technology and Research*, 6(1):19–21, April 1984.

[79] S. Kolling, A. Haufe, M. Feucht, and P.A. Du Bois. SAMP-1: A semi-analytical model for the simulation of polymers. In *4th LS-DYNA Anwenderforum, Bamberg*, pages 27–52. DYNAmore GmbH, 2005.

[80] R. Rolfes, G. Ernst, M. Vogler, and C. Hühne. Material and failure models for textile composites. In P.C. Camanho, C.G. Dávila, S.T. Pinho, and J.C. Rommers, editors, *Mechanical Response of Composites*, volume 10 of *Computational Methods in Applied Sciences*, pages 27–56. Springer Netherlands, 2008.

[81] J. Zhang, Z. Lin, A. Wong, N. Kikuchi, V. C. Li, A. F. Yee, and G. S. Nusholtz. Constitutive modeling and material characterization of polymeric foams. *Journal of Engineering Materials and Technology*, 119(3):284–291, 1997.

[82] Maria Raquel Valença. *Métodos Numéricos*. Instituto Nacional de Investigação Científica, 1990.

[83] P.P. Camanho and M. Lambert. A design methodology for mechanically fastened joints in laminated composite materials. *Composites Science and Technology*, 66(15):3004–3020, December 2006.

[84] S.W. Tsai. Strength theories of filamentary structures. In R.T. Schwartz and H.S. Schwartz, editors, *Fundamental Aspects of Fiber Reinforced Plastic Composites*, pages 3–11. Wiley International, 1968.

[85] Stephen W. Tsai and Edward M. Wu. A general theory of strength for anisotropic materials. *Journal of Composite Materials*, 5(1):58–80, January 1971.

[86] Z. Hashin and A. Rotem. A fatigue failure criterion for fiber reinforced materials. *Journal of Composite Materials*, 7(4):448–464, October 1973.

[87] Z. Hashin. Failure criteria for unidirectional fiber composites. *J. Appl. Mech.*, 47(2):329–334, June 1980.

[88] A. Puck and H. Schürmann. Failure analysis of FRP laminates by means of physically based phenomenological models. *Composites Science and Technology*, 58(7):1045–1067, July 1998.

[89] C.G. Dávila and P.P. Camanho. Failure criteria for FRP laminates in plane stress. Technical Report NASA/TM-2003-212663, NASA, November 2003.

[90] S.T. Pinho, C.G. Dávila, P.P. Camanho, L. Iannucci, and P. Robinson. Failure models and criteria for FRP under in-plane or three-dimensional stress states including shear non-linearity. Technical Report NASA/TM-2005-213530, NASA, February 2005.

[91] M. C. Lafarie-Frenot, C. Hnaff-Gardin, and D. Gamby. Matrix cracking induced by cyclic ply stresses in composite laminates. *Composites Science and Technology*, 61(15):2327–2336, November 2001.

[92] Thomas Hobbiebrunken, Masaki Hojo, Taiji Adachi, Claas De Jong, and Bodo Fiedler. Evaluation of interfacial strength in CF/epoxies using fem and in-situ experiments. *Composites Part A: Applied Science and Manufacturing*, 37(12):2248–2256, December 2006.

[93] Z. P. Luo and C. Y. Sun. Effect of the interfacial bonding status on the tensile fracture characteristics of a boron-fiber-reinforced aluminum composite. *Materials Characterization*, 50(1):51–58, January 2003.

[94] S. Pimenta, R. Gutkin, S.T. Pinho, and P. Robinson. A micromechanical model for kink-band formation: Part I – Experimental study and numerical modelling. *Composites Science and Technology*, 69(7-8):948–955, June 2009.

[95] John Summerscales. Lecture notes in composites design and manufacture (BEng) - MATS 324. Failure mechanisms. Fractography. Failure criteria. Fracture mechanics. Powerpoint presentation in: http://bit.ly/6LEVFU.

[96] Jon H. Gosse. Strain invariant failure criteria for fiber reinforced polymeric composite materials. In *Thirteenth International Conference on Composite Materials (ICCM-13): Extended Abstracts Jun 25-29, 2001 Beijing, China*, 2001.

[97] J.H. Gosse. Strain invariant failure criteria for polymers in composite materials. In *42nd AIAA/ASME/ASCE/AHS/ASC Structures, Structural Dynamics, and Materials Conferences and Exhibit*. AIAA-2001-1184, April 2001.

[98] S. Ghosh, J. Bai, and P. Raghavan. Concurrent multi-level model for damage evolution in microstructurally debonding composites. *Mechanics of Materials*, Article in Press(Article in Press):Article in Press, 2006.

[99] E. J. Barbero, G. F. Abdelal, and A. Caceres. A micromechanics approach for damage modeling of polymer matrix composites. *Composite Structures*, 67(4):427–436, March 2005.

[100] G. Lubineau, P. Ladevèze, and D. Violeau. Durability of CFRP laminates under thermomechanical loading: A micro-meso damage model. *Composites Science and Technology*, 66(7-8):983–992, June 2006.

[101] Albert S.D. Wang and Karen Chang Yan. On modeling matrix failures in composites. *Composites Part A: Applied Science and Manufacturing*, 36(10):1335–1346, October 2005.

[102] Cecilia Grufman and Fernand Ellyin. Numerical modelling of damage susceptibility of an inhomogeneous representative material volume element of polymer composites. *Composites Science and Technology*, 68(3-4):650–657, March 2008.

[103] Cecilia Grufman and Fernand Ellyin. Determining a representative volume element capturing the morphology of fibre reinforced polymer composites. *Composites Science and Technology*, 67(3-4):766–775, 2007.

[104] F. París, E. Correa, and J. Cañas. Micromechanical view of failure of the matrix in fibrous composite materials. *Composites Science and Technology*, 63(7):1041–1052, May 2003.

[105] E. Correa, V. Mantic, and F. París. Numerical characterisation of the fibre-matrix interface crack growth in composites under transverse compression. *Engineering Fracture Mechanics*, 75(14):4085–4103, September 2008.

[106] E. Correa, V. Mantic, and F. París. A micromechanical view of inter-fibre failure of composite materials under compression transverse to the fibres. *Composites Science and Technology*, 68(9):2010–2021, July 2008.

[107] H. Y. Jeong. A new yield function and a hydrostatic stress-controlled void nucleation model for porous solids with pressure-sensitive matrices. *International Journal of Solids and Structures*, 39(5):1385–1403, March 2002.

[108] Luis P. Canal, Javier Segurado, and Javier LLorca. Failure surface of epoxy-modified fiber-reinforced composites under transverse tension and out-of-plane shear. *International Journal of Solids and Structures*, 46(11-12):2265–2274, June 2009.

[109] A. Puck and H. Schürmann. Failure analysis of FRP laminates by means of physically based phenomenological models. *Composites Science and Technology*, 62(12-13):1633–1662, September 2002.

[110] Carlos González and Javier LLorca. Mechanical behavior of unidirectional fiber-reinforced polymers under transverse compression: Microscopic mechanisms and modeling. *Composites Science and Technology*, 67(13):2795–2806, October 2007.

[111] Essam Totry, Carlos González, and Javier LLorca. Failure locus of fiber-reinforced composites under transverse compression and out-of-plane shear. *Composites Science and Technology*, 68(3-4):829–839, March 2008.

[112] Essam Totry, Carlos González, and Javier LLorca. Prediction of the failure locus of C/PEEK composites under transverse compression and longitudinal shear through computational micromechanics. *Composites Science and Technology*, 68(15-16):3128–3136, December 2008.

[113] T. J. Vogler and S. Kyriakides. Inelastic behavior of an AS4/PEEK composite under combined transverse compression and shear. part I: experiments. *International Journal of Plasticity*, 15(8):783–806, 1999.

[114] R. Rolfes, G. Ernst, D. Hartung, and J. Tessmer. Strength of textile composites a voxel based continuum damage mechanics approach. In C.A. Mota Soares, J.A.C. Martins, H.C. Rodrigues, J.A.C. Ambrsio, C.A.B. Pina, C.M. Mota Soares, E.B.R. Pereira, and J. Folgado, editors, *III European Conference on Computational Mechanics – Solids, Structures and Coupled Problems in Engineering*, pages 32–64. Springer Netherlands, 2006.

[115] Zdeněk P. Bažant and B.H. Oh. Crack band theory for fracture of concrete. *Materials and Structures*, 16(3):155–177, May 1983.

[116] L.M. Kachanov. Time of the rupture process under creep conditions. *Isv. Nauk SSSR, Otd. Tehk. Nauk*, 8:26–31, 1958.

[117] Alix Cauvin and Rene B. Testa. Damage mechanics: basic variables in continuum theories. *International Journal of Solids and Structures*, 36(5):747–761, February 1999.

[118] Y.N. Rabotnov. Creep rupture. In M. Hetenyi and W.G. Vincenti, editors, *Proc. 12th Int. Congr. Appl. Mech.*, pages 342–349. Springer-Verlag, Berlin, 1968.

[119] Alix Cauvin and Rene B. Testa. Elastoplastic material with isotropic damage. *International Journal of Solids and Structures*, 36(5):727–746, February 1999.

[120] P. Ladevèze. Sur la mécanique de l'endommagement des composites. In C. Bathias and D. Menkès, editors, *Comptes rendus des JNC5*, pages 667–683. Pluralis, Paris, 1986.

[121] J. Lemaître and J.-L. Chaboche. *Mechanics of Solid Materials*. Cambridge University Press, 1990.

[122] P. Maimí, P.P. Camanho, J.A. Mayugo, and C.G. Dávila. A thermodynamically consistent damage model for advanced composites. Technical Report NASA/TM-2006-214282, NASA, March 2006.

[123] P. Maimí, J.A. Mayugo, and P.P. Camanho. A three-dimensional damage model for transversely isotropic composite laminates. *Journal of Composite Materials*, 42(25):2717–2745, 2008.

[124] Lawrence E. Malvern. *Introduction to the Mechanics of a Continuous Medium*. Engineering of the Physical Sciences. Prentice-Hall, 1969.

[125] J.C. Simo and J.W. Ju. Strain- and stress-based continuum damage models–I. formulation. *International Journal of Solids and Structures*, 23(7):821–840, 1987.

[126] J.C. Simo and J.W. Ju. Strain- and stress-based continuum damage models–II. computational aspects. *International Journal of Solids and Structures*, 23(7):841–869, 1987.

[127] S.T. Pinho, L. Iannucci, and P. Robinson. Physically based failure models and criteria for laminated fibre-reinforced composites with emphasis on fibre kinking. part ii: Fe implementation. *Composites Part A: Applied Science and Manufacturing*, 37(5):766–777, May 2006.

[128] Giuseppe Catalanotti. *Analytical, Numerical and Experimental Analysis of Multi-Material Joints*. PhD thesis, Faculdade de Engenharia da Universidade do Porto, 2010.

[129] T. Ishikawa. Anti-symmetric elastic properties of composite plates of satin weave cloth. *Fibre Science and Technology*, 15:127–, 1981.

[130] Takashi Ishikawa and Tsu-Wei Chou. Elastic behavior of woven hybrid composites. *Journal of Composite Materials*, 16(1):2–19, 1982.

[131] Jenn-Ming Yang, Chang-Long Ma, and Tsu-Wei Chou. Fiber Inclination Model of Three-Dimensional Textile Structural Composites. *Journal of Composite Materials*, 20(5):472–484, 1986.

[132] Thomas J. Whitney and Tsu-Wei Chou. Modeling of 3-D Angle-Interlock Textile Structural Composites. *Journal of Composite Materials*, 23(9):890–911, 1989.

[133] J. Byström, N. Jekabsons, and J. Varna. An evaluation of different models for prediction of elastic properties of woven composites. *Composites Part B: Engineering*, 31(1):7 – 20, 2000.

[134] M.J. King, P. Jearanaisilawong, and S. Socrate. A continuum constitutive model for the mechanical behavior of woven fabrics. *International Journal of Solids and Structures*, 42(13):3867 – 3896, 2005.

[135] Masaru Zako, Yasutomo Uetsuji, and Tetsusei Kurashiki. Finite element analysis of damaged woven fabric composite materials. *Composites Science and Technology*, 63(3-4):507–516, February 2003.

[136] E.J. Barbero, P. Lonetti, and K.K. Sikkil. Finite element continuum damage modeling of plain weave reinforced composites. *Composites Part B: Engineering*, 37(2-3):137–147, April 2006.

[137] Stepan V. Lomov, Dmitry S. Ivanov, Ignaas Verpoest, Masaru Zako, Tetsusei Kurashiki, Hiroaki Nakai, and Satoru Hirosawa. Meso-fe modelling of textile composites: Road map, data flow and algorithms. *Composites Science and Technology*, 67(9):1870–1891, July 2007.

[138] Ignaas Verpoest and Stepan V. Lomov. Virtual textile composites software wisetex: Integration with micro-mechanical, permeability and structural analysis. *Composites Science and Technology*, 65(15-16):2563–2574, December 2005.

[139] Saeed Moaveni. *Finite element analysis : theory and application with ANSYS*. Upper Saddle River, NJ : Pearson Prentice Hall, cop., 2003.

[140] S. Daggumati, W. Van Paepegem, J. Degrieck, J. Xu, S.V. Lomov, and I. Verpoest. Local damage in a 5-harness satin weave composite under static tension: Part ii - meso-fe modelling. *Composites Science And Technology*, 70:1934–1941, 2010.

[141] C. Chamis. Mechanics of composite materials past, present and future. Technical report, NASA technical memorandum 100793, 1984.

[142] Oscar Hoffman. The brittle strength of orthotropic materials. *Journal of Composite Materials*, 1(2):200–206, 1967.

[143] Edilar Paulo Predabon and Cássio Bocchese. *SolidWorks 2004 : projeto e desenvolvimento*, são paulo : Érica, 204 edition, 2004.

[144] UGS, The PLM Company. *FEMAP® Commands, Version 9.0*, 2005.

Appendix A

MATLAB® script for RAND_uSTRU_GEN

Appendix A contains the code used in the developed MATLAB® [29] script RAND_uSTRU_GEN. A folder with the files can be found on the CD attached.

This script can be used to generate spatial fibre distributions having a high fibre volume fraction in a short amount of time. Section 2.2 details its flowchart and input variables.

Different functions were developed along with the script for very special needs. These functions are also listed here. Among them is a function to determine if there is overlapping between any two fibres, a function to generate images of the fibre distribution along the process, a function to statistically characterise the generated distributions, a function to generate a 2D triangular mesh and a function to post-process the results from ABAQUS® [30].

Appendix B

MATLAB® script for pre-processing

Appendix B contains the code developed to perform all the analyses required for chapter 3. The scripts were all programmed in MATLAB® [29] and can be found in a folder on the attached CD.

The first script is the only one where the user is required to input data. It controls and makes use of all the following scripts as well as the script for generation of a random fibre distribution presented in appendix A. The second script is responsible for all the pre-processing required (as per section 3.2) – creation of the Python scripts needed for ABAQUS® [30] to generate the three dimensional mesh and definition of periodic boundary conditions. The third script is divided in several conditions, where each of these correspond to a different set of applied loads. The main `input` file for ABAQUS® [30] is generated here.

The fourth script is also divided in several conditions, one for each set of applied loads, but the objective now is to post-process the results from the finite element analyses performed.

Appendix C

FORTRAN code with plasticity model

Appendix C contains the FORTRAN code with the plasticity model for epoxy matrices explained in Chapter 4. The user subroutine which has been implemented in ABAQUS® [30] can be found in a folder in the attached CD.

Appendix D

UMAT with both constitutive models

Appendix D contains the FORTRAN code with the complete constitutive model to be applied for both matrix and fibre material, as it was presented in Chapter 5. The user subroutine which has been implemented in ABAQUS® [30] can be found in a folder in the attached CD.

There can be found three main subroutines:

- The first subroutine distinguishes the two materials based on their name as it is read in the `.inp` file.
- The second subroutine applies to the reinforcing material assuming it is a transversely isotropic material.
- The third subroutine applies to the matrix material assuming it is an isotropic material.

Appendix E

MATLAB® scripts for 5-harness satins

Appendix E contains the code developed to perform pre- and post-processing of the analyses executed for chapter 7. The scripts were all programmed in MATLAB® [29] and can be found in a folder on the attached CD.

There are three computer codes:

- The first script implements two dimensional periodic boundary conditions on the representative unit-cell of a weave (a 5-harness satin weave in the particular case, but the script can be applied to any type of textile pattern).
- The second script is an implementation of the `ORIENT` subroutine on the commercial finite element software ABAQUS® [30] which defines the material orientation for each element of the representative unit-cell under consideration.
- The third script provides the post-processing script which has been implemented in MATLAB® [29] to perform volumetric homogenisation on the results from the micromechanical analyses.